Frost heave in fine-grained material during artificial ground freezing under different boundary conditions

Von der Fakultät für Bauingenieurwesen
der Rheinisch-Westfälischen Technischen Hochschule Aachen
zur Erlangung des akademischen Grades einer Doktorin der Ingenieurwissenschaften
genehmigte Dissertation

vorgelegt von

Katharina Niggemann

Berichter: Univ.-Prof. Dr. Raul Fuentes
Univ.-Prof. Dr.-Ing. Conrad Boley

Tag der mündlichen Prüfung: 21.06.2024

Diese Dissertation ist auf den Internetseiten der Universitätsbibliothek online verfügbar.

Sweidan, A. H., Niggemann, K., Heider, Y., Ziegler, M., Markert, B. (2022): Experimental study and numerical modeling of the thermo-hydro-mechanical processes in soil freezing with different frost penetration directions. Acta Geotechnica, 17(1), pp. 231-255.
https://doi.org/10.1007/s11440-021-01191-z

Niggemann, K., Fuentes, R. (2023): New semi-analytical approach for ice lens heaving during artificial freezing of fine-grained material. Journal of Rock Mechanics and Geotechnical Engineering, 15(11), pp. 2994-3009.
https://doi.org/10.1016/j.jrmge.2023.07.004

Niggemann, K., Ziegler, M., Fuentes, R. (2024): Influence of freezing directions on ice lens formations in soils. Acta Geotechnica.
https://doi.org/10.1007/s11440-024-02259-2

D 82 (Diss. RWTH Aachen University, 2024)

Table of contents

List of Figures **III**

List of Tables **V**

List of Symbols **VII**

Kurzfassung **XI**

Abstract **XIII**

1 Introduction **1**

1.1. Motivation 1
1.2. Objective and structure of the work 2

2 Frozen ground **5**

2.1. Artificial ground freezing 5
2.2. Natural ground freezing 7
2.3. Differences between AGF and naturally frozen ground 9

3 Thermal basics of frozen soil **11**

3.1. Heat transfer mechanism 11
3.1.1. Heat conduction 12
3.1.2. Convection 13
3.2. Thermal properties of soils 13
3.2.1. Thermal conductivity 14
3.2.2. Heat capacity 16
3.2.3. Latent heat 16
3.3. Freezing soil characteristics 17
3.3.1. Freezing water 17
3.3.2. Phase change and freezing point depression 19
3.3.3. Pressure and temperature relations 21

4 Soil water **25**

4.1. Soil structure and water interaction 25
4.2. Soil water hydraulics 27
4.2.1. Darcy Law 27
4.2.2. Continuity 29
4.2.3. Fluid flow 30

4.3. Water transport mechanism 30

5 Frost heave with ice lens formation 33

5.1. Ice lens formation 33
5.1.1. Frozen Fringe 36
5.2. Factors affecting frost heave 38
5.3. Frost heave models 39
5.3.1. Capillary theory 39
5.3.2. Rigid Ice Model 40
5.3.3. Segregation Potential 41

6 Experimental and analytical study on frost heave with ice lens formation for an AGF 45

6.1. Paper #1 46
6.2. Paper #2 47
6.3. Paper #3 48

7 Summary and outlook 49

7.1. Key findings 49
7.2. Future research 51

References 53

Publications 61

Appendices 63

List of Figures

Figure 1: Application of soil stabilizing methods for different soils, after Johansson (2009) 6
Figure 2: Artificial ground freezing via a) Brine cooling and b) Liquid Nitrogen cooling, after Manassero (2020) 7
Figure 3: Special terrain features in permafrost areas, after Ladanyi and Andersland (2004) 8
Figure 4: Regions of prevailing influence of the various heat transfer mechanism in relation to grain size and saturation degree, after Frivik et al. (1977) and Johansen (1977b) 11
Figure 5: Mass-volume relationship for frozen and unfrozen soil, after Ladanyi and Andersland (2004) 14
Figure 6: Thermal conductivity of soil constituents, after Frivik (1981) 15
Figure 7: Temperature dependent specific heat of soil constituents, after Johansen (1977) 16
Figure 8: Phase diagram for pure water, after Atkins (1996) 18
Figure 9: Freezing curve for soil water, after Ladanyi and Andersland (2004) 19
Figure 10: Schematic illustration of the a) temperature-enthalpy curve during phase change, and b) temperature-time curve during solidification, after Frohberg (2009) 19
Figure 11:Free energy-temperature relation of water, soil water, and ice, after Williams and Smith (1989) 21
Figure 12: Non-single grain structures of fine soil material, after Kolymbas (2019) 25
Figure 13: Ion distribution in the electrical double layer, after Amelung et al. (2018) 26
Figure 14: Electro-molecular force effect in the environment of a solid particle in groundwater, after Busch et al. (1993) 26
Figure 15: Flow areas of the dynamic fundamental law of geohydraulics, after Busch et al. (1993) 29
Figure 16: Classification of frost susceptibility, after ZTV E-StB 17 (2017) 33
Figure 17: Rhythmic ice lens formation, after Konrad and Morgenstern (1980) 35
Figure 18: Schematic illustration of the frozen fringe, after Konrad (1993) 36
Figure 19: Characteristic of the frozen fringe at ice lens initiation and growth, after Sheng et al. (1995) 37
Figure 20: Experienced cracks after freezing of clay; vertical (A) and horizontal (B and C) sections, after Chamberlain and Gow (1979) 38
Figure 21: Schematic illustration of the theorized capillary pore, after Johansson (2009) 40
Figure 22: Frozen fringe characteristics of temperature, permeability, and suction, after Konrad and Morgenstern (1981) 42

List of Tables

Table 1: Listed publications during this thesis 45

List of Symbols

Latin Characters

A	[m^2]	cross-section/area
a	[m^2/s]	thermal diffusivity
C_r	[-]	proportionality factor
c_s	[J/kgK]	specific heat capacity
c_v	[J/m^3K]	volumetric heat capacity
d	[m]	soil grain diameter
d_{eff}	[m]	effective soil grain diameter
e	[-]	void ratio
e_{sep}	[-]	separating void ratio
G	[J]	free enthalpy/ Gibbs free energy
H	[J]	enthalpy
h	[m]	hydraulic height
h_s	[m]	segregation frost heave
i	[-]	hydraulic gradient
K	[m^2]	intrinsic permeability
k	[m/s]	hydraulic conductivity coefficient
L	[J/kg]	latent heat
L_f	[J/kg]	latent heat of fusion
l	[m]	length
l_{ff}	[m]	length of the frozen fringe
n	[-]	porosity
P	[Pa]	pressure
P_0	[Pa]	pressure at the frost line
P_{IL}	[Pa]	pressure at the ice lens
P_i	[Pa]	ice pressure
P_w	[Pa]	water pressure
q	[W/m^2]	heat flow

r	[-]	flow direction
r_i	[mm]	radius of soil ice curvature
r_p	[mm]	effective pore radius
S_r	[-]	degree of saturation
S_s	[-]	specific storage coefficient
s	[J/K]	entropy
T	[K]	temperature
T_f	[K]	freezing temperature
T_{IL}	[K]	ice lens temperature
T_l	[K]	liquidus temperature
T_{pc}	[K]	temperature of phase change
T_s	[K]	solidus temperature
T_{sc}	[K]	supercooled water temperature
T_{sf}	[K]	segregation-freezing temperature
T_{sm}	[K]	temperature when ice lens growth stops
T_w	[K]	soil water temperature
t	[s]	time
U	[J]	internal energy
V	[m^3]	volume
v	[m/s]	seepage velocity

Greek Characters

α, β	[-]	characteristic soil parameter
γ	[N/m]	interfacial tension
η	[Pas]	dynamic viscosity
θ_w	[-]	unfrozen water content
κ_{iw}	[1/m]	curvature of ice-water interface
λ	[W/mK]	thermal conductivity
λ_g	[W/mK]	thermal conductivity of soil particle
λ_i	[W/mK]	thermal conductivity of ice

λ_q	[W/mK]	thermal conductivity of quartz
λ_r	[W/mK]	thermal conductivity of remaining solids
λ_w	[W/mK]	thermal conductivity of water
μ	[J/mol]	chemical potential
ν	[m^2/s]	kinematic viscosity
ρ_{soil}	[kg/m^3]	density of soil
ρ_w	[kg/m^3]	density of water
σ	[Pa]	stress
σ'	[Pa]	effective stress
σ_n	[Pa]	neutral stress
σ_{OB}	[Pa]	overburden stress
σ_{sep}	[Pa]	separation stress
χ	[-]	quantity function
ψ_z	[J/kg]	gravitational potential
ψ_m	[J/kg]	matric potential
ψ_g	[J/kg]	gas potential
ψ_o	[J/kg]	osmotic potential

Common Indices

0	frost line
ff	frozen fringe
g	soil grain
IL	ice lens
i	ice
uf	unfrozen
w	water

Common Abbreviations

AGF	artificial ground freezing
BF	bottom freezing

LN	liquid nitrogen
NMR	nuclear magnetic resonance
PFM	phase-field modeling
SP	Segregation Potential
TF	top freezing
TPM	theory of porous media

Kurzfassung

Der weltweit steigende Bedarf an leistungsfähiger Infrastruktur erfordert zunehmend effektive und reversible Bauverfahren. Insbesondere im innerstädtischen Bereich werden Baumaßnahmen zunehmend unterirdisch geplant. Um bestehende Infrastruktur und Bauwerke über und unter Tage während der Bauphase nicht zu beeinträchtigen, werden spezielle Anforderungen an die Baumaßnahme gestellt. Dabei wird immer häufiger das spezielle Verfahren der künstlichen Bodenvereisung zur temporären Verbesserung der Bodeneigenschaften angewendet. Das Verfahren der künstlichen Bodenvereisung nutzt die Vorteile von Wasserdichtigkeit und Stabilität des gefrorenen Bodens und ist dazu ein reversibles Verfahren, da der gefrorene Boden nach der Baumaßnahme wieder auftaut. In Abhängigkeit von der Bodenart und den vorliegenden Randbedingungen kann der Phasenübergang von Wasser zu Eis jedoch Frosthebungen hervorrufen, die zu Bauschäden z. B. an Straßen, Wegen und Bebauungen führen können. Insbesondere das Gefrieren von sehr feinen Böden wie Schluff und Ton kann durch die Bildung von Eislinsen zu große Frosthebungen führen. In Abhängigkeit von den vorhandenen Randbedingungen können diese gefrorenen Bereiche mehrere Zentimeter hoch werden.

Die ersten Untersuchungen zur Eislinsenbildung stammen aus der Forschung in kalten Regionen oder Permafrostgebieten, wobei sich die Randbedingungen von denen einer künstlichen Bodenvereisung unterscheiden. Eine direkte Übertragung von wissenschaftlichen Erkenntnissen aus der Permafrostforschung ist daher nicht möglich. Die vorliegende Arbeit befasst sich mit der Bildung von Eislinsen in feinkörnigem Material während des Gefrierprozesses unter Berücksichtigung der Randbedingungen einer künstlichen Bodenvereisung. Dies beinhaltet einen Überblick über die thermischen und thermodynamischen Grundlagen gefrorenen Bodens sowie eine Zusammenfassung zum Stand der Forschung auf diesem Gebiet.

Der Hauptteil dieser Arbeit umfasst eine umfangreiche experimentelle Studie zur Eislinsenbildung unter Berücksichtigung der speziellen Randbedingungen einer künstlichen Bodenvereisung. Es wurde ein neues Versuchsgerät entwickelt, mit dem die Untersuchung der zwei Hauptgefrierrichtungen einer Bodenvereisung möglich ist. Dies beinhaltet das Gefrieren von unten nach oben (bottom freezing - BF) sowie das Gefrieren in entgegengesetzter Richtung von oben nach unten (top freezing - TF). Diese beiden Gefrierrichtungen wurden im Rahmen eines Untersuchungsprogramms mit 62 Gefrierversuchen miteinander verglichen, wobei verschiedene Parameter wie die Temperatur oder die Belastung verändert wurden. Jeder Versuch wurde in eine thermisch instationäre und eine thermisch stationäre Phase unterteilt. Während der thermisch instationären Phase ist die Gefrierfront aufgrund der thermischen Randbedingungen in Bewegung (vergleichbar mit der natürlichen Bodenvereisung). Mit der Zeit nimmt die Frosteindringgeschwindigkeit ab, bis ein thermisch (quasi-)stationärer Zustand mit einer

stationären Gefrierfront erreicht ist. Dieser Zustand ist vergleichbar mit der Haltephase bei einer künstlichen Bodenvereisung und insbesondere bei langen Bauphasen zu berücksichtigen.

Die Ergebnisse der experimentellen Frosthebungsuntersuchungen wurden genutzt, um einen neuen semi-analytischen Ansatz für die Berechnung von Frosthebungen zu entwickeln. Ziel war es, die komplexen Prozesse während der Eislinsenbildung in einem Ansatz, der keine zusätzlichen komplexen Untersuchungen oder Parameterannahmen erfordert, zu erfassen.

Das bestehende "Segregationspotential (SP)" von *Konrad und Morgenstern* wurde hauptsächlich und erfolgreich für die Berechnung von Hebungen infolge natürlichen Bodenfrosts in kalten Regionen eingesetzt. Für eine Hebungsprognose infolge einer künstlichen Bodenvereisung ist der Ansatz jedoch nicht geeignet. Der neu entwickelte semi-analytische Ansatz berücksichtigt die Randbedingungen einer künstlichen Bodenvereisung wie das Gefrieren von unten nach oben (BF), Temperaturgradienten zum Erreichen großer Gefriergeschwindigkeiten und eine Unterscheidung zwischen instationärem und stationärem Gefrierzustand. Um die Eignung des Ansatzes zu überprüfen, wird er ebenfalls auf das Top-down-Gefrieren (TF) angewendet. Der neue Ansatz wird anhand von zwei verschiedenen frostempfindlichen Böden und insgesamt 50 Frosthebungsversuchen validiert.

Abstract

The rising demand on infrastructure worldwide increasingly requires effective and reversible construction methods. Especially in inner-city areas, infrastructure engineering is increasingly planned underground. High standards must be fulfilled during the construction phase to ensure that the existing infrastructure and buildings above- and underground are not impaired. To meet these requirements one special technique is the artificial ground freezing (AGF), used as temporary soil-improving method. The AGF uses the advantages of waterproofness and stability of frozen soil and is reversible as the frozen soil thaws. However, depending on the soil type and the present boundary conditions, the phase change of water into ice may result in frost heave, which can lead to structural damage to, e.g., streets, tracks, and buildings. Especially the freezing of very fine soil, like silt and clay, may evoke great frost heave due to ice lens formation. Depending on the surrounding conditions these frozen water layers grow to several centimeters in height.

Initially, the study on ice lens formation comes from research in cold regions or permafrost areas with different boundary conditions than they present AGF. Therefore, a direct transfer of scientific findings from permafrost research is not proven. This work focus on the formation of ice lenses in fine-grained material during the freezing process considering the boundary conditions of an AGF. This includes an overview of thermal and thermodynamic basics of frozen soil as well as a review on work that has been done in this field.

The main part of this work includes an extensive experimental study on ice lens formation considering the special boundary conditions of an AGF. A new experimental set-up was built to focus on two main freezing directions during soil freezing. One is the freezing from the bottom upwards (bottom freezing – BF) and the other vice versa, from the top downwards (top freezing – TF). These two freezing directions were compared carrying out 62 freezing tests while changing different parameters, like temperature or overburden load. Each test was separated into a thermal transient and thermal steady-state phase. During the thermal transient phase, the freezing front is in motion due to the thermal boundary conditions (comparable with natural ground freezing). With time, the frost penetration velocity decreases until thermal (quasi-)equilibrium with a stationary freezing front is reached. This state is comparable with the holding phase of an AGF and important to consider at long construction durations.

The results of the experimental tests were used to develop a new semi-analytical approach for the calculation of frost heaving. The aim is to capture the complex processes during ice lens formation in one approach that does not require additional complex tests or parameter assumptions.

The existing “Segregation Potential (SP)” of *Konrad and Morgenstern* approach has been mainly and successfully applied to the heave calculation of natural-induced ground freezing in cold

regions. However, its application to AGF has been so far unsuccessful. The newly developed semi-analytical approach includes the AGF conditions such as bottom-up freezing, temperature gradients to reach great freezing velocities, and a distinction between the transient and steady-state freezing states. To test the approaches' ability, it is applied to the top-down freezing. The new approach is validated using two different frost-susceptible soils and, in total, 50 frost heave tests.

1 Introduction

1.1. Motivation

Frozen ground is a conglomerate of grains and pores filled with water, ice, or air. The ice phase takes over a binder function, improving the mechanical characteristics of the soil and making it almost impermeable (Manassero 2020). Artificial ground freezing (AGF) uses these advantages and is applied worldwide as a temporary soil-improving method. This includes forming frozen earth walls to support deep excavations, foundation improvement's structural underpinning, and temporary groundwater control (Viggiani & Casini 2015). Especially the increasing demand for infrastructural development, particularly in inner-city areas, is leading to an increasing application of AGF to ensure a required waterproofing function and stability during construction. However, depending on the soil type and the present boundary conditions, the phase change of water into ice may provoke frost heave, which can lead to structural damage to, e.g., streets, tracks, and buildings.

Frost heave results from the approximately 9% volume expansion during the phase change of water into ice. It broadly happens at two levels. One the one hand, the water at the soil pores freezes and on the other water migration through the frozen soil can lead to ice lens formation. Hence, the saturation degree and the hydraulic conductivity are very relevant characteristics. In frost-sensitive soils, like silt or clay, the water cannot be expelled during rapid cooling and freezes in situ due to their small hydraulic conductivity. Moreover, as mentioned, pure ice layers (ice lenses) can form in these fine-grained soils, growing to several centimeters in height depending on the boundary conditions.

The investigation of frost heaving with ice lens formation initially comes from research in cold regions or permafrost areas where the soil freezes naturally. For AGF, the freezing mechanism is similar, but the boundary conditions are different, which does not allow a direct transfer of scientific findings from permafrost research. At AGF, a frozen body grows radially around the freezing pipe, and ice lenses form perpendicular to the direction of heat transport. In contrast, at natural freezing, the frost penetrates the soil from the ground surface downwards due to ambient temperatures. In permafrost areas, freezing can also be directed upwards from the permafrost into the active area. Besides different freezing directions, natural and artificial freezing are different concerning:

- freezing duration and thermal state during freezing (transient or stationary),
- freezing temperature, and
- overburden load.

Conclusive investigations on the boundary conditions of an AGF heave prediction are missing. Analytical (e.g., Konrad & Morgenstern 1980; 1981; 1982; Han & Goodings 2006; Li et al. 2018;

Cai et al. 2019) and numerical (e.g., Gilpin 1980; O'Neill & Miller 1985; Fremond & Mikkola 1991; Nixon 1991; Hartikainen & Mikkola 1997; Hansson et al. 2004; Michalowski & Zhu 2006; Rempel 2007; Nishimura et al. 2009; Zhang & Michalowski 2015; Ji et al. 2019; Sweidan et al. 2021; Cai et al. 2022) approaches exist in the literature, but they do not fulfill the requirements for the prediction of frost heave including the calculation of ice lens formation during AGF. The existing numerical approaches are usually associated with a high experimental effort and special tests, so they are only used in practice in individual cases. Since the complex microscopic processes in ice lens formation have not yet been fully researched, parameters must be approximated or assumed in the numerical solution. The analytical approach of *Konrad and Morgenstern* has been used to predict frost heaving in cold or permafrost regions (Nixon 1982; Konrad & Shen 1996; Tiedje & Guo 2012; Zhang et al. 2020) but has its limitations concerning the heave prediction of an AGF.

The prediction of frost heaving with ice lens formation for AGF projects is hence, usually still based on soil frost susceptibility recommendations (Auld et al. 2015). Due to this lack of estimating tools, frost heave at the surface is mainly identified by observation methods and controlled by adapting the freezing operation accordingly during construction.

1.2. Objective and structure of the work

This work aims to investigate frost heave with ice lens formation considering the boundary conditions of an AGF. This includes the development of a new test device to carry out long-term freezing tests considering the specific boundary conditions. Imitating frost heave at the ground surface, this test device was able to simultaneously test the two main freezing directions from the top downwards (top freezing - TF) and from the bottom upwards (bottom freezing - BF). This enables the extent to which the direction of freezing influences frost heave to be investigated. Collaborating with the Chair and Institute of General Mechanics (IAM, RWTH Aachen University) within the framework of a DFG project, the first results of the experimental tests were used by the IAM to verify a numerical model to calculate soil expansion by freezing. Based on the findings of an extensive experimental program, a semi-analytical approach was developed to calculate frost heave with ice lens formation.

To achieve the work progress and aims, a literature review concerning the freezing methods, thermal fundamentals, information on soil water and their interaction, and the basics of frost heave with ice lens formation is given in chapters 2 to 5.

Essential information on natural freezing and AGF, as well as the differences between them, are given in chapter 2. The distinction between natural freezing and AGF is the basis for the investigated parameters in the experimental study.

Chapter 3 includes the thermal basics of frozen ground, explaining the heat transfer mechanism and the thermal properties of the soil. Further, fundamentals concerning the freezing characteristic are given. This includes information on the freezing point and the phase change of soil with its

pressure and temperature relations. These basics are essential to understand the freezing process, and the mechanism of ice lens formation explained in chapter 5.

The fundamentals of soil water interaction, groundwater hydraulics, and water transport mechanism in soils are given in chapter 4. This chapter includes general information about water flow in soils but also deals with the attraction of water to soil grains, which is a fundamental issue concerning ice lens formation.

In chapter 5, frost heave with ice lens formation is explained. Beginning with the definition of the frozen fringe as an area of ice lens formation and the liquid water film as a driving force concerning ice lens formation, factors affecting frost heave are listed. Subsequently, frost-heave theories or models are given. They include the Segregation Potential of *Konrad and Morgenstern*, which is the basis for the newly developed semi-analytical approach in this work.

Next, chapter 6 summarizes the conducted research, which is describes in detail in the attached contributions (Appendix A-C). It includes a description of the developed experimental device with its boundary conditions. Essential information about the mechanical and thermal soil parameters, extracted parameters during the test, and initial findings from the experiments are given. The first experimental test results are used to verify a numerical model built by the Chair and Institute of General Mechanics (RWTH Aachen University) to calculate soil expansion by freezing.

In total, 62 experiments were conducted. Each parameter variation was carried out for top downwards freezing (TF) and bottom upwards freezing (BF) and gave an insight into the differences in freezing direction. Detailed information about soil water distribution in the soil sample after freezing and the associated crack formation, which changes the hydraulic conductivity of the soil sample, is also given.

The findings of the experimental investigation were used to develop a semi-analytical approach for calculating frost heave with ice lens formation. The validation of the approach is done using two different frost-sensitive soils. The results are compared with the Segregation Potential approach of Konrad and Morgenstern (1980; 1981; 1982).

This work concludes with a summary of the main findings and an outlook on the need for further research.

2 Frozen ground

Frozen ground occurs when soil or rock is cooled down below 0°C. Assuming a total saturation of the ground, it usually consists of two to three phases with soil grains, water, or/and ice. The significant increase in soil strength and stability combined with its water-resisting property turns the frozen ground into an attractive engineering solution. However, it also has risks because ice lens formation can lead to ground heaving up to several meters in perennially frozen ground. Also, during AGF, the occurring heaves can reach centimeters or decimeters and may lead to enormous structural damage (Ladanyi & Andersland 2004).

The investigations carried out in this work refer to AGF so that the contents on natural ground freezing are presented for completeness but not in detail. Therefore, more extensive information about natural ground freezing can be found, for example, in Ladanyi and Andersland (2004).

2.1. Artificial ground freezing

Artificial ground freezing (AGF) was initially used in the mining industry by the engineer Herman Poetsch who invented it in 1883 (Staender 1967). The principle of ground freezing is to artificially extract heat from the ground so that the water in the ground freezes. The application of AGF to support unstable soils and systems became a prevalent method in the last decades, and the field of application is diverse, like excavation pits, underpinning, and tunneling. Especially for developing underground infrastructure in inner-city areas, AGF is a widespread method. Compared to other ground treatment methods, the application range covers all soil types (cf. Figure 1). However, strong groundwater flow can lead to difficult freezing conditions with no freezing success. The critical groundwater velocity given by Jessberger (1979) is about 2.0-3.0 m/d. A requirement for conducting ground freezing is a sufficiently available water content in the soil, which can be treated by controlled addition of water if necessary (Jessberger 1979; Orth 2018).

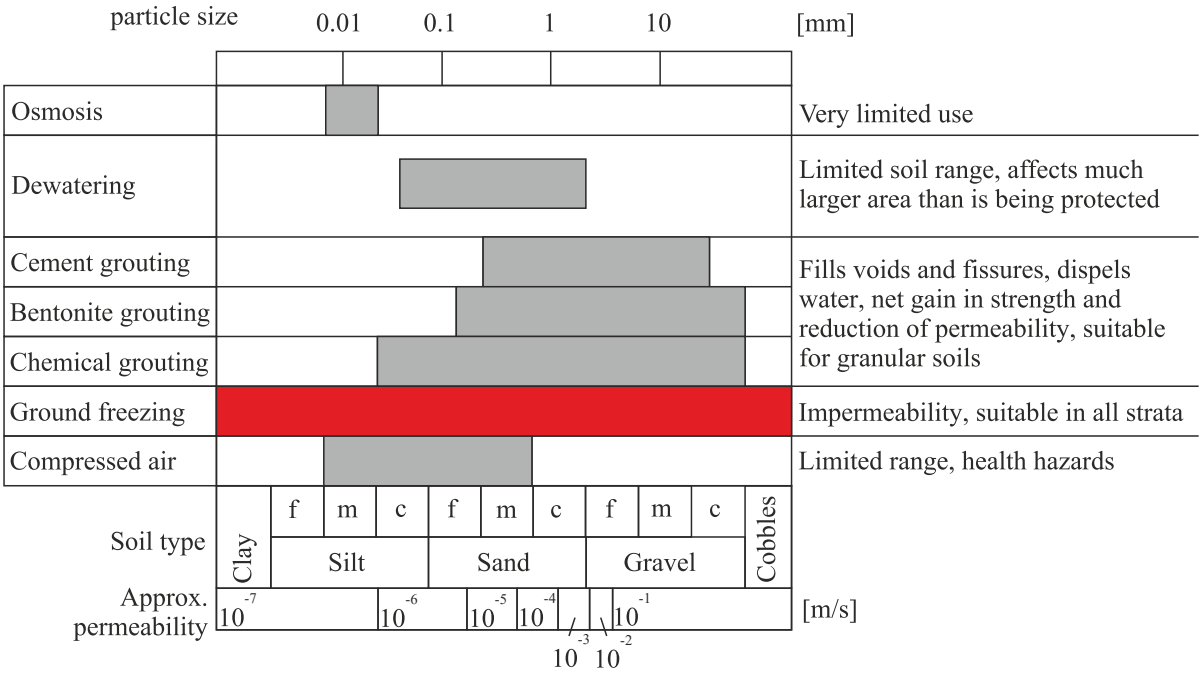

Figure 1: Application of soil stabilizing methods for different soils, after Johansson (2009)

To implement an artificially frozen ground, freezing pipes need to be installed in which a cooling medium circulates. This coolant extracts heat from the water-bearing soil and creates a frozen body. The installed freezing pipes form frozen soil columns, which grow until they merge. This is called ‘closure’. The freezing temperature is maintained during construction when the required frost body thickness is reached. The freezing pipes typically consist of a closed outer pipe and an open inner pipe. First, the coolant flows downwards through the inner pipe to its deepest point and, subsequently, upwards between the inner and outer pipes. During upward flow, heat from the ground is extracted.

Two well-known fluids used for ground freezing are Brine and Liquid Nitrogen (LN). The choice depends on the given boundary conditions as freezing duration, spatial circumstances, or general average temperature. For Brine cooling, an industrial refrigerating plant connected to the coolant system is installed (Figure 2a). It is a closed circuit, where the up-flowing warmed fluid is re-cooled by the refrigerating plant and returned to the ground through the inner pipe. Usually, a calcium chloride ($CaCl_2$) solution is pumped into the closed circuit at an initial freezing temperature between -28 and -35°C.

For LN cooling, the coolant nitrogen is stored in vacuum-insulated tanks at -196°C (Figure 2b). It is an open circuit process, where the LN flows along the pipes, evaporates during heat extraction, and is emitted into the atmosphere at temperatures between -100°C and -60°C.

Both methods can also be combined, e.g., using the LN cooling to build up the frost body (freezing phase) and afterward the brine cooling to maintain the frost body thickness (maintenance phase) (Ladanyi & Andersland 2004; Manassero 2020).

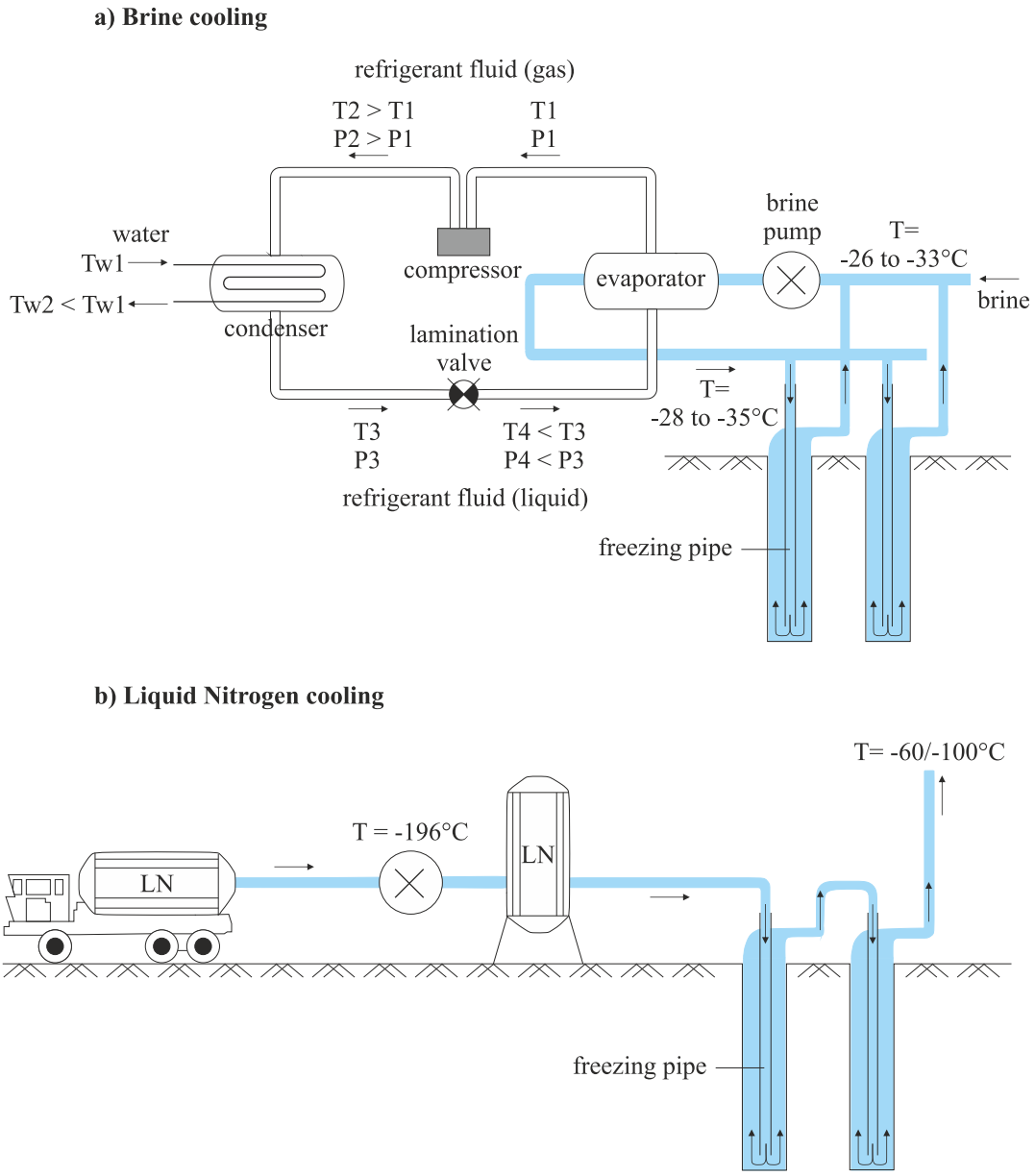

Figure 2: Artificial ground freezing via a) Brine cooling and b) Liquid Nitrogen cooling, after Manassero (2020)

2.2. Natural ground freezing

Natural ground freezing in cold regions of the Northern and Southern hemispheres can be divided into seasonally or perennially frozen ground. At seasonally ground freezing, the minimum annual ground surface temperature is less than 0°C, but the shallow subsurface (active zone) freezes and thaws within one year. The active layer thickness usually varies between 15 cm and 1 m.

Permafrost areas are characterized by a frozen subsurface (≤ 0°C) for at least two years with an active layer above the permafrost where freezing and thawing occur. Permafrost regions can be classified into regions with permanent permafrost ground (continuous permafrost) or regions with

sporadically permafrost ground (discontinuous permafrost). In the latter, the freezing depth varies between 10 cm to 100 m, although it can reach up to 1 km in continuous permafrost regions. Above the continuous frozen ground, an active soil layer that freezes and thaws seasonally exists.

Due to permanent freezing, special terrain features like ice wedges, ice-wedge polygons, pingos, or thermokarst topography reflect complex geomorphic processes (cf. Figure 3), e.g., frost action, patterned ground, and mass wasting, which may require complex and expensive construction solutions due to thermal changes (McFadden & Bennett 1991; Ladanyi & Andersland 2004; Johansson 2009).

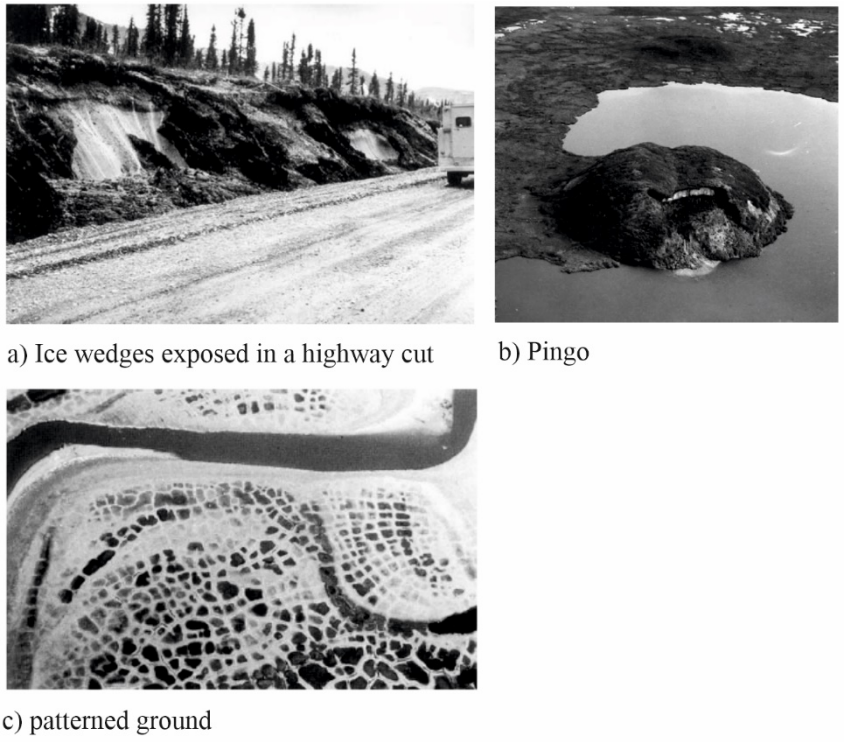

Figure 3: Special terrain features in permafrost areas, after Ladanyi and Andersland (2004)

Ice wedges (cf. Figure 3a) are vertically oriented ice masses that occur close to the permafrost surface. At the top they reach a width of 1-3 m and become narrower towards the bottom. The formation of ice wedges starts with an initial open crack due to decreasing ambient temperatures. Superficial layers tend to contract whereas the lower layers are more stable, thus cracks initiate when the tensile stresses exceed the frozen soil tensile strength. The arising cracks are only a few millimeters wide and are filled with meltwater, which freezes at subzero temperatures near the permafrost surface. During colder seasons, thermal contraction reopens the crack, whereas warmer temperature conditions lead to meltwater accumulation. This cycle creates ice wedges. Most common, ice wedges are connected at the surface and build a system of ice-wedge polygons.

Pingos (cf. Figure 3b) are defined as conical mounds with a circular base and a fissured summit. They occur in permafrost areas and are built by ground ice that is covered with soil and vegetation. The solid ice core expands by water supply from a seasonally thawed surface lake or artesian

ground water. According to the definition of Ladanyi and Andersland (2004), the width of a pingo is ≥10 m and the height is ≥100 m.

The expression of patterned ground in periglacial environment includes geometric forms such as polygons and circles illustrated in Figure 3c. The polygon patterned ground results from drying processes and frost cracking, whereas circular pattern can be attributed to local differential heaving. In heterogeneous material, the fine fraction has an improved water-binding function, occurring in greater freezing expansion. During thawing, the fines are more contracted by surface tension as coarser material. The amount of fines grow with freezing and thawing cycles whereas the coarser material is pushed outwards (Ladanyi & Andersland 2004; Johansson 2009).

2.3. Differences between AGF and naturally frozen ground

Temporal considerations

One main difference between AGF and naturally frozen ground is the temporal usage of frozen ground. At AGF, the frozen soil supports the construction phase temporarily with its advantages, like the waterproofing function or the increasing strength of the soil. After construction, the ground is thawed again. Conversely, permanent constructions in continuous frozen areas are generally designed for up to 100 years (Johansson 2009).

The freezing duration at AGF is individual and depends on the construction project. Usually, a construction measure goes on for weeks and months. Therefore, it is crucial that after the frost body thickness is reached, the frost line maintains a specific position holding this body thickness (thermal steady state). For energy reduction, options like intermitting freezing with a periodic activation and deactivation of the freezing system are used, which may lead to continuous changes in frost body thickness. At natural ground freezing, the freezing duration is seasonal or continuous, and the frost line is an ongoing moving boundary (thermal transient state). When the soil thaws at warmer temperatures, a supersaturated zone with a mushy consistency is created. This leads to a loss of the soil's load-bearing capacity. Highly saturated areas lead to considerable frost heave when the ground re-freezes. Therefore, freezing and thawing cycles causes special terrain features as shown in Figure 3 (Ladanyi & Andersland 2004; Johansson 2009).

Temperature

The freezing temperature at AGF depends on the cooling system but is less than -28°C (Brine) down towards -196°C (Nitrogen). The freezing occurs below the ground surface in multiple directions. The frozen body grows radially around the freezing pipe, and ice lenses can form in opposition to the direction of heat transport (Ladanyi & Andersland 2004).

For natural and continuously frozen ground, the annual temperature amplitude affects the soil temperature until a depth of approx. 15 m is reached. Below this level of zero annual temperature amplitude, the ground temperature increases with depth. The slope of the mean annual soil temperature (Geothermal Gradient) is typically considered to be 3°C per 100 m (McFadden & Bennett 1991). Generally, the freezing direction in naturally frozen areas is downwards into the

ground where the freezing air temperature freezes the ground. However, depending on these ambient temperature conditions, the thermal effect on the active layer can be dominated by underlying permafrost layer, in which case a two-way freezing with different boundary temperatures may be present.

Stress conditions

The difference in stress conditions between AGF and naturally freezing depends on the overburden. Because AGF is used for construction in the ground, the overburden is usually greater than the overburden on permafrost. For instance, an inner-city tunnel with a crown depth of approximately 13 m below the ground surface results in an overburden load of ~250 kPa ($\rho_{soil} \approx 1900$ kg/m^3). The overburden at natural ground freezing usually comes from buildings at the ground surface, and is typically one or two orders of magnitude smaller (Ladanyi & Andersland 2004; Johansson 2009). This, as will be shown later, has a direct impact on the deformation, as expected.

3 Thermal basics of frozen soil

3.1. Heat transfer mechanism

The thermal conductivity of soil depends on the heat energy flow through a unit area controlled by a unit temperature gradient. The temperature conditions, soil material, and particle size significantly affect heat transfer (Farouki 1986).

Figure 4 gives an overview of the predominant influences of the heat transfer mechanism in soils as a function of the soil grain size (d_{10}) and degree of saturation (S_r) when no mechanical induced water flow occurs.

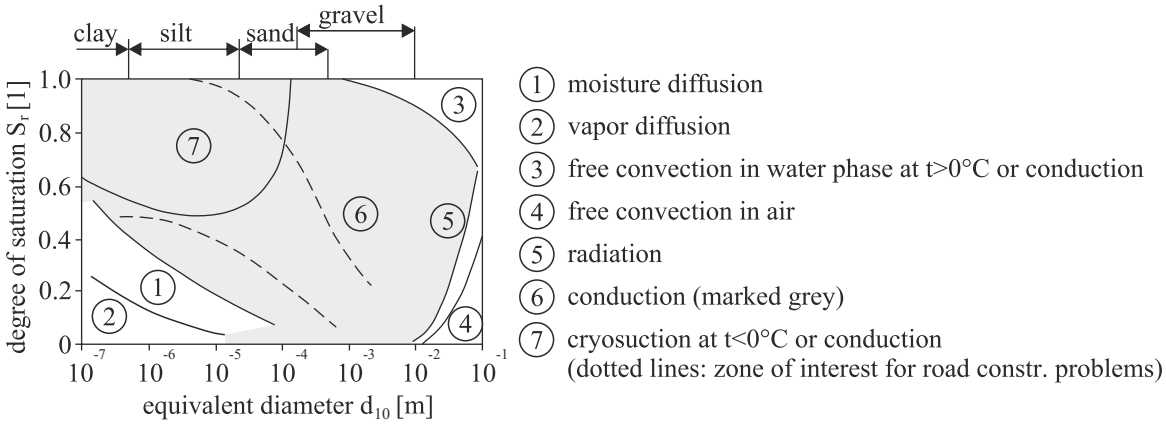

Figure 4: Regions of prevailing influence of the various heat transfer mechanism in relation to grain size and saturation degree, after Frivik et al. (1977) and Johansen (1977b)

As shown in Figure 4, conduction is the predominant heat transfer mechanism. With lower saturation degrees in fine-grained soils, the moisture migration by evaporation, vapor diffusion, and subsequently condensation leads to also heat transfer. Moisture content gradients cause vapor diffusion due to changes in relative humidity in the pore air as a function of water content. These significant variations in relative humidity only occur at low saturation degrees. With higher saturation, temperature gradients cause vapor diffusion in the pore air due to gradients in the water vapor saturation pressure. The temperature-dependent vapor diffusion also affects latent heat transport due to vaporization and condensation. In coarser-grained soils, lower saturation degrees lead to free air convection due to density changes and heat radiation between particles (Johansen 1977b; Farouki 1986).

At high degrees of saturation, the water phase in soils significantly influences heat transfer. Free convection in water occurs in coarse-grained material due to density gradients. With water movement, the heat can be transferred due to free convection but is limited by the permeability,

which decreases with lower saturation degrees (Johansen 1977b; Farouki 1986). For frost susceptible soils like clay or silt, cryogenic suction at subzero temperatures influences heat transfer (Frivik et al. 1977). Cryogenic suction occurs near the frost line at subzero temperatures (frozen fringe), where a minor part of unfrozen water remains and, therefore, is under tension to main its thermodynamic equilibrium. A cryogenic suction gradient is developed in response to the temperature gradient and draws unfrozen pore water towards the freezing front (Thomas et al. 2009).

The forced convection must be considered if ground water flows due to a present hydraulic gradient. Moisture and heat transfer mechanisms usually coexist. Considering ground freezing, the freezing and thawing of soil water includes latent heat effects that affect heat transfer (Johansen 1977b; Farouki 1986).

At ground freezing, a high saturation degree is necessary, which makes conduction and convection the governing heat transport mechanisms. Based on Figure 4, for fine-grained material, cryogenic suction should be clearly considered as well.

3.1.1. Heat conduction

Heat conduction in soils is a process of kinetic energy transfer from molecules from warmer to colder areas. Considering a soil element with a cross-section A, the transferred rate of heat flow q $[W/m^2]$ can be explained by Fourier's law:

$$q = \frac{Q}{A} = -\lambda \frac{dT}{dx} \left[\frac{W}{m^2}\right] \tag{3.1}$$

In equation 3.1, λ is the thermal conductivity, and dT/dx is the thermal gradient. The negative designation indicates positive defined heat flow towards low temperatures (Ladanyi & Andersland 2004).

If the heat transported into a soil element differs from the heat flowing out of it, its body temperature changes. The amount of temperature change due to a certain amount of heat flow is defined by the specific heat capacity c_s [J/kgK] or in terms of volume c_v in [J/m^{3}K].

Fourier's law leads to a heat equation defined for an isotropic and homogenous medium:

$$\frac{\partial T}{\partial t} = -\frac{\lambda}{c_v} \cdot \left(\frac{\partial^2 T}{\partial x^2} + \frac{\partial^2 T}{\partial y^2} + \frac{\partial^2 T}{\partial z^2}\right) \tag{3.2}$$

The thermal diffusivity a indicates how fast a temperature change occurs (Orth 2018):

$$a = \frac{\lambda}{c_v} \left[\frac{m^2}{s}\right] \tag{3.3}$$

3.1.2. Convection

Convection occurs due to the movement of warmer portions to cooler areas of a fluid that is typically also moving. The heat transport due to convection can occur as free or forced convection. Free convection results from movement caused by different fluid densities the result from a temperature gradient. For warmer temperatures, the density of the fluid is lower, and it streams upwards (buoyancy), carrying the heat (Farouki 1986). Free convection through air or water is negligible for soils, especially with microscopic pores (Victor 1969; Farouki 1981; Baier 2008).

During forced convection, the air or water are forced to move through soil pores by pressure differences caused by an external force. Flowing groundwater is a case of forced convection, where heat is transferred by the movement of water. In coarse-grained material, heat transfer can be enhanced by dispersion effects. The groundwater velocity follows Darcy's law (see section 4.2.1) under laminar flow conditions in soils. The convection effect is therefore more significant more soils with larger pores, or in other words, greater hydraulic conductivity (Farouki 1986).

For flowing pore water in soils, heat convection flow is defined by:

$$q_k = c_v \cdot v \cdot V \cdot \left(T_w - T_f\right) \left[\frac{J}{s}\right] \tag{3.4}$$

With the volumetric heat capacity c_v, the seepage velocity v, the transported volume V, the soil water temperature T_w, and the freezing temperature T_f (Orth 2018).

3.2. Thermal properties of soils

Soil is a multi-phase system of grains, pore water, and air. Only three components exist in the unfrozen state, whereas a four-phase model, which additionally contains pore ice, is usually present in the frozen state (Figure 5). Depending on the freezing temperature, salt content in porewater and the soil material, unfrozen water can be present at subzero temperatures. For example, coarse-grained materials are usually completely frozen at negative temperatures close to 0°C, whereas unfrozen water was observed for temperatures below -40°C for frozen silt and clay (Yoshikawa & Overduin 2005).

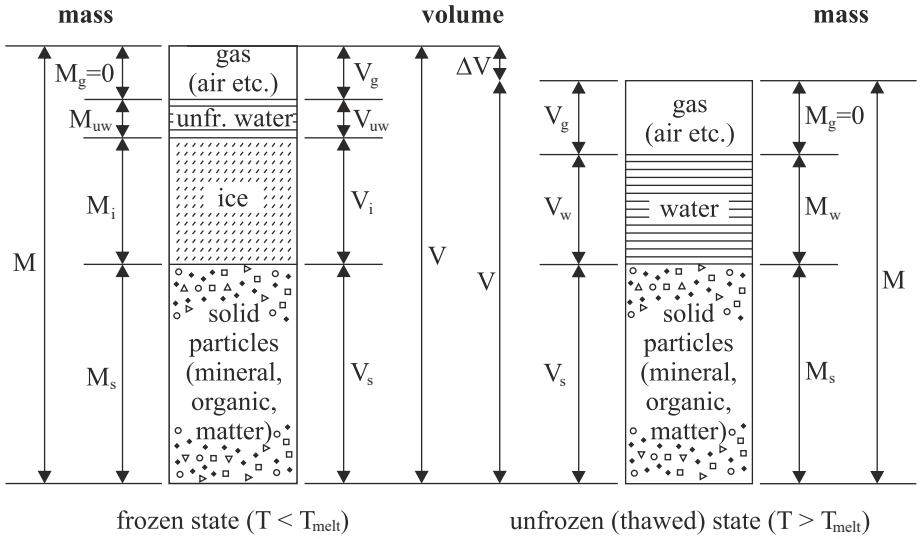

Figure 5: Mass-volume relationship for frozen and unfrozen soil, after Ladanyi and Andersland (2004)

The proportion of unfrozen water content affects the stress conditions in the soil and the hydraulic and thermal conductivity of porous media. In addition, water migration in areas < 0°C can lead to ice lens formation, which causes a significant heave at the ground surface. The amount of unfrozen water can be calculated by the empirical function of Anderson and Tice (1972), which is described in section 4.3.

The thermal properties of soil are defined by the thermal conductivity, the specific heat, and the heat of crystallization and fusion, also called latent heat. These soil properties depend on the proportion of the constituents, the soil type, the saturation degree, the density, and the temperature (Orth 2018).

3.2.1. Thermal conductivity

The thermal conductivity of soil is a direction-dependent variable that depends on dry weight, the pore fraction, mineral type, quartz fraction, and degree of saturation (Farouki 1986; Orth 2018). Critically, the thermal conductivity of ice is greater than water, which highlights the importance of accurately knowing each phase.

Farouki (1981) recommended using the geometric mean equation from the thermal conductivities of the soil grains λ_g, the ice λ_i, and water λ_w for the prediction of the thermal conductivity of saturated soil (equation 3.5) by Johansen (1977). This approach considers unfrozen water in volume θ_w at sub-zero temperatures. The porosity of the soil is considered by n. If no ice phase is present, the term λ_i is removed from the equation 3.5.

$$\lambda = \lambda_g^{1-n} \cdot \lambda_i^{n-\theta_w} \cdot \lambda_w^{\theta_w} \qquad 3.5$$

The temperature-dependent conductivity of water decreases with lower temperatures and can be calculated by the empirical equation of Kestin (1978). During the phase change from pure water to ice, the thermal conductivity increases to approximately a value of 2.22 W/(mK), which is almost four times higher than the conductivity of the fluid water phase and increases with decreasing temperature. The basis for calculating the thermal conductivity of ice is given in Fukusako (1990). An example for the temperature dependent thermal conductivity of soil constituents is given in Figure 6.

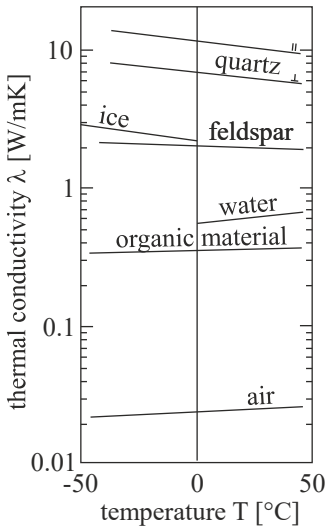

Figure 6: Thermal conductivity of soil constituents, after Frivik (1981)

The thermal conductivity of the soil grains mainly depends on the quartz content. Johansen and Frivik (1980) developed a function dependence on the quartz content q to calculate the thermal conductivity of soil grains λ_g. The thermal conductivities of quartz λ_q and the remaining solids λ_r are multiplied proportionally via the geometric mean that assumes a homogeneous distribution of quartz in the soil.

$$\lambda_g = \lambda_q^q \cdot \lambda_r^{(1-q)} \qquad 3.6$$

The average thermal conductivity of quartz is 7.7 W/(mK). The composition of soils varies greatly between sands, silts, and clays. For example, the conductivity of other solids varies between 2.0 W/(mK) for feldspar or mica to 3.5 W/(mK) for claystone. Coarser-grained material like sand has a significant amount of quartz, and finer material consists of feldspar, mica, and clay minerals (Johansen & Frivik 1980; Makowski 1986).

The volumetric proportions of the components determine the magnitude of thermal conductivity. Generally, an increasing dry density of the soil and a high degree of saturation improves the soil's thermal conductivity. In addition, freezing and thawing processes with compositional and structural changes lead to modifications in the thermal conductivity of the soil (Ladanyi & Andersland 2004).

3.2.2. Heat capacity

The heat capacity of a freezing soil is defined as the amount of heat that must be extracted from the soil for a temperature reduction of one degree. It gives information about the heat storage capacity of the soil and can be described as specific heat c_s [J/kgK] or, multiplied by the density, as volumetric heat c_v [J/m^{3}K]. Figure 7 specifies the temperature dependency of specific heat of different soil constituents. The volumetric heat capacity of dry soils is usually between 1.0 and 1.5 MJ/(m^{3}K) near 0°C. For wet soil, the heat capacity increases substantially and linearly with the increase in water content (Williams & Smith 1989).

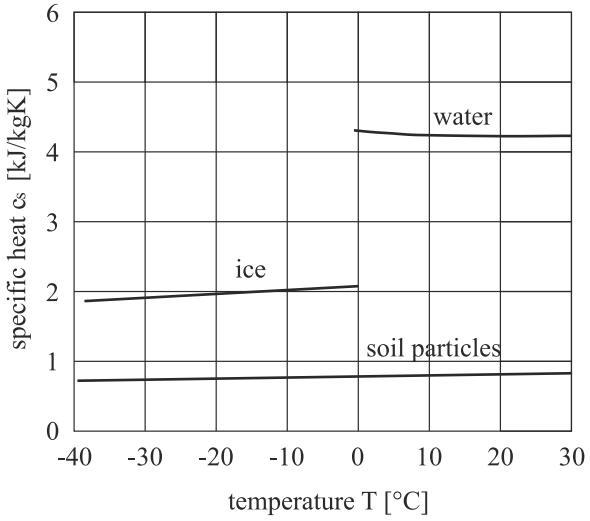

Figure 7: Temperature dependent specific heat of soil constituents, after Johansen (1977)

Considering a multiphase system, the total heat capacity is composed of single soil constituents. Suppose no excess water is supplied to the freezing soil. In that case, the total heat capacity c_v for a saturated soil can be expressed by the weighted arithmetic mean of the soil constituents soil grain (s), ice (i) and water (w), which amount depends on the total porosity n as well as the unfrozen water content θ_w (Makowski 1986; Williams & Smith 1989; Baier 2008).

$$c_v = \underbrace{c_{v,s} \cdot (1-n)}_{\text{soil}} + \underbrace{c_{v,i} \cdot (n-\theta_w)}_{\text{ice}} + \underbrace{c_{v,w} \cdot \theta_w}_{\text{water}} \qquad 3.7$$

3.2.3. Latent heat

The latent heat is defined as the change in enthalpy ΔH as a unit mass is converted isothermally and reversible from ice into water (Fukusako 1990). The conversion from water into ice is accompanied by an increasing energy density and, thus, the release of thermal energy or latent heat. For pure water, the latent heat is L = 333.600 J/kg (Makowski 1986). The total heat storage in frozen soils is composed of the volumetric heat capacity c_v and the latent heat of fusion L_f,

which is released over a negative temperature range dependent on the amount of unfrozen water content θ_w.

$$\Delta H = \int_{T_s}^{T_l} c_v \cdot dT + \int_{T_s}^{T_l} \rho_w \cdot L_f \cdot d\theta_w \qquad 3.8$$

In equation 3.8, $d\theta_w$ is the incremental unfrozen water content between the solid T_s and liquid temperature T_l, and ρ_w is the water density. Especially in fine material with unfrozen water many degrees under 0°C, changes in heat storage include a sizeable latent heat component until T_s is reached. During freezing, the latent heat delays the freezing process. Thus, the total freezing time increases. The latent heat effects are also described as *apparent heat capacity* for soils and can be included in equation 3.9 (Williams & Smith 1989).

$$c_v(T) = c_{v,s} \cdot (1 - n) + c_{v,i} \cdot (n - \theta_w) + c_{v,w} \cdot \theta_w + \rho_w \cdot L_f \cdot \frac{\partial \theta_w}{\partial T} \qquad 3.9$$

3.3. Freezing soil characteristics

3.3.1. Freezing water

When a liquid is cooled down, the thermal motion of the molecules decreases until the kinematic energy is so low that they arrange themselves and form a crystal. In this state, the freezing point of the liquid is reached and ice forms. For pure water at an atmospheric pressure of 101.3 kPa, this is at a temperature of 0°C. During phase change from water into ice, the temperature does not change (isothermal process; cf. section 3.3.2, Figure 10) but an increase in volume of about 9 % occurs. Depending on temperature and pressure conditions, the water exists in solid, liquid, or gaseous state (cf. Figure 8). Along one curve, water is in equilibrium in two, or, at the triple point, in three states. If the temperature and pressure exceed the conditions of the critical point, gas cannot be transferred into fluid. Instead, it becomes more compacted with increasing pressure (Hartge 1978; Atkins 1996).

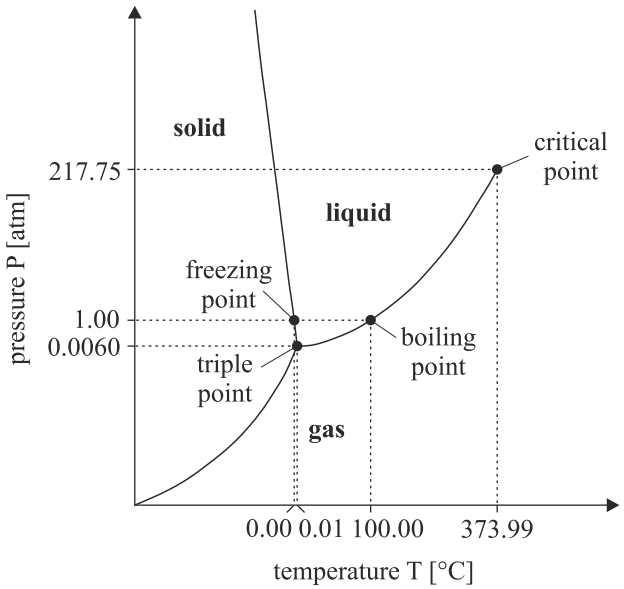

Figure 8: Phase diagram for pure water, after Atkins (1996)

Regarding a soil, freezing of the soil water depends on intermolecular forces between the water and soil grain surface; refer to section 4.1. The more the water is adsorbed to the grains, the lower the freezing point (Hartge 1978). Therefore, water in frozen soils is available in both solid (solidification of non or less bound liquid water) and liquid phases (bound water) at sub-zero temperatures. This phenomenon is rather attributed to the fine-grained soils.

Figure 9 shows the freezing curve for soil water. The free pore water (unbound water) does not start to freeze until T_{sc} is reached. Here the water is in a metastable equilibrium state and is referred to as supercooled water, which can achieve temperatures of approx. -22°C (Jessberger & Jagow-Klaff 1996). The phase change of the supercooled water into the solid state is triggered by crystallization nucleus (Ladanyi & Andersland 2004). The abrupt ice formation of the largest proportion of unbound water goes along with released latent heat; thus, the system's temperature rises but persists in the negative range. This initial freezing temperature T_f is very close to 0°C for cohesionless soils but can be lower (up to ΔT = 5°C) for fine-grained soils like silt or clay. Freezing of the remaining free water occurs at T_f, while the freezing temperature of the bound water depends on the degree of binding and can reach temperatures as low as T_e = -70°C. The released latent heat during freezing slows down the cooling rate (Ladanyi & Andersland 2004).

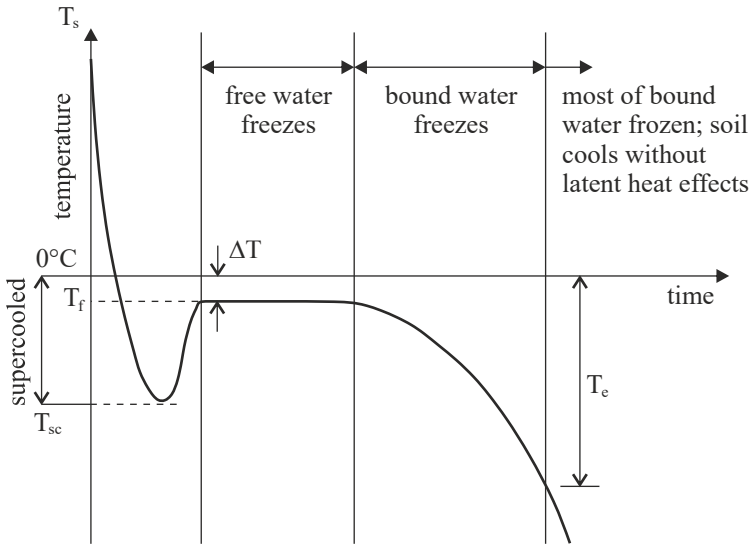

Figure 9: Freezing curve for soil water, after Ladanyi and Andersland (2004)

3.3.2. Phase change and freezing point depression

Phase changes, such as the transition from liquid water to ice, are fundamentally governed by thermodynamics, which can be explained through the interaction of internal energy, temperature, and phase stability under constant conditions of temperature and pressure. When water reaches its phase change temperature, T_{pc} (0°C at atmospheric pressure), the supplied heat (ΔH) is not used to increase temperature but is instead consumed entirely for the phase transition (Figure 10a). This phenomenon is graphically represented in a temperature-enthalpy curve and a temperature-time curve (Figure 10b) during solidification, where the temperature of the system remains constant during the phase change until the transition is complete.

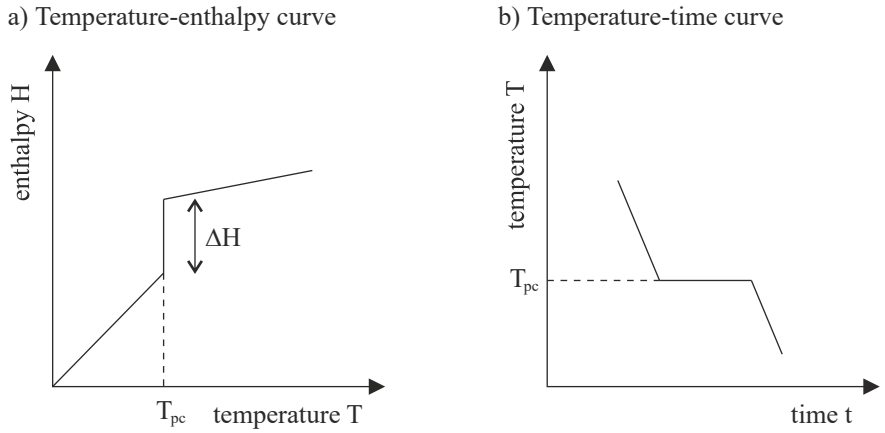

Figure 10: Schematic illustration of the a) temperature-enthalpy curve during phase change, and b) temperature-time curve during solidification, after Frohberg (2009)

The concept of melting enthalpy, which represents the energy required for the phase transition from solid to liquid, and its counterpart, solidification enthalpy (the negative of melting enthalpy),

are crucial for understanding this process. These enthalpies reflect the difference in the system's internal energy between the liquid and solid phases (Frohberg 2009).

Moreover, Gibbs free energy (G), or the energy available to perform work, plays a significant role in phase transitions. It is defined in relation to the system's total enthalpy (H), temperature (T), and entropy (s) - (cf. equation 3.10) - and changes in Gibbs free energy (dG) indicate the direction of spontaneous processes, such as phase changes (see equation 3.11). When $dG < 0$, the process is spontaneous; when $dG = 0$, the phases are in equilibrium. At the freezing point, the Gibbs free energy of liquid water and ice are equal, signifying phase equilibrium. Below this temperature, the free energy of the liquid phase is higher than that of the solid phase, driving the transition from water to ice as the system seeks to minimize its free energy (cf. Figure 11). Gibbs free energy is often referred to as the chemical potential (Williams & Smith 1989; Frohberg 2009).

The total enthalpy H can also be described by the internal energy U, the pressure P, and the volume V.

$$G = H - Ts = U + PV - Ts \tag{3.10}$$

$$dG = -sdT + VdP \tag{3.11}$$

Generally, the free energy of water or ice increases with lower temperatures. Since two phases with different free energy cannot coexist, the quantity of the phase with lower free energy increases; this explains the freezing process of pure water, which is transferred into the ice phase with lower free energy.

The presence of dissolved salts or the effects of capillarity and adsorption in soils can lower the free energy of water, thus depressing the freezing point, as shown in Figure 11. The impact of dissolved salts on the freezing point is generally minor, usually causing a depression of about 0.1°C. Freezing point depression by capillarity is responsible in a range between -1.5°C and 0°C, whereas the depression by adsorption starts below -1.5°C. This principle is particularly relevant in soil water, where these factors can cause water to freeze over a range of temperatures rather than at a single point, leading to the formation of ice lenses in the soil (Williams & Smith 1989; Wedler & Freund 2012).

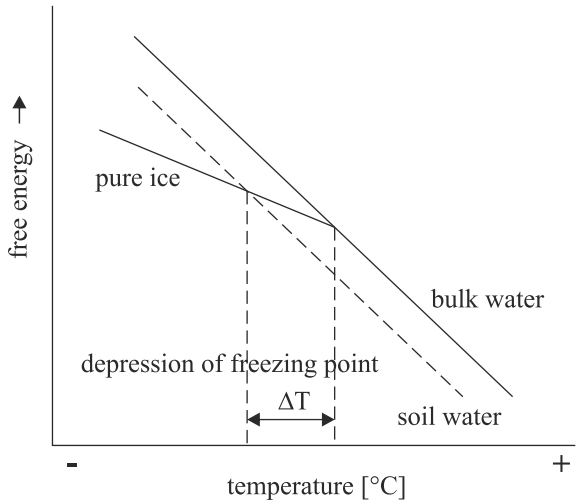

Figure 11:Free energy-temperature relation of water, soil water, and ice, after Williams and Smith (1989)

The Gibbs free energy difference in soil water is related to the matric potential, influenced by capillarity and adsorption, and the osmotic potential, influenced by dissolved salts. The matric potential can be expressed as a pressure dP; cf. equation 3.11. Since dissolved salts are not transferred into the solid phase, they can only change the chemical potential of the water. Considering a mixture of components, equation 3.11 extends to

$$dG = -sdT + VdP + \sum_i \mu_i dn_i \qquad 3.12$$

with the mass n_i and chemical potential μ_i of the components (Loch 1978; Williams & Smith 1989; Unold 2006).

3.3.3. Pressure and temperature relations

As explained in the previous section, two phases are in equilibrium as long as their Gibbs free energy is the same. Free energy decreases in a spontaneous change, and the system only remains in equilibrium when the free energy cannot decrease. Considering water and ice, an increase in pressure during constant temperature conditions will cause a more significant increase in free energy in ice compared to water. A decrease in free energy only results from a complete phase change into the liquid state. Lowering the pressure during constant temperature conditions, results in a decrease of the ice free energy that is larger than that of water. Hence, if ice and water are in equilibrium and pressure decreases, a total phase change from water into ice occurs.

If the pressure conditions stay constant and only temperature changes, a rising temperature will result in a phase change from ice, with the lowest specific entropy, into water. When the temperature decreases, the water, whose specific entropy is the greatest, will completely change into ice.

When the temperature and the pressure change simultaneously, there is a relation between temperature and pressure changes where the phases of water w and ice i can coexist. This can be expressed in the differential form of Gibbs free energy, recalling equation 3.11 (Edlefsen & Anderson 1943).

$$-s_w dT + V_w dP = -s_i dT + V_i dP \tag{3.13}$$

Rearranging equation 3.13 gives:

$$\frac{dP}{dT} = \frac{s_i - s_w}{V_i - V_w} \tag{3.14}$$

The change in entropy from ice into water $(s_i - s_w)$ is the difference in entropy of the two phases, with L_f as the latent heat of fusion of ice and T as the normal freezing point of 0°C = 273.15 K when the pressure is atmospheric.

$$s_i - s_w = \frac{L_f}{T} \tag{3.15}$$

The quantity $(V_i - V_w) = \Delta V$ gives the volume increase per gram by phase change from water into ice. From equation 3.13 - 3.15, the Clapeyron equation for water results:

$$\frac{dP}{dT} = \frac{L_f}{T\Delta V} \tag{3.16}$$

When the ice phase changes into the water phase, the latent heat, L_f, is positive, and the volume change is negative ΔV. A pressure change dP causes a decrease in the melting point of water dT, which explains the phenomenon of regelation (a particular case of this is the flow of glaciers). Due to applied pressure, the ice melts and refreezes at another location. The freezing point of water decreases by 0.074°C/MPa. For finite changes, equation 3.17 indicates the effect of hydrostatic pressure ΔP on the freezing-point depression of water ΔT by (Edlefsen & Anderson 1943; Williams & Smith 1989):

$$\Delta P = \frac{L_f \Delta T}{T\Delta V} \tag{3.17}$$

The Clapeyron equation 3.16 is valid when the pressure increment applies equally to the water and ice phases. This is often assumed, but it is not the usual circumstance when water freezes in soils. The ice pressure is at least as great as the pressure acting on the soil body or just atmospheric pressure for free-standing soil samples. However, the water in the frozen soil has different pressure conditions from atmospheric pressure (Williams & Smith 1989).

A provided form of the Clapeyron equation, for the case of varying ice pressure but constant water pressure, equation 3.18 is given. In this case, the melting temperature of ice decreases by 0.893°C/MPa (Edlefsen & Anderson 1943; Black 1995).

$$\frac{dP_i}{dT} = -\frac{L_f}{TV_i} \tag{3.18}$$

If the ice pressure remains constant but the water pressure changes, equation 3.19 is given. It describes the change of freezing point when the pressure on the water decreases. For example, a decrease in water pressure lowers the melting temperature by 0.819°C/MPa. Black (1995) defines this equation as valid only for conditions without overburden and a water table beneath the surface.

$$\frac{dP_w}{dT} = \frac{L_f}{TV_w} \tag{3.19}$$

To describe the equilibrium between ice and water solution in porous media, the so-called generalized Clapeyron equation is used. For this case dP in equation 3.13 is different for the water and ice phase and can be written as follows:

$$P_w \cdot V_w - P_i \cdot V_i = \frac{L_f(T - T_f)}{T} \tag{3.20}$$

In this equation, T_f is the freezing temperature of water under atmospheric pressure (Edlefsen & Anderson 1943; Loch 1978; Williams & Smith 1989).

Equation 3.20 is only valid for the case of thermodynamic equilibrium. If the left expression of equation 3.20 is smaller than the right term, e.g., by local temperature drop, a penetrating frost front results, and equation 3.20 is no longer applicable. This also applies if the local pressure conditions change by increasing heave pressure at the ice lens, which is equal to the ice pressure at the ice lens, or decreasing suction (Loch 1978).

Biermans et al. (1978) showed the validity of the generalized Clapeyron equation by closed system freezing and constant temperature conditions. For this, they experimentally investigated the influence of pressure on water flow toward an ice front. The tests kept the temperatures, ice, and water pressure constant. However, the generality of applying the generalized Clapeyron equation for frozen soil heaving is questioned in the literature (Penner 1986; Ma et al. 2015). Especially open system freezing with water flow does not satisfy the equilibrium conditions. The phase equilibrium cannot be achieved when processes like soil skeleton deformation (elastic, plastic, or viscous), water flow, and ice deformation (rheological behavior or regelation) are present. Further aspects, as the effect of regelation, which explains pressure induced melting and refreezing at another location, or the presence of solutes in the pore water, which increase in the soil water during freezing by solute rejection, show that the generalized Clapeyron equation is only valid for general conditions.

4 Soil water

4.1. Soil structure and water interaction

The geometrical soil structure can be divided into a single grain structure, e.g., stones, gravel, sand, or coarse silt, and non-single grain structures with intergranular forces that individual bond grains, e.g., silt and clay. Non-single grain structures appear, for example, in hexagonal (Figure 12a) or clustered structures (Figure 12b). In dense bedding, clay particles form a parallel structure; see Figure 12c (Jessberger & Jagow-Klaff 1996).

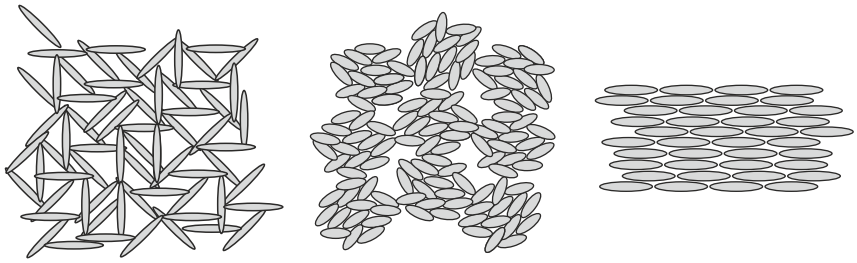

a) hexagonal structure b) clustered structure c) parallel structure

Figure 12: Non-single grain structures of fine soil material, after Kolymbas (2019)

Due to this complex structure, there are different pore types to consider. For example, the primary pores are between grains, whereas the secondary pores are between the particle aggregates and cracks due to drying, freezing, or mechanical load (Jessberger & Jagow-Klaff 1996).

Differently to granular material, clay particles consist of flat platelets with a surface that is not charge neutral (cf. Figure 13). The negative charged surface of clay particles attracts ions (cations) as well as water molecules, and a double layer is formed with a diffuse boundary (Kolymbas 2019). The double layer consists of another ion composition than in the surrounding free solution. The spatial separation of the ions in the form of an electric double layer creates an electric field that can be described by an electric potential. The electric potential influences the colloidal properties of the soil particles, especially their interaction with other particles (Amelung et al. 2018).

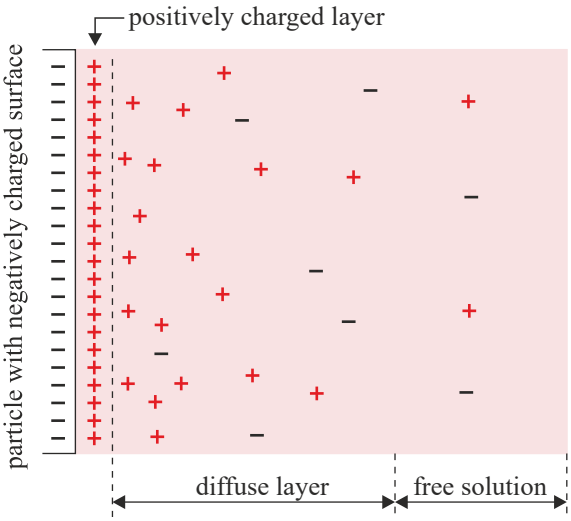

Figure 13: Ion distribution in the electrical double layer, after Amelung et al. (2018)

The water layer closest to the grain is tightly bound due to adsorption and osmotic forces between the solid and water molecule, and the bonding decreases with distance (cf. Figure 14). The electro-molecular attraction is very large (> 1.000 MPa) on the negatively charged mineral grain surface and decreases with increasing distance from the grain. A distinction is made between strongly bound adsorption water, loosely bound adhesion water, and free water (Busch et al. 1993).

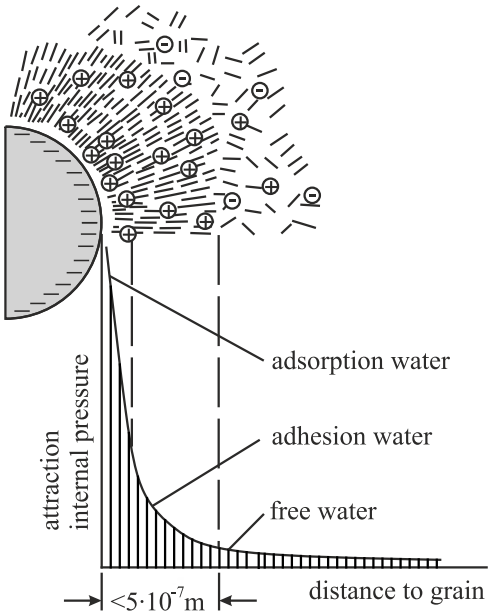

Figure 14: Electro-molecular force effect in the environment of a solid particle in groundwater, after Busch et al. (1993)

The water encases the grain without creating menisci. Adsorption forces are Van-der-Waals-forces and electrostatic forces due to the ion composition around the soil grain. Sorbed ions increase the amount of adsorption water due to their hydration capacity, which depends on the mineral. The water content increases with the increasing relative water vapor pressure of the air and with

decreasing grain size or increasing specific surface of the grain. According to Hartge (1978), the influence of the mineral type is subordinate to the grain size.

The strongly bound water molecules around the soil grains are inhibited in their motion. Thus, they absorb less energy compared to free water molecules. This reduces the heat capacity of the adsorbed water. With increasing bonding, the adsorbed water is restrained from turning into ice during freezing, decreasing the freezing point (cf. section 3.3). This usually occurs in fine-grained soils like silt or clay (Hartge 1978; Amelung et al. 2018).

Another mechanism of adsorption, which is independent of the water layer thickness, is the osmotic effect. It is present when the concentration of the sorbed ions around the soil grain is higher than in the free water. The sorbed ions accumulate water molecules in between to balance the osmotic pressure gradient (Hartge 1978).

The water films around the soil grains are connected mainly by menisci between the grains, being in or creating an equilibrium state. These strongly curved water menisci are built by capillary water with a greater surface tension than free water. The boundary surface between water and air has the effort to minimize to reach a lower energy state. The formation of menisci is based on the interaction of adhesion forces on the solid surface and cohesion forces between the water molecules. The smaller the void, the greater the water bonding. With increasing water content, capillary binding predominated over adsorptive binding (Amelung et al. 2018).

4.2. Soil water hydraulics

4.2.1. Darcy Law

Groundwater flows from higher to lower energy regimes (Kolymbas 2019). The fluid flow in a porous medium, where flow velocities are small, is primarily related to the pressure altitude ($\partial p/\partial r$), gravity ($\rho \cdot g \cdot \partial z \,/\, \partial r$), and laminar friction ($C_r \cdot \eta \cdot v_r$) with the flow direction r. The term laminar friction depends on pore geometry and fluid viscosity, with C_r as the proportionality factor defining the frictional resistance of the solid matrix, η as dynamic viscosity ($= \nu \cdot \rho$, with ν as kinematic viscosity), and v_r as seepage velocity (Busch et al. 1993).

$$\frac{\partial p}{\partial r} + \rho \cdot g \cdot \frac{\partial z}{\partial r} + C_r \cdot \eta \cdot v_r = 0 \tag{4.1}$$

$$v_r = -\left(\frac{1}{\rho \cdot g}\frac{\partial p}{\partial r} + \frac{\partial z}{\partial r}\right) \cdot \frac{g}{C_r \nu} \tag{4.2}$$

The last term of equation 4.2 represents the permeability coefficient k in the flow direction. Assuming isotropic conditions, the Darcy law can be then generalized:

$$v_r = -\left(\frac{1}{\rho \cdot g} grad\ p + grad\ z\right) \cdot k \tag{4.3}$$

The permeability coefficient k [m/s] can be described by the intrinsic permeability K [m^2] with the following relationship:

$$k = K \cdot \frac{\rho \cdot g}{\eta} = K \cdot \frac{g}{\nu} \tag{4.4}$$

It must be taken into account that the dynamic η or kinematic viscosity ν of the fluid is temperature-dependent. According to DIN EN ISO 17892-11 (2021), k is defined for water at a temperature of 10°C (von Soos & Engel 2008).

If the fluid density ρ in equation 4.3 is constant, the water head gradient can be used to describe seepage velocity:

$$\overrightarrow{v_r} = -grad\ h \cdot k \tag{4.5}$$

The Darcy law in the presented form neglects inertial and turbulent frictional forces at large seepage velocities and adhesive forces at a very low flow velocity. Suppose the importance of the neglected forces becomes greater, the Darcy law in the presented form with a constant coefficient of permeability is no longer valid, and a pre-linear and post-linear range is referred to (Busch et al. 1993). In DIN EN ISO 17892-11 (2021), a constant permeability coefficient is assumed, but it is remarked that this is not valid without restrictions.

The Darcy law is valid for laminar flow. According to OHDE these exist if the following equation is fulfilled:

$$i \leq \frac{0{,}1}{{d_{eff}}^3} = i_{crit} \tag{4.6}$$

The effective grain diameter d_{eff} [mm] is generally between d_{10} and d_{25}. For $i > i_{crit}$, turbulent flow in the post-linear region is expected. The flow velocity increases, and inertial forces become dominant (von Soos & Engel 2008).

The pre-linear range is reached when the static friction becomes more significant with small flow channel cross-sections. Due to the molecular force effect, the water behaves like a non-Newtonian fluid at small pressure gradients. Due to electro-molecular forces between the fluid and mineral, the fluid's viscosity increases with the reduced distance of the fluid to the mineral grain surface (Busch et al. 1993).

Often, a simplified relationship is used in practice to consider the pre-linear, linear, and post-linear ranges. Here, the permeability coefficient k^* is represented as a function dependent on the potential gradient $gradh$.

$$k^* = f(grad\ h) = k|gradh|^{\alpha-1} \qquad 4.7$$

For the pre-linear range $\alpha > 1$, for the linear range $\alpha = 1$, and for the post-linear range $1 > \alpha > 0.5$ is assumed. At fully developed turbulence, $\alpha = 0.5$ is used.

Figure 15 summarizes the change of the k-value depending on the defined flow range (Busch et al. 1993).

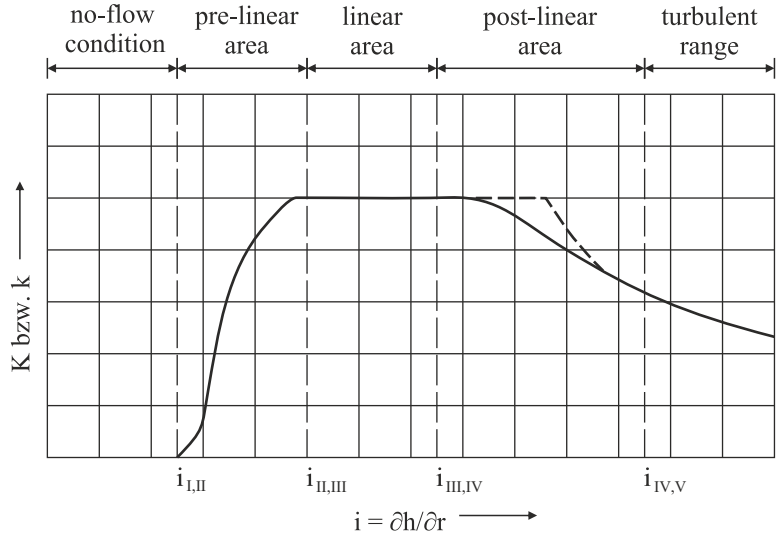

Figure 15: Flow areas of the dynamic fundamental law of geohydraulics, after Busch et al. (1993)

The hydraulic conductivity of a porous medium is mainly determined by the void content, the patency of the voids, and the deformability of the porous medium, which causes a change in the storage capacity as well as the permeability (Busch et al. 1993).

The effective porosity is smaller compared to the total porosity of the soil. It depends mainly on the connectivity of the pore system. The pore channels in fine-grained materials such as silt and clay become smaller due to the adsorption water bound to the solid matrix (cf. section 4.1).

In stratified soils, the flow velocity in the horizontal direction largely depends on the layer with the greatest permeability. Concerning vertical flow, the water flows through all layers with the same velocity but with a different potential decrease in the individual layers. In this case, the flow velocity is mainly determined by the layer with the lowest permeability (von Soos & Engel 2008).

4.2.2. Continuity

Besides Darcy, the continuity equation is fundamental to describing groundwater flow. It defines mass conservation and states that the difference between inflows and outflows at a water-saturated control volume must be zero for steady state conditions.

$$-\frac{\partial v_x}{\partial x}-\frac{\partial v_y}{\partial y}-\frac{\partial v_z}{\partial z}=0 \tag{4.8}$$

For transient flow conditions, the changing groundwater volume stored within the control volume must also be considered along with the change in groundwater potential over time. The inflow and outflow balance at the control volume must correspond to the time-dependent change in water volume in the control volume. Assuming a constant specific storage coefficient S_s, the continuity equation for water-saturated flow is (Odenwald et al. 2018):

$$-\frac{\partial v_x}{\partial x}-\frac{\partial v_y}{\partial y}-\frac{\partial v_z}{\partial z}=S_s\frac{\partial h}{\partial t} \tag{4.9}$$

4.2.3. Fluid flow

If the continuity equation is combined with the Darcy equation, the flow equation with anisotropic permeabilities in the principal axes is obtained.

$$k_{xx}\frac{\partial^2 h}{\partial x^2}+k_{yy}\frac{\partial^2 h}{\partial y^2}+k_{zz}\frac{\partial^2 h}{\partial z^2}=0 \tag{4.10}$$

Assuming isotropic conditions, the Laplace equation results.

$$\frac{\partial^2 h}{\partial x^2}+\frac{\partial^2 h}{\partial y^2}+\frac{\partial^2 h}{\partial z^2}=0 \tag{4.11}$$

For transient and water-saturated flow conditions, it follows the partial differential equation 4.12, which is the physical diffusion equation (Odenwald et al. 2018).

$$\frac{\partial^2 h}{\partial x^2}+\frac{\partial^2 h}{\partial y^2}+\frac{\partial^2 h}{\partial z^2}=\frac{S_s}{k}\frac{\partial h}{\partial t} \tag{4.12}$$

4.3. Water transport mechanism

Frozen soil is often considered to have the properties of an impermeable barrier. However, this is not generally valid and primarily depends on the soil type. Williams and Smith (1989) describe frozen soil as a confining medium of low, but finite, permeability. The driving force of the water movement is the potential differences. The total potential includes the gravitational potential ψ_z, matric potential ψ_m, gas potential ψ_g, and osmotic potential ψ_o.

$$\psi=\psi_z+\psi_m+\psi_g+\psi_o \tag{4.13}$$

The gravitational potential corresponds to the work required to raise water from a reference level to a certain height. It is also referred to as geodetic potential. The matric potential is a measure of the effect exerted by the matric-related forces (capillary and adsorption forces) on the soil water. The less water a soil contains, the stronger the matric forces hold it in place. The matric forces react in opposite direction to the gravitational forces, thus, the matric potential is negatively defined. Gas potential must be considered if the air pressure in the ground does not correspond to the pressure at the reference level. Osmotic potential arises when different salt concentrations are present in the soil. Only the solvent (water) that moves along the concentration gradient can compensate for the difference in concentration by mixing. The potential corresponds to the work that has to be done to get a unit quantity of water through the soil (Amelung et al. 2018).

At sub-zero temperatures, most water is transported in liquid phase via water films around the soil grains. However, the mechanism of regelation, which implicate a translational movement of the ice body, and vapor diffusion are also known.

When saturated soil freezes, most of the soil water solidifies into ice, except the adsorbed water films that are firmly bound to the soil grains by high intermolecular forces that suppress freezing. Subsequently, the matric potential of the unfrozen water at subzero temperatures significantly influences the total soil water potential, which is proportional to the temperature decrease. This causes the water in non-frozen regions to move towards areas with sub-zero temperatures. At a specific level, where the hydraulic conductivity runs toward zero, water accumulates, and pore ice particles grow until they contact each other and form an ice lens. This ice lens growth perpendicular to the heat and water flow direction (Keinonen 1977; Sheng et al. 1995).

A liquid film, which ensures a water supply into the frozen fringe, was confirmed experimentally by Wilen and Dash (1995) by studying the liquid flow in a surface-melted layer of ice. They introduced an ice disc into a liquid bath and covered the outer rim with a flexible membrane to measure ice growth. A generated temperature gradient induces a liquid flow from the periphery to the center of the ice disc with a fixed subzero temperature, where the film thickness becomes thinner. Thus, the supplied liquid crystallizes and an uneven ice surface topography results, measured by interference microscopy. The experiment shows that frost heave can be induced by inflowing water, even if the surface forces caused by capillarity are neglectable.

The amount of unfrozen liquid at subzero temperatures and, therefore, the ability of ice lens growth is strongly affected by the specific surface area of the soil grains. Depending on the soil, unfrozen water was determined by NMR measurement below -40°C. Anderson and Tice (1972) developed an empirical equation to determine the unfrozen water content in the semi-frozen soil by a power curve that depends on the freezing temperature T (°C) and α and β as characteristic soil parameters.

$$\theta_w = \alpha T^{\beta} \qquad 4.14$$

Tice et al. (1976) give a simple empirical method to calculate the characteristic soil parameters α and β by water content measurements similar to the liquid-limit test devised by *Atterberg*.

The regelation is caused by changes in the equilibrium pressure difference between ice and water. The phase equilibrium condition of pure water states that the freezing temperature falls with increasing pressure (cf. Figure 8, section 3.3.1). During freezing, new ice forms on the warm side of the ice body and the ice pressure increases, which influences the pressure conditions on the cold side of the ice body. If the water pressure on the cold side does not change, the equilibrium temperature decreases and favors melting (cf. equation 3.20, section 3.3.3).

Vapor diffusion is a transport mechanism occurring in unsaturated soils. Vapor diffuses from the warmer and more humid to colder and dryer areas, where it condenses into liquid water. The vapor density gradient is maintained according to the temperature gradient (O'Neill & Miller 1985; Williams & Smith 1989). After O'Neill and Miller (1985), the vapor flow makes a negligible contribution to the total moisture transport in a freezing soil.

5 Frost heave with ice lens formation

Frost heave occurs primarily in fine-grained soil. According to ZTV E-StB 17 (2017), the frost susceptibility of soils is defined by the uniformity coefficient, C_U, and the fine fraction ($d \leq 0.063$ mm). Figure 16 provides a classification of the frost susceptibility of soils. This categorizes soils into the following three classes:

- F1: not frost-sensitive soils
- F2: low to medium frost-sensitive soils
- F3: very frost-sensitive soils

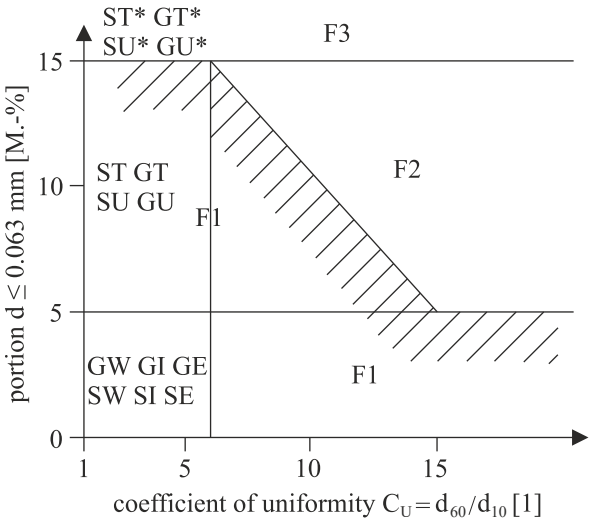

Figure 16: Classification of frost susceptibility, after ZTV E-StB 17 (2017)

Beyond the soil type, Jessberger and Jagow-Klaff (1996) defined soil properties that have an impact on the soil's sensitivity to frost:

- surface area of the soil grains, especially for clay
- soil structure and pore size distribution
- permeability and water mobilization during freezing
- filter stability
- load-bearing capacity and compaction

5.1. Ice lens formation

In one of the first ice lens observations, Taber (1929; 1930) pointed out that not only capillary forces attracting water to the ice lens, but also the action of thin water films under high tension

between the solid ice and the grains. He showed that water migrates from warmer to colder regions and accumulates in thick ice layers. To prove that water accumulation is the main component of frost heaving, he carried out tests using a liquid that contracts during freezing (benzene) that still resulted in heave. Taber (1930) hypothesizes that the pores below the warm side of the ice lens freeze until the water transport to the ice lens stops and a new ice lens forms near the frost line. Then, the remaining water in the pores between the two ice lenses freezes or is sucked in by the existing ice lens. He assumes that the air in the soil is displaced towards the emerging ice lens, which gives the ice lens a white thread-like structure in the direction of heat conduction.

Ruckli (1944) pointed out that capillary theory is insufficient to describe ice lens formation because it does not consider that under saturated conditions, no free menisci can be formed under the ice lenses. He describes that ice and the soil grains are enclosed by an liquid adsorption film, similar to Taber (1930). The film thickness depends on actual stresses, so increasing load leads to a decreasing film thickness. If the ice crystal releases heat from external cooling, it can extract water molecules from the film and incorporate them into its lattice. The thin film draws free water from the surrounding pore space to restore the film equilibrium.

Martin (1959) developed a theory of rhythmic ice banding under unsteady heat flow conditions. Ice nucleation begins at a temperature lower than the temperature at which ice crystals grow significantly. The ice crystals grow by water transport from adjacent soil and their growth rate is proportional to the area of contact with unfrozen water. A requirement for rhythmic ice lens formation is that the permeability of the soil must be such that a steady heat flux can be temporarily maintained due to a specific heat extraction rate and heat supply. With decreasing permeability in the unfrozen zone, ice lens growth stops, and a new ice lens forms when the nucleation temperature is reached at another position, therefore, repeating this rhythmic process.

Konrad and Morgenstern (1980) introduce a new mechanistic theory of rhythmic ice lens formation in fine-grained soils during unsteady heat flow (cf. Figure 17). It states that ice lenses occur in the frozen fringe, a semi-frozen area behind the frost line, which contains unfrozen water films around soil particles and ice in thermodynamic equilibrium. Once an ice lens is formed, the unfrozen water film constitutes the water supply provided to the ice lens. Water from the unfrozen region is drawn into the frozen fringe to maintain the film thickness or thermodynamic equilibrium. The location of ice lens formation during frost penetration depends on local permeability, with a critical permeability that prevents further water migration toward the frozen part. They defined a segregation-freezing temperature, T_{sf}, that is associated to the critical permeability. T_{sf} is unique for a given soil and independent of the temperature boundary conditions under zero external load. When T_{sf} is reached during frost penetration, an ice lens initiates. At a temperature T_{sm}, also unique for a soil, the ice lens growth stops due to extremely low permeability. At the beginning of frost penetration, no visible ice lenses develop due to rapid freezing velocities. When the temperature gradient decreases, thin ice lenses with small vertical spacing appear. The thickness of ice lenses depends on the time interval in which water can be drawn to the base of the ice lens. The largest ice lens forms when the frost line stops moving and the temperature T_{sm} can no longer be reached. This last ice lens is also referred to as the decisive

ice lens; a name given due to its greater thickness. Since thermal processes are still occurring during ice lens formation, this phase is also called the quasi-steady state (Zhou et al. 2009).

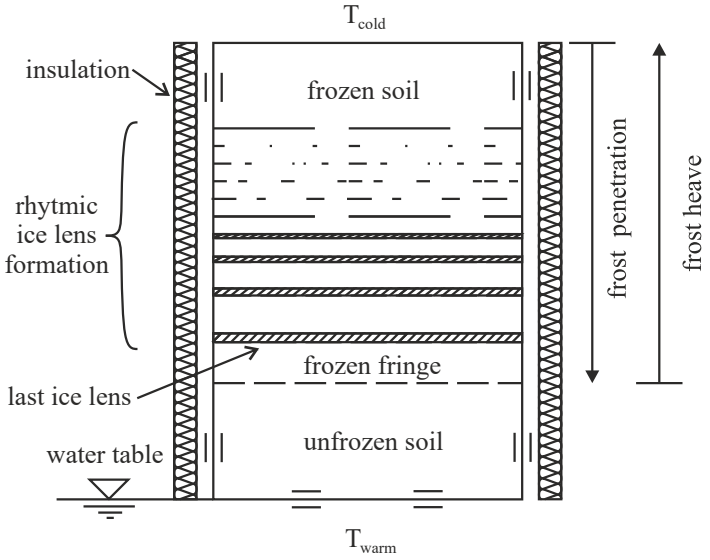

Figure 17: Rhythmic ice lens formation, after Konrad and Morgenstern (1980)

In 1972, Miller pointed out that ice lenses do not form until the pore water pressure is high enough to separate the soil particles. O'Neill and Miller (1982; 1985) introduced a secondary frost heave model, with ice lens formation in the frozen fringe. During freezing, the ice body grows through an existing pore system or builds on pre-existing ice. This generates an interconnected ice body of pore ice and ice lens. This solid body moves towards the cold boundary condition during frost heave with spatially uniform velocity. Water flow ensures ice lens growth, enabled by pressure and hydraulic conductivity changes along the fringe. Ice lenses grow due to the thermal regelation of pore ice and by the water flow of the unfrozen water films around the soil grains towards the ice lens.

Gilpin (1980) and O'Neill and Miller (1982; 1985) explain the ice lens initiation using a pressure-dependent approach. Gilpin (1980) introduced the concept of separation pressure σ_{sep}, defined as interfacial pressure in a semi-frozen area. It can be calculated by the overburden pressure σ_{OB} and additional pressure that considers surface tension due to geometrical conditions at the solid-liquid interface σ_{γ}.

$$\sigma_{sep} = \sigma_{OB} + \sigma_{\gamma} \tag{5.1}$$

O'Neill and Miller (1982; 1985) define neutral stress σ_n as the sum of water pressure P_w and ice pressure P_i weighted by a quantity function χ related to the unfrozen water content θ_w in the soil.

$$\sigma_n = \chi(\theta_w) \cdot P_w + (1 - \chi(\theta_w)) \cdot P_i \tag{5.2}$$

When the neutral stress σ_n equals the overburden pressure σ_{OB}, the effective stress σ' becomes zero, and a new ice lens can initiate.

$$\sigma' = \sigma_{OB} - \sigma_n \tag{5.3}$$

These concepts, in their origin or adjusted form, are widely used to explain and predict frost heave with ice lens formation, e.g., Horne (1987); Nixon (1991), Saarelainen (1992), Fowler and Krantz (1994), Black (1995), Sheng et al. (1995); Talamucci (2003), Kim et al. (2008).

A newer concept to define the beginning of ice lens formation is formulated by Zhou and Li (2012) using a concept of a separating void ratio e_{sep}, e.g., applied by Sweidan et al. (2021). If e_{sep} is reached, pore ice grains can connect, and an ice lens starts to build. The separation void ratio is equal to the largest void ratio for silt, typically defined as e_{max}.

$$e \geq e_{sep} \tag{5.4}$$

5.1.1. Frozen Fringe

The frozen fringe is characterized as a transition area that contains unfrozen water and ice at the same temperatures, e.g., Miller (1972), Konrad and Morgenstern (1980), Gilpin (1980), O'Neill and Miller (1982; 1985). Figure 18 gives a schematic view of the frozen fringe, which is thermally restricted by the temperature at the frost line (0°C-Isotherme) and the warm side temperature of the ice lens.

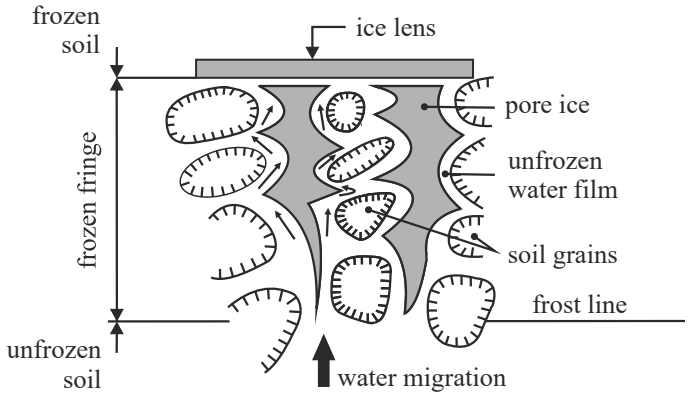

Figure 18: Schematic illustration of the frozen fringe, after Konrad (1993)

The head of pore water pressure, the unfrozen water content and the permeability decrease through the fringe towards the ice lens. The water pressure at the warm side of the ice lens depends on the segregation temperature and the overburden pressure. Figure 19 shows the characteristic temperature T, the water pressure P_w, and the permeability k_f of the frozen fringe during ice lens initiation and growth. The temperature profile is assumed to be linear in the frozen fringe (Sheng et al. 1995). Konrad and Morgenstern (1980) also assume that the temperature gradient in the frozen fringe is similar to the gradient in the unfrozen zone at the beginning of the steady state phase. Akagawa (1988) confirmed this by using the X-Ray photography technique to examine the frozen fringe characteristic. The water pressure P_w at the warm side of the ice lens is negative (suction) and increases towards the frost line. For fine grained soil, the water pressure at the frost

line is still negative and changes to atmospheric pressure in the unfrozen area. The permeability k_f at the frost line is similar to unfrozen conditions and runs toward zero along the frozen fringe.

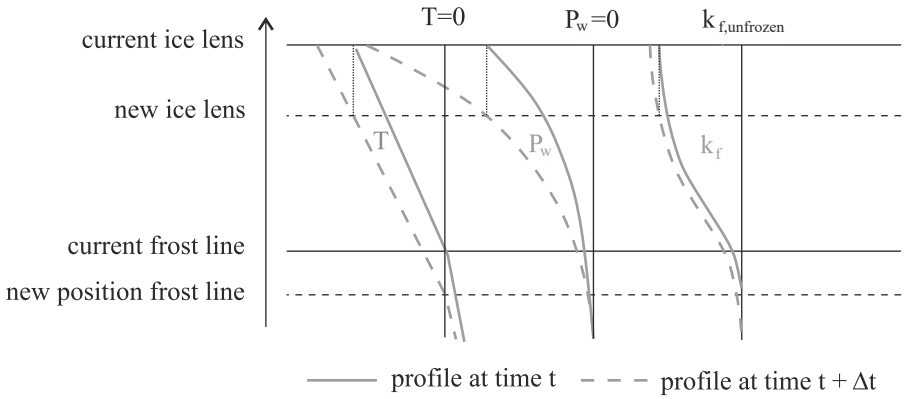

Figure 19: Characteristic of the frozen fringe at ice lens initiation and growth, after Sheng et al. (1995)

The segregation temperature at the warm side of the ice lens drops gradually during ice lens formation. Thus, the liquid water content and the permeability close to the ice lens decrease until water migrations to the ice lens stop and the water accumulation occurs at another level (Sheng et al. 1995).

Penner (1986) and Konrad (1989) used the X-Ray photography technique to prove that the ice lens temperature reduces during growth, increasing the thickness of the frozen fringe in clayey soils. The ice lens temperatures, measured by a dense arrangement of temperature sensors, have an initiation temperature below 0°C and decrease during ice lens growth. The measured temperature difference increases with decreasing cooling rate. A reduced heave rate during ice lens formation results from the decreasing permeability in the frozen fringe due to an increasing ice content.

Chamberlain and Gow (1979) and Akagawa (1988) experienced crack formation during freezing due to shrinkage processes near the ice lens. Vertical cracks arise near the warmest ice lens in the frozen fringe. During freezing tests on fully consolidated silt and clay slurries, Chamberlain and Gow (1979) found that the cracks are linked together, forming columns with a polygonal cross-section (cf. Figure 20). These formed polygons lead to an increase in density and permeability. Arenson et al. (2007; 2008) investigated these vertical “ice veins” during freezing a Devon silt, that initiated when the soil reaches its tensile strength due to the suction in the frozen fringe. These vertical cracks go through the frozen fringe down to the unfrozen zone. Conversely to horizontal ice lenses, they do not significantly change their thickness with time. Even if the small cracks are ice-filled in the frozen fringe, they lead to better water flow to the ice lens via thin water films.

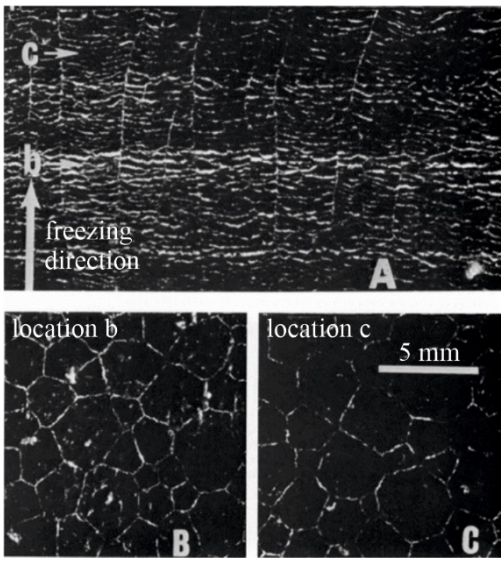

Figure 20: Experienced cracks after freezing of clay; vertical (A) and horizontal (B and C) sections, after Chamberlain and Gow (1979)

5.2. Factors affecting frost heave

Different factors affect frost heave and ice lens formation. Taber (1930) identified the main factors as the size and shape of soil particles, amount of water availability, size and percentage of the void, cooling rate, and the surface load or resistance to heaving.

Particle size

The grain size is the most relevant parameter according to the frost sensitivity classification (e.g., ZTV E-StB 17 ,2017). The smaller the grains, the greater the specific surface and the more water can be bound. This explains why frost heaves of clay can be typically greater than that of sand, even though some water remains unfrozen at negative temperatures in clay. Corte (1962) investigated that, depending on the grain size and the freezing velocity, fine soil grains are pushed ahead the ice interface during freezing while the ice engulfed greater soil grains. The fine soil grains form a layer that tends to bound water favoring ice lens formation. Greater particles lying cross the freezing plane restrain frost heave due to frictional resistance. The faster the frost penetration, the smaller the particles that are engulfed (Corte 1962; Kaplar 1970).

Water availability

Chamberlain (1981) defines the depth of the water table as one of the significant factors in frost heaving. Saturated voids and a water table near the frost line is the most critical condition for frost heave. Dagli (2017) used PIV to observe soil deformations due to freezing and thawing and mentioned the importance of water availability in the surrounding area for ice lens formation. The closer the frost depth reaches the groundwater level, the more significant the ice lens formation occurs. Maximum heave occurs when the soil is saturated, and the water table is at the frost line.

Voids

The voids and the saturation degree significantly affect frost heave concerning pore water expansion. The more water-filled voids exist, the greater the heave expansion. Conversely, with a lower saturation degree, the voids may act as expansion space for the freezing water with less significant deformation.

Water movement in partially frozen soil occurs through small pores, where the pore water is unfrozen. The finer the pore size, the greater the moisture tension during freezing, thus, available moisture for heaving. Moisture tension can develop during freezing point depression, which decreases in small pores (Penner 1957; Hoekstra 1969).

Cooling rate

The cooling rate influences the frost penetration velocity. A fast frost penetration during transient freezing leads to less water accumulation for ice lens formation and decreases the thickness and frequency of ice lenses (Loch & Kay 1978; Penner 1986). In addition, Kaplar's (1970) studies show that the cooling rate influences soil heaving by dividing the total heave rate into the void water heave rate and ice segregation rate. The heave rate increases linearly with frost penetration velocity, whereas the ice segregation rate only increases until a specific frost penetration rate is reached and decreases after reaching the peak to zero ice segregation.

Surface load

A pressure load can reduce or prevent ice lens formation. The free energy available during phase change at the ice lens heaves the frozen part and maintains film thickness by sucking additional water toward the ice lens. If an additional load is applied, less energy is left for moisture transport, and the film thickness decreases (Aitken 1974). If water molecules are prevented from increasing their distance due to loading, a change into a solid phase is impossible, and heaving stops. The load, where no heaving occurs, is called shut-off pressure and can be reached 1.500 kPa for pure clay (Taber 1930; Hill & Morgenstern 1977). The effect of freezing point depression due to loading with 0.0073 K/bar is neglectable for engineering purposes. If the stress range is great enough that a depression would have a remarkable effect, the soil consolidation primarily will affect the pore water stress behavior (Unold 2006).

5.3. Frost heave models

Various models for calculating frost heave have been proposed in the past decades. The three most important models that describe discrete ice lens formation are given in this section: capillary theory, rigid ice model and segregation potential.

5.3.1. Capillary theory

The capillary theory uses the phenomenon of capillary rise due to interfacial tension between water and air but adapted to the water and ice interface. The pressure difference across a curved ice-

water interface ($P_i - P_w$) leads to suction and, therefore, water migration to the frost line. The capillary model does not consider a frozen fringe so the sucked-in water accumulates at the frost line forming an ice lens. The head of suction in the capillary model depends on the surface tension of water and ice γ and the radius of the curvature of soil ice r_i. (Williams 1967; Johansson 2009):

$$P_i - P_w = \frac{2\gamma}{r_i} \qquad 5.5$$

If the ice radius r_i is larger than the effective pore radius r_p (cf. Figure 21), no ice penetration into the pores occurs. The ice can only penetrate through the pores when the pressure difference between water and ice becomes large enough so that the ice radius gets equal to the effective pore radius by regelation. The frost heave stops when ice penetrates the pores and prevents water migration towards the growing ice lens (Peppin & Style 2013).

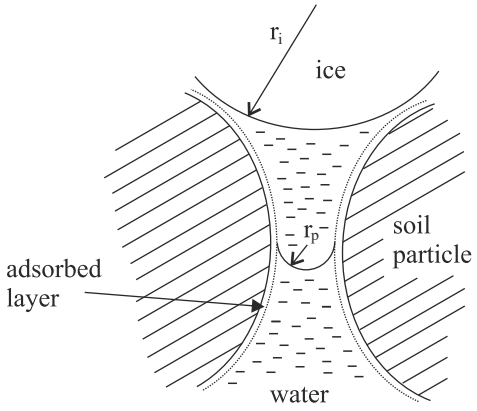

Figure 21: Schematic illustration of the theorized capillary pore, after Johansson (2009)

The ice accumulation only occurs at the freezing front, and the suction only comes from soil characteristics. Temperature-dependent boundary conditions like the temperature gradient, which influences the frost penetration rate, are not considered. Water migration only occurs in the unfrozen part (Ladanyi & Shen 1989). Furthermore, there is no plausible mechanism within the capillary theory to explain rhythmic ice lens formation.

Researchers like Hoekstra (1969) and Loch and Kay (1978) investigated water migration experimentally behind the frost line, which makes the capillary theory insufficient to explain ice lens heave.

5.3.2. Rigid Ice Model

The rigid ice model was developed by O'Neill & Miller (1982; 1985), who distinguished between primary and secondary heaving. The primary heave is similar to the capillary theory, with ice growing on top of some unfrozen soil. Water migrates towards the ice, but no ice penetrates the soil pores, meaning heave only occurs through ice lens formation. The secondary heave includes penetrating soil ice with water migration via adsorbed water films to the ice, accumulating there. The rigid ice assumption states that soil ice forms on preexisting ice and growth through the soil

pores to form a semi-frozen zone, the so-called frozen fringe. During freezing, the total rigid body moves toward the cold side boundary by melting ice from the warm side and transporting the unfrozen water to the cold side, where it freezes again (thermally-induced regelation). An ice lens initiates when the increasing ice pressure can move the soil particles apart. Hence, the ice lens grows due to water accumulation from unfrozen regions through the fringe. The pore ice from the frozen fringe is rigidly connected to the rising ice lens. A new ice lens initiation goes along with a cut-off water flow to the previous ice lens.

O'Neill and Millers model is based on conservation laws for mass and energy. The relative ice and water proportions in the frozen fringe are mostly controlled by the temperature and pressure conditions. The ice-water pressure difference ($P_i - P_w$) depends on the mean curvature of the ice-water interface κ_{iw} and the interfacial tension γ.

$$P_i - P_w = \kappa_{iw}\gamma \tag{5.6}$$

Within the freezing process, the ice penetrates smaller pores, and the curvature of the interface increases, which affects the water-ice pressure difference. Darcy's law is used in the unfrozen and frozen zone to calculate water migration, considering the decreasing hydraulic conductivity in the fringe. Ice lens initiation is obtained by force balance. If the overburden load gets equal to the pressure in the unfrozen water film, the effective stress becomes zero, and a new ice lens can be formed (cf. equations 5.2 and 5.3, section 5.1). The ice lens grows by the upward extruding of pore ice due to regelation and by upwards moving water through the unfrozen water films between soil particles and ice (O'Neill & Miller 1982; O'Neill & Miller 1985; Rempel 2010).

Rempel (2010) pointed out that for frost heave prediction using the rigid ice model, no geometrical details of the ice-water interface must be solved. However, there is a theoretical basis on the microscopic level for the force balance equation missing. However, O'Neill and Miller (1985) pointed out that the model requires considerable computational expense due to the simulation of the initiation and growth of each lens.

5.3.3. Segregation Potential

The section focuses on the Segregation Potential approach by *Konrad and Morgenstern.* The approach has been mainly and most successfully applied to the heave calculation of natural-induced ground freezing in cold regions (Nixon 1982; Horne 1987; Konrad & Shen 1996; Tiedje & Guo 2012; Zhang et al. 2020) and is the bases of the new semi-analytical approach developed in this thesis.

Konrad and Morgenstern (1980; 1981; 1982) propose this approach to calculate frost heaving during frost penetration. The Segregation Potential SP can be treated as a soil constant for one specific soil, calculated by the water inflow v and the temperature gradient along the unfrozen soil ∇T_{uf}. The value for SP is calculated at the end of transient freezing because, just before thermal steady state conditions, the required parameters can be considered constant.

$$SP = \frac{v}{\nabla T_{uf}} = const. \tag{5.7}$$

Once SP is known, the determination of ice lens temperature, frozen fringe permeability, and freezing suction is not necessary to predict frost heave of a particular soil.

The grown ice lens separates the soil into an active part, which includes the unfrozen soil and the frozen fringe, and a passive part, which is the frozen soil. Water flow only happens in the active part of the soil, and water accumulation only occurs on the warm side of the ice lens. The water flow rate into the frozen fringe $v(t)$ is proportional to the segregation frost heave $h_s(t)$ due to ice lens formation.

$$h_s(t) = \int_0^t \frac{dh_s}{dt} dt = 1{,}09 \int_0^t v(t) dt \tag{5.8}$$

Figure 22 gives the actual (dashed line) and simplified (solid line) progress of temperature T, permeability K_f, and suction P along the length of the frozen fringe l_{ff}, which is restricted by the warm side of the ice lens (IL) and the frost line (0°C). The temperature progress is almost linear and similar to the temperature gradient in the unfrozen soil part. *Konrad and Morgenstern* assume that an ice lens is built at the same temperature for one specific soil. The permeability in the fringe is temperature dependent but, in the model, averaged along the frozen fringe length. The suction profile along the frozen fringe is assumed to be linear according to the generalized Clausius-Clapeyron equation but only valid for as long as no loading is applied. Further assumptions of the approach are:

- validity of Darcy‘s law
- full water saturation of the soil
- the incompressibility of the grain structure
- no consideration of dissolved salts in soil or soil water
- neglect of changed thermal conductivity between unfrozen and semi-frozen soil in the frozen fringe

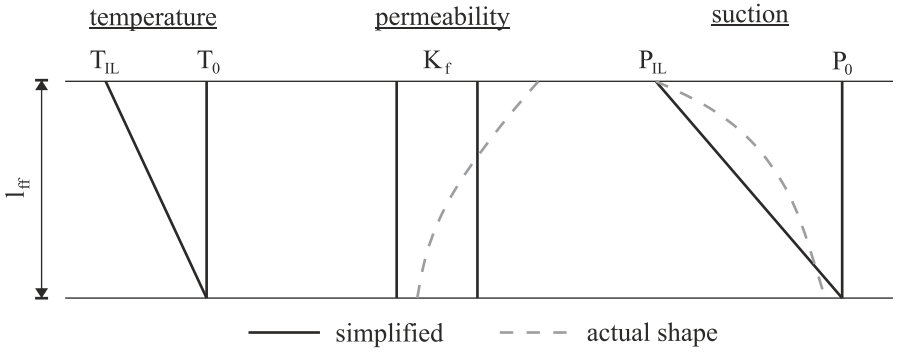

Figure 22: Frozen fringe characteristics of temperature, permeability, and suction, after Konrad and Morgenstern (1981)

Supposing the same soil is loaded under different temperature gradients, a different length of the frozen fringe results. Konrad and Morgenstern assume that the mean temperature, permeability, and suction are independent of the fringe length. If the temperature at the ice lens and the mean permeability are the same regardless of the length of the frozen fringe, the product of the water inflow velocity v_i and the frozen fringe thickness l_i is constant.

$$v_1 \cdot l_1 = v_2 \cdot l_2 \tag{5.9}$$

The frozen fringe length l_i depends on the ice lens temperature T_{IL} and the temperature gradient in the frozen fringe, which is assumed to be the same as in the unfrozen part ∇T_{uf}.

$$l_i = \frac{|T_{IL}|}{\nabla T_{uf}} \tag{5.10}$$

Using Darcy's law, it follows:

$$v = \frac{P_{IL} - P_0}{|T_{IL}|/\nabla T_{uf}} \cdot \overline{K_{f,ff}} \tag{5.11}$$

The parameters that are the same for one soil, like the temperature-dependent suction at the ice lens P_{IL} and at the frost line P_0, as well as the overall permeability of the fringe $\overline{K_{f,ff}}$, are summarized in the soil constant SP (cf. equation 5.7).

$$v = SP \cdot \nabla T_{uf} \tag{5.12}$$

Only a limited number (≥1) of soil freezing tests is required to calculate SP.

Konrad and Morgenstern (1982b) also give an empirical relationship between the SP and applied pressure P near the thermal steady state:

$$SP_P = SP \cdot e^{-aP} \tag{5.13}$$

The Segregation Potential SP at zero load can be determined by equation 5.12. The constant a is related to the soil frost heave sensitivity to overburden pressure and empirically determined.

6 Experimental and analytical study on frost heave with ice lens formation for an AGF

The following subsections summarize the main points of the research on frost heave with ice lens formation for AGF boundary conditions shown in detail in the following three published contributions, which are attached in appendix A-C.

Table 1: Listed publications during this thesis

No.	Contribution	Appx.
1	Sweidan, A. H., **Niggemann, K.**, Heider, Y., Ziegler, M., Markert, B. (2022): Experimental study and numerical modeling of the thermo-hydro-mechanical processes in soil freezing with different frost penetration directions. Acta Geotechnica, 17(1), pp. 231-255. https://doi.org/10.1007/s11440-021-01191-z	A
2	**Niggemann, K.**, Ziegler, M., Fuentes, R. (2024): Influence of freezing directions on ice lens formations in soils. Acta Geotechnica. https://doi.org/10.1007/s11440-024-02259-2	B
3	**Niggemann, K.**, Fuentes, R. (2023): New semi-analytical approach for ice lens heaving during artificial freezing of fine-grained material. Journal of Rock Mechanics and Geotechnical Engineering, 15(11), pp. 2994-3009. https://doi.org/10.1016/j.jrmge.2023.07.004	C

6.1. Paper #1

Experimental study and numerical modeling of the thermo-hydro-mechanical processes in multi-directional soil freezing with different frost penetration directions

This research work presents an experimental and numerical study of the coupled thermo-hydro-mechanical (THM) processes that occur during soil freezing. With focusing on the artificial ground freezing (AGF) technology, a new testing device is built, which considers a variety of AGF-related boundary conditions and different freezing directions. In the conducted experiments, a distinction is made between two thermal states: (1) The thermal transient state, which is associated with ice penetration, small deformations, and insignificant water suction. (2) The thermal (quasi-) steady state, which has a much longer duration and is associated with significant ice lens formation due to water suction. In the numerical modeling, a special focus is laid on the processes that occur during the thermal transient state. Besides, a demonstration of the micro-cryo-suction mechanism and its realization in the continuum model through a phenomenological retention-curve-like formulation is presented. This allows modeling the ice lens formation and the stiffness degradation observed in the experiments. Assuming a fully saturated soil as a biphasic porous material, a phase-change THM approach is applied in the numerical modeling. The governing equations are based on the continuum mechanical theory of porous media (TPM) extended by the phase-field modeling (PFM) approach. The model proceeds from a small-strain assumption, whereas the pore fluid can be found in liquid water or solid ice state with a unified kinematics treatment of both states. Comparisons with the experimental data demonstrate the ability and usefulness of the considered model in describing the freezing of saturated soils.

(The own contribution of the work on this paper includes the experimental part with the introduction of the new test device, the investigation of material parameters and the implementation and evaluation of the first freezing tests to provide a comprehensive data base for the numerical validation.)

6.2. Paper #2

Influence of freezing directions on ice lens formations in soils

This research work presents a comprehensive experimental study of frost heave in a fine-grained material to investigate the effects of top freezing (TF) and bottom freezing (BF) mechanisms with ice lens formation. A novel test device was built to investigate artificial ground freezing (AGF)-related temperature and load boundary conditions. This paper includes 62 frost heave experiments and test observations up to 10 days. The long test duration allows a precise examination of ice lens growth during thermal steady state when the frost line remains largely stable and the ice lens grows. This state corresponds to the holding phase of a practical in situ AGF implementation where the cooling is used to maintain the frozen body thickness. The freezing observations show that BF heaving is larger than TF heaving in most cases. This is caused by the more favorable hydraulic conditions caused by gravitational effects and vertical cracking that occurs during ice lens formation due to suction. This facilitates water accumulation at the ice lens. An applied load reduces the differences between BF and TF conditions beyond a certain value which corresponds to an overburden capable of preventing the formation of the longitudinal cracks.

6.3. Paper #3

New semi-analytical approach for ice lens heaving during artificial freezing of fine-grained material

The calculation of frost heaving with ice lens formation is still not standard for construction projects using artificial ground freezing (AGF). In fine-grained material, ice lenses may initiate and lead to significant heaving at the ground surface, which should be considered in advance. However, the complex processes during ice lens formation are still not fully understood and difficult to capture in a simple approach. In the past, the semi-analytical approach of Konrad and Morgenstern used one soil constant, the "Segregation Potential (SP)". It has been mainly and most successfully applied to the heave calculation of natural-induced soil freezing in cold regions. Its application to AGF has been so far unsuccessful. To solve this, a new semi-analytical approach is presented in this paper. It includes AGF conditions such as bottom-up freezing, temperature gradients to reach great freezing velocities, and a distinction between two freezing states. One is the freezing-up state until a certain frost body thickness is reached (thermal transient state), and the other is a holding phase where the frost body thickness is kept constant (thermal quasi-steady state). To test its ability, the results are applied to another freezing direction, the top-down freezing. The new approach is validated using two different frost-susceptible soils and, in total, 50 frost heave tests. In the thermal transient region, where the SP is applicable, the two semi-analytical approaches are compared, showing improved performance of the current method by about 15%.

7 Summary and outlook

Artificial ground freezing (AGF) has become established in construction projects worldwide because it improves the properties of the ground, e.g., stability and water impermeability. In fine-grained soil, like silt or clay, frost heaves in the centimeter range may occur due to pore water expansion and ice lens formation. This causes damage to exist infrastructure like, e.g., streets, tracks, or buildings. The calculation of frost heaving with ice lens formation is still not standard for AGF projects, and heave prediction is usually based on soil frost susceptibility recommendations. The complex processes during ice lens formation are still not fully explored and challenging to combine in a practical approach. A semi-analytical approach, the Segregation Potential (SP) of Konrad and Morgenstern (1980; 1981; 1982), finds application in heave prediction of natural-induced soil freezing in cold regions. The approach uses an experimental investigated soil constant SP, which includes unknown or difficult exploring parameters. Transferred to an AGF, the approach in its known form reaches its limitations.

The objective of the thesis was to enhance the understanding of frost heave in fine-grained material during AGF under different boundary conditions. Therefore, a comprehensive experimental test program was conducted in this work to quantify frost heave considering the AGF boundary conditions. Based on the findings, a new semi-analytical approach was developed that fulfills the requirements of an AGF.

7.1. Key findings

Paper #1

A new test device was developed to simultaneously freeze two samples, one from the top downwards (top freezing – TF) and the other from the bottom upwards (bottom freezing – BF) to imitate the two main freezing directions and quantify the frost heave. Freezing tests were carried out with a lean clay in which ice lenses are formed. The first freezing results were used by the Chair and Institute of General Mechanics (IAM, RWTH Aachen University) within the framework of a DFG project to develop a thermo-hydro-mechanical model that augments the macroscopic theory of porous media (TPM) with the phase-field modeling (PFM) to simulate the freezing process.

Thermal, mechanical, and hydraulic boundary conditions were demonstrated, and important thermal and mechanical soil parameters were carried out for the numerical calculation. The evaluation process was explained which includes the evaluation of frost heave, temperature measurements and the amount of sucked water into the soil sample. Within the test observation

two thermal states were defined. One is the thermal transient state during frost penetration with moving frost line and primary pore water expansion. The other is the thermal steady state when the frost line maintains a specific position due to thermal (quasi-)equilibrium (there are still thermal processes due to ice lens formation, but of minor interest concerning frost penetration) with only ice lens formation. This state corresponds to the holding phase where the cooling is used to maintain the frozen body. Regarding an in-situ AGF implementation, at the thermal steady state a large ice lens can grow, so this state is of main interest. The first experimental results showed the expected differences between TF and BF during freezing which encouraged a more detailed study considering the boundary conditions of an AGF.

Paper #2

Based on the first test results a large parameter study to investigate the influence of freezing directions on lens formation was carried out. The experimental tests focused on relevant boundary conditions of an AGF, and the results of TF-tests were compared with the BF-test results. The experimental study included 62 frost heave tests with test observations up to 10 days. The long test duration allowed a precise examination of the ice lens growth during the thermal steady state when only ice lens forms. In each experiment, a separation was made between the thermal transient and the thermal steady state. The tests included observation with different absolute freezing temperatures, temperature gradients, and external loads. During the experiment, free access to a water source (reservoir) at the warm side of the soil sample was available. Additionally, a test was carried out with a restricted water supply.

The visual observation of the tests revealed a crack formation in the unfrozen area, which changes the hydraulic conductivity in the soil sample and, therefore, influences ice lens formation. With wider crack openings, more water reaches the ice lens. This effect is particularly noticeable at BF, as the water flows in the direction of gravity. The cracks emerge when water at the warm side of the ice lens is drained off for ice lens growth. A series of images is provided which shows that a greater load reduces crack formation.

During the thermal transient state there was only a negligible ice lens formation observed and can be related to the freezing rate. Generally, frost heaving during TF is usually larger than BF heave which is attributed to greater soil weight and consolidation effects in the BF conditions.

At thermal steady state one relevant factor with great impact on the magnitude of frost heaving is the length of the unfrozen soil which is equivalent to the flow path of the water from the reservoir towards the ice lens. A shorter flow path due to lower freezing temperatures increases the hydraulic gradient for the same boundary hydraulic conditions and, therefore, the water flow velocity to the ice lens independently of the freezing direction. But during ice lens formation, BF indicates greater frost heave than TF for almost all conditions. The greatest frost heave occurs with short flow path and cracks reaching the unfrozen surface. The application of vertical load reduces crack formation and for the given soil, an applied load of 150 kPa (≈ 8 m overburden, with $\rho_{soil} \approx 1.9$ g/cm^3) seemed to be the threshold from which the cracks would not form.

Paper #3

The requirement for the new semi-analytical approach is the focus on AGF conditions. These are the freezing direction from the bottom upwards, temperature gradients to reach great freezing velocities, and a distinction between two freezing states, the thermal transient state and thermal steady state. The new approach was validated using two different frost susceptible soils and 50 frost heave tests. In the thermal transient region, where the SP approach of Konrad and Morgenstern (1980; 1981; 1982) is applicable, it was compared with the new approach presented here.

For thermal transient conditions, it was inferred that using the soil constant C is sufficient to calculate the ice lens heave of a specific soil for different thermal boundary conditions. The calculation of C only requires one frost heave test (test 1). For the thermal steady state, one additional test (test 2) with a freezing temperature deviating from test 1 is necessary to calculate the function $f(t)$. The function $f(t)$ is the same for one specific soil under different thermal boundary conditions. Both equations for the calculation of C and $f(t)$ contain parameters representing the length of the unfrozen soil area or flow path of sucked water, respectively, which was defined as a driving force concerning the observations of ice lens formation during the experimental observation (cf. paper #2). Within the validation of the approaches using the two different soils, there is very good agreement regarding the actual ice lens growth. The calculated heaving using the SP (only valid for the thermal transient state) overestimates the measured data, attributed to the focus on the temperature gradient but not the flow path of sucked water. In comparison with the SP approach, the current method shows an improved performance by about 15 %.

The advantage of the semi-analytical approach is that for one specific soil only two frost heave tests must be performed to calculate frost heaving for the thermal transient and thermal steady state. No special soil testing is required since the calculated constant C (thermal transient state), or the function $f(t)$ (thermal steady state) include the specific soil parameters which control the freezing suction and thus the water accumulation at the ice lens. Once C and $f(t)$ are known, frost heave with ice lens formation can be predicted for different thermal conditions.

In conclusion, this research presented a comprehensive study on frost heave in fine-grained material during AGF under different boundary conditions based on experimental investigations, which were used to implement a new semi-analytical approach for frost heave calculation.

7.2. Future research

The results of the experimental investigations have proven that BF frost heave exceeds TF frost heave in dependence on the vertical load conditions. The vertical cracks that arise during freezing are diminished with increasing load and a threshold from which vertical cracks no longer form was found for the given soil. Initially, quantifying the dependence of crack openings to different frost-susceptible soils is highly important. The focus should be on the content of the fine fraction which controls the water availability for ice lens formation and makes the greatest contribution to

the tensile strength of unfrozen soil. For the investigation of the cracks initiation, growth, and size, visual methods like particle image velocimetry (PIV) can be used to determine particle movement in specific time intervals. As the grain size of frost susceptible soil is very small colored particles could be used as tracer. In this case it is important that supplements do not change chemical properties of the material. Further, the load threshold for crack opening of different soil compositions can be investigated and be correlated with the fine fraction of the soil. Therefore, a substantial soil database needs to find correlations.

Further, the integration of an overburden load can extend the semi-analytical approach. The overburden load can prevent frost heaving when the load approaches or reaches the heaving pressure at the ice lens. However, the heaving pressure is different for various soils. Thus, empirical correlations between the load and the soil composition can be used to implement the overburden load.

In the derivation of the semi-analytical approach, the nonlinear relationship between the flow velocity (= heave rate) and the hydraulic gradient is explained by entrapped soil air accumulates at the warm end of the ice lens and forms a barrier reducing the flow velocity with time. This nonlinear relation slightly changes with time during the thermal steady state. This has been considered empirically in this thesis by the coefficients $m(t)$ and $n(t)$. Studying the water flow through the frozen fringe for thermal steady state conditions can give a deeper insight into this time-dependent mechanism occurring during ice lens formation. This can be done experimentally by precise determining the water supply (e.g., ultrasonic sensor for hoses) into the frozen fringe or adding a defined quantity by simultaneously measuring the ice lens growth (e.g., optical measuring).

References

Aitken, G.W. (1974): Reduction of frost heave by surcharge stress, Corps of Engineers, US Army Cold Regions Research and Engineering Laboratory.

Akagawa, S. (1988): Experimental study of frozen fringe characteristics. Cold Regions Science and Technology, Vol. 15 (3), pp. 209-223.

Amelung, W., Blume, H.-P., Fleige, H., Horn, R., Kandeler, E., Kögel-Knabner, I., Kretzschmar, R., Stahr, K., Wilke, B.-M. (2018): Scheffer/Schachtschabel Lehrbuch der Bodenkunde, Springer-Verlag.

Anderson, D.M., Tice, A.R. (1972): Predicting unfrozen water contents in frozen soils from surface area measurements. Highway research record, Vol. 393 (2), pp. 12-18.

Arenson, L., Azmatch, T., Sego, D., Biggar, K. (2008): A new hypothesis on ice lens formation in frost-susceptible soils. In: Proceedings of the ninth international conference on permafrost, Fairbanks, Alaska, Vol. 1, pp.59-64.

Arenson, L., Sego, D., Take, W.A. (2007): Measurement of ice lens growth and soil consolidation during frost penetration using particle image velocimetry (PIV). In: 60th Canadian Geotechnical Conference & 8th Joint CGS/IAH-CNC Groundwater Conference, Ottawa, Ontario, Canada, pp. 2046-2053.

Atkins, P.W. (1996): Physikalische Chemie, 2. Aufl., Weinheim VCH Verlagsgesellschaft.

Auld, F.A., Belton, J., Allenby, D. (2015): Application of artificial ground freezing. In: Proceedings of the XVI ECSMGE, Geotechnical Engineering for Infrastructure and Development, pp. 901-906.

Baier, C. (2008): Thermisch-hydraulische Simulationen zur Optimierung von Vereisungsmaßnahmen im Tunnelbau unter Einfluss einer Grundwasserströmung. Doktorarbeit, Lehrstuhl für Geotechnik im Bauwesen, RWTH Aachen University.

Biermans, M.B.G.M., Dijkema, K.M., de Vries, D.A. (1978): Water movement in porous media towards an ice front. Journal of Hydrology, Vol. 37 (1-2), pp. 137-148.

Black, P.B. (1995): Applications of the Clapeyron equation to water and ice in porous media. CRREL - Cold Regions Research & Engineering Laboratory, Vol. 95-6.

Black, P.B. (1995): Rigidice model of secondary frost heave. CRREL - Cold Regions Research & Engineering Laboratory, Vol. 95-12.

Busch, K., Luckner, L., Tiemer, K. (1993): Geohydraulik, 3. Auflage, Gebrüder Bornträger, Berlin.

Cai, H., Hong, R., Xu, L., Wang, C., Rong, C. (2022): Frost heave and thawing settlement of the ground after using a freeze-sealing pipe-roof method in the construction of the Gongbei Tunnel. Tunnelling and Underground Space Technology, Vol. 125, p. 104503.

Cai, H., Liu, Z., Li, S., Zheng, T. (2019): Improved analytical prediction of ground frost heave during tunnel construction using artificial ground freezing technique. Tunnelling and Underground Space Technology, Vol. 92, p. 103050.

Chamberlain (1981): Frost susceptibility of soil - Review of index tests. CRREL - Cold Regions Research & Engineering Laboratory, Vol. 81-2.

Chamberlain, E.J., Gow, A.J. (1979): Effect of freezing and thawing on the permeability and structure of soils. Engineering Geology, Vol. 13 (1-4), pp. 73-92.

Corte, A.E (1962): The frost behaviour of soils, field and laboratory data for a new concept, 1. Vertical sorting, 2. Horizontal sorting. CRREL - Cold Regions Research & Engineering Laboratory, Vol. 85.

Dagli, D. (2017): Laboratory investigations of frost action mechanisms in soils. Doctoral dissertation, Department of Civil, Environmental and Natural Resources Engineering, Luleå University of Technology.

DIN EN ISO 17892-11:2021-03: Geotechnische Erkundung und Untersuchung - Laborversuche an Bodenproben - Teil 11: Bestimmung der Wasserdurchlässigkeit.

Edlefsen, N., Anderson, A. (1943): Thermodynamics of soil moisture. Hilgardia, Vol. 15 (2), pp. 31-298.

Farouki, O.T. (1981): The thermal properties of soils in cold regions. Cold Regions Science and Technology, Vol. 5 (1), pp. 67-75.

Farouki, O.T. (1986): Thermal properties of soils. Series on Rock and Soil Mechanics, Trans Tech Publications, Vol. 11, pp. 1-133.

Fowler, A.C., Krantz, W.B. (1994): A generalized secondary frost heave model. Siam Journal on Applied Mathematics, Vol. 54 (6), pp. 1650-1675.

Fremond, M., Mikkola, M. (1991): Thermomechanical modelling of freezing soil. In: International symposium on ground freezing, pp. 17-24.

Frivik, P. (1981): State-of-the-art report. Ground freezing: thermal properties, modelling of processes and thermal design. Engineering Geology, Vol. 18, pp. 115-133.

Frivik, P., Thorbergsen, E., Del Giudice, S., Comini, G. (1977): Thermal design of pavement structures in seasonal frost areas. Journal of Heat Transfer, Vol 99 (4), pp. 533-540.

Frohberg, M.G. (2009): Thermodynamik für Werkstoffingenieure und Metallurgen: Eine Einführung.- John Wiley & Sons.

Fukusako, S. (1990): Thermophysical properties of ice, snow, and sea ice. International Journal of Thermophysics, Vol. 11 (2), pp. 353-372.

Gilpin, R.R. (1980): A model for the prediction of ice lensing and frost heave in soils. Water Resources Research, Vol. 16 (5), pp. 918-930.

Han, S., Goodings, D. (2006): Practical model of frost heave in clay. Journal of geotechnical and geoenvironmental engineering, Vol. 132 (1), pp. 92-101.

Hansson, K., Šimůnek, J., Mizoguchi, M., Lundin, L.C., Van Genuchten, M.T. (2004): Water flow and heat transport in frozen soil: Numerical solution and freeze–thaw applications. Vadose Zone Journal, Vol. 3 (2), pp. 693-704.

Hartge, K.H. (1978): Einführung in die Bodenphysik. Stuttgart, Ferdinand Enke Verlag.

Hartikainen, J., Mikkola, M. (1997): General thermomechanical model of freezing soil with numerical applications. In: Ground Freezing 97; Frost Action in Soils, Balkema, pp. 101-105.

Hill, D., Morgenstern, N. (1977): Influence of load and heat extraction on moisture transfer in freezing soils. In: International symposium on frost action in soils. Lulea: University of Lulea.

Hoekstra, P. (1969): Water movement and freezing pressures. Soil Science Society of America Journal, Vol. 33 (4), pp. 512-518.

Horne (1987): Prediction of frost heave using the segregation potential. Thesis, Department of Civil Engineering, The University of Alberta, Edmonton, Alberta.

Jessberger, H., Jagow-Klaff, R. (1996): Frost im Baugrund. Grundbau-Taschenbuch, Teil 1: Geotechnische Grundlagen, Witt, K. J. (ed.), Ernst & Sohn, Berlin, pp. 497-534.

Jessberger, H.L. (1979): Gefrierverfahren im Bauwesen. Theorie und Anwendungsgrenzen des Gefrierverfahrens im Bauwesen. Schweizerische Ingenieur- und Architektenverein, Referate der Studientage, ETH Zürich, Vol. 32, pp. 7-29.

Ji, Y., Zhou, G., Zhou, Y., Vandeginste, V. (2019): Frost heave in freezing soils: A quasi-static model for ice lens growth. Cold Regions Science and Technology, Vol. 158, pp. 10-17.

Johansen, O. (1977): Frost penetration and ice accumulation in soils. In: Proceedings of the International Symposium on Frost Action in Soils, University of Luleå, Sweden, Vol. 1, pp. 102-111.

Johansen, O. (1977b): Thermal conductivity of soils. CRREL - Cold Regions Research & Engineering Laboratory, TL 637.

Johansen, O., Frivik, P. (1980): Thermal properties of soils and rock materials. In: Proceedings of the 2nd International Symposium on Ground Freezing, NTH, Trondheim, Norwegen, pp. 427-452.

Johansson, T. (2009): Artificial ground freezing in clayey soils: Laboratory and field studies of deformations during thawing at the Bothnia Line. Doctoral dissertation, Department of Civil and Architectural Engineering, KTH Royal Institute of Technology Stockholm, Sweden.

Kaplar, C.W. (1970): Phenomenon and mechanism of frost heaving. Highway Research Record, Vol. 304, pp. 1-13.

Keinonen, L. (1977): A thermodynamic description of the ice lensing process. In: Proceedings of the International Symposium on Frost Action in Soils, University of Luleå, Sweden, Vol. 1, pp. 54-58.

Kestin, J. (1978): Thermal-conductivity of water and steam. Mechanical Engineering, Vol. 100 (8), pp. 46-48.

Kim, K., Zhou, W., Huang, S.L. (2008): Frost heave predictions of buried chilled gas pipelines with the effect of permafrost. Cold Regions Science and Technology, Vol. 53 (3), pp. 382-396.

Kolymbas, D. (2019): Geotechnik: Bodenmechanik, Grundbau und Tunnelbau. Spinger Berlin Heidelberg.

Konrad, J.-M. (1989): Pore water pressure at an ice lens: Its measurement and interpretation. Cold Regions Science and Technology, Vol. 16, pp. 63-74.

Konrad, J.-M. (1993): Frost Heave Potential. In: Soil Sampling and Methods of Analysis, Carter, M. R. (ed.), Canadian Society of Soil Science, Lewis Publisher, pp. 797-806.

Konrad, J.-M., Morgenstern, N.R. (1980): Mechanistic theory of ice lens formation in fine-grained soils. Canadian Geotechnical Journal, Vol. 17 (4), pp. 473-486.

Konrad, J.-M., Morgenstern, N.R. (1981): The segregation potential of a freezing soil. Canadian Geotechnical Journal, Vol. 18 (4), pp. 482-491.

Konrad, J.-M., Morgenstern, N.R. (1982): Prediction of frost heave in the laboratory during transient freezing. Canadian Geotechnical Journal, Vol. 19 (3), pp. 250-259.

Konrad, J.-M., Morgenstern, N.R. (1982b): Effects of applied pressure on freezing soils. Canadian Geotechnical Journal, Vol. 19 (4), pp. 494-505.

Konrad, J.-M., Shen, M. (1996): 2-D frost action modeling using the segregation potential of soils. Cold Regions Science and Technology, Vol. 24 (3), pp. 263-278.

Ladanyi, B., Andersland, O. (2004): Frozen ground engineering. John Wiley & Sons.

Ladanyi, B., Shen, M. (1989): Mechanics of freezing and thawing soils. In: Proceedings of the International Symposium of Frost in Geotechnical Engineering, VTT Technical Research Centre, Finland, Vol. 1 (94), pp. 73-103.

Li, T., Zhou, Y., Shi, X.-y., Hu, X.-x., Zhou, G.-q. (2018): Analytical solution for the soil freezing process induced by an infinite line sink. International Journal of Thermal Sciences, Vol. 127, pp. 232-241.

Loch, J.P.G. (1978): Thermodynamic equilibrium between ice and water in porous media. Soil Science, Vol. 126 (2), pp. 77-80.

Loch, J.P.G., Kay, B.D. (1978): Water redistribution in partially frozen, saturated silt under several temperature gradients and overburden loads. Soil Science Society of America Journal, Vol. 42 (3), pp. 400-406.

Ma, W., Zhang, L., Yang, C. (2015): Discussion of the applicability of the generalized Clausius–Clapeyron equation and the frozen fringe process. Earth-Science Reviews, Vol. 142, pp. 47-59.

Makowski, E. (1986): Modellierung der künstlichen Bodenvereisung im grundwasserdurchströmten Untergrund mit der Methode der finiten Elemente. Schriftenreihe des Instituts für Grundbau, Wasserwesen und Verkehrswesen, Ruhr-Universität Bochum, Serie Grundbau, Nr. 10.

Manassero, V. (2020): Monitoring artificial ground freezing and relevant fundamental observations. In: Tunnels and Underground Cities: Engineering and Innovation Meet Archaeology, Architecture and Art, Peila, Viggiani & Celestino (eds.), Taylor & Francis Group, London, pp. 1389-1398.

Martin, R.T. (1959): Rhythmic ice banding in soil. Highway Research Board Bulletin, Vol. 218, pp. 11-23.

McFadden, T.T., Bennett, F.L. (1991): Construction in cold regions: a guide for planners, engineers, contractors, and managers. John Wiley & Sons.

Michalowski, R.L., Zhu, M. (2006): Frost heave modelling using porosity rate function. International journal for numerical and analytical methods in geomechanics, Vol. 30 (8), pp. 703-722.

Miller, R. (1972): Freezing and heaving of saturated and unsaturated soils. Highway Research Record, Vol. 393 (1), pp. 1-11.

Nishimura, S., Gens, A., Olivella, S., Jardine, R. (2009): THM-coupled finite element analysis of frozen soil: formulation and application. Géotechnique, Vol. 59 (3), pp. 159-171.

Nixon, J.F. (1982): Field frost heave predictions using the segregation potential concept. Canadian Geotechnical Journal, Vol. 19 (4), pp. 526-529.

Nixon, J.F. (1991): Discrete ice lens theory for frost heave in soils. Canadian Geotechnical Journal, Vol. 28 (6), pp. 843-859.

O'Neill, K., Miller, R.D. (1982): Numerical solutions for a rigid-ice model of secondary frost heave. CRREL - Cold Regions Research & Engineering Laboratory, Vol. 82-13.

O'Neill, K., Miller, R.D. (1985): Exploration of a rigid ice model of frost heave. Water Resources Research, Vol. 21 (3), pp. 281-296.

Odenwald, B., Hekel, U., Thormann, H. (2018): Grundwasserströmung - Grundwasserhaltung. In: Grundbau-Taschenbuch, Teil 2: Geotechnische Verfahren, Witt, K.J. (ed.), Ernst & Sohn, Berlin, pp. 635-814.

Orth, W. (2018): Bodenvereisung. Grundbau-Taschenbuch, Teil 2: Geotechnische Verfahren, Witt, K. J. (Ed.), Ernst & Sohn, Berlin, pp. 299-373.

Penner, E. (1957): Soil moisture tension and ice segregation. Fundamental and practical concepts of soil freezing, Highway Research Board Bulletin (168), Highway Research Board, pp. 50-64.

Penner, E. (1986): Aspects of ice lens growth in soils. Cold Regions Science and Technology, Vol. 13 (1), S. 91-100.

Peppin, S.S., Style, R.W. (2013): The physics of frost heave and ice-lens growth. Vadose Zone Journal, Vol. 12 (1), pp. 1-12.

Rempel, A.W. (2007): Formation of ice lenses and frost heave. Journal of Geophysical Research, Vol. 112, F02S21, pp. 1-17.

Rempel, A.W. (2010): Frost heave. Journal of Glaciology, Vol. 56 (200), pp. 1122-1128.

Ruckli, R. (1944): Die Eislinsenbildung im Strassenuntergrund. Schweizerische Bauzeitung, Vol. 124 (16), pp. 206-210.

Saarelainen, S. (1992): Modelling frost heaving and frost penetration in soils at some observation sites in Finland: the SSR model. Doctoral dissertation, VTT Technical Research Centre, Tampere University of Technology, Finland.

Sheng, D., Axelsson, K., Knutsson, S. (1995): Frost heave due to ice lens formation in freezing soils: 1. Theory and Verification. Hydrology Research, Vol. 26 (2), pp. 125-146.

Staender, W. (1967): Das Gefrierverfahren im Schacht-, Grund-und Tunnelbau. In: Die Anwendung der Kälte in der Verfahrens-und Klimatechnik, Biologie und Medizin, H. Baur et al. (eds.), Biologie und Medizin, Springer-Verlag Berlin Heidelberg, pp. 173-227.

Sweidan, A., Niggemann, K., Heider, Y., Ziegler, M., Markert, B. (2021): Experimental study and numerical modeling of the thermo-hydro-mechanical processes in soil freezing with different frost penetration directions. Acta Geotechnica, Vol. 17 (1), pp. 231-255.

Taber, S. (1929): Frost heaving. The Journal of Geology, Vol. 37 (5), pp. 428-461.

Taber, S. (1930): The mechanics of frost heaving. The Journal of Geology, Vol. 38 (4), pp. 303-317.

Talamucci, F. (2003): Freezing processes in porous media: formation of ice lenses, swelling of the soil. Mathematical and computer modelling, Vol. 37 (5-6), pp. 595-602.

Thomas, H.R., Cleall, P., Li, Y.-C., Harris, C., Kern-Luetschg, M. (2009): Modelling of cryogenic processes in permafrost and seasonally frozen soils. Geotechnique, Vol. 59 (3), pp. 173-184.

Tice, A.R., Anderson, D.M., Banin, A. (1976): The prediction of unfrozen water contents in frozen soils from liquid limit determinations. CRREL - Cold Regions Research & Engineering Laboratory, Vol. 76-8.

Tiedje, E., Guo, P. (2012): Frost heave modeling using a modified segregation potential approach. In: Proceedings of the International Conference on Cold Regions Engineering 2012: Sustainable Infrastructure Development in a Changing Cold Environment, pp. 686-696.

Unold, F. (2006): Der Gefriersog bei der Bodenfrostung und das Kompressionsverhalten des wieder aufgetauten Bodens. Dissertation, Institut für Bodenmechanik und Grundbau, Universität der Bundeswehr München, München.

Victor, H. (1969): Die Frostausbreitung beim künstlichen Gefrieren von Böden unter dem Einfluss strömenden Grundwassers. Schriftreihe des Instituts für Bodenmechanik und Grundbau, Technische Hochschule Fridericiana, Karlsruhe, Nr. 42.

Viggiani, G.M.B., Casini, F. (2015): Artificial ground freezing: from applications and case studies to fundamental research. In: Geotechnical engineering for infrastructure and development: XVI European conference on soil mechanics and geotechnical engineering, Winter, M. (ed.), ICE Publishing, London, UK, Vol. 1, pp. 65–92.

von Soos, P., Engel, J. (2008): Eigenschaften von Boden und Fels - ihre Ermittlung im Labor. Grundbau-Taschenbuch, Teil 1: Geotechnische Grundlagen, Witt, K. J. (ed.), Ernst & Sohn, Berlin, pp. 123-218.

Wedler, G., Freund, H.-J. (2012): Lehrbuch der physikalischen Chemie. Weinheim Wiley-VCH-Verlag.

Williams, P.J. (1967): Properties and behaviour of freezing soils. Norwegian Geotechnical Institute Publication, Oslo, Norwegian, No. 72.

Williams, P.J., Smith, M.W. (1989): The frozen earth: fundamentals of geocryology. Cambridge University Press, Cambridge, UK.

Yoshikawa, K., Overduin, P.P. (2005): Comparing unfrozen water content measurements of frozen soil using recently developed commercial sensors. Cold Regions Science and Technology, Vol. 42 (3), pp. 250-256.

Zhang, X., Sheng, Y., Huang, L., Huang, X., He, B. (2020): Application of the segregation potential model to freezing soil in a closed system. Water, Vol. 12 (9), 2418.

Zhang, Y., Michalowski, R.L. (2015): Thermal-hydro-mechanical analysis of frost heave and thaw settlement. Journal of Geotechnical and Geoenvironmental Engineering, Vol. 141 (7), 04015027.

Zhou, G., Zou, Y., Boley, C. (2009): Reduktion der Frosthebungen bei der künstlichen Bodenvereisung. Bautechnik, Vol. 86 (9), pp. 566-573.

Zhou, J., Li, D. (2012): Numerical analysis of coupled water, heat and stress in saturated freezing soil. Cold Regions Science and Technology, Vol. 72, pp. 43-49.

ZTV E-StB 17:2017-09: Zusätzliche Technische Vertragsbeding Zhou, J., Li, D. (2012): Numerical analysis of coupled water, heat and stress in saturated freezing soil. Cold Regions Science and Technology,bandungen und Richtlinien für Erdarbeiten im Straßenbau. Forschungsgesellschaft für Straßen- und Verkehrswesen (FGSV), Arbeitsgruppe "Erd- und Grundbau“:

Publications

Partial results from this dissertation have been published in the following scientific journals and conference proceedings:

Niggemann, K. (2019): Untersuchung der Frosthebungen für die Randbedingungen einer künstlichen Baugrundvereisung. Fachsektionstage Geotechnik - Interdisziplinäres Forum: 29.-30. Oktober 2019, Congress Centrum Würzburg: Tagungsband / DGGT Deutsche Gesellschaft für Geotechnik e.V., 2019, pp. 426-431.

Niggemann, K., Ziegler, M. (2019): Neues Verfahren zur Bestimmung von Frosthebungen infolge künstlicher Baugrundvereisung im Tunnelbau: Versuche und verbesserte Berechnungsansätze. U-Verkehr und unterirdisches Bauen: STUVA-Tagung 2019 - Internationales Forum für Tunnel und Infrastruktur, 26. bis 28. November 2019, Langfassungen der Vorträge / veranstaltet von der Studiengesellschaft für Tunnel- und Verkehrsanlagen e.V. - STUVA, Köln, 2019, pp. 162-167, DOI: 10.18154/RWTH-2019-11383.

Niggemann, K. (2020): Investigation of Frost Heave Considering the Boundary Conditions of Artificial Ground Freezing. Transportation Soil Engineering in Cold Regions: Proceedings of TRANSOILCOLD 2019in St. Petersburg, Volume 2, Springer Singapore, pp. 273-283, DOI: 10.1007/978-981-15-0454-9_29.

Sweidan, A. H., Niggemann, K., Heider, Y., Ziegler, M., Markert, B. (2022): Experimental study and numerical modeling of the thermo-hydro-mechanical processes in soil freezing with different frost penetration directions. Acta Geotechnica, 17(1), pp. 231-255, DOI 10.1007/s11440-021-01191-z.

Niggemann, K., Fuentes, R. (2023): New semi-analytical approach for ice lens heaving during artificial freezing of fine-grained material. Journal of Rock Mechanics and Geotechnical Engineering, 15(11), pp. 2994-3009, DOI 10.1016/j.jrmge.2023.07.004.

Niggemann, K., Ziegler, M., Fuentes, R. (2024): Influence of freezing directions on ice lens formations in soils. Acta Geotechnica, DOI 10.1007/s11440-024-02259-2

.

Appendices

A Paper #1 **64**

B Paper #2 **90**

C Paper #3 **123**

A Paper #1

Experimental study and numerical modeling of the thermo-hydro-mechanical processes in soil freezing with different frost penetration directions

Sweidan, A. H., Niggemann, K., Heider, Y., Ziegler, M., Markert, B. (2022): Experimental study and numerical modeling of the thermo-hydro-mechanical processes in soil freezing with different frost penetration directions. Acta Geotechnica, 17(1), pp. 231-255. https://doi.org/10.1007/s11440-021-01191-z

Acta Geotechnica (2022) 17:231–255
https://doi.org/10.1007/s11440-021-01191-z

RESEARCH PAPER

Experimental study and numerical modeling of the thermo-hydro-mechanical processes in soil freezing with different frost penetration directions

A. H. Sweidan[1] · K. Niggemann[2] · Y. Heider[1] · M. Ziegler[2] · B. Markert[1]

Received: 10 December 2020 / Accepted: 16 March 2021 / Published online: 28 April 2021
© The Author(s) 2021

Abstract
This research work presents an experimental and numerical study of the coupled thermo-hydro-mechanical (THM) processes that occur during soil freezing. With focusing on the artificial ground freezing (AGF) technology, a new testing device is built, which considers a variety of AGF-related boundary conditions and different freezing directions. In the conducted experiments, a distinction is made between two thermal states: (1) The thermal transient state, which is associated with ice penetration, small deformations, and insignificant water suction. (2) The thermal (quasi-) steady state, which has a much longer duration and is associated with significant ice lens formation due to water suction. In the numerical modeling, a special focus is laid on the processes that occur during the thermal transient state. Besides, a demonstration of the micro-cryo-suction mechanism and its realization in the continuum model through a phenomenological retention-curve-like formulation is presented. This allows modeling the ice lens formation and the stiffness degradation observed in the experiments. Assuming a fully saturated soil as a biphasic porous material, a phase-change THM approach is applied in the numerical modeling. The governing equations are based on the continuum mechanical theory of porous media (TPM) extended by the phase-field modeling (PFM) approach. The model proceeds from a small-strain assumption, whereas the pore fluid can be found in liquid water or solid ice state with a unified kinematics treatment of both states. Comparisons with the experimental data demonstrate the ability and usefulness of the considered model in describing the freezing of saturated soils.

Keywords Experimental study · Frost heave · Ice lens formation · Phase-field modeling · Soil freezing · Thermo-hydro-mechanical coupling

1 Introduction

The need for efficient, environmentally friendly and modern infrastructures, especially in big cities with a high population density, has led to an increase in the dependency on underground constructions such as underground traffic routes. Moreover, in areas with difficult geological conditions, such as hills, mountains, and river crossings, relying on underground constructions, such as tunnels, provides feasible economical and ecological solutions. In the construction of underground structures especially in inner-city areas, artificial ground freezing (AGF) is a widely used technology. It utilizes the advantages of frozen soils, which can bear static loading and have a water-proofing functionality. Nevertheless, the accompanying volumetric expansions might lead to soil deformations and frost heave at the ground surface and, thus, damaging the

A. H. Sweidan and K. Niggemann have contributed equally to this work.

✉ Y. Heider
heider@iam.rwth-aachen.de

A. H. Sweidan
sweidan@iam.rwth-aachen.de

K. Niggemann
niggemann@geotechnik.rwth-aachen.de

M. Ziegler
ziegler@geotechnik.rwth-aachen.de

B. Markert
markert@iam.rwth-aachen.de

[1] Institute of General Mechanics, RWTH Aachen University, Aachen, Germany

[2] Chair of Geotechnical Engineering, RWTH Aachen University, Aachen, Germany

nearby constructions. This occurs frequently in fine-grained soils due to ice lens formation. In particular, ice lenses are pure ice layers in the soil, which evolve at negative temperatures near the frost line by the accumulation of sucked groundwater. This suction occurs during the phase-change process in the partially frozen area (frozen fringe) and leads to water transport from the unfrozen area toward the ice lenses (see, e.g., [7, 21, 57, 96, 102, 110, 117]). Different case studies in connection with projects related to the AGF technique could be found in [3, 12, 74].

Early studies of ice lens formation in open systems were carried out by [109, 110] who investigated the frost penetration into the soil due to low ambient temperatures. He considered different types of soils, investigated the effect of overburden pressure and studied several factors that contribute to the water suction. Additionally, Taber [109] pointed out that the grain sizes, the water availability, the size and percentage of voids, as well as the cooling rate play a major role in the frost heave and the ice lens formation. To quantify the frost heave onset due to soil freezing, tests on a macroscopic level were carried out by, e.g., [4, 55, 57, 60, 62, 64–66, 69] and [93]. Moreover, microscopic tests and studies using X-ray images [5, 61, 92], particle image velocimetry [9, 29], and time lapse photography using fluorescent tracer [118] helped in better understanding the formation process of discrete ice lenses and the frozen fringes characteristics.

While most of the studies on soil freezing that can be found in the literature are motivated by weather-induced freezing and considered the corresponding boundary conditions, they overlooked the differences in the soil behavior between naturally induced and artificially induced soil freezing. Of particular importance in this regard are the effects of freezing direction and the different thermal boundary conditions. In this work, frost heave experiments are carried out, which include an investigation of the variation of the thermal state during AGF, the different freezing directions, the temperature conditions, the water pressure change and the overburden loading. Therefore, the outlined results in this paper focus on investigations of thermal states and freezing directions at different temperature boundary conditions. For an appropriate evaluation of the experimental results, the different thermal states during freezing have to be considered. The ice lenses can initiate during the thermal transient state. However, with the decrease in the frost penetration rate, the ice lens thickness increases until the frost penetration rate becomes almost zero and the thermal (quasi-) steady state is reached. At a given water availability, the heave due to ice lens formation during the thermal (quasi-) steady state can significantly exceed the heave due to ice formation during the thermal transient state. The consideration of the thermal (quasi-) steady state is important since the artificial ground freezing is usually used for long construction periods. For this reason, both thermal states are considered separately in the analysis of frost heave tests. Previous studies on frost heave with ice lens formation mostly refer to the natural frost penetration in cold regions and, therefore, focus on the transient state [63].

Due to gravity effects, soil freezing is direction-dependent, which is addressed in the underlying study. For instance, in tunnel construction with horizontal or slightly inclined freezing pipes, ice accumulates around the pipes, however, more rapidly upward as the gravity enhances the water flow toward the freezing area. In this connection, it is worth mentioning that [8, 25] and Niggemann [81] reported increasing permeability in the vertical direction as a result of longitudinal shrinkage cracks.

In the underlying work, a numerical modeling framework that takes the multi-physical thermo-hydro-mechanical (THM) processes of ground freezing into account is presented. In this, a saturated soil is treated as a non-isothermal, deformable, fully saturated biphasic porous material with a single fluid that can change depending on the thermal conditions between a solid ice and a liquid water state. The model is based on a coupled phase-field-porous media approach [108], where the main focus is laid on the temperature-driven processes that lead to the phase transition between water and ice and the freezing-related deformations that can be observed in the experiments. The governing equations of the macroscopic model are based on the well-founded theory of porous media (TPM) extended by the phase-field modeling (PFM), whereas the combined PFM-TPM approach is implemented within a finite element method (FEM) framework to reliably simulate the coupled process of soil freezing.

The macroscopic TPM [19, 32, 36, 40, 70, 71], which extends the Theory of Mixtures (TM) [18, 113] by the concept of volume fractions is used as a continuum-mechanical framework for the description of the deformable, heterogeneous porous solid. For a more detailed discussion of the general frame of the TPM, its extensions, solution schemes, applications and historical development, the interested reader is referred to [20, 24, 31, 35, 36, 49, 50, 52, 71, 85, 101] among others. Besides, the phase-field model (PFM) is employed for deriving a unified kinematics formulation for the phase changing fluid constituent. Details and references related to the energetic PFM for phase-change materials description can be found in, e.g., [16, 59, 105, 115].

In the literature, different THM models within porous media frameworks have been developed to capture the multi-physical phenomena related to soil freezing, see, e.g., [28, 56, 68, 79, 80, 82]. Additionally, several THM numerical models were developed within the AGF context,

to capture the volume expansion of water transforming into ice and the contribution of the micro-cryo-suction mechanism responsible for driving liquid water toward the frozen zone, see, e.g., [23, 112, 124, 125]. Related to the physical aspects and modeling of the ice lens formation during the freezing process, several theories and models that utilize different ice lens formation criteria were proposed in [10, 67, 76, 77, 88, 123]. Recently, Gawin et al. [45] presented a new poro-mechanical model of the coupled THM processes in partially saturated porous materials that are exposed to temperatures below the freezing point of the pore water. Their model considered freezing-thawing cycles, and can capture important events, such as the effects of hysteresis, the water supercooling, and the cyclic freezing strains.

In related research works, thermodynamically consistent modeling of the phase-change process in porous materials were developed [30, 33]. Considering liquid/gas phase transitions within saturated elasto-plastic porous media, TPM models were later presented in [37, 38]. Related to the freezing and thawing in porous media including the accompanied phase transition process and volumetric deformation, several models were proposed [14, 15, 98, 99]. In the aforementioned publications, the phase-change process was modeled by imposing a mass production term in the mass balance relation to describe the mass transfer from one phase to another. This method, however, added some complexity and numerical stability challenges to their models. To overcome such problems, an artificial restriction for the volume fraction of the liquid during freezing has to be provided; otherwise, the volume fraction tends to become negative. In the present work, this challenge is avoided by employing the energetic phase-field method to describe the phase-change. Consequently, we consider that ice and water phases belong to the same pore-fluid and are described using PFM-based unified kinematics, thus a more stable and easier computational treatment is provided.

Utilizing the energy-based PFM [11, 16, 95, 105], explicit tracking of the freezing interface is completely avoided, which makes it more attractive among the other interface capturing methods, e.g., the level-set [89] and the volume-of-fluid [54], and easy to implement in finite-element codes. In the context of PFM, a phase-field variable ϕ is employed to indicate the phases of the material, i.e., $\phi = 0$ for the solid and $\phi = 1$ for the liquid states. The PFM allows for a smooth variation between these distinct values across the interface, resulting in a finite interface thickness. A certain evolution equation for ϕ can rigorously be derived from thermodynamically consistent theories of continuum phase transitions (see, e.g., [115]). The development and applications of phase-field models in the context of continuum models of phase transitions have been presented by many researchers [16, 27, 43, 58, 59, 78, 105, 115, 119, 122]. Away from the phase-change applications, the PFM can also be found in recent contributions within fracture mechanics and crack propagation as, e.g., [6, 39, 51–53, 84, 90, 91, 94]. The PFM is being recently applied to tackle phase-change problems on the macroscale [107, 120, 121], especially for studying the behavior of phase-change materials (PCMs). However, none of the above mentioned phase-change-PFM-based articles considered the challenging problem of porous structure deformation due to the volume changes of the fluid during solidification or melting. In the current contribution, this challenge will be tackled using an efficient thermodynamically consistent combined TPM-PFM approach.

In a nutshell, the major objective of this work is to gain new insight into the challenging coupled thermo-hydro-mechanical processes that occur during soil freezing via applying an advanced experimental and numerical study. This is achieved by (1) building a new multi-directional soil freezing testing device that allows the application of different mechanical and thermal boundary conditions, (2) measuring the time-dependent thermo-hydro-mechanical changes in the domain and at the boundaries of the specimens, (3) implementation and validation of a simplified unified water/ice kinematics porous media approach to model the coupled phase-change thermo-hydro-mechanical processes, and (4) extending the modeling framework via a retention-curve-like formulation to consider the micro-cryo-suction mechanism and, thus, allowing to capture the deformations in the transient and the (quasi-) steady state due to ice lens formation.

To give an overview, Sect. 2 describes the experimental method with specifications of the test setup, the existing boundary conditions and the properties of the test material. The evaluation of the experimental data is explained in Sect. 3, including the measured experimental data as well as the distinction of thermal transient and thermal (quasi-) steady state. In Sect. 4, the results of the two test series with different thermal boundary conditions as well as considering the different freezing directions, are explained. Section 5 provides a description of the fundamental kinematics and basic principles of the TPM and PFM and introduces the governing balance relations. Moreover, an extension of the model for the description of ice lens formation is presented in this section. Section 6 presents the numerical treatment of the governing equations, including the weak formulations, as well as the spatial and the temporal discretization. Verification of the numerical model for the thermal transient state based on experimental data is carried out in Sect. 7.1. Section 7.2 presents the numerical results related to the ice lens formation and a comparison with the experimental results for the thermal steady state.

Finally, a brief summary, conclusions and an outlook of future works are presented in Sect. 8.

2 Experimental method

2.1 Setup of the test device

This project focuses on frost heave analysis due to AGF, which includes different freezing directions. This mimics real AGF scenarios as, e.g., via using horizontal freezing pipes, in which the vertical freezing direction toward the ground surface is decisive in the resulting maximum heave. To investigate the maximum frost heave, an experimental testing device is constructed, which allowed for the examination of the one-dimensional upward freezing (bottom freezing - BF). The results are then compared to one-dimensional downward-freezing tests (top freezing—TF) with a more common setup used for frost heave tests with regard to pavement freezing in cold regions (Fig. 1).

The dimensions of the cylindrical specimen are $d = 25$ cm in diameter, and $h = 20$ cm in height. Each specimen is placed in a special test cylinder to achieve a uniaxial deformation during freezing. It consists of eight PVC ring elements with a 2.5 cm thickness. During the freezing test, the ring elements can be pulled apart, so that the soil samples do not undergo any frictional resistance due to the vertical expansion. The top and the bottom of the samples, respectively, are cooled by a freezing element ①, which is connected to a cooling circulation thermostat (CC-508, Huber Kaeltemaschinenbau AG, Germany). A water reservoir ⑥ is connected to a filter plate ② at the warm side of the sample, providing a water supply under atmospheric pressure for ice lens formation. The warm end of the soil sample is additionally heated by a heating plate ③, that is connected to a warming circulation thermostat (Kiss 104A, Huber Kaeltemaschinenbau AG, Germany) to avoid freezing of the whole sample. All tests are carried out in a climatic chamber with a constant temperature of 15°C and humidity of 40% to exclude influences such as seasonal fluctuations.

For data recording, temperature sensors (MWT1/10, TMH GmbH, Germany) ④ are distributed over the sample height. In order to calculate the temperature profile as a function of time, the vertical displacements of the temperature sensors during frost heave are measured using displacement transducers (LRW2-C-50, WayCon Positionsmesstechnik GmbH, Germany). The uniaxial deformations at the top of the specimen are also recorded by displacement transducers (LRW2-C-50, WayCon Positionsmesstechnik GmbH, Germany) ⑤. To determine the water inflow into the sample due to suction, the mass of the water supply is recorded by a load cell (S2, HBM, Austria) ⑥.

2.1.1 Boundary conditions

In the following, the thermal, the hydraulic, and the mechanical boundary conditions in connection with the test device setup are defined, which are also going to be considered in the related numerical models. Figure 2 shows the boundary conditions for the bottom as well as for the top freezing setups. The freezing element cools down the surface of the soil sample and leads to axial soil deformations. The PVC cylinder avoids a radial expansion of the freezing sample. After reaching the set temperature, the freezing element maintains a constant temperature. The radial heat transfer can be neglected, which is ensured by an insulating PVC cylinder and an additional extruded polystyrene resistance foam covering the test cylinder. The environmental conditions are controlled by the climatic chamber. The ambient temperature for the test series presented here is $\theta_a = 15°C$, which is also the initial temperature θ_i of the soil sample. During the entire experiment, water can be sucked from an external supply, which is located at the warm side of the sample. For the presented study, the overburden load results only from construction elements (i.e., the porous heating plate for BF and the freezing plate for TF) and an additional static 10 kg load to ensure a frictional connection between the plates and the sample. This results in a total load of $p = 3.6$ kPa.

2.2 Test material and procedure

The experiments are carried out by considering a lean clay (CL, classified by the Unified Soil Classification System), see, Fig. 3 for the particle size distribution, with a liquid limit of 32.9% and a plasticity index of 14.5%.

The material is produced artificially to ensure an equal composition for all tests and, thus, to improve the comparability of the results. The material is prepared with a water content of 20% to ensure a high saturation up to 95% as well as an appropriate consistency. For saturation, the dry soil is mixed with the required amount of water and stored for 24 hours to ensure that water can penetrate the pores. Afterward, the soil is installed in the test cylinder. The water content present is checked for each soil by a drying procedure.

The essential material properties are summarized in Table 1. These include the mechanical properties, which are determined via tests carried out at the Chair of Geotechnical Engineering, RWTH Aachen University, and the thermal properties, which are determined via tests at the Institute of Applied Geophysics and Geothermal Energy, RWTH Aachen University.

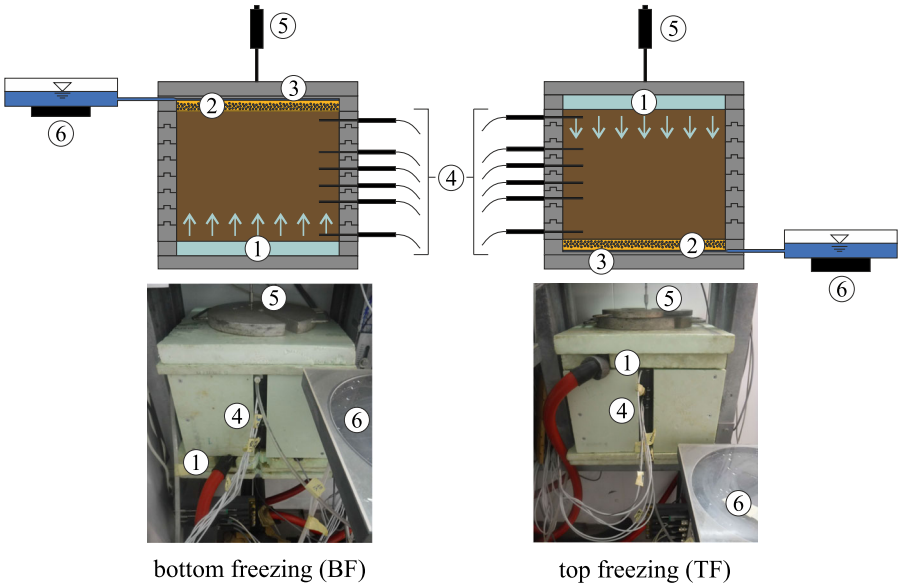

Fig. 1 Freezing cell: ① freezing element, ② porous plate with water supply, ③ heating plate, ④ temperature sensors, ⑤ displacement transducer, ⑥ water reservoir on load cell

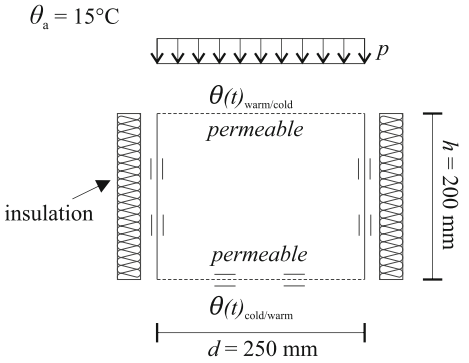

Fig. 2 Boundary conditions for bottom/top freezing

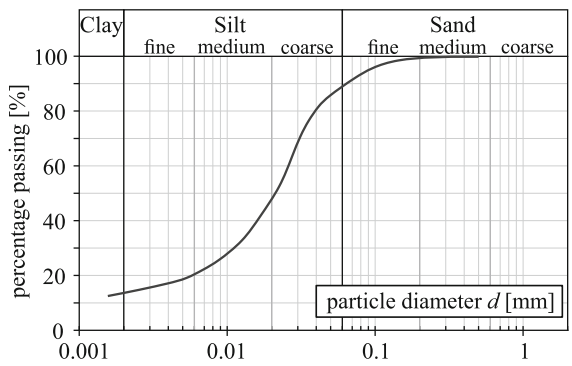

Fig. 3 Particle size distribution

The prepared soil is stored for approx. 24 hours in the climatic chamber at 15°C to ensure a uniform material temperature at the beginning of each test. After acclimatization, the freezing process is turned on. At the same time, the tempering process also starts on the warm side of the sample. During the freezing process, liquid water through a reservoir is provided at the permeable warm boundary, so that the suction from external source is not barriered. The duration of the freezing process is about 10 days per experiment.

Table 1 Material properties

Parameters	Values
Grain material density ρ^{SR} (kg/m^3)	2683
Intrinsic permeability K_{0S}^{S} (m^2)	1.8×10^{-17}
Water content w (%)	20
Saturation S_r (%)	90–95
Young's modulus E^{S*} (kPa)	670
Shrinkage limit SL (%)	16.8
Plastic limit PL (%)	18.4
Liquid limit LL (%)	32.9
Plasticity index PI (%)	14.5
Thermal conductivity H^{SR} (W/(m · K))	3
Specific heat capacity C_p^S (J/(kg · K))	776

∗ for a low stress range up to 25.0 kPa

2.3 Test series

Two test series are carried out focusing on the effects of freezing directions (BF and TF) and the temperature boundary conditions.

In *test series 1*, the frost penetration is not regulated by the warm side temperature but only by the cold side

temperature. With temperature-induced freezing at the bottom or top boundary, the applied temperature varies between approx. −5°C to approx. −15°C. On the warm side, there is only a minimal heat penetration to prevent freezing of the whole sample. The temperature at the warm boundary changes between approx. 5°C to approx. 10°C depending on the set cold side temperature. In this series, the final frost depth at thermal (quasi-) steady state changes with the applied temperature at the freezing boundary. Thus, the temperature gradients over the sample height at thermal (quasi-) steady state are constants (grad θ = const.).

To investigate the influence of different temperature gradients, *test series 2* includes experiments carried out with adjusted warm side temperatures to reach the same frost penetration depth at different freezing temperatures (grad $\theta \neq$ const.). The set temperature gradient in the frozen area grad θ_f varies between 0.6°C/ cm and 1.6°C/ cm.

3 Experimental evaluation

3.1 Extracted parameters

The results of each frost heave test (BF and TF) include the measured

- total frost heave,
- temperatures at six measuring points (incl. motion of sensors),
- sucked water mass during ice lens formation.

The total frost heave is measured at the top of the sample to record uniaxial deformations due to pore water expansion and ice lens formation. To determine the position of the frost line during the freezing test, the temperature along the sample height is measured. Figure 4 shows the time-dependent measured temperature along the soil sample and the resulting calculated temperature surface. This space-time temperature contour plot is used to determine the frost line at 0°C (see Sect. 3.2 for more details). The recorded sucked water from the reservoir provides information about the reservoir water mass used for ice lens formation and, therefore, the influence of gravitational forces (only at BF), which favor the inflow of water.

After each freezing test, the water content is determined in the longitudinal direction of the soil sample to examine the water distribution after freezing. For this purpose, the sample is divided into approx. 2.5 cm thick layers.

3.2 Definition of thermal states

During artificial ground freezing, two thermal states result from different operating phases. Initially, the frost body

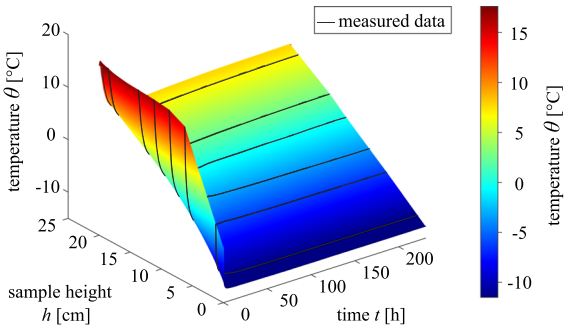

Fig. 4 Measured temperature space-time distribution during a representative BF test

freezes to the required static thickness with a continuously changing frost line position ("moving ice/water boundary"). The penetration velocity depends on the temperature gradient. This state is referred to as the thermal transient state with pore water expansion and less ice lens formation due to freezing pore channels and therefore a restricted water supply. In the subsequent thermal steady state, the thickness of the frozen body is maintained. Since a last ice lens is still formed in this state, it is also called thermal (quasi-) steady state. With unrestricted water supply, the last ice lens causes a very large heave over time. Therefore, this state is especially decisive for long-term projects. In order to investigate the ice lens formation at the thermal (quasi-) steady state, the beginning of this state must be defined in the experiments.

The definition of the thermal (quasi-) steady state, when no further frost penetration occurs, is based on the course of the 0°C-isotherm (Fig. 5, left), which is determined by the temperature space-time distribution in Fig. 4 defining the 0°C over time. The time derivative of the 0°C-isotherm (Fig. 5, right) gives the frost penetration velocity v_{fp}, which approaches zero at (quasi-) steady state conditions. The beginning of the thermal (quasi-) steady state is defined by a critical frost penetration velocity $v_{fp,crit}$ less than 0.01 cm/ h. From this point onward, the water flow to the ice lens is not prevented by freezing pore spaces due to a moving frost line and the frost heave significantly exceeds the heave at the transient state.

Figure 6 shows the results of frost heave H at thermal transient and (quasi-) steady state. In the transient state, the pore water heave H_{PW} is determined by the one-dimensional pore water expansion of 9% due to the frost penetration $x(t)$, under consideration of the of the volumetric porosity n^F and the saturation degree S_r. In the following equation, it is assumed that the water freezes at 0°C and does not expand into air filled voids.

$$H_{PW}(t) = 0.09 \cdot n^F \cdot S_r \cdot x(t) \quad (1)$$

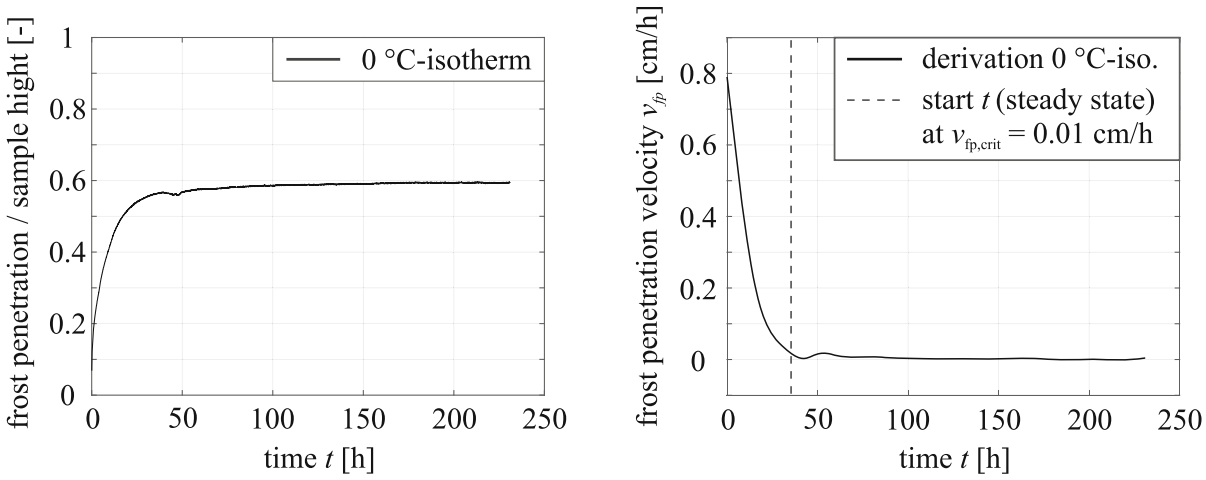

Fig. 5 Graphs of the 0°C-isotherm (*left*) and frost penetration velocity (*right*) for BF

The difference between total heave and pore water expansion is the calculated ice lens formation at the transient state. Compared to the ice lens formed at the (quasi-) steady state, the heave due to ice lens formation in the transient state is minor. This is particularly the case for long periods under (quasi-) steady state conditions.

4 Experimental test results

4.1 Water content after freezing

The measured water mass sucked in from the reservoir does not reflect the total water mass used for ice lens formation. A comparison of the sucked in reservoir water with the total water mass, calculated back from the total heave due to ice lens formation, shows a difference, which reflects the sucked in pore water. The amount of sucked in reservoir and pore water depends on the flow path length between the water reservoir and the ice lens. A longer flow path leads to a lower pressure gradient over the unfrozen part and thus a lower water accumulation of reservoir water. With a decreasing water supply from the reservoir, the amount of pore water of the unfrozen soil, which contributes to the ice lens formation, increases. Figure 7 (left) shows an example of the ratio of sucked water from the reservoir and pore water to the total water mass used to form ice lenses. At the beginning of ice lens formation, most of the water that forms the ice lens is pore water. This is due to the low permeability of the soil and the long flow path from the reservoir to the ice lens, which restricts the flow rate of the reservoir water. The unfrozen soil shrinks as water drains off, resulting in longitudinal cracks along the sample, whereby the permeability of the unfrozen soil increases and additional reservoir water flows through the unfrozen part to the arising ice lens. This phenomenon of crack formation was also observed earlier by other scientists (e.g., [8, 25, 109]) and is attributed to particularly impermeable soils. Figure 7 (right) shows the water content along the soil sample (about 2.5 cm layers) after freezing. Compared to the initial water content (20%) the unfrozen part shows a lower water content, especially near the last ice lens. In the frozen area it is higher compared to the initial state caused by slight ice lens formation during the thermal transient state.

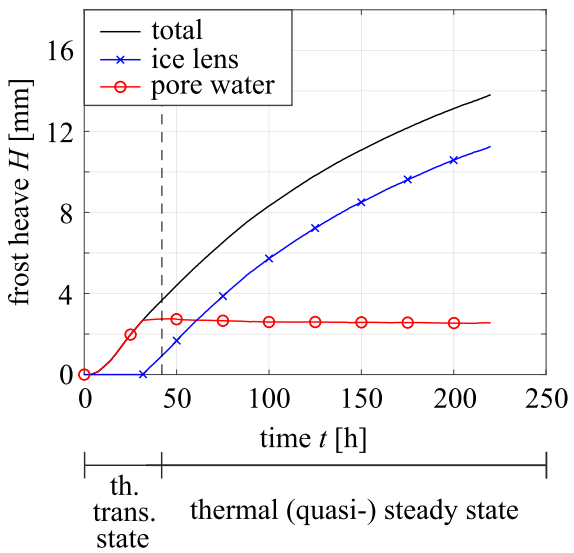

Fig. 6 Frost heave at thermal transient and (quasi-) steady state for BF

4.2 Test series 1

In *test series 1*, only the cold side temperature is varied between −5°C and −15°C to reach different frost penetrations. The ice lens heave at the thermal (quasi-) steady

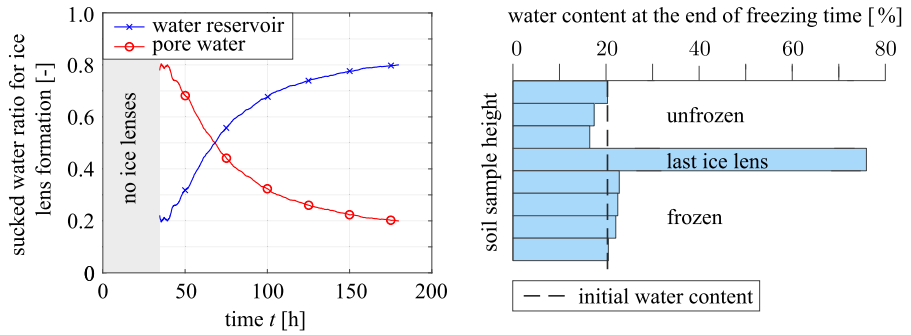

Fig. 7 Estimated sucked-water time history from the soil ambient (pore water) and the external source (reservoir) during ice lens formation (*left*), and water content at the end of the BF test (*right*)

state H_{IL} depends on the length of the unfrozen part or flow path d_{uf} between the ice lens and the sample surface with water supply (see, Fig. 8). With a lower temperature at the freezing boundary θ_f, greater frost penetration and, therefore, a decrease in the flow path occurs. The shorter flow path enhances the water supply for ice lens formation due to an increased water flow velocity from the water reservoir to the ice lens. Thus, more frost heave due to ice lens formation occurs.

The frost heave H results in Figs. 9 and 10 show differences between BF and TF at thermal transient and (quasi-) steady states. Considering the thermal transient state (Fig. 9), the differences between the TF and the BF result from the different frost depth due to the freezing temperature. A comparison between the two different freezing directions shows the influence of overburden soil pressure. The higher the overweight during BF, the lower is the heave gradient at the beginning, which results in a lower total heave at the end of the thermal transient state.

A comparison of the ice lens heave H_{IL} with different freezing directions shows that the BF exceeds the TF with smaller flow paths d_{uf} (Fig. 10, left). A similar result is shown for the sucked water mass m_w (Fig. 10, right). The increasing heave difference between BF and TF is also attributed to better water accumulation in the unfrozen part according to the formation of longitudinal cracks during freezing (Fig. 11). At BF, water accumulation increases due to gravity, especially when the frost line is near the sample surface, causing the cracks to extend to the warm sample surface where the water from the reservoir can flow into the sample. The better water supply results in larger heave due to ice lens formation. If the frost line is not close to the warm side, the cracks do not reach the water source (warm side surface). In this case, the heave difference between BF and TF is primarily due to the overburden load. Depending on the position of the frost line, the overburden load also changes slightly. This effect cannot be excluded, thus further research needs to be carried out to investigate the influence of overburden pressure.

4.3 Test series 2

In *test series 2*, the freezing and heating temperatures were set to achieve the frost line at thermal (quasi-) steady state approximately in the center of the sample. The set temperature gradient in the frozen area grad θ_f varies between 0.6°C/ cm and 1.6°C/ cm.

During thermal transient state, the ice lens formation depends on the temperature gradient, because a slow frost penetration rate improves water accumulation. For the researched temperature gradients the heave differences were negligible in comparison to the final ice lens that is formed at (quasi-) steady state conditions.

Figure 12 (left) shows the frost heave 150 hours after the beginning of the thermal (quasi-) steady state for different temperature gradients in the frozen area grad θ_f. The

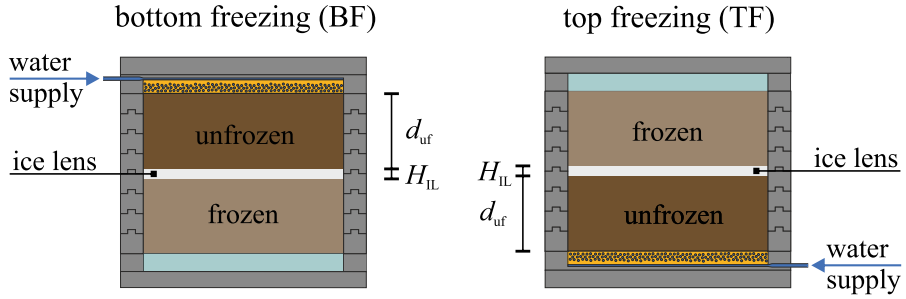

Fig. 8 Illustration of the ice lens-induced heave H_{IL} and the unfrozen part height (shortest flow path) d_{uf} for BF and TF

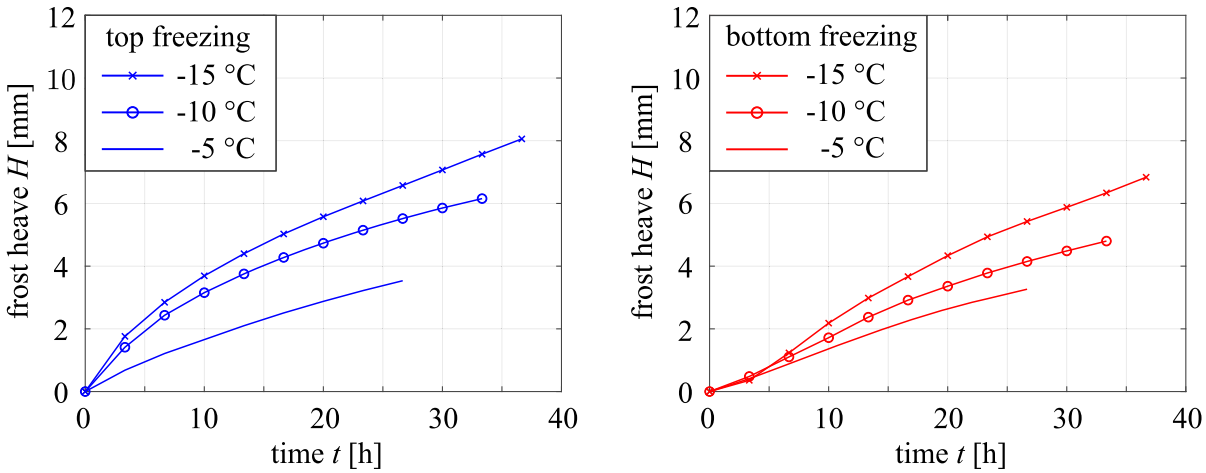

Fig. 9 Frost heave time trajectory during the thermal transient state for different freezing temperatures

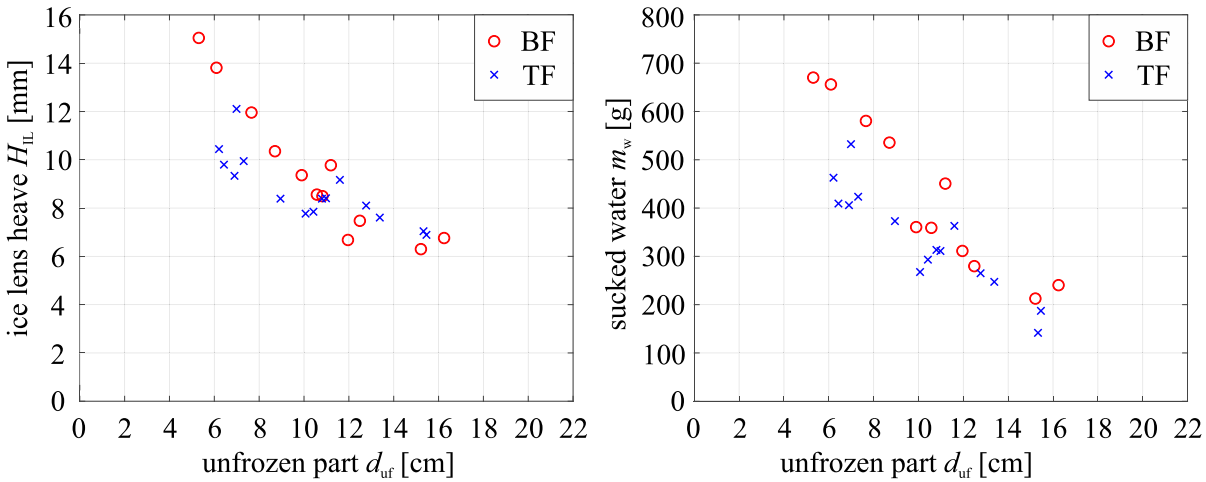

Fig. 10 Ice lens-induced heave (*left*) and sucked water (*right*) vs. the height of the unfrozen domain after 150 h from the beginning of the (quasi-) steady state

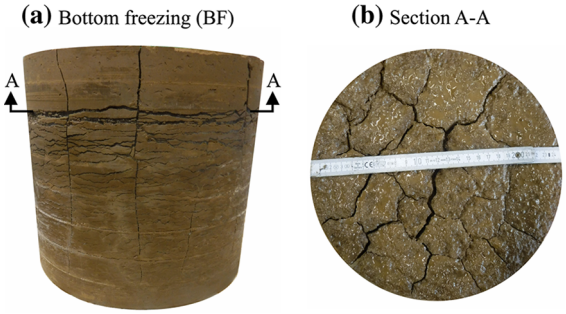

Fig. 11 Illustration of crack formation due to bottom freezing

corresponding heights of the unfrozen area or flow path lengths d_{uf} are shown in Fig. 12 (right) and are controlled to be similar by the temperature boundary conditions. Despite different temperature gradients in the frozen area $\operatorname{grad}\theta_f$, the same frost heaves H_{IL} occur. It can be concluded that the temperature gradient in the frozen area $\operatorname{grad}\theta_f$ have no decisive impact on the formation of ice lenses at thermal (quasi-) steady state in the investigated range.

5 Multiphase continuum porous media frost action model

We start in this section with a mathematical model that describes the main physical mechanisms occurring in the thermal transient state during the saturated-soil freezing. In particular, there are the temperature-field distribution, the phase-field evolution, the volume expansion, and the accompanying frost heave. In an additional section, we will briefly demonstrate and include the micro-cryo-suction effect, which is the main driving force for the water suction toward the frozen area and the ice lens formation, which occur mainly during the thermal (quasi-) steady state.

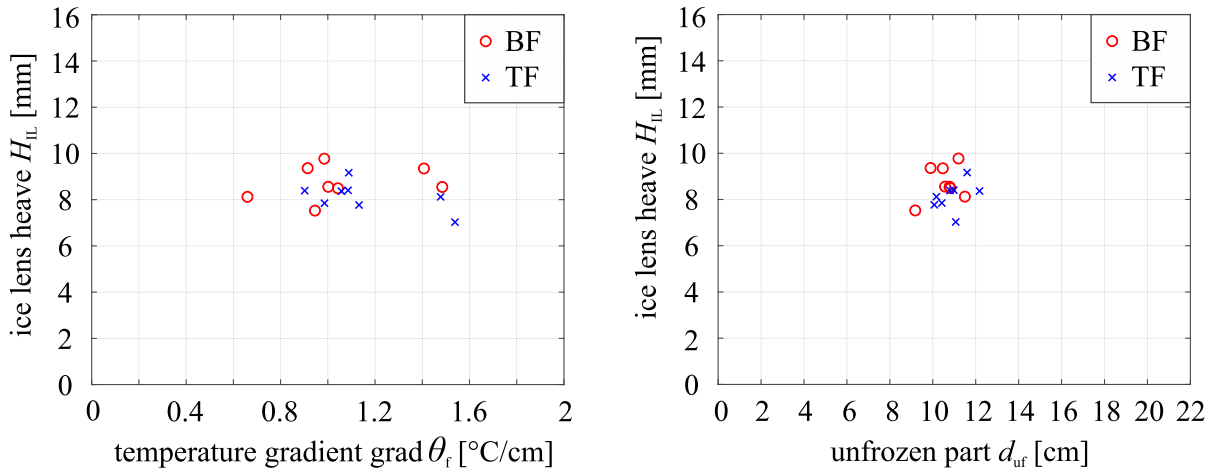

Fig. 12 Ice lens-induced heave 150 h after the beginning of the (quasi-) steady state for different temperature gradients (*left*). Ice lens-induced heave 150 h after the beginning of the (quasi-) steady state vs. the height of the unfrozen domain (*right*)

5.1 Porous media homogenization and extension via the phase-field approach

5.1.1 Homogenization, volume fractions and densities

In the current study, the saturated soil is modeled as a two-phase material consisting of immiscible solid ($\alpha = S$) and fluid ($\alpha = F$) constituents. In the macroscopic TPM-based description of the microscopically heterogeneous two-phase material, representative volume elements (RVEs) are chosen and homogenized so that each macroscopic portion of the material φ consists of superimposed and interacting constituents φ^α. While the solid phase φ^S undergoes linear elastic deformations, the fluid phase φ^F undergoes a phase transition, where it could be found either in a liquid state ($\overline{\varphi}^L$), an ice state ($\overline{\varphi}^I$), or a liquid-ice mixed state representing the interface zone separating ($\overline{\varphi}^L$) and ($\overline{\varphi}^I$). Therefore, the following relations are assigned for any macroscopic spatial point $\mathbf{x}(t)$ at any time $t \in [t, T]$:

$$\varphi = \bigcup_\alpha \varphi^\alpha = \varphi^S \cup \varphi^F \quad \text{with} \quad \varphi^F = \bigcup_\alpha \overline{\varphi}^\beta = \overline{\varphi}^L \cup \overline{\varphi}^I \,. \tag{2}$$

The volume fraction n^α, which describes the local composition of the single constituent, is defined as the ratio of the volume element $\mathrm{d}v^\alpha$ of the constituent φ^α with respect to the volume element $\mathrm{d}v$ of the overall aggregate φ with $0 < n^\alpha := \mathrm{d}v^\alpha/\mathrm{d}v < 1$. Analogously, volume fractions representing the liquid ($\beta = L$) and the frozen ($\beta = I$) states of the pore-fluid, can also be defined as $\overline{n}^\beta := \mathrm{d}v^\beta/\mathrm{d}v$ with $0 \leq \overline{n}^\beta \leq n^F$. Having both the solidity (n^S) and the porosity (n^F), the saturation constraint for the case of a fully saturated medium can be given as

$$\sum_\alpha n^\alpha = n^S + n^F = 1$$
$$\text{with } n^F = \begin{cases} \bar{n}^L & : \text{liquid state}, \\ \bar{n}^I & : \text{ice state}, \\ \bar{n}^L + \bar{n}^I & : \text{interfacial state}. \end{cases} \tag{3}$$

Moreover, for each constituent, one defines a material (intrinsic) density $\rho^{\alpha R} := \mathrm{d}m^\alpha/\mathrm{d}v^\alpha$ and a partial density $\rho^\alpha := \mathrm{d}m^\alpha/\mathrm{d}v$ with $\mathrm{d}m^\alpha$ being the local mass element of φ^α. Both densities are related to each other via $\rho^\alpha = n^\alpha \rho^{\alpha R}$.

5.1.2 Phase-field modeling of pore-fluid freezing

The phase-change process during the pore-fluid freezing is modeled based on the PFM. The PFM is an interface-capturing approach that treats the occurring mushy zone between the liquid and ice states as a diffusive interface, where an auxiliary phase-field variable $\phi^F(\mathbf{x}, t)$ is used to indicate the phases. In particular, this can be expressed as

$$\phi^F(\mathbf{x}, t) \in [0, 1]$$
$$\text{with } \begin{cases} \phi^F = 1 & : \text{liquid phase}, \\ \phi^F = 0 & : \text{ice phase}, \\ 0 < \phi^F < 1 & : \text{diffusive interface}. \end{cases} \tag{4}$$

Using ϕ^F, a constitutive interpolation polynomial $\mathcal{P}(\phi^F)$ representing an averaging function that interpolates between the bulk properties and free energies of the liquid and ice phases is employed to allow for a phase-field-dependent smooth variation of the different thermo-mechanical properties between the liquid and frozen phases, e.g., [95]. It can be expressed as

$$\mathcal{P}(\phi^F) = (\phi^F)^3 \left[6\,(\phi^F)^2 - 15\,\phi^F + 10\right] \\ : \begin{cases} \mathcal{P}(\phi^F) = 1 & : \text{ liquid phase}\,, \\ \mathcal{P}(\phi^F) = 0 & : \text{ ice phase}\,, \\ 0 < \mathcal{P}(\phi^F) < 1 & : \text{ diffusive interface}\,. \end{cases} \tag{5}$$

For instance, the fluid material density is expressed as $\rho^{FR} = \mathcal{P}(\phi^F)\,\rho^{LR} + \big(1 - \mathcal{P}(\phi^F)\big)\rho^{IR}$. The phase-field-dependent variation of other kinematic or material properties across the diffusive interface will briefly be discussed in the subsequent sections. More details can also be found in [108].

5.2 Kinematics of multi-phase materials

In a fluid-solid aggregate, the deformation of the solid matrix is given within a Lagrangian description using the solid displacement vector $\mathbf{u}_S$ and velocity $\mathbf{v}_S$, whereas the fluid constituents are described in a modified Eulerian setting by use of the seepage velocities $\mathbf{w}_F$, i.e.,

$$\mathbf{u}_S = \mathbf{x} - \mathbf{X}_S\,, \qquad \mathbf{v}_S = (\mathbf{u}_S)'_S\,, \qquad \mathbf{w}_F = \mathbf{v}_F - \mathbf{v}_S\,, \tag{6}$$

where $\mathbf{v}_F$ is the fluid velocity. Additionally, the material time derivative of an arbitrary vector quantity $(\bullet)$ following the motion of φ^α is expressed with respect to the motion of the solid constituent as

$$(\bullet)'_\alpha := \frac{\mathrm{d}_\alpha(\bullet)}{\mathrm{d}t} = \frac{\partial\,(\bullet)}{\partial\,t} + \Big(\mathrm{grad}\,(\bullet)\Big)\mathbf{w}_F\,. \tag{7}$$

In the present contribution, the model development is restricted to linear isotropic thermo-elasticity. Thus, the linearized infinitesimal solid strain tensor $\boldsymbol{\varepsilon}$ can be expressed as

$$\boldsymbol{\varepsilon}_S = \frac{1}{2}\,(\mathrm{grad}\,\mathbf{u}_S + \mathrm{grad}^{\mathrm{T}}\mathbf{u}_S)\,. \tag{8}$$

5.3 Governing balance relations

The present work proceeds from the following assumptions and simplifications:

- There is no mass production or mass exchange between the solid and the fluid constituents, i.e., in Eq. (9) $\hat{\rho}^\alpha = 0$.
- Deformation occurs under quasi-static conditions, i.e., $(\mathbf{v}_\alpha)'_\alpha = \mathbf{0}$.
- Equilibrium thermal model is employed, where the local Kelvin's temperatures of all constituents are equal ($\theta^S = \theta^F = \theta$).
- External heat supply terms are not taken into consideration ($\rho^\alpha\, r^\alpha = 0$).
- Non-dissipative phase transition, i.e., the capillary hysteresis during freeze-thaw cycles is ignored.
- The freezing-point depression of the pore water is neglected.

The discussed mathematical description for the freezing process in a fluid-saturated porous medium results in the following coupled partial differential equations (PDE) with primary variables $\{p^F,\, \mathbf{w}_F,\, \mathbf{u}_F,\, \mathbf{u}_S,\, \theta,\, \phi^F\}$, where p^F is the pore-fluid (ice or water) pressure. More details about the derivation of the balance and constitutive relations can be found in [108].

5.3.1 Mass balance of φ^F

$$(\rho^F)'_F + \rho^F \mathrm{div}\,\mathbf{v}_F = 0\,, \tag{9}$$

This mass balance could be reformulated based on Eq. (7), the derivative of the saturation condition (3), and the volume balance of the solid, $(n^S)'_S = -n^S \mathrm{div}\,\mathbf{v}_S$, yielding

$$n^F\,(\rho^{FR})'_S + \mathrm{div}(n^F\,\rho^{FR}\,\mathbf{w}_F) + \rho^{FR}\,\mathrm{div}\,\mathbf{v}_S = 0\,. \tag{10}$$

Assuming a barotropic pore fluid as discussed in [17, 53, 106], a relation among the material density ρ^{FR}, the pore-fluid pressure p^F and the fluid compressibility $\kappa^F := \mathcal{P}(\phi^F)\,\kappa^L + \big(1 - \mathcal{P}(\phi^F)\big)\kappa^I$ can be expressed as

$$(\rho^{FR})'_S = \rho^{FR}\,\frac{(p^F)'_S}{\kappa^F}\,. \tag{11}$$

Inserting this relationship into Eq. (10) yields the governing equation of fluid mass balance as

$$n^F\,\rho^{FR}\,\frac{(p^F)'_S}{\kappa^F} + \mathrm{div}(n^F\,\rho^{FR}\,\mathbf{w}_F) + \rho^{FR}\,\mathrm{div}\,\mathbf{v}_S = 0\,. \tag{12}$$

It is worth mentioning here that the volume balance of the materially incompressible solid phase under the small-strains assumption yields the deformation-dependent solid volume fraction as $n^S = n^S_{0S}\,(1 - \mathrm{div}\,\mathbf{u}_S)$ with n^S_{0S} representing the initial value of n^S.

5.3.2 Momentum balance of the overall aggregate φ

The momentum balance of the overall aggregate results from the sum of the momentum balances of the individual constituents φ^α yielding

$$\mathrm{div}\,\underbrace{\big(\mathbf{T}^S_E + \mathbf{T}^F_E - p^F\,\mathbf{I}\big)}_{\boldsymbol{\sigma}} + \big(\rho^S + \rho^F\big)\mathbf{b} = \mathbf{0}\,. \tag{13}$$

Herein, $\mathbf{T}^\alpha_E$ with $\alpha \in \{S, F\}$ represent the effective stress tensors and $\mathbf{b}$ denotes the mass-specific body force. The effective stress tensors of the solid and fluid constituents can be expressed according to [108] as

$$
\begin{aligned}
\mathbf{T}_E^S &= \frac{\rho^S}{\rho_{0S}^S}\left[2\,\mu^S\,\boldsymbol{\varepsilon}_S^D + \kappa^S(\boldsymbol{\varepsilon}_S\cdot\mathbf{I})\,\mathbf{I} + m_\theta^S\,\Delta\theta_0^S\,\mathbf{I}\right],\\
\mathbf{T}_E^F &= \mathcal{P}(\phi^F)\,\mathbf{T}_E^L + \left(1-\mathcal{P}(\phi^F)\right)\mathbf{T}_E^I\\
&= \mathcal{P}(\phi^F)\,\frac{\rho^F}{\rho_{0L}^{LR}}\left[\kappa^L\,(\boldsymbol{\varepsilon}_F\cdot\mathbf{I})\,\mathbf{I} + m_\theta^L\,\mathbf{I}\,\Delta\theta_0^F\right] +\\
&\quad \left(1-\mathcal{P}(\phi^F)\right)\,\frac{\rho^F}{\rho_{0I}^{IR}}\left[2\,\mu^I\boldsymbol{\varepsilon}_F^D + \kappa^I\,\mathbf{I}\,(\boldsymbol{\varepsilon}_F\cdot\mathbf{I})\right.\\
&\quad \left. + m_\theta^I\,\mathbf{I}\,\Delta\theta_0^F - 3\,\kappa^I\,\alpha_v^I\,\mathbf{I}\right].
\end{aligned}
\tag{14}
$$

Therein, $\boldsymbol{\varepsilon}_\alpha^D$ represents the deviatoric strain tensor, κ^α and μ^α are the compression and shear moduli, respectively, and $m_\theta^\alpha = -3\,\kappa^\alpha\alpha_\theta^\alpha$ is the stress-temperature modulus with α_θ^α being the coefficient of thermal expansion. α_v^I denotes the volumetric expansion coefficient due to phase change of φ^F and $\Delta\theta_0^\alpha$ represents the temperature variation compared to the reference temperature θ_0^α. The subscript $\{0\,\alpha\}$ refers to the quantity in the reference configuration. The quantities defined in Eq. (14) are obtained based on the restrictions following the evaluation of the entropy inequality and the definition of the free energies ψ^α where $\mathbf{T}_E^\alpha := \rho^\alpha\,\partial\,\psi^\alpha/\partial\,\boldsymbol{\varepsilon}_\alpha$. For the detailed explanation and derivations the interested reader could refer to [46, 48, 108]. Noting here that the fluid displacement, needed in the computation of $\boldsymbol{\varepsilon}_F$ in the case of ice, is computed based on the fluid velocity through integrating the equation of the material time derivative together with the governing equations at each time step, i.e.,

$$
(\mathbf{u}_F)'_S + (\operatorname{grad}\mathbf{u}_F)\mathbf{w}_F - \mathbf{v}_F = \mathbf{0}\,. \tag{15}
$$

5.3.3 Momentum balance of φ^F

Neglecting the dynamic effects and assuming isotropic permeability throughout the freezing and deformation processes, the momentum balance for φ^F can expressed as

$$
\mathbf{0} = \operatorname{div}\mathbf{T}_E^F - n^F\operatorname{grad}p^F + \rho^F\,\mathbf{b} - \frac{(n^F)^2\,\mu^{FR}}{K^S}\,\mathbf{w}_F\,. \tag{16}
$$

Herein, $\mu^{FR} > 0$ is the fluid dynamic viscosity and K^S represents the isotropic intrinsic permeability. The deformation dependence of K^S is being considered following [41] via

$$
K^S := \left(\frac{1-n^S}{1-n_{0S}^S}\right)^{\kappa} K_{0S}^S \qquad \text{with} \qquad \kappa > 0\,, \tag{17}
$$

where K_{0S}^S is the intrinsic permeability of the undeformed porous solid and κ is a material parameter that governs the dependency of the permeability on the solid deformation. For more information regarding the permeability with anisotropic properties, the reader is referred to [24]. The term K^S/μ^{FR} in Eq. (16) represents the specific permeability K^F, which decreases to a very low value upon ice formation as the fluid dynamic viscosity is given as $\mu^{FR} = \mathcal{P}(\phi^F)\mu^{LR} + \left(1-\mathcal{P}(\phi^F)\right)\mu^{IR}$ with $\mu^{IR} \gg \mu^{LR}$. This resembles the decrease in the hydraulic conductivity or Darcy flow coefficient as ice forms and also ensures that the fluid velocity $\mathbf{v}_F$ reduces to values almost equal to the solid velocities $\mathbf{v}_S$ when the fluid is in the frozen state.

5.3.4 Energy balance of the overall aggregate φ

The local energy balance for the homogenized medium is reformulated using the Legendre transformation to determine the internal energy via $\varepsilon^\alpha = \psi^\alpha + \theta\,\eta^\alpha$ with η^α being the specific entropy. Considering the thermal-equilibrium assumption in this work, the temperatures of the constituents at each material point are approximately the same. Thus, it is suitable to consider the energy balance for the overall aggregate, which is concluded via the sum of energy balances of the individual constituents. Moreover, since the current numerical study is restricted to the small deformation regime, it is convenient to neglect the influences of the deformations on the internal energy. The nonlinear terms were proved in [108] to have a negligible effect based on the numerical simulations. Therefore, the simplified version of the energy balance for the overall aggregate φ could be expressed as

$$
\begin{aligned}
&\rho^S\,C_p^S\,(\theta)'_S + \rho^F\,C_p^F\,(\theta)'_F\\
&\quad + \frac{\rho^F}{\rho_{0F}^{FR}}\left(W\,\mathcal{G}'(\phi^F)(\phi^F)'_F + \epsilon^2\operatorname{grad}\phi^F\cdot\operatorname{grad}(\phi^F)'_F\right)\\
&\quad + \rho^F\left[\frac{\rho_{0L}^{LR}-\rho_{0I}^{IR}}{(\rho_{0F}^{FR})^2}\left(\frac{1}{2}\,\epsilon^2\,|\operatorname{grad}\phi^F|^2 + W\,\mathcal{G}(\phi^F)\right)\right.\\
&\quad \left. + \left(C_p^L - C_p^I\right)\Delta\theta_0^F + L^F\right]\mathcal{P}'(\phi^F)(\phi^F)'_F\\
&= \operatorname{div}\left[\left(n^F\,H^{FR} + n^S\,H^{SR}\right)\operatorname{grad}\theta\right] - \hat{\mathbf{p}}^F\cdot\mathbf{w}_F\,.
\end{aligned}
\tag{18}
$$

In this equation, $\theta^\alpha = \theta$, cf. Sect. 5.3, C_p^α represents the specific heat capacity, L^F is the latent heat of fusion of ice at the freezing point, $H^{\alpha R}$ represents the scalar-valued heat conductivity coefficient, and $\hat{\mathbf{p}}^F$ is the fluid direct momentum production. Related to the PFM, ϵ is the gradient energy coefficient that controls the width of the transition zone between the solid and liquid zones, W is an energy hump parameter and $\mathcal{G}(\phi^F) = (\phi^F)^2\,(1-\phi^F)^2$ is a double-well energy function. $\mathcal{G}'(\phi^F)$ and $\mathcal{P}'(\phi^F)$ are the

derivatives of $\mathcal{G}(\phi^F)$ and $\mathcal{P}(\phi^F)$ with respect to ϕ^F, respectively.

5.3.5 Phase-field evolution equation

The evolution equation for ϕ^F is obtained as constitutive equation based on the evaluation of the entropy inequality as discussed in [108]:

$$\begin{aligned}\frac{1}{M}\,(\phi^F)'_F = \Bigg[& \rho^{FR}_{0F}\left(C^L_p - C^I_p\right)\left(\theta \ln\frac{\theta}{\theta^F_0} - \Delta\theta^F_0\right) \\ & + \rho^{FR}_{0F}\,\frac{L^F}{\theta^F_0}\,\Delta\theta^F_0 \\ & + \frac{\rho^{LR}_{0L} - \rho^{IR}_{0I}}{\rho^{FR}_{0F}}\left(\frac{1}{2}\,\epsilon^2\,|\mathrm{grad}\,\phi^F|^2 + W\,\mathcal{G}(\phi^F)\right) \\ & + p^F\,\frac{\rho^{FR}_{0F}}{(\rho^{FR})^2}\left(\rho^{LR} - \rho^{IR}\right)\Bigg]\,\mathcal{P}'(\phi^F) \\ & - W\mathcal{G}'(\phi^F) + \epsilon^2\,\nabla^2\phi^F\,.\end{aligned} \tag{19}$$

In this, $M > 0$ is the interface mobility parameter. According to [16, 116], the parameters ϵ, M and W could be obtained by relating them to the material parameters via

$$\epsilon = \sqrt{6\,\gamma^{IL}\,\delta}, \qquad W = 3\,\frac{\gamma^{IL}}{\delta}, \qquad M = \frac{v^F_k\,\theta^F_0}{6\,\rho^{FR}_{0F}\,\delta\,L^F} \tag{20}$$

with γ^{IL}, v^F_k and δ being the ice-water surface tension, kinetic coefficient and interface width of the fluid, respectively. The derivation of such parameters is based on solving the one-dimensional phase-field equation for isothermal coexistence of liquid and solid phases at a planar interface of a pure substance, see, [115, 116].

5.4 Model extension toward ice lens formation

5.4.1 Ice-water equilibrium in pores

Following well-established premelting dynamics theories, which describe liquid freezing in the pores of a porous solid material, a thin unfrozen liquid film is assumed to exist at the interface between the frozen liquid and the curved solid grains (pore wall), see, e.g., [97]. The existence of this premelted liquid film can be explained based on the minimization of the surface energies at equilibrium, where the surface energy of ice-grains interface (γ^{IS}) is greater than the sum of the surface energies of the ice-liquid (γ^{IL}) and liquid-grains (γ^{LS}) interfaces. This liquid film is characterized by a low pressure, which induces suction of liquid from the surrounding unfrozen ambient leading to additional ice lens formation and frost heave. In this work, to take this suction effect in the soil freezing continuum model into account, a phenomenological formulation similar to the soil/water retention curve (SWRC) in unsaturated soils is implemented. More details about frost heave physics and modeling within a continuum mechanical framework can also be found in [79, 87, 88, 104]. Starting with the mechanical equilibrium at the microscopic pore scale, the relationship between the pressures of the liquid water and the ice crystals can be described by the Young-Laplace's law as

$$p^I - p^L = \frac{2\,\gamma^{IL}}{r}\,, \tag{21}$$

where γ^{IL} stands for the interface energy between ice and liquid water ($\mathrm{J/m^2}$) and r denotes the mean curvature radius of the interface separating the crystal from the adjacent liquid water. Similarly to Eq. (21), the mechanical equilibrium between vapor (gas) and liquid water of unsaturated porous materials obeys also the Young-Laplace's law as

$$p^G - p^L = \frac{2\,\gamma^{GL}}{r}\,, \tag{22}$$

where γ^{GL} is the liquid-air interface energy. The similarity between Eqs. (21) and (22) paves the path to implement similar macroscopic formulations that consider the suction effects. In particular, we proceed from the van Genuchten model [114], which is used to express the relationship between the pore capillary pressure and the liquid saturation $\overline{\chi}^L$ during the drying process of unsaturated porous materials and is expressed as

$$p^G - p^L = \mathcal{N}^*\left[(\overline{\chi}^L)^{-\frac{1}{m^*}} - 1\right]^{1-m^*} \qquad \text{with} \qquad 0 < m^* < 1\,. \tag{23}$$

In this, p^G is the gas pressure, whereas $\mathcal{N}^*$ and m^* are adjustable model parameters related to the material pore structure and pore-fluid properties. In analogy, the cryogenic suction due to the ice/water interface tension, i.e., $\mathcal{S}_{cryo} := p^I - p^L$, can be expressed by the following phenomenological relationship

$$\mathcal{S}_{cryo} = p^I - p^L = \mathcal{N}\left[(\chi^L)^{-\frac{1}{m}} - 1\right]^{1-m} \quad \text{with} \quad 0 < m < 1\,, \tag{24}$$

where $\mathcal{N}$ and m are retention model parameters, adjusted depending on the solid and fluid phases properties. The function in (24) is introduced as a non-hysteretic phenomenological characteristic function to relate the liquid water saturation χ^L with the pressure difference between the crystal ice and the liquid water ($\mathcal{S}_{cryo} = p^I - p^L > 0$) [82, 124]. In our treatment of unified water/ice kinematics,

the phase-field variable ϕ^F is utilized as the degree of water saturation and, thus, corresponds to χ^L.

In order to include the suction effect in the macroscopic model presented in Sect. 5.3, one has to distinguish between p^L and p^I, whereas $p^I - p^L$ can explicitly be determined from Eq.(24). For this purpose, the definition of the net pore pressure $\bar{p} := p^F$ is exploited, which is equal to the weighted sum of the pore ice pressure p^I and the pore water pressure p^L [88]. Based on the PFM formulation with $\chi^L \approx \phi^F$, this can be described as

$$\begin{aligned} p^F &= \chi^L p^L + (1-\chi^L) p^I \quad \overset{\text{reformulation}}{\longrightarrow} \\ p^F &= p^L + (1-\chi^L) S_{cryo}\,. \end{aligned} \tag{25}$$

This reformulation is applied to eliminate the ice phase pressure p^I from the primary variables by expressing it as a function of the liquid phase pressure p^L and the cryo-suction S_{cryo}. Note that in the current reformulation, p^L becomes the primary pressure variable instead of p^F. Therefore, to overcome the instability challenges, a quasi-compressibility method is used to enforce the stability via adding a stabilization term of the form "$-\alpha \operatorname{div}(\operatorname{grad} p^L)$" as mentioned in Sect. 6.

5.4.2 Ice segregation criterion

A stress criterion for the initiation of a new ice lens and, thus, degradation of the solid stiffness, was adopted by many researchers [47, 83, 88]. The stress-based method considers that in a one-dimensional configuration, the soil stiffness degrades and a new ice lens forms when the pore pressure exceeds the sum of the overburden stress p_{ob} and the separation strength of the soil p_{sep}. The frost heave then results from the moisture accumulation and the volumetric expansion due to ice lens formation. In this paper, an alternative criterion approach presented by [123] and [77] is adopted, where a separating porosity or void ratio, as a counterpart to the critical separation stress, determines the formation of ice lenses. In particular, when the void ratio $e := n^F/n^S$ is greater than or equal to the separation void ratio e_{sep}, i.e., $e \geq e_{sep}$, ice crystals interconnect and ice lenses begin to form. The separation void ratio can be expressed in one-dimensional space according to [77, 123] as

$$e_{sep} := \frac{1+e_0}{E^S}\left(p_{ob} + p_{sep} - \int_y^h (\gamma - \gamma_0)\mathrm{d}y\right) + e_0\,. \tag{26}$$

Herein, $\gamma := g(n^S\rho^{SR} + n^W\rho^{WR} + n^I\rho^{IR})$ is the unit weight of the soil, and the subscript 0 refers to the initial state. To represent the damage to the solid phase once ice segregation takes place, the stiffness of soil is allowed to degrade to a very low value by multiplying the effective stress by a degradation function Υ_d. This method is chosen in analogy to degradation of the stiffness of the solid matrix during the crack growth in porous media [52, 53]. Moreover, this method agrees with described methods in the literature as in [103, 111], which utilize other approaches for ice lens formation. In particular, a phenomenological parameter is presented in the sense of an indicator function for ice lens formation. It can be expressed for a smooth transition as

$$\begin{aligned} d_e &= \begin{cases} 0 & (e < e_{sep}) \\ \dfrac{e - e_{sep}}{e_{max} - e_{sep}} & (e_{max} \geq e \geq e_{sep}) \\ 1 & (e > e_{max})\,, \end{cases} \quad \text{yielding} \\ \Upsilon_d &:= (1-\kappa_D)\,(1-d_e) + \kappa_D, \end{aligned} \tag{27}$$

where κ_D is the residual stiffness after separation, which is set 10^{-2} in the simulations so that no numerical stability problems occur. Moreover, e_{max} is a maximum value of the void ratio, after which the stiffness of the solid phase is considered to be completely lost. In the ice lenses simulation, the degradation function in Eq. (27) is multiplied by the solid effective stress $\mathbf{T}_E^S$ defined in Eq. $(14)_1$. Therefore, the momentum balance of the overall aggregate φ in Eq. (13) can be written as

$$\begin{aligned} &\operatorname{div} \underbrace{\left(\Upsilon_d\,\mathbf{T}_E^S + \mathbf{T}_E^F - p^L\mathbf{I} - (1-\chi^L)\,S_{cryo}\,\mathbf{I}\right)}_{\boldsymbol{\sigma}} \\ &\quad + \left(\rho^S + \rho^F\right)\mathbf{b} = \mathbf{0}\,, \end{aligned} \tag{28}$$

which is applied in the ice-lens modeling.

6 Numerical Implementation

In the numerical solution of the coupled partial-differential equations (PDEs), the finite element method (FEM) within a Bubnov–Galerkin approach is applied. As a representative case, the original model presented in Sect. 5.3 will be considered, whereas the modified model in Sect. 5.4 can be treated in a similar fashion. In this, the PDEs with primary variables $\boldsymbol{\xi}(\mathbf{x},t) := [p^F \;\; \mathbf{w}_F \;\; \mathbf{u}_F \;\; \mathbf{u}_S \;\; \theta \;\; \phi^F]^T$ are multiplied by the corresponding independent test functions $\delta\boldsymbol{\xi}(\mathbf{x}) := [\delta p^F \;\; \delta\mathbf{w}_F \;\; \delta\mathbf{u}_F \;\; \delta\mathbf{u}_S \;\; \delta\theta \;\; \delta\phi^F]$ and integrated over the spatial domain Ω^T to derive the weak formulation. Thereafter, the product rule and the Gaussian integral theorem are utilized to extract the boundary terms $\Gamma_\xi = \partial\,\Omega_\xi$, where Γ_ξ is split into Dirichlet (essential) and Neumann (natural) boundaries, see, e.g., [49, 50, 73, 126]

for analogous treatment. For the case of a nearly incompressible pore fluid, i.e., a very high bulk modulus κ^F, the term corresponding to $(p^F)'_S$ in the fluid mass balance Eq. (12) tends to vanish, and Eq. (12) becomes independent of the pressure variable. Thus, numerical instabilities appear in the monolithic solution due to the violation of the *inf-sup* condition. To overcome this instability challenge, a quasi-compressibility method is used to enforce the stability via adding a stabilization term of the form "$-\alpha\,\mathrm{div}\,(\mathrm{grad}\,p^F)$" to Eq. (12) with α as a small stabilization parameter. Following this, the weak form of the governing equations read:

- **Mass balance of** φ^F

$$\begin{aligned}&\int_\Omega \delta p^F\,\rho^{FR}\left[n^F\,\frac{(p^F)'_S}{\kappa^F}+\mathrm{div}\,\mathbf{v}_S\right]\mathrm{d}v\\&-\int_\Omega \mathrm{grad}\,\delta p^F\cdot\left(\rho^F\mathbf{w}_F-\alpha\,\mathrm{grad}\,p^F\right)\mathrm{d}v\\&+\int_{\Gamma_w}\delta p^F\,\overline{w}\,\mathrm{d}a-\int_{\Gamma_p^F}\delta p^F\,\alpha\left(\mathrm{grad}\,p^F\right)\cdot\mathbf{n}\,\mathrm{d}a=0\,,\end{aligned}\tag{29}$$

where $\overline{w}=\rho^F\,\mathbf{w}_F\cdot\mathbf{n}$ is the mass efflux of the fluid draining through the Neumann boundary Γ_w with outward-oriented unit surface normal $\mathbf{n}$.

- **Momentum balance of** φ^F

$$\begin{aligned}&\int_\Omega\left(\mathbf{T}_E^F-n^F\,p^F\,\mathbf{I}\right)\cdot\mathrm{grad}\,\delta\mathbf{w}_F\,\mathrm{d}v\\&-\int_\Omega\delta\mathbf{w}_F\cdot\left[\frac{n^F\,\mu^F}{K_\phi^S}\,\mathbf{w}_F-\rho^F\mathbf{b}\right]\mathrm{d}v\\&-\int_{\Gamma_{\mathbf{t}^F}}\delta\mathbf{w}_F\cdot\overline{\mathbf{t}}^F\,\mathrm{d}a=0\,.\end{aligned}\tag{30}$$

Herein, $\overline{\mathbf{t}}^F=\left(\mathbf{T}_E^F-n^F\,p^F\,\mathbf{I}\right)\mathbf{n}$ represents the external fluid load vectors acting on the Neumann boundary $\Gamma_{\mathbf{t}^F}$. The extra equation induced by the use of the relation $\mathbf{v}_F=(\mathbf{u}_F)'_F$ reads in weak form

$$\int_\Omega\delta\mathbf{u}_F\cdot\left[(\mathbf{u}_F)'_S+\mathrm{grad}\,\mathbf{u}_F\cdot\mathbf{w}_F-\mathbf{v}_F\right]\mathrm{d}v=0\,.\tag{31}$$

- **Momentum balance of** φ

$$\begin{aligned}&\int_\Omega\boldsymbol{\sigma}\cdot\mathrm{grad}\,\delta\mathbf{u}_S\,\mathrm{d}v+\int_\Omega\delta\mathbf{u}_S\cdot\left(\rho^S+\rho^F\right)\mathbf{b}\,\mathrm{d}v\\&-\int_{\Gamma_\mathbf{t}}\delta\mathbf{u}_S\cdot\overline{\mathbf{t}}\,\mathrm{d}a=0\,,\end{aligned}\tag{32}$$

where $\overline{\mathbf{t}}=\boldsymbol{\sigma}\,\mathbf{n}$ represents the external solid load vector acting on Neumann boundary $\Gamma_\mathbf{t}$.

- **Energy balance of the mixture** φ

$$\begin{aligned}&\int_\Omega\delta\theta\Bigg(\rho^F\,C_p^F(\theta)'_F+\rho^S\,C_p^S(\theta)'_S\\&+\frac{\rho^F}{\rho_{0F}^{FR}}\left[W\,\mathcal{G}'(\phi^F)(\phi^F)'_F+\epsilon^2\,\mathrm{grad}\,\phi^F\cdot\mathrm{grad}\,(\phi^F)'_F\right]\\&+\left[\frac{\rho_{0L}^{LR}-\rho_{0I}^{IR}}{(\rho_{0F}^{FR})^2}\left(\frac{1}{2}\,\epsilon^2\,|\mathrm{grad}\,\phi^F|^2+W\,\mathcal{G}(\phi^F)\right)\right.\\&\left.+\left(C_p^L-C_p^I\right)\Delta\theta+L^F\right]\rho^F\,\mathcal{P}'(\phi^F)\,(\phi^F)'_F\\&+\hat{\mathbf{p}}^F\cdot\mathbf{w}_F\Bigg)\,\mathrm{d}v\\&+\int_\Omega H^{SF}\,(\mathrm{grad}\,\theta)\cdot\mathrm{grad}\,\delta\theta\,\mathrm{d}v\\&-\int_{\Gamma_{q^{SF}}}\delta\theta\,\overline{q}^{SF}\,\mathrm{d}a\end{aligned}\tag{33}$$

where H^{SF} represents H^S+H^F and $\overline{q}^{SF}=H^{SF}\,(\mathrm{grad}\,\theta)\cdot\mathbf{n}$ is the heat flux acting on Neumann boundary $\Gamma_{q^{SF}}$.

- **Phase-field evolution of** φ^F

$$\begin{aligned}&\int_\Omega\delta\phi^F\Bigg(\frac{1}{M}\,(\phi^F)'_F-\Bigg[\rho_{0F}^{FR}\left(C_p^L-C_p^I\right)\\&\left(\theta\ln\frac{\theta}{\theta_0^F}-\Delta\theta_0^F\right)\\&+\rho_{0F}^{FR}\,\frac{L^F}{\theta_0^F}\,\Delta\theta_0^F+\frac{\rho_{0L}^{LR}-\rho_{0I}^{IR}}{\rho_{0F}^{FR}}\\&\left(\frac{1}{2}\,\epsilon^2\,|\mathrm{grad}\,\phi^F|^2+W\,\mathcal{G}(\phi^F)\right)+W\mathcal{G}'(\phi^F)\\&+p^F\,\frac{\rho_{0F}^{FR}}{(\rho^{FR})^2}\left(\rho^{LR}-\rho^{IR}\right)\Bigg]\mathcal{P}'(\phi^F)\Bigg)\mathrm{d}v\\&+\int_\Omega\epsilon^2\,\mathrm{grad}\,\phi^F\cdot\mathrm{grad}\,\delta\phi^F\,\mathrm{d}v\\&-\int_{\Gamma_{\phi^F}}\delta\phi^F\,\epsilon^2\left(\mathrm{grad}\,\phi^F\right)\cdot\mathbf{n}\,\mathrm{d}a\end{aligned}\tag{34}$$

In this, the term $\epsilon^2\left(\mathrm{grad}\,\phi^F\right)\cdot\mathbf{n}$ vanishes on the Neumann boundary Γ_{ϕ^F}.

The TPM-PFM coupled problem is solved using the FEM package FlexPDE (professional, ver. 7.15.), where the time

discretization of the equations is carried using the second-order implicit backward difference formula. For the spatial discretization, the Galerkian method with quadratic shape functions is applied. Having the time-dependent nodal values vector of the primary variables $\boldsymbol{\xi}(t) := [\mathsf{p}^F \ \mathsf{w}_F \ \mathsf{u}_F \ \mathsf{u}_S \ \boldsymbol{\theta} \ \boldsymbol{\phi}^F]^T$, the coupled PDE system after spatial discretization can be written in an abstract form as

$$\begin{aligned}
&\mathcal{G}_{p^F}(\mathsf{p}^F, \mathsf{w}_F, \mathsf{u}_S)\\
&\mathcal{G}_{\mathbf{w}_F}(\mathsf{w}_F, \mathsf{p}^F, \mathsf{u}_F, \mathsf{u}_S, \boldsymbol{\theta}, \boldsymbol{\phi}^F)\\
&\mathcal{G}_{\mathbf{u}_F}(\mathsf{u}_F, \mathsf{w}_F, \mathsf{u}_S)\\
&\mathcal{G}_{\mathbf{u}_S}(\mathsf{u}_S, \mathsf{p}^F, \mathsf{u}_F, \boldsymbol{\theta}, \boldsymbol{\phi}^F)\\
&\mathcal{G}_{\theta}(\boldsymbol{\theta}, \mathsf{p}^F, \mathsf{w}_F, \mathsf{u}_F, \boldsymbol{\phi}^F)\\
&\mathcal{G}_{\phi^F}(\boldsymbol{\phi}^F, \mathsf{p}^F, \mathsf{w}_F, \boldsymbol{\theta})
\end{aligned} \tag{35}$$

where $\mathcal{G}_{\mathsf{p}^F}$, $\mathcal{G}_{\mathbf{w}_F}$, $\mathcal{G}_{\mathbf{u}_F}$, $\mathcal{G}_{\mathbf{u}_S}$, $\mathcal{G}_{\theta}$ and $\mathcal{G}_{\phi^F}$ represent the space-discrete fluid mass balance, fluid momentum balance, fluid displacement, mixture momentum balance, mixture energy balance, and the phase-field evolution equation, respectively.

Related to the time integration, the volumetrically coupled thermo-mechanical problem is solved using a monolithic implicit scheme with the quasi-compressibility stabilization scheme for the case of a low-compressible fluid. It is worth mentioning that the computational efficiency gained by the staggered strategy in thermo-elasticity is not guaranteed for the case where the differential equations are strongly coupled (many nonlinear dependencies) [42]. In the current implementation, time-stepping adaptivity is applied to keep the solution within the specified limits of accuracy. Regarding the system of nonlinear differential equations, a modified Newton–Raphson iteration procedure is utilized by FlexPDE to attain the numerical solution, where the Jacobian matrix of the current system equations is computed and Newton iterations are performed at each time step until the convergence is reached. Useful and detailed information to the solution of coupled problems can be found in [1, 2, 72, 73, 85, 107] and the included references.

In dealing with the phase-change process, the mesh size should be small enough so the solid-liquid interface is efficiently covered. For an accurate representation of the physical processes at the moving, diffusive front, it is very important to have small values of the parameter ϵ since it plays a central role in the sense that the diffusive interface converges to a sharp one for $\epsilon \to 0$. However, from the computational cost viewpoint, it is desirable for ϵ to be as large as possible so that a solution of the phase-field equation can be obtained for a practical computational effort. In this sense, interfaces are taken artificially wide in most of the phase-field simulations to decrease the computational costs. In several studies it was shown that when the PFM is applied to model the phase-change process on the macroscale, without the interest in capturing the microstructural evolution and dendrite growth, the interface width could be increased by orders of magnitude without significantly affecting the result [22, 108, 120]. This serves significantly in decreasing the computational costs by eliminating the need for a very fine mesh size.

7 Numerical results

7.1 Numerical model validation in the thermal transient phase

The objective in this section is to validate the numerical model and demonstrate its capability in capturing important thermo-hydro-mechanical responses during the phase transition of the pore fluid from liquid water to ice. The numerical simulations are conducted for two different types of experiments, i.e., top-freezing (TF) and bottom-freezing (BF). For each type of experiment, we apply two sets of different thermal boundary conditions. The comparisons between the numerical and experimental data include the temperature fields at different positions, the 0 °C-isotherm position, and the frost heave time history. The numerical simulations in this section are carried out for the thermal transient phase (frost penetration phase), whereas the formation of the ice lenses will be addressed in a subsequent section. A detailed explanation of the experimental setup and specifications of the different materials are provided in Sect. 2. The properties of the solid phase are given in Table 1, while those of ice and water are adopted from [13]. Other material parameters related to the PFM are chosen as follows: $\gamma^{IL} = 0.065 \ \mathrm{J/\,m^2}$, $v_k^F = 0.001\,\mathrm{m/s \cdot K}$, $\delta = 0.5\,\mathrm{mm}$, and $\epsilon = 0.8\,(\mathrm{J/\,m})^{\frac{1}{2}}$. Additionally, triangular grids with mesh size of ca. 4 mm was chosen for all the simulations. The initial conditions for both BF and TF are the same, where water is found in a liquid state at an ambient temperature of $\theta_i = 15\,^{\circ}\mathrm{C}$. The drained boundary conditions are prescribed by imposing zero pore pressure $p^F = 0\,\mathrm{Pa}$ at the heating boundary of each case to allow for water supply, while impermeable boundary conditions are set at the other boundaries. Moreover, a total mechanical load of $p_{ob} = 3.6\,\mathrm{kPa}$ corresponding to the overburden pressure is applied to the top boundary, see, Fig. 2 for illustration. In both BF and TF, the sample is being cooled along the cold boundary, while the warm boundary is slightly heated to prevent freezing of the complete sample as discussed in Sect. 2. The cooling and heating temperature loads for the

BF and TF tests, which are also applied in the numerical models, are illustrated in Fig. 13.

In discussing the numerical results, the relevant phase-field and temperature contour plots for the BF and TF tests after 20 and 25 hours are shown in Figs. 14 and 15, respectively.

The different positions of the temperature sensors (six sensors) in the experiments are illustrated in Fig. 16. A comparison between the experimental and numerical results of the temperature-time history at different sensor positions is given in Fig. 17. In both BF and TF cases, the temperature starts decreasing due to cooling until reaching 0 °C, where the water starts freezing. The temperature continues decreasing with time while the thickness of the ice layer grows continuously as shown in Fig. 18.

Figure 19 shows the frost heave evolution extracted from the FE simulations and compared to the measured data. These simulations are performed proceeding from elastic solid skeleton deformations, whereas the heave evolution is measured at the top surface. The resulting frost heave in the transient phase is mainly due to the volume expansion of the sample due to ice formation. These results, which cover the phase change process and the thermo-mechanical behavior of soil during freezing, show a good agreement between the numerical and the experimental date. However, simplification in the applied model, such as ignoring the plastic deformations of soil, have presumably contributed to the deviation in the displacement field in Fig. 19 between the numerical and experimental results.

To provide a percentage-based deviation measure of the predicted numerical results from the reference experimental data, several methods could be found in the literature. In this, the mean absolute percentage error (MAPE) [34] provides a simple dimensionless measure that could easily be computed and interpreted

$$\mathrm{MAPE} := \frac{1}{n}\sum_{t=1}^{n}\left|\frac{F_t - Y_t}{Y_t}\right| \times 100\,. \tag{36}$$

Here, Y_t denotes the measured data (experimental data) at time t, F_t is the forecast data (numerical predicted data) and n is the number of different times for which the considered variable is forecast. However, this method has inherent difficulty in handling low and zero values in the denominator. Moreover, having a single case with large error can dominate the overall result of the MAPE. To overcome these challenges, especially related to the 'infinite error', the weighted mean absolute percentage error (WMAPE) [75, 86] can alternatively be used. This is equivalent to dividing the sum of absolute differences of the measured and forecast values by the sum of the measured values yielding

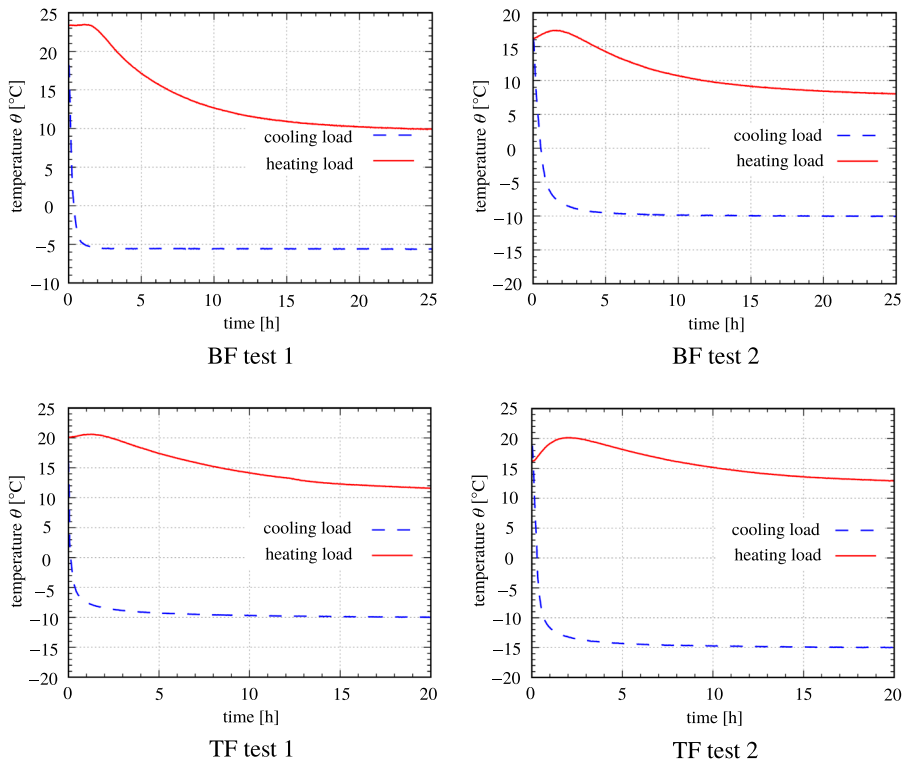

Fig. 13 Thermal loading applied in both the experiments and the numerical models of the BF and TF boundary-value problems

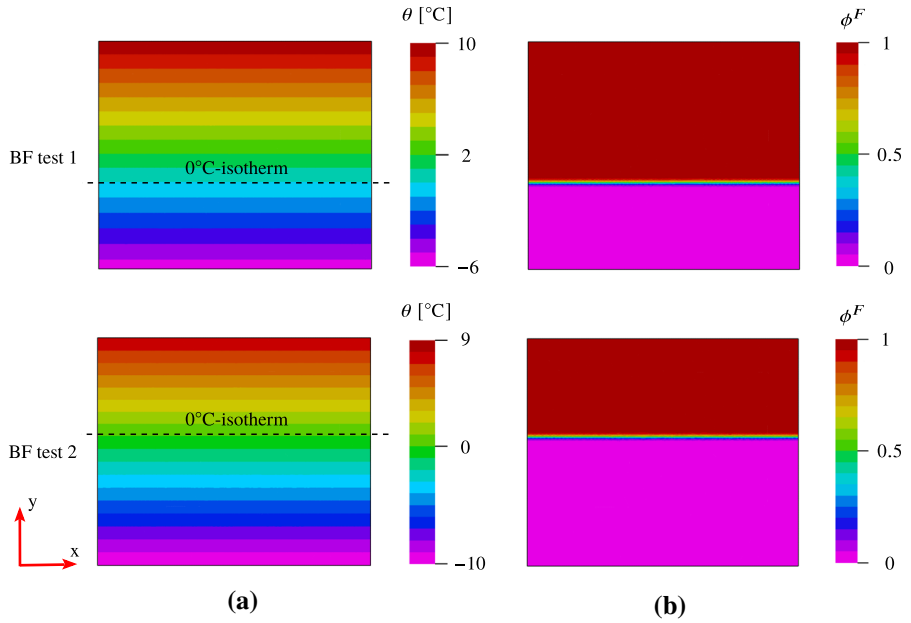

Fig. 14 Contour plots of **a** spatial temperature distribution and **b** phase-field evolution for the BF case after 25 hours

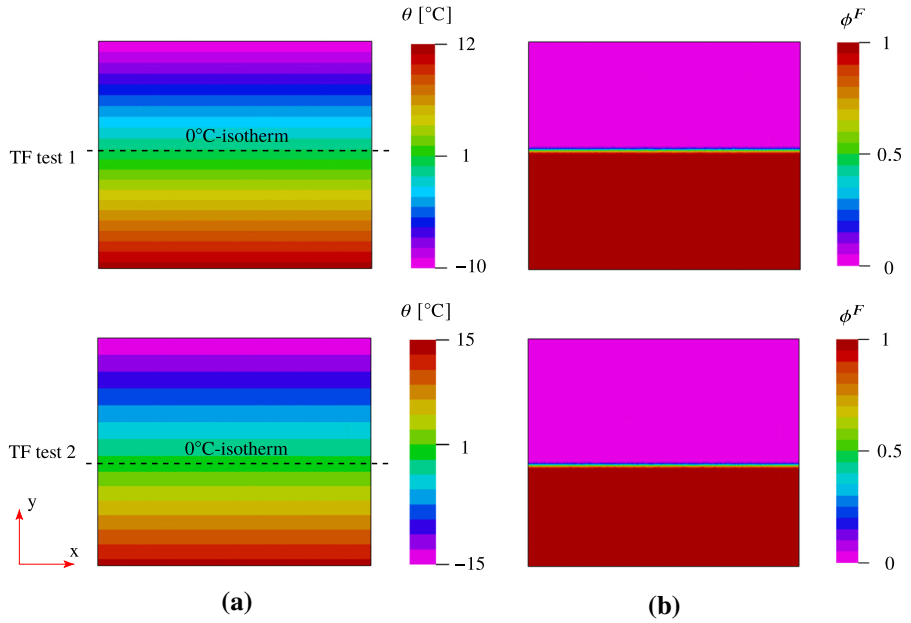

Fig. 15 Contour plots of **a** temperature distribution and **b** phase-field evolution for TF case after 20 hours

$$\mathrm{WMAPE} = \frac{\sum_{t=1}^{n} |F_t - Y_t|}{\sum_{t=1}^{n} |Y_t|} \times 100\,. \tag{37}$$

Another alternative for the MAPE is the symmetric mean absolute percentage Error (SMAPE) [44, 100], where it expresses the absolute error as a percentage of the average of the forecast and the measured values. However, this measure is found not to be suitable when interpreting percentage errors of data including mixed positive and negative values (as, e.g., temperatures on a °C-scale in our case). Moreover, undefined values could appear when the sum of the measured and forecast values is zero in the denominator. An overview of the different types of measures, including scale-dependent measure and relative-based measures, can be found in [26, 44]. According to this, we employ the WMAPE (Eq. (37)) for quantitative comparisons between the experimental and the numerical results related to the different outputs, i.e., the frost heave, the temperature field, and the ice/water interface position.

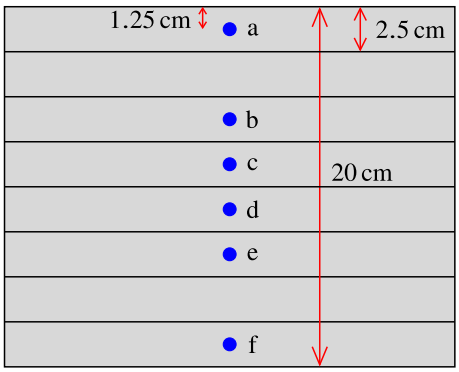

Fig. 16 Temperature sensor positions

As shown in Table 2, the lowest WMAPE values are recorded for the interface position in each test. In the TF tests, the temperatures show the largest deviations followed by the frost heave, while, for the BF tests the frost heave shows the largest deviations among the other outputs. This could be attributed, as discussed previously, to neglecting the plastic deformations of the solid phase in the freezing process. In general, these deviation errors remain in acceptable range, especially that the previously discussed figures showed almost similar trends between the simulation and experimental curves for the different studied cases.

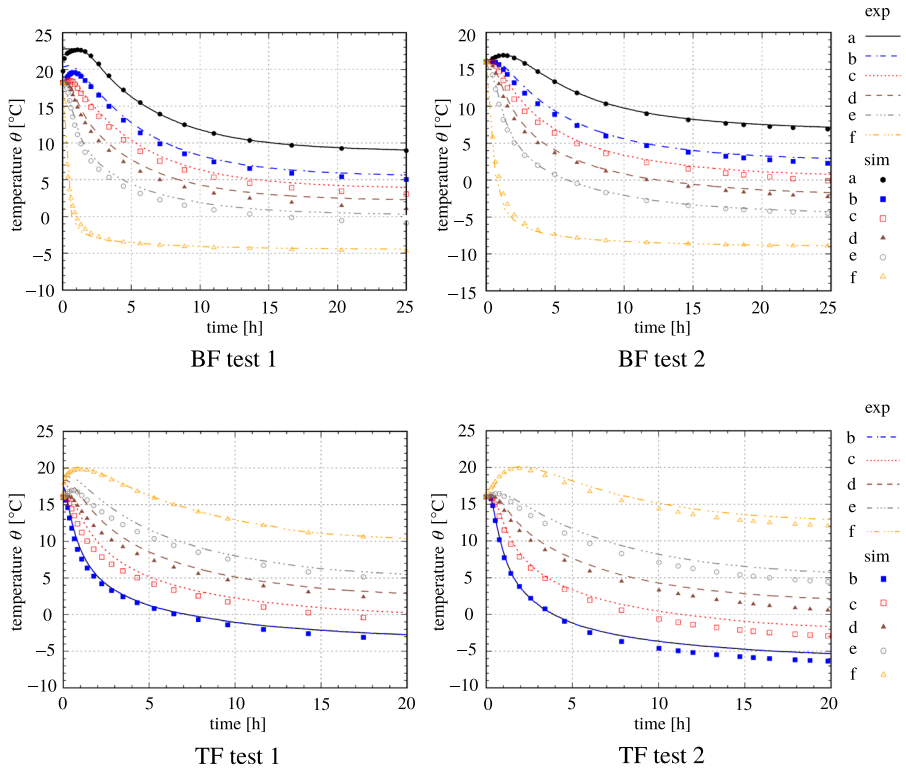

Fig. 17 Model validation with regard to temperature evolution at six sensor positions for the BF and TF tests

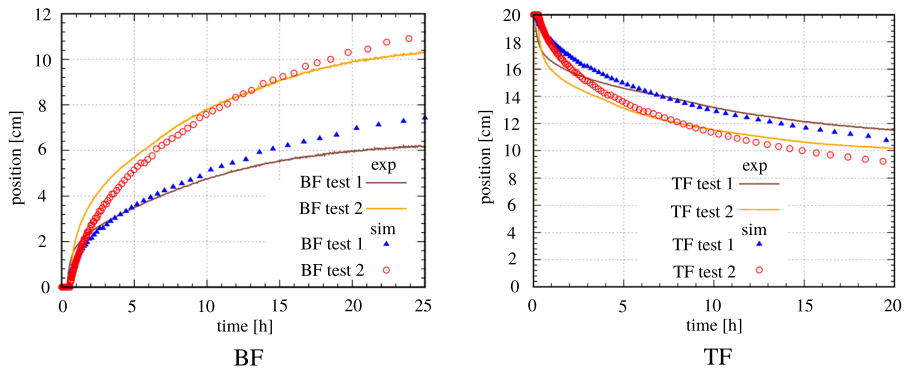

Fig. 18 Numerical and experimental 0°C-isotherm position over time for the different freezing configurations

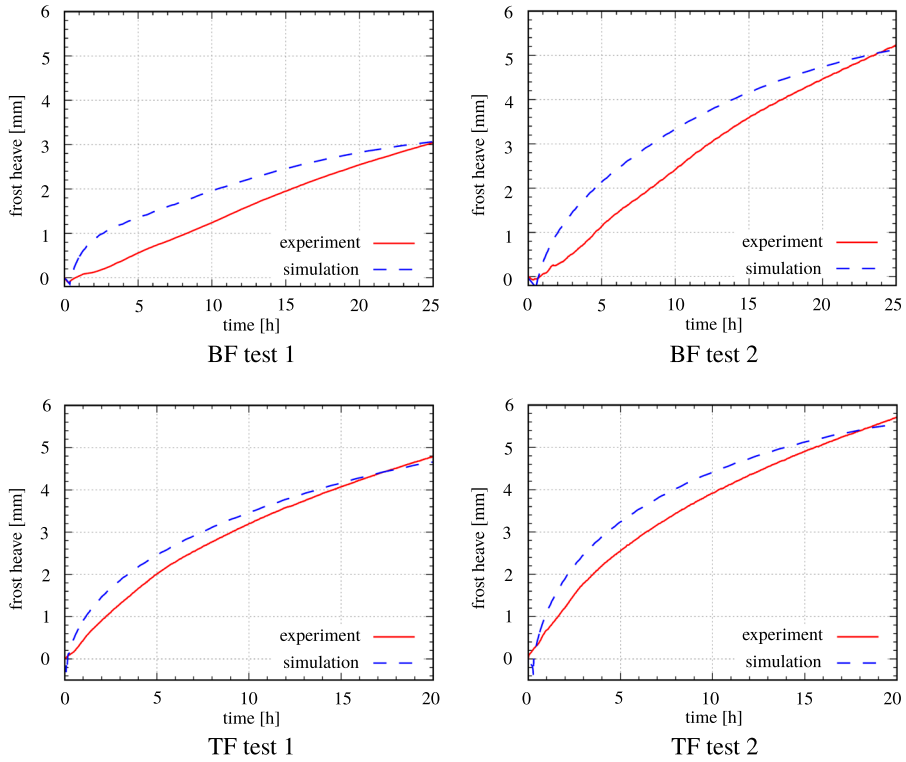

Fig. 19 Numerical simulation and experimental data of the vertical displacement of upper surface for the BF and TF cases

Table 2 WMAPE values indicating the percentage error between the numerical and experimental results

Performance parameter	Test type			
	BF test 1	BF test 2	TF test 1	TF test 2
temperature θ	11.18%	7.9%	13.70%	15.28%
0°C-isotherm position	10.64%	5.44%	3.2%	5.14%
frost heave	32.08%	19.88%	7.17%	11.1%

Based on these results and comparisons between the numerical and the experimental data for the different studied cases, we conclude that the proposed TPM-PFM approach is powerful in the simulation of phase-change processes and in the description of the non-isothermal behavior during freezing of water-saturated soils.

7.2 Numerical results related to the ice lens formation

For the current numerical study, the suction-related parameters $\mathcal{N}$ and m are chosen as 0.1 MPa and 0.5, respectively, which gives a good fit with the experimental data. Here, we consider BF test 3 as a representative case. The boundary and initial conditions are the same as described in the previous sections. We assume a separation strength of the soil p_{sep} of 200 kPa, which corresponds according to Eq. (26) to $e_{sep} \approx 1.1$. The temperature loads for this representative case are shown in Fig. 20.

7.2.1 Frost heave

A comparison of the frost heave resulting from the simulations with that of the experimental data is presented in Fig. 21. During the transient freezing process and frozen fringe formation, the heave occurs due to the volumetric expansion of the frozen water (ice-water phase change). As the temperature gradient becomes steady, the rate of frozen front penetration decreases while the frost heave continues its gradual increase. In this phase, the pore water migrates from the unfrozen zone and accumulates at the freezing front, which results in the ice lens formation. This indicates

that the heave due to ice lens formation in the thermal (quasi-) steady state is of great importance. The results also show the capability of the proposed numerical model in predicting the total heave due to pore-water freezing. Regarding the percentage error related to numerical and experimental results of the frost heave, the WMAPE results in a value of 15.57%.

Referring to Fig. 11 and the obtained results in the related section, at the early stages of the experiments (during the thermal transient state), the vertical cracks are insignificant, and the frost heave is mainly due to the ice expansion upon phase-change. In the later steady-state phase, the frost heave is mainly due to the sucked water that comes from the unfrozen surrounding and the external supply through the surrounding, which accumulates and freezes at the freezing front. The vertical cracks grow significantly at the late stages of the steady-state phase, where they play a bigger role in altering the sample's permeability and increasing the frost heave. Figure 21 shows that the frost heave in the numerical result at the late stage of the steady state is less compared to the experimental result. This could be due to the vertical cracks that formed at that stage and the relevant vertical permeability enhancement, which has not been taken into consideration in the model.

Ice lens contour plot at two different times of the freezing and scaled deformations by factor 7. The red color refers to a complete loss of solid stiffness (separation) and a continuous ice lens formation

7.2.2 Ice lens distribution

The predicted ice lens, which fulfills the condition $e \geq e_{sep}$, is illustrated in Fig. 22, where a scaling factor of 7 is used. As long as the time ≤ 40 h, the height of the soil column is increasing, but no visible ice lenses are formed, i.e., the

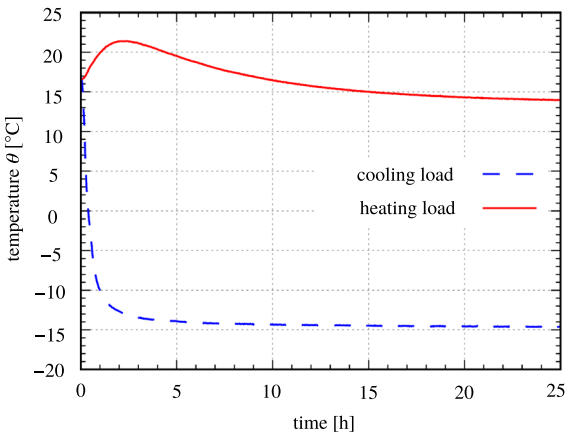

Fig. 20 Temperature load applied in both the numerical model and representative BF test 3 experiment

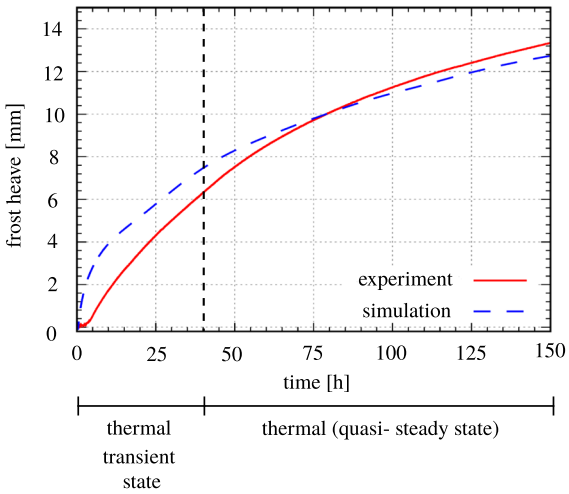

Fig. 21 A comparison of frost heave between the simulation results and the experimental data until 150 s

void ratio in the domain is less than e_{sep}. As the rate of the frozen front penetration decreases in the thermal (quasi-) steady state, water in the unfrozen zone has enough time to flow to the frozen zone (suction effect) and to form a localized ice lens. In other words, as time goes by, the ice lens becomes larger and forms at greater spacing progressively ($e \gg e_{sep}$) causing an increase in the frost heave. The numerical analysis agrees with the experimental results regarding the position of the final ice lens. This shows that the proposed model could serve well in the description of the ice lens formation.

8 Conclusions and future work

Ground frost and the resulting heave-induced damages are mainly known from road construction in cold regions. However, they can also occur during artificial ground freezing. The boundary conditions resulting from artificial ground freezing differ in some aspects from the boundary conditions in road construction, for example, concerning the decisive freezing direction, which runs toward the ground surface during ground freezing. This and other influences on frost heave during artificial ground freezing are investigated in this research work using a newly designed experimental device.

In artificial ground freezing, the frost body first freezes to the static required thickness and is maintained on this thickness thereafter. Due to the large temperature gradients at the beginning of freezing (thermal transient state), less ice lens formation occurs. In this, the experimental results showed that the frost heave due to the formation of the last ice lens in the thermal (quasi-) steady state significantly exceeds the frost heave at the thermal transient state. The

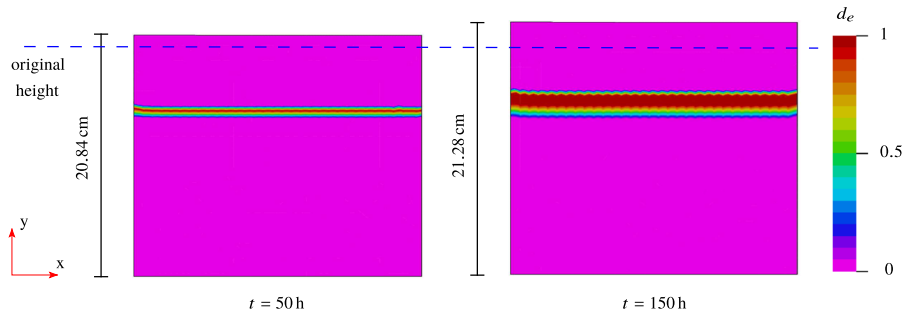

Fig. 22 Ice lens contour plot at two different times of the freezing and scaled deformations byfactor 7. The *red color* refers to a complete loss of solid stiffness (separation) and a continuousice lens formation

(quasi-) steady state is therefore decisive in the process of artificial ground freezing.

The outlined results show that the unfrozen area, which provides a flow path to the ice lens, has a major influence on ice lens growth. A shorter flow path leads to an increase in the pressure gradient and, therefore, an increase in the pore-water velocity toward the ice lens. In contrast, no significant influence of different temperature gradients on ice lens formation in the (quasi-) steady state could be observed. A comparison of the freezing directions BF and TF showed that especially with short flow paths, the frost heave of the BF experiments exceeds those of the TF. This could be attributed to the effect of gravity and the longitudinal crack formation during freezing. In particular, the hydraulic conductivity increases due to the initiation of the cracks, so that an improved water supply is provided.

The results presented here are part of a comprehensive study to determine frost heave for the boundary conditions of artificial ground freezing. Further experimental investigations concerning the overburden load and the influence of water pressure are pending.

In the numerical simulation of soil freezing and the related instances, a thermo-hydro-mechanical model that augments the macroscopic theory of porous media (TPM) with the phase-field modeling (PFM) for simulating the freezing process in a fluid-saturated porous medium is presented. The water-saturated soil is described within a continuum mechanical framework as a biphase porous material, consisting of an elastic solid (soil skeleton), and pore-fluid (pore-water/ice). In this context, thermodynamically consistent constitutive relationships and phase-field evolution obtained based on satisfying the entropy inequality are utilized. A special feature of the current work lies in presenting a unified phase-field kinematic framework for treating the ice and water phases, considering that both phrases refer to the same pore-fluid. Moreover, the PFM ensures a smooth transition for the different thermo-mechanical properties during the phase-change process.

The mathematical description of the coupled porous-media phase-field problem results in six partial-differential equations. The numerical solution of these equations is carried out using a monolithic scheme within the finite element framework. The numerical solutions of the proposed TPM-PFM approach together with the qualitative comparisons with experimental results showed the capability of the proposed model to efficiently capture the coupled processes of temperature field development in space and time, the phase-change process, and the volumetric expansion due to ice formation during freezing, and the formation of ice lenses together with solid stiffness degradation.

To this end, the presented numerical model in this research work can serve as a base for future studies and real applications in the field of soil freezing. However, improvement areas are to be addressed in the future work of this research project. Future works will focus on providing a more realistic description of the soil freezing phenomenon by extending the model toward unsaturated porous media. Additionally, the initiation and formation of ice lens will be modeled in future works based on the phase-field diffusive fracture approach. This would require extending the energy formulation through providing a thermodynamically consistent derivation of the fracture-related PF-equation while considering the associated THM changes in the domain.

Acknowledgements This work is supported by the German Research Foundation (DFG) under the project "Investigation and calculation of frost heave considering specific boundary conditions of ground freezing", grant number 409760547. The funding is herewith gratefully acknowledged.

Funding Open Access funding enabled and organized by Projekt DEAL.

Open Access This article is licensed under a Creative Commons Attribution 4.0 International License, which permits use, sharing, adaptation, distribution and reproduction in any medium or format, as long as you give appropriate credit to the original author(s) and the source, provide a link to the Creative Commons licence, and indicate if changes were made. The images or other third party material in this

article are included in the article's Creative Commons licence, unless indicated otherwise in a credit line to the material. If material is not included in the article's Creative Commons licence and your intended use is not permitted by statutory regulation or exceeds the permitted use, you will need to obtain permission directly from the copyright holder. To view a copy of this licence, visit http://creativecommons.org/licenses/by/4.0/.

References

1. Abed AA, Sołowski WT (2017) A study on how to couple thermo-hydro-mechanical behaviour of unsaturated soils: Physical equations, numerical implementation and examples. Comput Geotech 92:132–155
2. Abed AA, Sołowski WT (2020) Finite element method algorithm for geotechnical applications based on runge-kutta scheme with automatic error control. Comput Geotech 128
3. Afshani A, Akagi H (2015) Artificial ground freezing application in shield tunneling. Jpn Geotech Soc Special Pub 3(2):71–75
4. Aitken GW (1974) Reduction of frost heave by surcharge stress. Corps of engineers. US Army Cold Regions Research and Engineering Laboratory
5. Akagawa S (1988) Experimental study of frozen fringe characteristics. Cold Reg Sci Technol 15(3):209–223
6. Alber H, Markert B (2012) Minisymposia mechanics 3. PAMM 12(1):31–34
7. Anderson D, Tice AR (1973) The unfrozen interfacial phase in frozen soil water systems. Physical aspects of soil water and salts in ecosystems. Springer, Berlin, pp 107–124
8. Arenson LU, Azmatch TF, Sego DC, Biggar K (2008) A new hypothesis on ice lens formation in frost-susceptible soils. In: Proceedings of the ninth international conference on permafrost, Fairbanks, Alaska 1:59–64
9. Arenson LU, Sego DC, Take WA (2007) Measurement of ice lens growth and soil consolidation during frost penetration using particle image velocimetry (piv). In: 60th Canadian Geotechnical Conference, Ottawa, ON, pp 2046–2053
10. Azmatch TF, Sego DC, Arenson LU, Biggar KW (2012) New ice lens initiation condition for frost heave in fine-grained soils. Cold Reg Sci Technol 82:8–13
11. Beckermann C, Diepers HJ, Steinbach I, Karma A, Tong X (1999) Modeling melt convection in phase-field simulations of solidification. J Comput Phys 154(2):468–496
12. Betten J (1996) Einführung in die Kontinuumsmechanik. ZAMM—Journal of Applied Mathematics and Mechanics/Zeitschrift für Angewandte Mathematik und Mechanik 76(1):34–34
13. Bluhm J, Bloßfeld WM, Ricken T (2014) Energetic effects during phase transition under freezing-thawing load in porous media—a continuum multiphase description and FE-simulation. ZAMM Zeitschrift fur Angewandte Mathematik und Mechanik 94(7–8):586–608
14. Bluhm J, Ricken T, Bloßfeld M (2011) Ice formation in porous media. In: B Markert (ed) Lecture notes in applied and computational mechanics, vol 59. LNACM, Springer, Berlin, pp 153–174
15. Bluhm J, Setzer MJ, Kruschwitz J (2005) Modeling of ice formation in porous media. In: Gladwell GML, Huyghe JM, Raats PAC, Cowin SC (eds) Solid mechanics and its applications, vol 125. Springer Netherlands, Dordrecht, pp 329–334
16. Boettinger WJ, Warren JA, Beckermann C, Karma A (2002) Phase-field simulation of solidification. Annu Rev Mater Res 32:163–194
17. Borja RI, White JA (2013) Conservation laws for coupled hydro-mechanical processes in unsaturated porous media. John Wiley & Sons Ltd, Chapter 8, pp 185–208
18. Bowen RM (1976) Theory of mixture. In: Continuum physics, vol 3, Academic Press, pp 2–129
19. Bowen RM (1980) Incompressible porous media models by use of the theory of mixtures. Int J Eng Sci 18(9):1129–1148
20. Bowen RM (1982) Compressible porous media models by use of the theory of mixtures. Int J Eng Sci 20(6):697–735
21. Burt TP, Williams PJ (1976) Hydraulic conductivity in frozen soils. Earth Surf Process 1(4):349–360
22. Caginalp G, Socolovsky E (1991) Computation of sharp phase boundaries by spreading: the planar and spherically symmetric cases. J Comput Phys 95(1):85–100
23. Casini F, Gens A, Olivella S, Viggiani GM (2016) Artificial ground freezing of a volcanic ash: laboratory tests and modelling. Environ Geotech 3(3):141–154
24. Chaaban M, Heider Y, Markert B (2020) Upscaling LBM-TPM simulation approach of Darcy and non-Darcy fluid flow in deformable, heterogeneous porous media. Int J Heat Fluid Flow 83:108566
25. Chamberlain EJ, Gow AJ (1979) Effect of freezing and thawing on the permeability and structure of soils. Dev Geotech Eng 26:73–92
26. Chen C, Twycross J, Garibaldi JM (2017) A new accuracy measure based on bounded relative error for time series forecasting. PLOS One 12(3):1–23
27. Chen L-Q (2002) Phase-field models for microstructure evolution. Annu Revi Mater Res 32:113–140
28. Coussy O (2005) Poromechanics of freezing materials. Journal of the Mechanics and Physics of Solids 53(8):1689–1718
29. Dagli D (2017)LInaboratory investigations of frost action mechanisms in soils. In: Ph.D. thesis, Luleå University of Technology, Luleå University of Technology
30. de Boer R (1993) Thermodynamics of phase transitions in porous media. Appl Mech Rev 46:1–48
31. De Boer R (1996) Highlights in the historical development of the porous media theory: toward a consistent macroscopic theory. Appl Mech Rev 49(4):201–262
32. de Boer R (2000) Theory of porous media: highlights in the historical development and current state. Springer, Berlin
33. De Boer R, Bluhm J (1999) Phase transitions in gas- and liquid-saturated porous solids. Transp Porous Media 34(1–3):249–267
34. de Myttenaere A, Golden B, Le Grand B, Rossi F (2016) Mean absolute percentage error for regression models. Neurocomputing, 192
35. Ehlers W (1993) Constitutive equations for granular mɛaterials in geomechanical Context. In: Continuum mechanics in environmental sciences and geophysics, Springer Vienna, Vienna, pp 313–402
36. Ehlers W (2002) Foundations of multiphasic and porous materials. In: Ehlers W, Bluhm J (eds) Porous media. Springer, Berlin, pp 3–86
37. Ehlers W, Graf T (2007) SSaturated elasto-plastic porous media under consideration of gaseous and liquid phase transitions. In: Schanz T (ed) Theoretical and numerical unsaturated soil mechanics. Berlin, pp 111–118
38. Ehlers W, Häberle K (2016) Interfacial mass transfer during gas-liquid phase change in deformable porous media with heat transfer. Transp Porous Media 114(2):525–556
39. Ehlers W, Luo C (2018) A phase-field approach embedded in the theory of porous media for the description of dynamic

hydraulic fracturing, part II: the crack-opening indicator. Comput Methods Appl Mech Eng 341:429–442
40. Ehlers W, Wagner A (2019) Modelling and simulation methods applied to coupled problems in porous-media mechanics. Archive Appl Mechs 89(4):609–628
41. Eipper G (1998) Theorie und Numerik finiter elastischer Deformationen in fluid-gesättigten porösen Medien. In: Ph.D. thesis, University of Stuttgart, University of Stuttgart
42. Felippa CA, Park KC (2004) Synthesis tools for structural dynamics and partitioned analysis of coupled systems. In: NATO Advanced Research Workshop, pp 50–110
43. Ferreira AF, De Olivé Ferreira L, Da Costa Assis A (2011) Numerical simulation of the solidification of pure melt by a phase-field model using an adaptive computation domain. J Braz Soc Mech Sci Eng 33(2):125–130
44. Flores BE (1986) A pragmatic view of accuracy measurement in forecasting. Omega 14(2):93–98
45. Gawin D, Pesavento F, Koniorczyk M, Schrefler BA (2020) Poro-mechanical model of strain hysteresis due to cyclic water freezing in partially saturated porous media. Int J Solids Struct
46. Ghadiani SR (2005) A multiphasic continuum mechanical model for design investigations of an effusion-cooled rocket thrust chamber. In: Ph.D. thesis, University of Stuttgart, University of Stuttgart
47. Gilpin RR (1980) A model for the prediction of ice lensing and frost heave in soils. Water Resour Res 16(5):918–930
48. Graf T, Ehlers W (2003) On the theoretical and numerical modelling of unsaturated soil. Pamm 3(1):278–279
49. Heider Y (2012) Saturated porous media dynamics with application to earthquake engineering. In: Ph.D. thesis, University of Stuttgart, University of Stuttgart, ISBN: 3-937399-22-4
50. Heider Y, Avci O, Markert B, Ehlers W (2014) The dynamic response of fluid-saturated porous materials with application to seismically induced soil liquefaction. Soil Dyn Earthquake Eng 63:120–137
51. Heider Y, Markert B (2017) A phase-field modeling approach of hydraulic fracture in saturated porous media. Mech Res Commun 80:38–46
52. Heider Y, Reiche S, Siebert P, Markert B (2018) Modeling of hydraulic fracturing using a porous-media phase-field approach with reference to experimental data. Eng Fract Mech 202:116–134
53. Heider Y, Sun WC (2020) A phase field framework for capillary-induced fracture in unsaturated porous media: drying-induced vs. hydraulic cracking. Comput Methods Appl Mech Eng 359:112647
54. Hirt CW, Nichols BD (1981) Volume of fluid (VOF) method for the dynamics of free boundaries. J Comput Phys 39(1):201–225
55. Horiguchi K (1977) Frost heave character in freezing of powder materials. Int Symp Frost Action Soils, pp 67–75
56. Kang Y, Liu Q, Huang S (2013) A fully coupled thermo-hydro-mechanical model for rock mass under freezing/thawing condition. Cold Regions Sci Technol 95:19–26
57. Kaplar CW (1970) Phenomenon and mechanism of frost heaving. Highway Res Record, 304
58. Karma A, Rappel WJ (1996) Phase-field method for computationally efficient modeling of solidification with arbitrary interface kinetics. Phys Rev E Stat Phys Plasmas Fluids Related Interdiscip Topics 53(4):R3017–R3020
59. Kobayashi R (1993) Modeling and numerical simulations of dendritic crystal growth. Phys D Nonlinear Phenomena 63(3–4):410–423
60. Konrad J (1987) Procedure for determining the segregation potential of freezing soils. Geotech Testing J 10(2):51–58
61. Konrad J-M (1989) Influence of cooling rate on the temperature of ice lens formation in clayey silts. Cold Regions Sci Technol 16(1):25–36
62. Konrad J-M, Morgenstern N (1982a) Effects of applied pressure on freezing soils. Can Geotech J 19(4):494–505
63. Konrad J-M, Morgenstern N (1982b) Prediction of frost heave in the laboratory during transient freezing. Can Geotech J 19(3):250–259
64. Konrad J-M, Morgenstern NR (1980) A mechanistic theory of ice lens formation in fine-grained soils. Can Geotech J 17(4):473–486
65. Konrad J-M, Morgenstern NR (1981) The segregation potential of a freezing soil. Can Geotech J 18(4):482–491
66. Konrad J-M, Nixon J (1994) Frost heave characteristics of a clayey silt subjected to small temperature gradients.Cold Regions Sci Technol 22(3):299–310
67. Lai Y, Pei W, Zhang M, Zhou J (2014) Study on theory model of hydro-thermal-mechanical interaction process in saturated freezing silty soil. Int J Heat Mass Transf 78:805–819
68. Li N, Chen F, Xu B, Swoboda G (2008) Theoretical modeling framework for an unsaturated freezing soil. Cold Regions Sci Technol 54(1):19–35
69. Loch J, Kay B (1978) Water redistribution in partially frozen, saturated silt under several temperature gradients and overburden loads. Soil Sci Soc Am J 42(3):400–406
70. Markert B (2007) A constitutive approach to 3-d nonlinear fluid flow through finite deformable porous continua. Transp Porous Media 70(3):427–450
71. Markert B (2011) Coupled thermo- and electrodynamics of multiphasic continua. Adv Extend Multifield Theories Continua. Springer, Berlin, pp 129–152
72. Markert B (2013) A survey of selected coupled multifield problems in computational mechanics. J Coupled Syst Multiscale Dyn 1(1):22–48
73. Markert B, Heider Y, Ehlers W (2010) Comparison of monolithic and splitting solution schemes for dynamic porous media problems. Int J Numer Methods Eng 82:1341–1383
74. Mauro A, Normino G, Cavuoto F, Marotta P, Massarotti N (2020) Modeling artificial ground freezing for construction of two tunnels of a metro station in napoli (italy). Energies 13(5)
75. Merkel G, Povinelli R, Brown R (2018) Short-term load forecasting of natural gas with deep neural network regression. Energies 11:2008
76. Mikkola M, Hartikainen J (2001) Mathematical model of soil freezing and its numerical implementation. Int J Numer Methods Eng 52(56):543–557
77. Ming F, Li DQ (2015) Experimental and theoretical investigations on frost heave in porous media. Math Prob Eng 2015:1–9
78. Moelans N, Blanpain B, Wollants P (2008) An introduction to phase-field modeling of microstructure evolution. Calphad Comput Coupling Phase Diag Thermochem 32(2):268–294
79. Na SH, Sun WC (2017) Computational thermo-hydro-mechanics for multiphase freezing and thawing porous media in the finite deformation range. Comput Methods Appl Mech Eng 318:667–700
80. Neaupane KM, Yamabe T (2001) A fully coupled thermo-hydro-mechanical nonlinear model for a frozen medium. Comput Geotech 28(8):613–637
81. Niggemann K (2020) Investigation of frost heave considering the boundary conditions of artificial ground freezing. Transp Soil Eng Cold Regions, Vol 2. Springer, Berlin, pp 273–283
82. Nishimura S, Gens A, Olivella S, Jardine RJ (2009) THM-coupled finite element analysis of frozen soil: formulation and application. Géotechnique 59(3):159–171
83. Nixon JF (1992) Discrete ice lens theory for frost heave beneath pipelines. Can Geotech J 29(3):487–497

84. Noii N, Aldakheel F, Wick T, Wriggers P (2020) An adaptive global-local approach for phase-field modeling of anisotropic brittle fracture. Comput Methods Appl Mech Eng 361
85. Obaid A, Turek S, Heider Y, Markert B (2017) A new monolithic Newton-multigrid-based FEM solution scheme for large strain dynamic poroelasticity problems. Int J Numer Methods Eng 109(8):1103–1129
86. Oesterreich M (2015) Application of descriptive models to forecasting seasonal time series with gaps. Ekonometria
87. O'Neill K (1983) The physics of mathematical frost heave models: a review. Cold Reg Sci Technol 6(3):275–291
88. O'Neill K, Miller RD (1985) Exploration of a rigid ice model of frost heave. Water Resour Res 21(3):281–296
89. Osher S (2001) Book Review: Level set methods and fast marching methods: evolving interfaces in computational geometry, fluid mechanics, computer vision, and materials science. Math Comput 70(233):449–451
90. Padilla CA, Patil SP, Heider Y, Markert B (2017) 3D modelling of brittle fracture using a joint all-atom and phase-field approach. GAMM Mitteilungen 40(2):91–101
91. Patil SP, Heider Y (2019) A review on brittle fracture nanomechanics by all-atom simulations. Nanomaterials 9(7):1050
92. Penner E (1986) Aspects of ice lens growth in soils. Cold regions science and technology 13(1):91–100
93. Penner E, Ueda T (1977) The dependence of frost heaving on load application-preliminary results. Proc Int Symp Frost Action Soils 1:92–101
94. Pillai U, Heider Y, Markert B (2018) A diffusive dynamic brittle fracture model for heterogeneous solids and porous materials with implementation using a user-element subroutine. Comput Mater Sci 153:36–47
95. Provatas N, Elder K (2010) Phase-field methods in materials science and engineering. Wiley-VCH Verlag GmbH & Co, KGaA, Weinheim, Germany
96. Rempel AW (2010) Frost heave. J Glaciol 56(200):1122–1128
97. Rempel AW, Wettlaufer JS, Worster MG (2004) Premelting dynamics in a continuum model of frost heave. J Fluid Mech 498(498):227–244
98. Ricken T, Bluhm J (2010) Modeling fluid saturated porous media under frost attack. GAMM Mitteilungen 33(1):40–56
99. Ricken T, Bluhm J (2014) Modeling of liquid and gas saturated porous solids under freezing and thawing cycles. In: Schanz T, Hettler A (eds) Aktuelle Forschung in der Bodenmechanik 2013. Springer, Berlin, pp 23–42
100. Schnaars SP (1986) Long-range forecasting: from crystal ball to computer. J Scott Armstrong, 2nd edn. Wiley, New York, (1985) 22.95 (paper), pp 689. Int J Forecast 2(3):387–390
101. Sedlacek G, Miehe A, Libreros A, Heider Y (2012) Geotechnical stability of gravity base foundations for offshore wind turbines on granular soils. In: Proceedings of the international conference on offshore mechanics and arctic engineering—OMAE, vol 4. American Society of Mechanical Engineers, pp 57–63
102. Sheng D, Axelsson K, Knutsson S (1995) Frost heave due to ice lens formation in freezing soils: 1. theory and verification. Hydrol Res 26(2):125–146
103. Sheng D, Zhang S, He Z (2014) Assessing frost susceptibility of soils. J Rock Mech Eng 33(3):594–605
104. Spaans EJA, Baker JM (1996) The soil freezing characteristic: its measurement and similarity to the soil moisture characteristic. Soil Sci Soc Am J 60(1):13–19
105. Steinbach I (2009) Phase-field models in materials science. Modell Simul Mater Sci Eng 17(7)
106. Sun W (2015) A stabilized finite element formulation for monolithic thermo-hydro-mechanical simulations at finite strain. Int J Numer Methods Eng 103(11):798–839
107. Sweidan AH, Heider Y, Markert B (2020) Modeling of PCM-based enhanced latent heat storage systems using a phase-field-porous media approach. Contin Mech Thermodyn 32:861–882
108. Sweidan AH, Heider Y, Markert B (2020) A unified water/ice kinematics approach for phase-field thermo-hydro-mechanical modeling of frost action in porous media. Comput Methods Appl Mech Eng 372:113358
109. Taber S (1929) Frost heaving. J Geol 37(5):428–461
110. Taber S (1930) The mechanics of frost heaving. J Geol 38(4):303–317
111. Thomas HR, Cleall P, Li YC, Harris C, Kern-Luetschg M (2009) Modelling of cryogenic processes in permafrost and seasonally frozen soils. Geotechnique 59(3):173–184
112. Tounsi H, Rouabhi A, Tijani M, Guérin F (2019) Thermo-hydro-mechanical modeling of artificial ground freezing: application in mining engineering. Rock Mech Rock Eng 52(10):3889–3907
113. Truesdell C (1984) The origins of rational thermodynamics. Springer, New York, NY
114. van Genuchten MT (1980) A closed-form equation for predicting the hydraulic conductivity of unsaturated soils. Soil Sci Soc Am J 44(5):892–898
115. Wang SL, Sekerka RF, Wheeler AA, Murray BT, Coriell SR, Braun RJ, McFadden GB (1993) Thermodynamically-consistent phase-field models for solidification. Phys D Nonlinear Phenomena 69(1–2):189–200
116. Warren JA, Boettinger WJ (1995) Prediction of dendritic growth and microsegregation patterns in a binary alloy using the phase-field method. Acta Metallurgica Et Materialia 43(2):689–703
117. Wilen L, Dash J (1995) Frost heave dynamics at a single crystal interface. Phys Rev Lett 74(25):5076
118. Xia D, Arenson LU, Biggar KW, Sego DC (2005) Freezing process in devon silt-using time-lapse photography. In 58th Canadian geotechnical conference, saskatoon, saskatchewan
119. Zaeem MA, Yin H, Felicelli SD (2012) Comparison of cellular automaton and phase field models to simulate dendrite growth in hexagonal crystals. J Mater Sci Technol 28:137–146
120. Zhao Y, Zhao CY, Xu ZG (2018) Numerical study of solid-liquid phase change by phase field method. Comput Fluids 164:94–101
121. Zhao Y, Zhao CY, Xu ZG, Xu HJ (2016) Modeling metal foam enhanced phase change heat transfer in thermal energy storage by using phase field method. Int J Heat Mass Transf 99:170–181
122. Zhou B, Heider Y, Ma S, Markert B (2019) Phase-field-based modelling of the gelation process of biopolymer droplets in 3D bioprinting. Comput Mech 63(6):1187–1202
123. Zhou J, Li D (2012) Numerical analysis of coupled water, heat and stress in saturated freezing soil. Cold Reg Sci Technol 72:43–49
124. Zhou MM, Meschke G (2013) A three-phase thermo-hydro-mechanical finite element model for freezing soils. Int J Numer Anal Methods Geomech 37(18):3173–3193
125. Zhou M-M, Meschke G (2014) Numerical modeling of artificial ground freezing: multiphase modeling and strength upscaling. Ground improvement and geosynthetics. American Society of Civil Engineers, Reston, VA, pp 209–219
126. Zienkiewicz OC, Taylor RL (2000) The finite element method volume 1: the basis, vol 1. Butterworth-Heinemann, Oxford, Boston, 5th edn.

Publisher's Note Springer Nature remains neutral with regard to jurisdictional claims in published maps and institutional affiliations.

B Paper #2

Influence of freezing directions on ice lens formations in soils

Niggemann, K., Ziegler, M., Fuentes, R. (2024): Influence of freezing directions on ice lens formations in soils. Acta Geotechnica. https://doi.org/10.1007/s11440-024-02259-2

Acta Geotechnica
https://doi.org/10.1007/s11440-024-02259-2

REVIEW PAPER

Influence of freezing directions on ice lens formations in soils

K. Niggemann[1] · M. Ziegler[2] · R. Fuentes[1]

Received: 29 August 2022 / Accepted: 9 January 2024
© The Author(s) 2024

Abstract
This research work presents a comprehensive experimental study of frost heave in a fine-grained material to investigate the effects of top freezing (TF) and bottom freezing (BF) mechanisms with ice lens formation. A novel test device was built to investigate artificial ground freezing (AGF)-related temperature and load boundary conditions. This paper includes 62 frost heave experiments and test observations up to 10 days. The long test duration allows a precise examination of ice lens growth during thermal steady state when the frost line remains largely stable and the ice lens grows. This state corresponds to the holding phase of a practical in situ AGF implementation where the cooling is used to maintain the frozen body thickness. The freezing observations show that BF heaving is larger than TF heaving in most cases. This is caused by the more favorable hydraulic conditions caused by gravitational effects and vertical cracking that occurs during ice lens formation due to suction. This facilitates water accumulation at the ice lens. An applied load reduces the differences between BF and TF conditions beyond a certain value which corresponds to an overburden capable of preventing the formation of the longitudinal cracks.

Keywords Artificial ground freezing · Bottom freezing · Experimental study · Frost heave · Ice lenses · Top freezing

1 Introduction

The method of artificial ground freezing (AGF) was adapted to Civil Engineering works from the mining industry, after the engineer Herman Poetsch invented it in 1883 [1]. The application of AGF to support unstable soils and systems became a very popular method in the last decades, especially for the development of underground infrastructure in inner-city areas. It is an efficient method with a double temporary soil supporting and waterproofing function. However, freezing is also associated to frost-induced soil deformations and frost heave that can cause damage to pipelines, pavements as well as foundations and buildings. The pore water volume expands by 9% approximately during freezing [2]. Depending on the saturation degree and the hydraulic conductivity, a part of the water can be drained off during freezing. However, in more frost sensitive soils, like silt or clay, the water cannot be expelled during rapid cooling and freezes in situ due to their small hydraulic conductivity. Moreover, pure ice layers (ice lenses) can form in these fine-grained soils which can grow to several centimeters in height depending on the boundary conditions. As water is, by definition, available in soils where AGF is applied, this source of water supports ice lens formation.

One of the first ice lens observations was done by Taber [3, 4]. His freezing studies in different soils pointed out that not only capillary forces pull the water to the ice lens but also thin water films between the solid ice and the grains under high tension led to water movement during freezing. He showed that water migrates from warmer to colder regions and accumulates in thick ice layers, leading to enormous heaving. Ruckli [5] described that ice and the soil grains are enclosed by an adsorption film, with the highest density at the surface of the solid soil grain. The film thickness depends on the load pressure, so increasing load leads to a decreasing film thickness. The presence of the adsorption film was confirmed experimentally by Wilen and

✉ K. Niggemann
niggemann@gut.rwth-aachen.de

M. Ziegler
ziegler@zai-ingenieure.de

R. Fuentes
raul.fuentes@gut.rwth-aachen.de

[1] Institute of Geomechanics and Underground Technology, RWTH Aachen University, Aachen, Germany

[2] Ziegler und Aulbach Ingenieurgesellschaft GmbH (Formerly RWTH Aachen University), Aachen, Germany

Published online: 28 February 2024

Dash [6] by studying the liquid flow in a surface-melted layer of ice. Martin [7] introduced a theory of rhythmic ice banding under unsteady heat flow conditions. The ice crystals grow by water transport from adjacent soil. With decreasing permeability in the unfrozen zone, ice lens growth stops, and a new ice lens forms when the nucleation temperature is reached at another level. Ice nucleation begins at a temperature lower than the temperature at which ice crystals grow significantly (frost line). The freezing point depression is primary affected by capillarity, adsorption and dissolved salts in the soil water [8–10]. The area between ice lens and frost line is called frozen fringe which contains unfrozen water films around the soil particles and ice in thermodynamic equilibrium [11–19]. Once an ice lens is formed, water from the unfrozen region is drawn into the frozen fringe to maintain the film thickness or thermodynamic equilibrium. The largest ice lens forms when the frost line stops moving because water can be drawn without thermal restriction. This lens is referred to as the decisive ice lens in connection to its greater thickness. Since thermal processes are still occurring during ice lens formation, this phase is also called the quasi-steady state [20].

The thickness of the ice lenses depends on the particle size [21, 22], pore size [23, 24], water availability [25, 26], cooling rate [22, 27, 28] and surface load [4, 10, 29, 30].

In very fine soils, cracking was observed during freezing due to shrinkage processes near the ice lens [31–34]. Vertical cracks arise near the ice lens in the frozen fringe which are linked together, forming columns with a polygonal cross section. These formed polygons lead to an increase in density and permeability. In difference to horizontal ice lenses, the vertical cracks do not significantly change their thickness with time. Even if the small cracks are ice-filled in the frozen fringe, they lead to better water flow to the ice lens via thin water films.

The initiation of ice lenses can be described by temperature [12] or stress conditions [15, 35]. Konrad and Morgenstern [12] introduced a segregation temperature where a new ice lens starts to form. The temperature-dependent critical permeability prevents further water migration toward the frozen soil. O'Neill and Miller [15, 35] introduced the secondary frost heave model. Ice lens initiation occurs by a pressure-dependent approach, when the sum of water and ice pressure in the frozen fringe equals the overburden pressure. These concepts, in their origin or adjusted form, are widely used to explain and predict frost heave with ice lens formation, e.g., [16, 36–42]. A newer concept to define the beginning of ice lens formation is formulated by Style et al. [43] declaring ice lens initiation where supercooling reaches maximum. Zhou and Li [44] using a concept of a separating void ratio, e.g., applicated by Sweidan et al. [45]. The separating void ratio is equal to the void ratio in its most uncompacted status and enables pore ice to connect.

During ice lens formation with water migration and accumulation, hydrothermal properties and the microstructure changes continuously which causes complex mass and energy transfer [46]. Frost heave models have been used to simulate processes of ice lens formation. Ji et al. [47] classified numerical models into the mechanistic frost heave model and the physical field models. The mechanistic frost heave model explains the mechanism of frost heaving and the initiation of discrete ice lenses within the frozen fringe. These models consider the interfacial pressure between water and solid which causes freezing suction [13, 15, 37, 47–51]. Physical field models focus on the moisture, mechanical and temperature field prediction. Freezing expansion is considered by an increasing finite volume of the soil [45, 52–55]. Analytical solutions of frost heave calculation were proposed by Cai et al. [56, 57], using the stochastic medium theory for heave calculation, and by Niggemann et al. [58], using a semi-analytical approach to achieve properties of the frozen fringe for a multifaceted application.

AGF and natural soil freezing in fine material present similar soil freezing mechanisms, including the formation of ice lenses. However, the different boundary conditions present in both scenarios on the total heave and ice lens formation have not been fully presented to date. The freezing direction is of interest and shows different characteristics as explained in the next section and observed from the literature presented in Table 1. In AGF, freezing occurs in multiple directions (e.g., tunnel cross section), where the largest surface heave occurs due to upward freezing (Fig. 1) using brine at temperatures of ≈ -35 °C [59]. Considering seasonally soil freezing in natural conditions, the frost penetrates the soil from the top downward due to subzero temperatures, a condition that may also apply to AGF, but usually at temperatures above -15 °C [60]. The different temperatures are important as larger temperature gradients are known to reduce ice lens formation during frost penetration.

At natural freezing, the investigations focus on frost heave during ongoing frost penetration. In that case the frost line, where ice lenses form, is a moving boundary and the ice lens formation is restricted by the freezing velocity. An apparently infinite ice lens can form when the frost line maintains at a specific position due to thermal (quasi-) equilibrium. (There are still thermal processes due to ice lens formation, but of minor interest concerning frost penetration.) This quasi-steady state is comparable with the holding phase at AGF, where the thickness of the frozen body is only preserved but over a longer time period. Assuming infinite ice lens growth, the quasi-steady state at the AGF is the governing state to be considered.

Table 1 Frost heave test conditions from the literature

	Specimen size [cm]	Soil type	Freezing direction	Freezing temperature/-conditions	Load [kPa]
Kaplar [61]	h=15.2 d_{top}=14.6 d_{bottom}=14.0	Gravelly silty sand	TF	Near 0 °C; Frost Penetration: 0.6–1.3 cm/d	3.4
Penner and Ueda [62]	h=10.2 d=10.2	Silty sand, sandy silt, clayey silt	BF	up to −2 °C	consol.: 392–490 freezing test: 49–490
Loch and Kay [8]	h=7.0–7.4 d=3.7	New Hampshire Silt	BF	up to −7 °C	7.7–65.2
Konrad and Morgenstern [12]	h=25.0 d=10.0	Devon Silt	TF	−2.5 to −6.2 °C	consol.: 210
Konrad and Morgenstern [64]			TF	−3.5 to −6.0 °C	freezing test: –
Konrad and Morgenstern [65]			BF	$gradT_f$= 0.63–1.11 °C/cm	consol.: 210 freezing test: 45–400
Jin et al. [63]	h=10.0 d=10.0	Joomunjin Sand and Kaolinite, weathered granite	BF	−8 to −9.5 °C	1.62

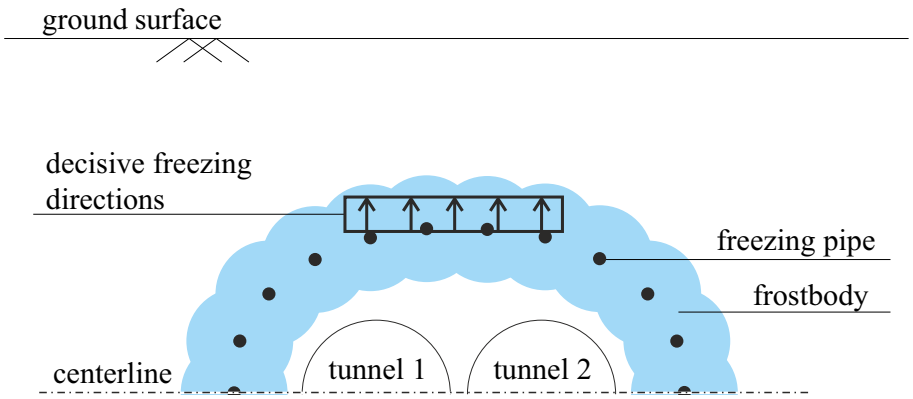

Fig. 1 Freezing directions at AGF of a tunnel cross section

In the last decades, many frost heave tests were carried out by several researchers who investigated the frost sensitivity of different soils as well as the influences of freezing temperatures and/or loads on frost heave, e.g., [12, 27, 61–65]. Table 1 summarizes the test conditions. The dimensions of the test cylinders vary in height h between 7 and 25 cm and in diameter d between 3.7 and 14.6 cm. Kaplar [61] used a conical test cylinder to reduce friction between the specimen and the cylinder during frost heaving while freezing the sample from the top downward (top freezing—TF). Others have used freezing conditions from the bottom upward to reduce friction (bottom freezing—BF).

The literature shows frost heave observations using different freezing directions to improve the technical implementation (cf. Table 1), frost heave tests and models considering multidirectional freezing [66, 67], or permeability investigations due to direction dependent freeze–thaw cycles [68]. But a systematic study to compare the

heave development of the two main freezing directions associated to natural and artificial freezing is missing. Experimental frost heave studies are usually conducted with standard test devices investigating one freezing direction. Therefore, this study focuses on the frost heave development using a test device which allows a simultaneous investigation of two samples, one freezes from the top, the other from the bottom. This enables a direct comparison of heaving under identical thermal or load conditions.

Hence, we quantify heave differences for top-down freezing (TF) and bottom-up (BF) freezing in terms of AGF-related boundaries concerning thermal and load conditions, which are different to natural soil freezing conditions. We carried out 62 frost heave experiments in a novel frost heave apparatus to ensure identical boundary conditions. In comparison to common frost heave tests, a long test duration of 10 days was selected because it is necessary to investigate the thermal steady state in which the largest ice lens is formed. These observations are also novel, especially in combination with different boundary conditions.

For this purpose, basics on the experimental design, the instrumentation, the test material and the testing program are given in Sect. 2. The following Sect. 3 explains the test evaluation, which includes necessary information for the result analysis in Sect. 4. Finally, the results are briefly summarized, and conclusions are given in Sect. 5.

2 Experimental design and test description

2.1 Setup

The new experimental setup is shown in Fig. 2, and detailed descriptions of specific elements and instrumentation are given in Table 2. The dimensions of the cylindrical specimen are 25 cm in diameter and 20 cm in height. The test cylinder consists of eight PVC ring elements, with a thickness of 2.5 cm, connected by a tongue and groove system to prevent lateral displacement. The ring elements lying on top of each other were sealed by a rubber ring so that no water leaks out of the unfrozen soil. For specimen installation, the rings were additionally screwed together. During the freezing test, the ring elements can be pulled and move apart vertically, so that the soil samples do not undergo any frictional resistance due to the vertical expansion. The top and the bottom of the samples, respectively, were cooled by a freezing element ①. The freezing temperature was controlled by a temperature sensor placed in the freezing element. A water reservoir ② was connected to a filter plate ③ at the warm side of the sample, providing a constant water supply under atmospheric pressure for ice lens formation. In the BF tests, the position of the water reservoir placed at the top of the sample was adjusted during the freezing test to compensate for the vertical specimen expansion. The warm end of the soil sample was additionally heated by a heating plate ④ to avoid freezing of the overall sample. The test cylinders were covered with a Styrodur insulation (BASF, Germany). All tests were carried out in a climatic chamber with a constant temperature of 15 °C (initial temperature of the soil before freezing) and humidity of 40% to exclude influences such as seasonal fluctuations.

For the experimental study without considering overburden pressure (Fig. 2a), a load results only from the apparatus elements (i.e., the porous heating plate for BF and the freezing plate for TF) and an additional static 10 kg load to ensure a frictional connection between the plates and the sample. This results in a total load of p=3.6 kPa.

The test series considering overburden load (Fig. 2b) were carried out using a drive ⑤ to apply loads between 50 and 250 kPa to the sample from the top. After consolidation, the soil has settled in the test cylinder. Using an adapter (steel plate) ⑥ that was installed between the soil and the freezing element from the beginning, heat transfer from the freezing element into the soil by conduction was ensured during the whole test procedure. (The freezing element cannot enter the test cylinder due to connections.)

2.2 Instrumentation

For data recording, temperature sensors ⓐ are distributed over the sample height, see Fig. 2 and Table 2. After consolidation, the temperature sensors were placed into the soil sample through small openings in the ring elements. During frost heaving, the sensors move together with the ring elements. The vertical deformation was measured by displacement transducers that are connected to the temperature sensors ⓑ. The displacement transducers were attached to the ring elements that move vertically during the freezing process. For the data recording of the total uniaxial deformation at the top of the specimen, the same type of displacement transducer was used ©. This temperature and displacement monitoring allows the calculation of the freezing front velocity, which is important to distinguish between the thermal transient and steady state (cf. sub-Sect. 3.2.1). To determine the water inflow into the sample due to suction, the mass of the water supply was recorded by a load cell ⓓ. The load of the drive was controlled by a connected load cell ⓔ.

2.3 Test material and preparation

The test material was produced artificially to ensure an equal composition for all tests and, thus, to improve the repeatability and consistency of the results. With a liquid

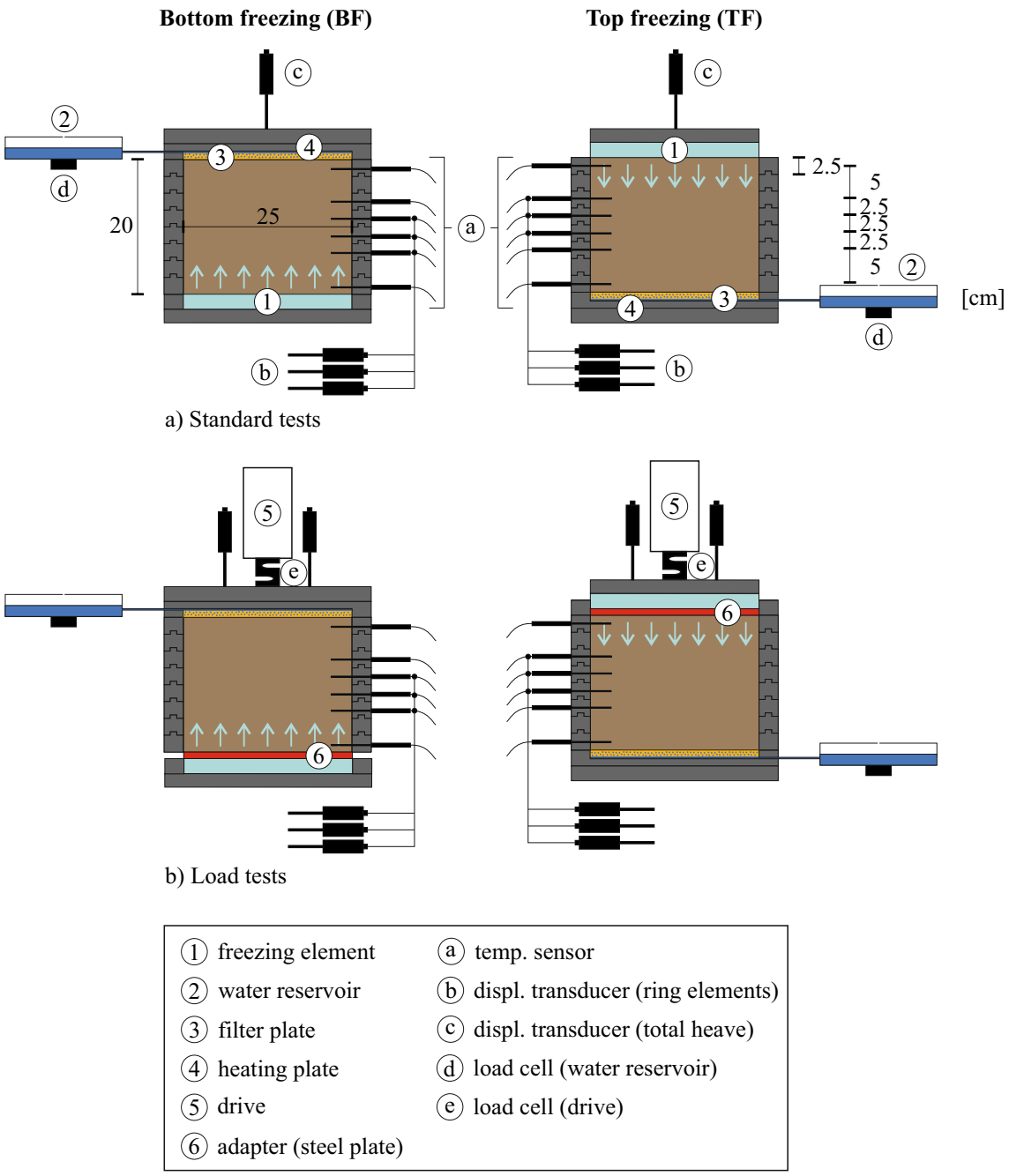

Fig. 2 Test setup for TF and BF, for **a** standard tests and **b** load tests

limit (LL) of 32.9% and a plasticity index (PI) of 14.5%, the soil can be classified as a lean clay (CL, Unified Soil Classification System). The grain size distribution can be found in [40]. The dry material was prepared with an initial mass water content of 20% to ensure a high saturation as well as an appropriate consistency, and subsequently stored for 24 h to ensure that the water can penetrate into the pores. Afterward, the initial water content of the soil was proved for each test by a drying procedure where the material is heated up to 105 °C for 4 days to determine the previous water content in the sample. The values of the initial mean mass water content $\bar{x}_w$ and saturation $\bar{x}_{Sr}$, and standard deviation σ_w and σ_{Sr} for the 32 TF and 30 BF tests, presented in Table 3, confirm the good repeatability of the process.

The hydraulic conductivity of the soil was tested several times with the same initial conditions of porosity and saturation degree as the test specimen. The mean value is $1.3 \cdot 10^{-10}$ m/s ($\sigma_k = 5.3 \cdot 10^{-11}$ m/s) or $1.8 \cdot 10^{-17}$ m^2 ($\sigma_K = 7.0 \cdot 10^{-18}$ m^2). The soil was compacted in eight layers in the

Table 2 Description of setup elements and instrumentation

Name	Function	Description
① freezing element	sample cooling	connected to circulation thermostat (CC-508, Huber Kaeltemaschinenbau AG, Germany)
		refrigerant: silicone oil (Thermofluid M60.115/200.05, Huber Kaeltemaschinenbau AG, Germany)
② water reservoir	water supply	connected to a filter plate ③
		large diameter (d=29 cm)
		o sufficient water availability
		o very low water head of approx. 1 cm
③ filter plate	water distribution	connected to the heating plate ④
④ heating plate	sample heating	connected to a warming circulation thermostat (Kiss 104A, Huber Kaeltemaschinenbau AG, Germany)
		circulating fluid: water
⑤ drive	applying load	load application by cylinder connected to electric spindle (Spindeltrieb 10 kN+SMS 94, Pero, Germany)
		deformation-controlled loading (0.5 mm/min) until the required load was applied
		constant load during consolidation and freezing phase
		automatic load control every 60 s
⑥ steel plate	adapter for load tests	d=1 cm (equal in all load tests depending on the pretested settlement after maximum loading with 250 kPa)
ⓐ temp. sensors	temperature measurement	MWT1/10, TMH GmbH, Germany
		measurement precision 1/10 DIN B: $\Delta T = \pm(1/10(0.30°C + 0.005\ T))$; T=temperature [°C]
ⓑ displacement transducer	vertical displacement measurement	LRW2-C-50, WayCon Positionsmesstechnik GmbH, Germany
	(ring elements)	measurement precision:±0.1%
ⓒ displacement transducer	vertical displacement measurement	LRW2-C-50, WayCon Positionsmesstechnik GmbH, Germany
	(total heave)	measurement precision:±0.1%
ⓓ load cell	load measurement	for calculation of the water intake into the soil sample
	(water reservoir)	S2, HBM, Austria
		measurement precision:±0.02%
ⓔ load cell	load measurement (drive)	load control of the drive KDB, Pero, Germany
		measurement precision:±0.02%

Table 3 Mean value $\bar{x}$ and standard deviation σ of initial water content w and saturation S_r for TF and BF

	$n[-]$	$\bar{x}_w[\%]$	$\sigma_w[\%]$	$\bar{x}_{Sr}[\%]$	$\sigma_{Sr}[\%]$
TF	32	20.37	0.55	91.70	2.60
BF	30	20.33	0.60	91.30	2.73

test cylinder by 40 blows with a 4.5 kg proctor hammer. The mean moist density achieved is 2.022 g/cm^3 (σ_ρ = 0.017 g/cm^3).

The prepared soil in the test cell was stored for approx. 24 h in the climatic chamber at 15 °C to ensure a uniform material temperature at the beginning of each test. The material temperature was monitored by the temperature sensors already installed. After acclimatization, when all sensors reached 15 °C, the freezing process started. Simultaneously, the tempering process began on the warm side of the specimen. Depending on the thermal boundary conditions, one freezing test took up to 2 days to reach thermal quasi-steady state conditions. Afterward, the test ran about 8 more days to provide a long thermal steady state phase.

2.4 Testing program

The main task of the experimental program is the observation of TF versus BF under variation of the following parameters:

- absolute freezing temperature T_f
- temperature gradient in the frozen area $gradT_f$
- external load p

Additionally, a test was carried out with *restricted water supply* W_{ws0} at a freezing temperature of $T_f = -10$ °C to study the effect of no additional available water.

Table 4 summarizes the main values of the tests. The parameter $T_{c,ts}$ describes the recorded cold side temperature during steady-state conditions measured by the nearest temperature sensor to the cold edge (cf. Fig. 2). Similarly, $T_{w,ts}$ describes the measured temperature on the warm side. A fully water supply by the external reservoir is given by

Table 4 Main values of the experimental parameter study

Tested parameter	T_f [°C]	$T_{c,ts}$ [°C]	$T_{w,ts}$ [°C]	W_{ws} [%]	$gradT_f$ [°C/cm]	p [kPa]	n_{TF} [−]	n_{BF} [−]
T_f [°C]	−5	−4.3	10.4	100	1.0	0	3	3
	−7.5	−6.9	8.6				2	2
	−10	−9.0	8.0				6	4
	−12.5	−11.3	6.9				1	1
	−15	−13.9	5.4				4	4
	−17.5	−16.0	4.6				1	1
W_{ws0}[−]	−10	−9.2	6.9	0	1.0	0	1	1
$gradT_f$[°C]	−15	−13.5	13.6	100	1.5	0	3	3
	−7	−6.5	5.2		0.8		3	3
p* [kPa]	−12.5	−12.2	6.0	100	1.0	50	1	1
		−12.2	5.5			100	1	1
		−12.4†	5.2			150	1	1
		−12.4†	4.7			200	1	1
		−12.5†	5.0			250	1	1
	−5	−4.9	9.8			50	1	1
		−5.0†	9.2			250	1	1
	−10	−9.6†	6.7			250	1	1

*placement of temperature sensors after consolidation

†extrapolated values on cold side; due to consolidation the nearest cold side temperature sensor could not be placed

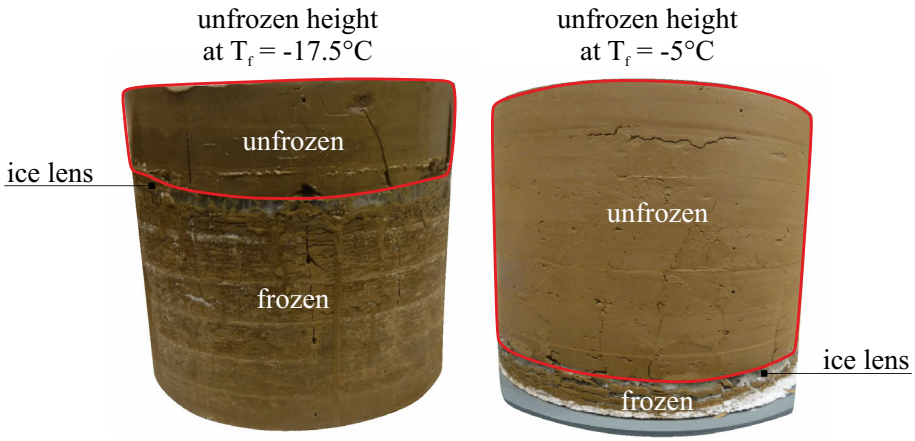

Fig. 3 Unfrozen soil part/flow path (red box) for a freezing temperature of −17.5 °C (left) and −5 °C (right), BF (color figure online)

W_{ws} = 100%, whereas W_{ws} = 0% means no water supply from the reservoir. The values for n_{TF} and n_{BF} correspond to the number of experiments for one parameter variation. Where more than one test was performed, the figures are mean values for that single parameter combination.

The *absolute freezing temperature* T_f controls the frost penetration as show in Fig. 3 for a BF test. Values of T_f between −5 and −17.5 °C were imposed using a temperature sensor placed in the freezing element as control. On the warm side, the water is heated up to 25 °C that prevents freezing of the whole sample. (Please note the actual temperature of the warm side is lower than 25 °C due to the higher cooling capacity in the system.) The temperature gradients along the frozen or unfrozen soil remain constant after reaching thermal quasi-steady state conditions.

To investigate the influence of different *temperature gradients* $gradT_f$ in the frozen area on frost heave and ice lens formation, the cold and warm side temperatures were adjusted to reach the same frost penetration depth (in the center of the sample) at different freezing and heating

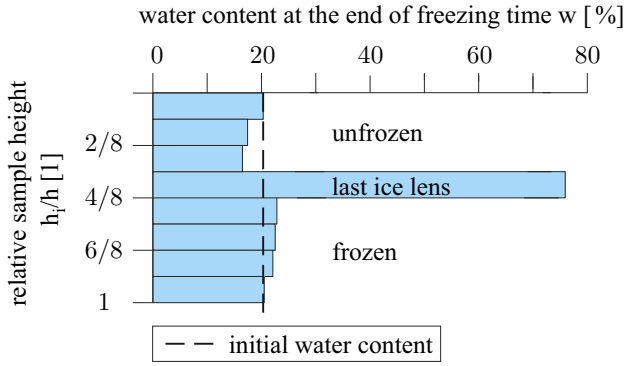

Fig. 4 Soil water distribution after freezing (T_f = −10 °C) for BF

temperatures. The resulting temperature gradients are 0.8 °C/cm, 1.0 °C/cm and 1.5 °C/cm (see Table 4).

For the tests with *external load p*, the soil samples were loaded between 50 and 250 kPa, 50 kPa intervals, from the top of the sample, corresponding to overburdens of approximately 2.6 m, 5.3 m, 7.9 m, 10.5 m and 13.2 m ($\rho_{soil} \approx 1.9$ g/cm^3).

3 Evaluation of experimental tests

3.1 Sample examination at the end of the freezing test

After each test, the sample was removed from the test cylinder and visually observed. Subsequently, the sample water content w was determined in the longitudinal direction by drying procedure (cf. subsection 2.3). For this purpose, the sample (total height h) was divided into 8 layers with a thickness of approx. $h_i \approx 2.5$ cm. (The final ice lens thickness was between ≈ 0.5 cm and ≈ 1.5 cm.) The results provide details about the water distribution in the soil sample after freezing. Figure 4 shows the water distribution at the end of BF with a freezing temperature of −10 °C as an example. (Others are provided in the Supplementary Material 1 and 2) With different freezing temperatures the position of the ice lens changes, but qualitatively the water distribution in the frozen and unfrozen part is very similar. In the frozen area, the water content slightly increases due to minor ice lens formation during transient freezing. In the unfrozen area close to the last ice lens, which is built under quasi-steady state conditions, the water content decreases. It indicates that soil water was drained off the area near the ice lens without a direct flow from the reservoir water through suction [69].

This effect is clarified by Fig. 5, which shows the measured reservoir water mass that is sucked into the soil sample as a proportion of the total water mass that is used for the ice lens formation. The dashed line indicates the pore water mass used for ice lens formation, calculated as the difference between the measured sucked water from the reservoir and the total water mass for ice lens formation. The latter is calculated as the ice lens heave (heave measurement) divided by the expansion factor of 1.09 due to phase change. At the beginning of ice lens formation, most of the sucked water comes from water-filled soil pores, because the water from the external reservoir is initially saturating air-filled pores before reaching an unrestricted flow to the ice lens. With time, most water for ice lens formation comes from the reservoir, but the initial water content at the growing ice lens cannot be restored, resulting in a final soil water distribution as shown in Fig. 4. The water near the growing ice lens drains of without sufficient water supply and a pattern cross section with openings growing along the unfrozen sample height is formed (Fig. 6).

The cracks were investigated after each freezing process (Fig. 6). This phenomenon of crack formation was also observed by other scientists, e.g., [31, 33] and [70], and it applies particularly to impermeable soils where greater suctions occur. The crack formation increases the water migration to the ice lens [34, 45, 71, 72].

The lower the freezing temperature the shorter it takes for the water from the reservoir to reach the ice lens and become dominant. With lower freezing temperatures and, therefore, a shorter unfrozen height or flow path, increasingly reservoir water is used for ice lens formation. The shorter flow path of the external water to the ice lens influences the hydraulic gradient, which is calculated by the pressure difference between ice lens and water reservoir and the flow path. Figure 5 shows that for BF, the supply of reservoir water is improved in comparison to TF which can be explained by longitudinal cracks along the unfrozen sample height that enhance the water supply by gravity at BF.

3.2 Evaluation of measured data

3.2.1 Determination of 0 °C isotherm

Figure 7 shows the recorded temperature and position over time for each temperature sensor used to calculate the moving frost line, or 0 °C isotherm. (Sensor positions are given in Fig. 2.)

This is important to calculate the temperature gradients in the frozen and unfrozen soil. The temperature distribution is also necessary for the definition of the thermal transient and quasi-steady states. Since the measured isotherms around 0 °C almost run parallel (cf. Fig. 7), the course of the 0 °C isotherm was used to define the onset of the quasi-steady state and, therefore, the ice lens formation. Figure 8 shows a calculated 0 °C isotherm position (a) and the corresponding

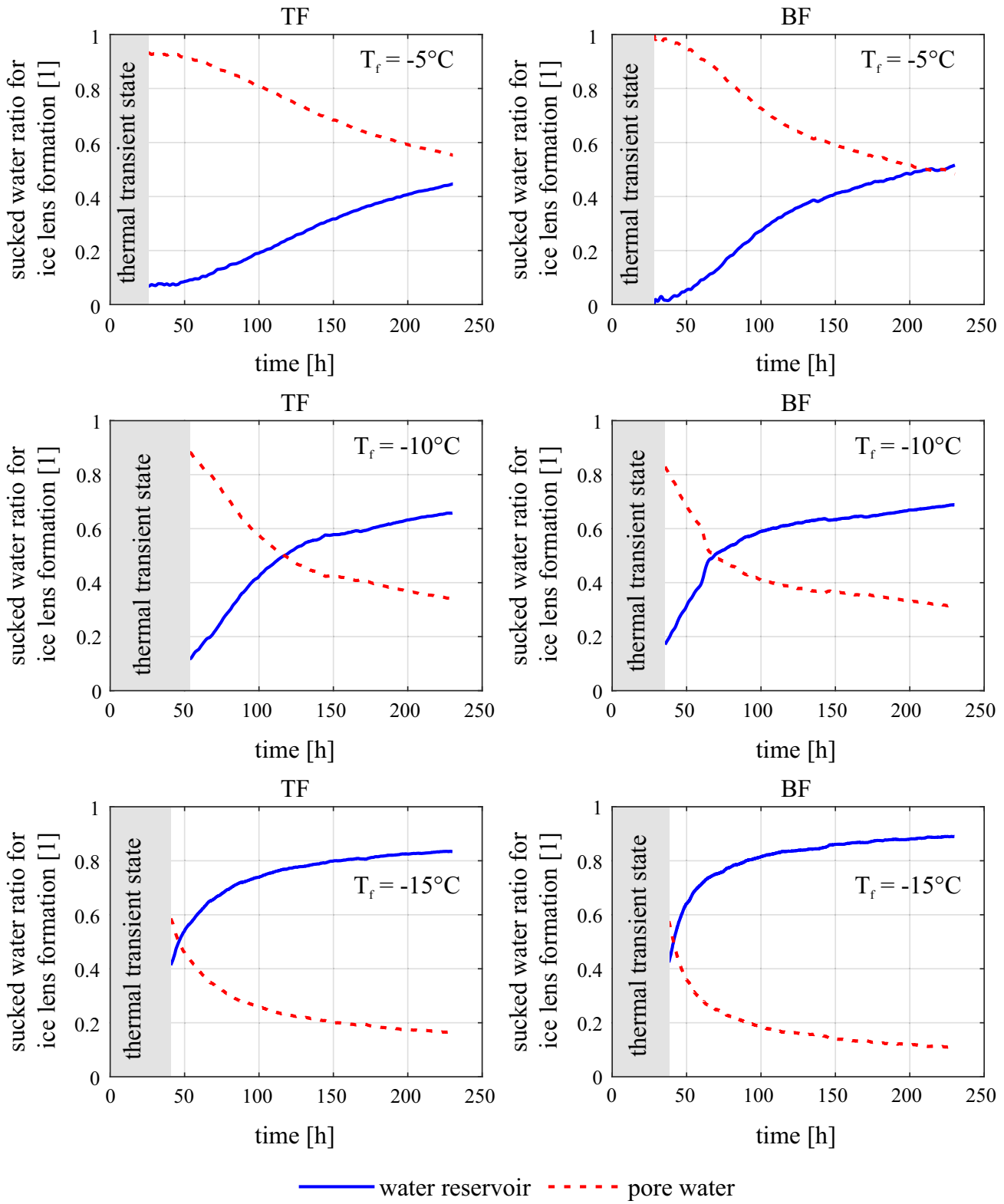

Fig. 5 Origin of the water for the formation of ice lenses at different freezing temperatures for TF and BF

frost penetration velocity v_{fp} (b). Figure 8b allows differentiating between the two distinct stages. When reaching thermal quasi-steady-state conditions, the frost penetration velocity approaches zero. The beginning of the thermal quasi-steady state is also defined by a critical frost penetration velocity $v_{fp,crit}$ less than 0.01 cm/h. From this point

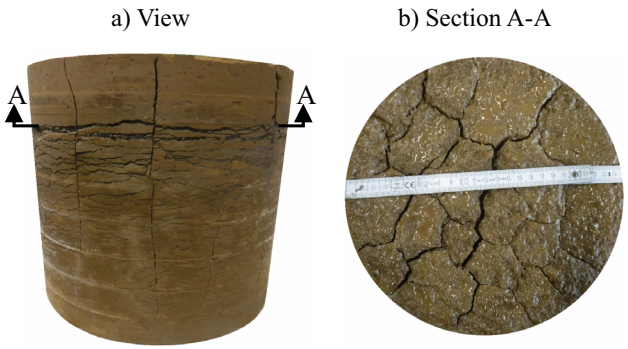

Fig. 6 Longitudinal crack formation of a BF sample

onward only ice lens growth occurs. Similar graphs apply to other temperatures and are presented in the Supplementary Material 3–6.

3.2.2 Determination of the heave proportions

Figure 9 shows the results of frost heave at thermal transient and quasi-steady state for BF at a freezing temperature of −10 °C. The total heave at thermal transient conditions is very low compared to the total heave at the thermal quasi-steady state, showing the importance of the thermal quasi-steady state for AGF. In the thermal transient state, the pore water heave h_{PW} is determined by the one-dimensional pore water expansion of 9% due to the frost penetration $x(t)$ using the porosity n and the saturation degree S_r as shown in Eq. 1. It is assumed that the water freezes at 0 °C and does not expand in air-filled voids.

$$h_{PW}(t) = 0,09 \cdot n \cdot S_r \cdot x(t) \tag{1}$$

The difference between total heave (h_{tot}) and pore water expansion (h_{PW}) is the calculated ice lens heave (h_{IL}). Consolidation effects are neglected because the load on the soil is very low at about 5 kPa, except for load tests. For thermal quasi-steady state, the ice lens heave is equal to the total heave.

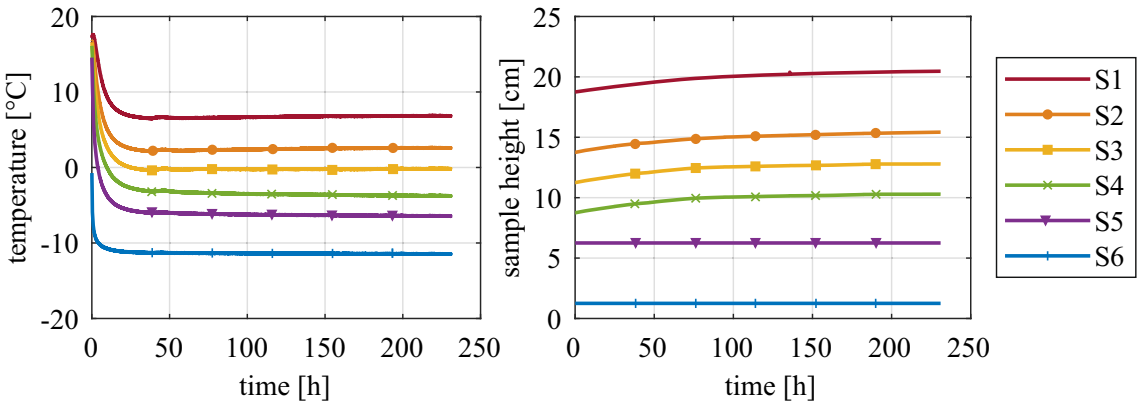

Fig. 7 Recorded temperature and position over time for the temperature sensors (S) for BF with a freezing temperature of −12.5 °C

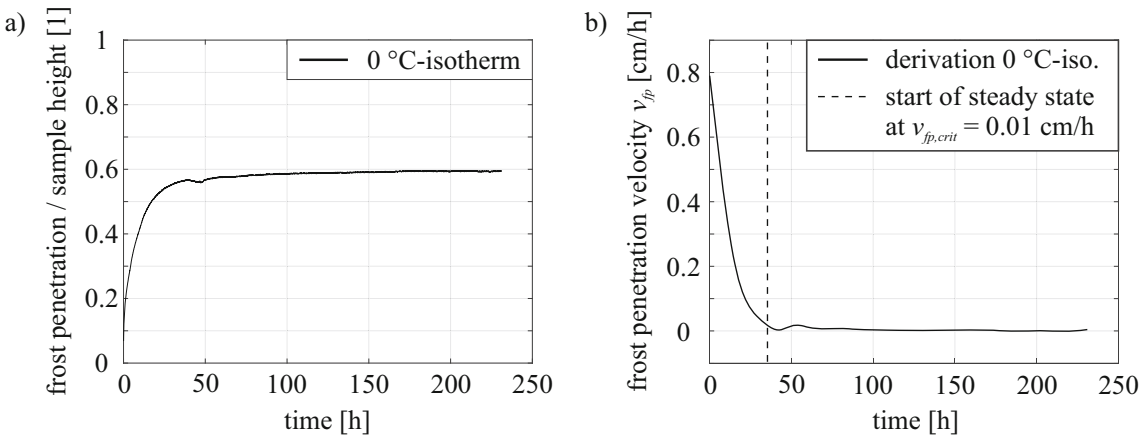

Fig. 8 **a** Course of the 0 °C isotherm and **b** corresponding frost penetration velocity for BF with a freezing temperature of −12.5 °C

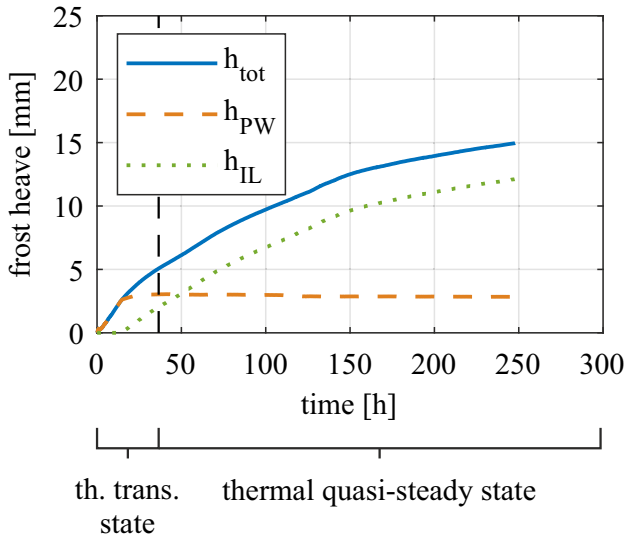

Fig. 9 Frost heave during thermal transient and quasi-steady state for a freezing temperature of −10 °C, BF

4 Test results

The following subsections contain the frost heave results of 62 experiments according to the parameter variations explained in subsection 2.4 and summarized in Table 4.

4.1 Absolute freezing temperature T_f

The actual freezing temperature (T_f) determines the frost penetration depth and therefore the frozen and unfrozen soil height. The lower the freezing temperature the greater the frost penetration or frozen part of the soil at the thermal quasi-steady state. To compare the results during thermal transient freezing, with pore water expansion and minor ice lens formation, the frost heave is related to the frozen part. The relationship between frost heave and the height of the frozen part is proportional because all tests have similar values of volumetric porosity n and saturation degree S_r (cf. Table 3 and Eq. 1 in subSect. 3.2.2). Figure 10 shows a similar curve for all tests. At TF, the slope of the frost heave related to the frozen height is greater at the beginning, decreases with time and ends up in a straight line that indicates a constant rate of frost heave. At BF, the curve is like TF, except of a lower gradient at the beginning of freezing due to the overburden soil weight which decreases frost heaving.

Table 5 Linear heave slope for transient freezing

	(Frost heave/frozen height)/time [1/h]	
	TF	BF
$\boldsymbol{T_{f,-5}}$	**0,00131**	**0,00139**
$\boldsymbol{T_{f,-7.5}}$	**0,00099**	**0,00118**
$T_{f,-10}$	0,00077	0,00083
$T_{f,-12.5}$	0,00083	0,00103
$T_{f,-15}$	0,00091	0,00087
$T_{f,-17.5}$	0,00084	0,00089
$W_{ws,-10}$	0,00075	0,00087

Generally, ice lenses grow thicker (greater heave) at a decreasing frost penetration rate (i.e., higher freezing temperatures) because more time is available for water accumulation (refer also to Fig. 5).

Of particular interest is that most lines show a similar linear trend toward the end of this transient stage. Table 5 shows a straight line fit to the lines for this latter part, showing that for all temperatures with absolute temperature lower than −10 °C, the frost heave increases at the same rate with time. This agrees with the fact that during this transient stage, the ice lens formation is minimal, and the frost heave is a consequence of porewater expansion, which depends on porosity and the amount of freezing water, which can be estimated as the position of the frost line. However, for higher temperatures, −5 °C and −7.5 °C, the heave grows faster relative to the frozen height (Table 5, in bold) indicating additional heaving by ice lenses.

The differences between BF and TF are related to the absolute values shown in Fig. 10 where BF shows generally lower values of heave. This shift is possibly due to the increased overburden in BF. Table 5 shows that the actual trends are generally very similar between BF and TF which indicates that, even at transient stage, the frost heave growth rate is governed by the temperature boundary conditions.

Furthermore, the heave result due to a restricted water supply (W_{ws0}) follows the other curves, showing that the restricted water supply does not have an impact on frost heave during transient freezing because of minor ice lens formation.

The heave at thermal quasi-steady-state conditions results only from ice lens formation and is shown in Fig. 11. In general, the lower the temperature, the larger the ice lens heave is. The increasing frost penetration due to the lower temperature boundary condition decreases the flow path between ice lens and water reservoir. A shorter flow path enhances the water supply for ice lens formation due to an increasing water flow velocity from the water reservoir to the ice lens. Therefore, at thermal quasi-steady-state conditions, the frost heave depends on the flow path (unfrozen soil height) and is not controlled by the height of the frozen part (cf. transient state). The frost heave rate due to a restricted water supply (W_{ws0}) strongly decreases over time as only the surrounding soil water can be used to form the ice lens. At this stage, it is therefore critical that water is available for heave to continue.

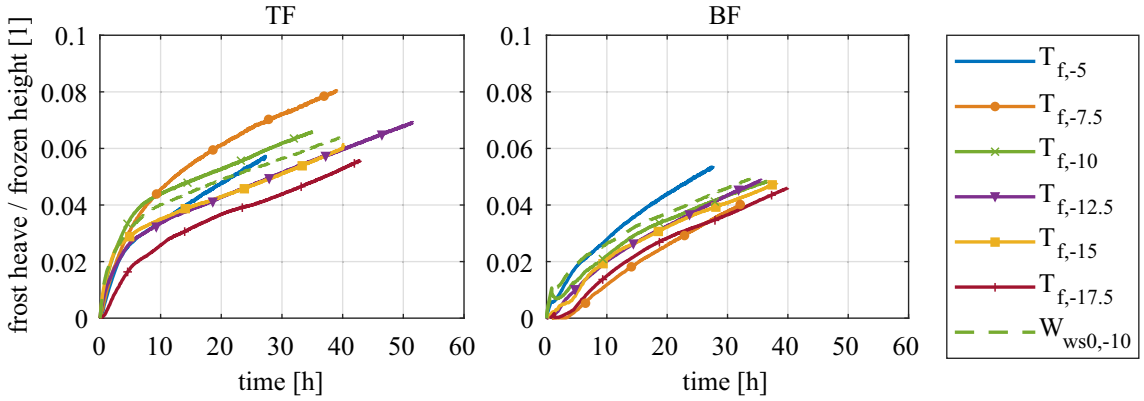

Fig. 10 Frost heave related to the frozen soil part at the thermal transient state for varied absolute freezing temperatures (T_f in °C) with (W_{ws0}) and without restricted water supply over time for TF and BF

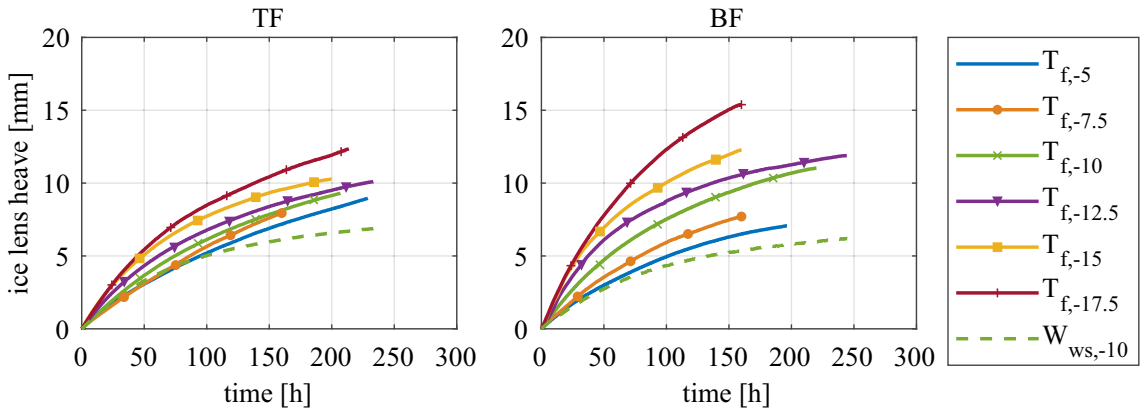

Fig. 11 Ice lens heave at the thermal quasi-steady state for different absolute freezing temperatures (T_f in °C) with (W_{ws0}) and without restricted water supply over time for TF and BF

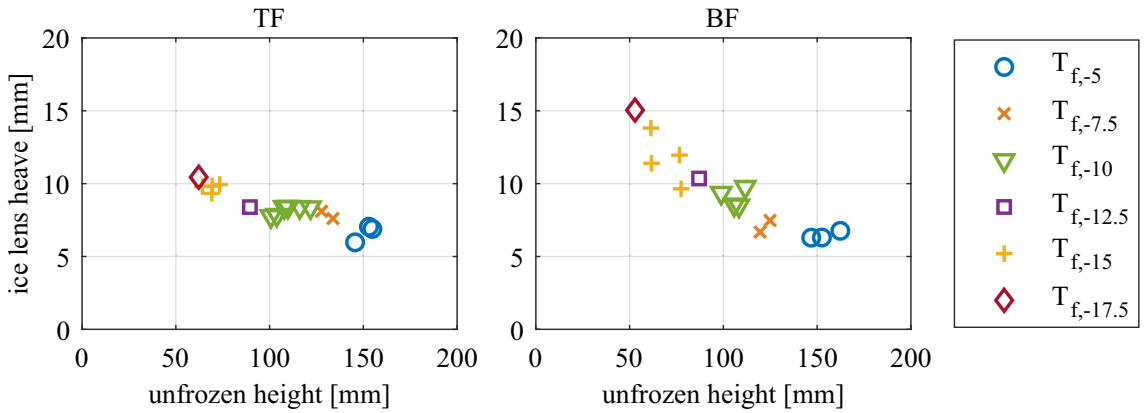

Fig. 12 Ice lens heave for different absolute freezing temperatures (T_f in °C) over the height of the unfrozen part after 150 h from the beginning of the quasi-steady state for TF and BF

Figure 12 shows the dependency between frost heave due to ice lens formation and the length of the flow path (unfrozen height) 150 h after the beginning of quasi-steady-state conditions. With decreasing flow path, ice lens heave increases especially for BF conditions. We explain this difference with TF due to the formation of longitudinal

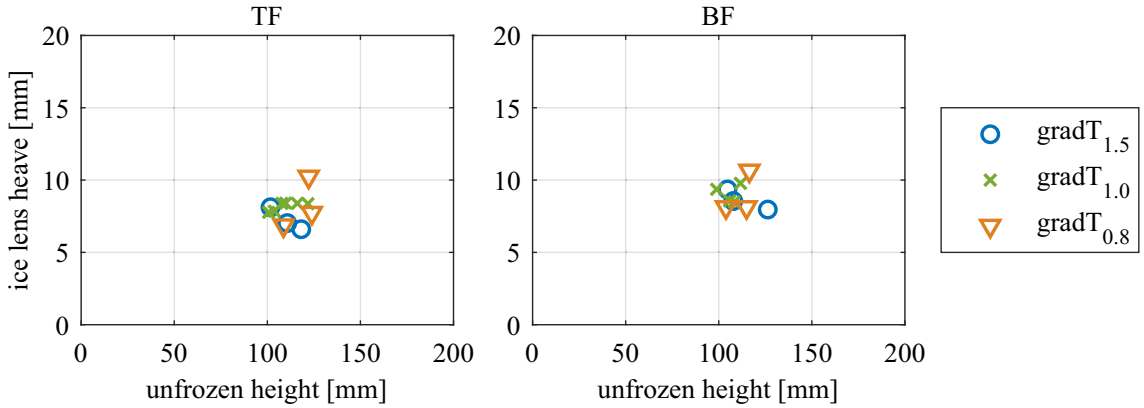

Fig. 13 Ice lens heave for different temperature gradients ($gradT_f$ in °C/cm) along the frozen soil over the height of the unfrozen part after 150 h from the beginning of the quasi-steady state for TF and BF

cracks that facilitate water flow (cf. Fig. 6 in subSect. 3.1) which is exacerbated by the fact that in BF, the water flows downward aided by gravity.

The effect of gravitational water inflow decreases with a thicker unfrozen soil part (i.e., warmer freezing temperatures, T_f) because the cracks do not fully penetrate the unfrozen soil, as shown for temperatures of −5 °C and −7.5 °C. This explains why for these temperatures, both values in Fig. 12 are very similar for BF and TF. In this case, the heave difference between BF and TF is primarily caused by the overburden load which changes slightly depending on the position of the frost line.

Concluding, the differences on frost heave between TF and BF are attributed to the water flow direction in or against gravity, supported by permeability changes due to cracking. The lower the unfrozen soil height, the greater effect of gravitational water inflow at BF. This can be explained by the hydraulic gradient which increases with decreasing flow path if the hydraulic head and the suction force at the ice lens are the same at each test. This can be assumed because the suction at the ice lens mainly depends on temperature (e.g., Clausius–Clapeyron equation) and, moreover, the same soil was used for all tests, so the segregation temperature should be the same.

4.2 Temperature gradient gradT$_f$

Figure 13 shows the ice lens heave 150 h after the beginning of the thermal quasi-steady state for temperature gradients of 0.8 °C/cm, 1.0 °C/cm (corresponds to the experiments with T_f = −10 °C in subSect. 4.1 due to same freezing depth at thermal quasi-steady state) and 1.5 °C/cm along the frozen area. The corresponding heights of the unfrozen area or flow paths are controlled by the temperature boundary conditions. Despite different temperature gradients in the frozen area, the same frost heave occurs. It can be therefore, concluded that the temperature gradient in the frozen area has no relevant impact on the formation of ice lenses at thermal quasi-steady state in the investigated range. This result corresponds to the findings in subSect. 4.1, where the unfrozen height or flow path mainly influences the ice lens heave.

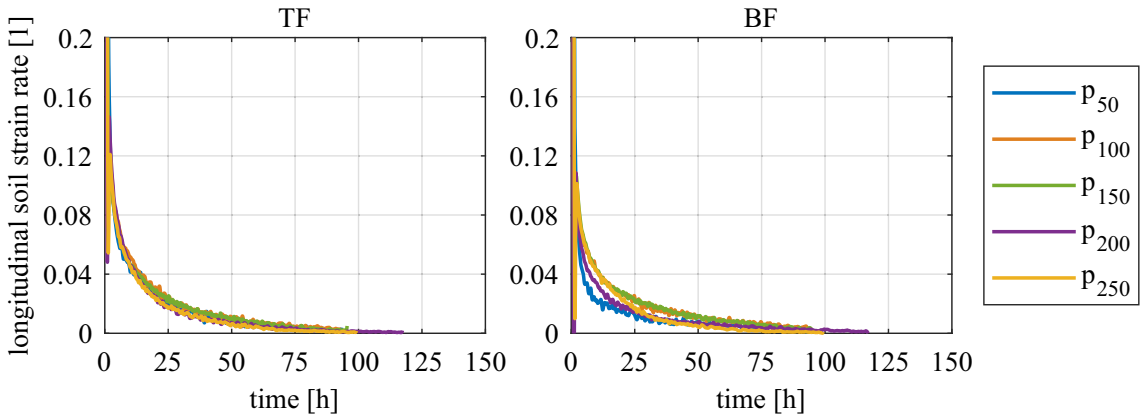

Fig. 14 Longitudinal soil strain during the consolidation phase for different loads (p in kPa) for TF and BF

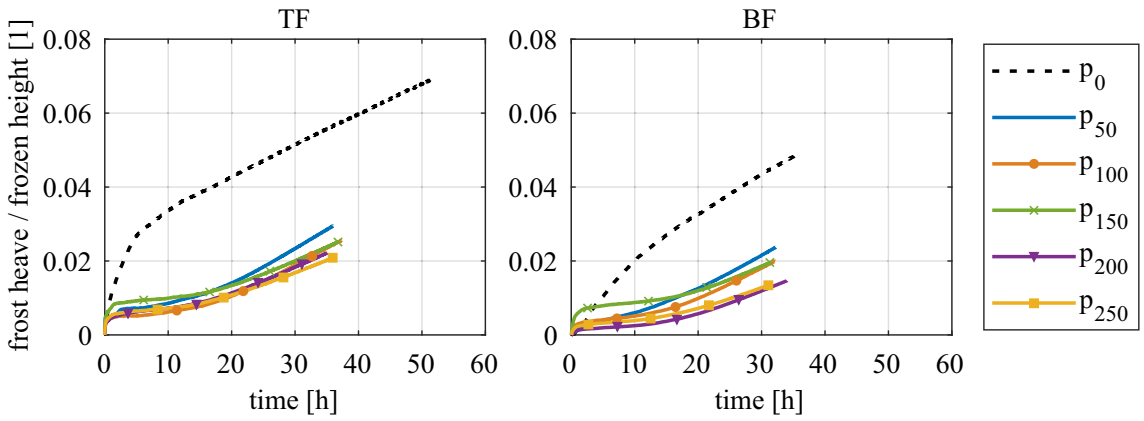

Fig. 15 Frost heave related to the frozen height at the thermal transient state for a freezing temperature of −12.5 °C and varied loads (p in kPa) for TF and BF

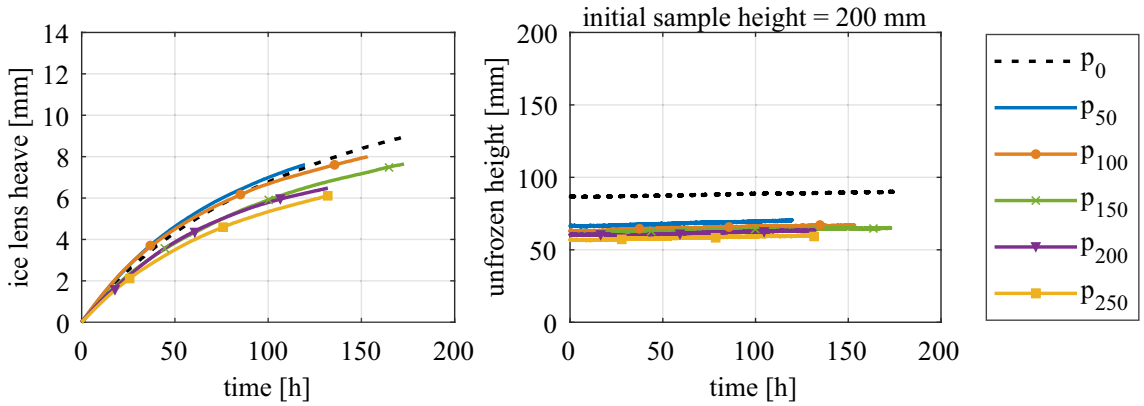

Fig. 16 Ice lens heave (left) and associated unfrozen soil height (right) at the thermal quasi-steady state for a freezing temperature of −12.5 °C and varied loads (p in kPa) for TF

4.3 External load *p*

The following tests were carried out by applying a load (p) on the soil sample. Each experiment contains a consolidation and freezing phase. During consolidation phase the soil settles under a defined constant load until the deformation stops. Afterward, the freezing process with a temperature of −12.5 °C is initiated and frost heaving starts.

Figure 14 shows the longitudinal soil strain rate during consolidation for TF and BF calculated as soil deformation over the maximum settlement at the end of consolidation. After approx. 4 days (96 h) of consolidation, the freezing phase was initiated. The measured settlement fluctuates slightly since the automatic load readjustment just took place every 60 s. The calculation of settlement difference over a time step produces the oscillating curve. At the beginning of the consolidation phase, the specimen is less stiff which increases this effect. To focus the relevant progress over time the ordinate in Fig. 14 ends at 0.2.

During the consolidation phase, the soil settles and water is expelled out of the sample into the external reservoir. With the beginning of the freezing process, the sample starts to expand due to pore water expansion. Further the emerging suction as a result of thermodynamic unbalance causes the water to flow back into the soil sample and heave due to ice lens formation occurs. The frost heave results during thermal transient freezing are given in Fig. 15 and during thermal quasi-steady state in Fig. 16. For both thermal states, the results are compared with zero load tests p_0.

The frost heaves during thermal transient freezing (Fig. 15) are related to the height of the frozen part, similar to Fig. 10 (subSect. 4.1), to eliminate influences of the freezing depth on frost heave. The lower porosity resulting from the consolidation phase reduces the frost heave due to pore water expansion compared to zero load freezing. With greater load, frost heave slightly decreases, although the results show the differences between different applied loads are not dramatic. The deviating curve at a load of 150 kN in BF is attributed to irregularities in the initial temperature. Importantly, the formation of a dominating single ice lens at the end of thermal transient freezing, as experienced at zero

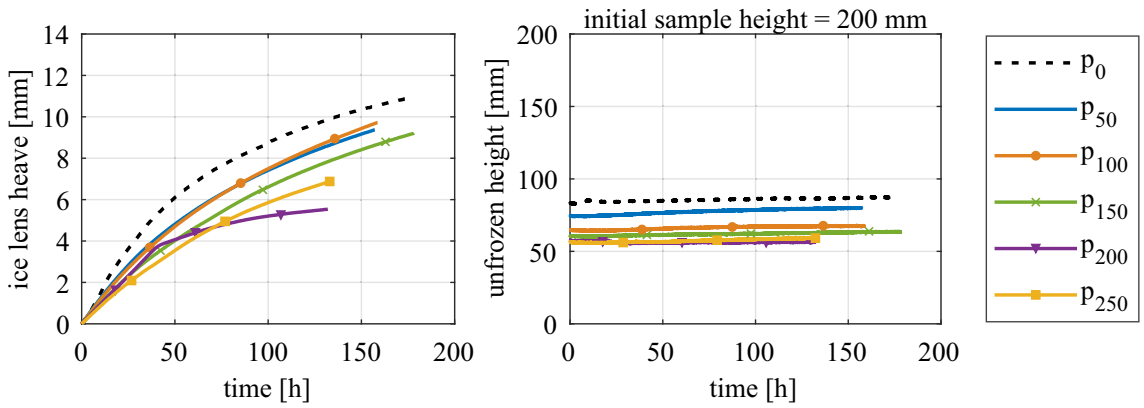

Fig. 17 Ice lens heave (left) and associated unfrozen soil height (right) at the thermal quasi-steady state for a freezing temperature of −12.5 °C and varied loads (p in kPa) for BF

load tests (cf. Fig. 10), was not observed. Qualitatively there are no differences between the TF and BF results with load, but quantitatively the heave results of TF exceed BF because of less additional soil weight that has to be overcome.

Figures 12 and 13 are shown that the height of the unfrozen area has a great effect on ice lens formation during thermal quasi-steady state. For the examination of ice lens heave during loading, the influence of the unfrozen soil height should be minimized to focus on heave reduction based on the specific load. For this, all tests were carried out with the same freezing temperature of -12.5 °C. However, during consolidation at different load magnitudes changes in porosity and water content occur and influence heat conduction. Thus, the unfrozen heights differ despite of same freezing temperatures (Fig. 16, right, and Fig. 17, right).

Figures 16 and 17 show the ice lens heave as well as the height of the unfrozen soil at the thermal quasi-steady state for a freezing temperature of −12.5 °C and varied loads. Generally, the frost heave increases with lower loading, but the results question the influence of the unfrozen height on heaving. For example, comparing BF (Fig. 17) with a load of 50 and 100 kPa the frost heave results are almost similar, but the unfrozen height or flow path for sucked water at 50 kPa is greater. At BF (Fig. 17), the lowest heave value is reached at 200 kPa instead of 250 kPa which could only be explained if the displacement transducer did not work properly in this test. This is because other measured parameters, such as temperature and surcharge are constant when the curve bends.

Besides the effect of unfrozen soil height, the greater difference at BF (Fig. 17) between unloaded and low loaded test results is attributed to the crack formation which influences the sample permeability in the unfrozen area. As expected, greater loading reduces crack formation. (Images are provided in the Supplementary Material 7).

Figure 18 shows, similar to Figs. 12 and 13, the ice lens heave at quasi-steady state conditions for different unfrozen heights 100 h after reaching the thermal quasi-steady state. Since the consolidation phase takes approx. 4 days the freezing phase was selected to 100 h, as 150 h freezing at

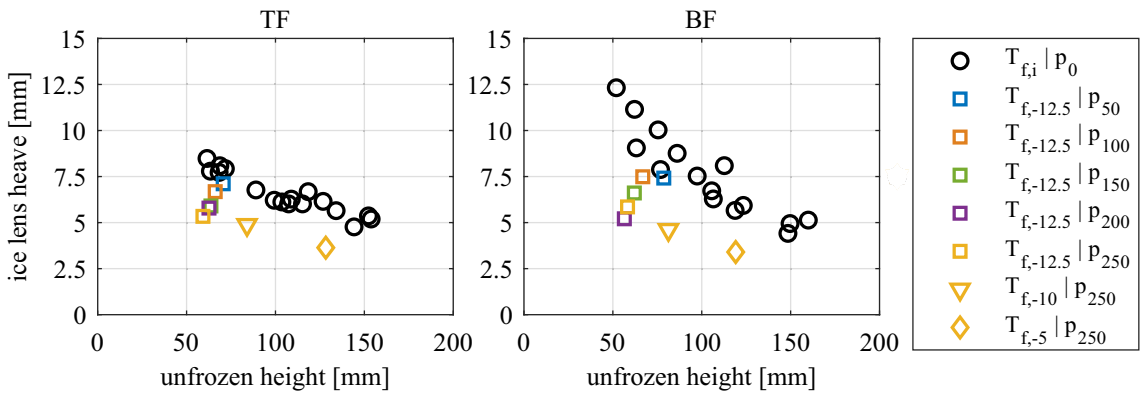

Fig. 18 Ice lens heave at different temperatures (T_f in °C) and loads (p in kPa) over the height of the unfrozen part after 100 h from the beginning of the quasi-steady state for TF and BF

thermal quasi-steady-state conditions (cf. Figs. 12 and 13) was not applicable. The black circles indicate the heave results under zero load, carried out in subSect. 4.1.

To investigate the influence of temperature, additional tests using a freezing temperature of −10 °C and −5 °C are used for the maximum load of 250 kPa. The ice lens heaving decreases with greater load and, at TF (Fig. 18, left), for 250 kPa is almost parallel to zero load results. At BF (Fig. 18, right), loaded frost heave results are not parallel to the results without loading. It is assumed that the reduced crack formation reduces permeability and therefore the growth of the ice lens. With higher loading TF and BF heaving results are more consistent which emphasize the assumption that the crack-induced increasing permeability and better water accumulation due to gravitational effects at BF is reduced by surcharge.

The results show that besides loading, the influence of the unfrozen soil height or the flow path of sucked water, respectively, is present. The TF and BF results differ as long as the crack formation in the unfrozen area has an effect on the permeability. The greater the magnitude of loading the more crack opening is impeded by confining pressure and the minor heave differences between TF and BF.

5 Conclusion

The method of AGF is common for inner-city tunneling construction projects. Since ice lenses form especially in frost susceptible soils, strong deformations occur, which magnitude depends on the boundary conditions. In this work, the influence of different freezing directions, TF versus BF, on frost heaving, is investigated considering the special thermal and load boundary conditions of an AGF. Therefore, 62 frost heave tests were carried out in a novel test device with testing periods up to 10 days, providing a comprehensive database of ice lens formation during the thermal steady state. This state simulates the holding phase of an AGF, where cooling only maintains the thickness of the frozen body and no further frost penetration occurs.

During the thermal transient phase which is characterized by a growing frost body with moving frost line, there was only a negligible ice lens formation observed which is due to fast frost penetration. The process is dominated by the magnitude of the boundary cold temperatures only. Frost heaving during TF is usually larger than BF heave which is attributed to greater soil weight and consolidation effects in the BF conditions.

At thermal steady state, one relevant factor with great impact on the magnitude of frost heaving is the height of the unfrozen soil, which can also be seen as proxy for the water flow path. This is directly a function of temperature at the boundary conditions where lower temperatures reduce the unfrozen part (i.e., the colder it is the boundary, the smaller the unfrozen region of the soil). A shorter unfrozen part increases the hydraulic gradient for the same boundary hydraulic conditions and, thus, the water flow velocity to the ice lens. This effect is observed independently of the freezing direction.

Conversely to the transient stage, BF exhibits larger frost heave than TF conditions for almost all conditions. This is due to the formation of longitudinal cracks along the unfrozen zone that initiate during ice lens formation and are caused by suction. The cracks emerge when water at the warm side of the ice lens is drained off for ice lens growth. These cracks favor water flow toward the ice lens, hence, increasing the ice lens size. The closer the ice lens to the water reservoir, the greater is the effect of an improved water accumulation at the growing ice lens. The greatest frost heave occurs when the unfrozen part is short, and cracks reach the unfrozen surface. Equivalent hydraulic conditions can naturally occur in real applications when AGF is used within an aquifer. The application of vertical load reduces crack formation and therefore, for this cases, BF and TF present similar heave magnitudes. In the case of our tests, an applied load of 150 kPa seemed to be the threshold from which the cracks would not form.

The relationship between the unfrozen soil height and the ice lens heave is not linear and different for BF and TF freezing. This is of interest for long-term soil freezing and will be analyzed in detail in future research work.

Supplementary Information The online version contains supplementary material available at https://doi.org/10.1007/s11440-024-02259-2.

Acknowledgements This work was supported by the German Research Foundation (DFG) under the project "Investigation and calculation of frost heave considering specific boundary conditions of ground freezing," grant number 409760547. The funding is herewith gratefully acknowledged.

Author contributions All authors contributed to the study conception and design. Material preparation, data collection and analysis were performed by KN. The first draft of the manuscript was written by KN, and all authors commented on previous versions of the manuscript. All authors read and approved the final manuscript.

Funding Open Access funding enabled and organized by Projekt DEAL.

Data availability The data generated or analyzed during this study are provided within the published article or are available from the corresponding author on reasonable request.

Declarations

Conflict of interest The authors declare there are no competing interests

Open Access This article is licensed under a Creative Commons Attribution 4.0 International License, which permits use, sharing, adaptation, distribution and reproduction in any medium or format, as long as you give appropriate credit to the original author(s) and the source, provide a link to the Creative Commons licence, and indicate if changes were made. The images or other third party material in this article are included in the article's Creative Commons licence, unless indicated otherwise in a credit line to the material. If material is not included in the article's Creative Commons licence and your intended use is not permitted by statutory regulation or exceeds the permitted use, you will need to obtain permission directly from the copyright holder. To view a copy of this licence, visit http://creativecommons.org/licenses/by/4.0/.

References

1. Staender W (1967) Das gefrierverfahren im schacht-, grund-und tunnelbau. Die anwendung der kälte in der verfahrens-und klimatechnik, Biologie und Medizin, pp 173–227
2. Hartge KH (1978) Einführung in die bodenphysik. Ferdinand Enke Verlag, Stuttgart
3. Taber S (1929) Frost heaving. J Geol 37:428–461
4. Taber S (1930) The mechanics of frost heaving. J Geol 38(4):303–317
5. Ruckli R (1944) Die eislinsenbildung im strassenuntergrund. Schweizerische Bauzeitung 124(16):206–210
6. Wilen LA, Dash JG (1995) Frost heave dynamics at a single crystal interface. Phys Rev Lett 74(25):5076
7. Martin RT (1959) Rhythmic ice banding in soil. Highway Research Board Bulletin, p **218**
8. Loch JPG (1978) Thermodynamic equilibrium between ice and water in porous media. Soil Sci 126(2):77–80
9. Williams PJ, Smith MW (1989) The frozen earth: fundamentals of geocryology. Cambridge University Press, Cambridge
10. Unold F (2006) Der Gefriersog bei der Bodenfrostung und das Kompressionsverhalten des wieder aufgetauten Bodens. Universität der Bundeswehr München, München, Institut für Bodenmechanik und Grundbau
11. Miller R (1972) Freezing and heaving of saturated and unsaturated soils. Highway Res Rec 393(1):1–11
12. Konrad J-M, Morgenstern NR (1980) Mechanistic theory of ice lens formation in fine-grained soils. Can Geotech J 17(4):473–486
13. Gilpin RR (1980) A model for the prediction of ice lensing and frost heave in soils. Water Resour Res 16(5):918–930
14. Nixon JF (1982) Field frost heave predictions using the segregation potential concept. Can Geotech J 19(4):526–529
15. O'Neill K, Miller RD (1985) Exploration of a rigid ice model of frost heave. Water Resour Res 21(3):281–296
16. Sheng D, Axelsson K, Knutsson S (1995) Frost heave due to ice lens formation in freezing soils: 1. Theory Verif Hydrol Res 26 (2):125–146
17. Ladanyi B, Andersland O (2004) Frozen ground engineering. Wiley
18. Rempel AW (2010) Frost heave. J Glaciol 56(200):1122–1128
19. Zhang M, Zhang X, Lai Y, Lu J, Wang C (2020) Variations of the temperatures and volumetric unfrozen water contents of fine-grained soils during a freezing–thawing process. Acta Geotech 15:595–601
20. Zhou G, Zou Y, Boley C (2009) Reduktion der Frosthebungen bei der künstlichen Bodenvereisung. Bautechnik 86(9):566–573
21. Corte AE (1962) The frost behavior of soils. I. vertical sorting. Highway Res Board Bull, p 317
22. Kaplar CW (1970) Phenomenon and mechanism of frost heaving. Highway Res Rec 304:1–13
23. Penner E (1957) Soil moisture tension and ice segregation. Highway Res Board Bull, p 168
24. Hoekstra P (1969) Water movement and freezing pressures. Soil Sci Soc Am J 33(4):512–518
25. Chamberlain EJ (1981) Frost susceptibility of soil. U.S. army corps of engineers—cold regions research and engineering laboratory
26. Dagli D (2017) Laboratory investigations of frost action mechanisms in soils. Department of Civil, Environmental and Natural Resources Engineering, Luleå University of Technology
27. Loch JPG, Kay BD (1978) Water redistribution in partially frozen, saturated silt under several temperature gradients and overburden loads. Soil Sci Soc Am J 42:400–406
28. Penner E (1986) Aspects of ice lens growth in soils. Cold Reg Sci Technol 13(1):91–100
29. Aitken GW (1974) Reduction of frost heave by surcharge stress. Corps of engineers, US army cold regions research and engineering laboratory
30. Hill D, Morgenstern N (1977) Influence of load and heat extraction on moisture transfer in freezing soils. In: International symposium on frost action in soils, Lulea, University of Lulea
31. Chamberlain EJ, Gow AJ (1979) Effect of freezing and thawing on the permeability and structure of soils. Eng Geol 13(1–4):73–92
32. Akagawa S (1988) Experimental study of frozen fringe characteristics. Cold Reg Sci Technol 15(3):209–223
33. Arenson L, Sego D, Take WA (2007) Measurement of ice lens growth and soil consolidation during frost penetration using particle image velocimetry (PIV). In: 60th Canadian geotechnical conference & 8th joint CGS/IAH-CNC groundwater conference, Ottawa, Ontario, Canada
34. Arenson LU, Azmatch TF, Sego DC, Biggar KW (2008)A new hypothesis on ice lens formation in frost-susceptible soils. In: Ninth international conference on permafrost, Fairbanks, Alaska. 1: 59–64
35. O'Neill K, Miller RD (1982) Numerical solutions for a rigid-ice model of secondary frost heave. US army corps of engineers, cold regions research & engineering laboratory
36. Horne WT (1987) Prediction of frost heave using the segregation potential. Department of Civil Engineering, The University of Alberta, Edmonton, Alberta
37. Nixon JF (1991) Discrete ice lens theory for frost heave in soils. Can Geotech J 28(6):843–859
38. Saarelainen S (1992) Modelling frost heaving and frost penetration in soils at some observation sites in Finland: the SSR model. VTT Technical Research Centre of Finland, Tampere University of Technology
39. Fowler AC, Krantz WB (1994) A generalized secondary frost heave model. SIAM J Appl Math 54(6):1650–1675
40. Black PB (1995) Rigidice model of secondary frost heave. CRREL report, U.S. Army Cold Regions Research and Engineering Laboratory. 95(12)
41. Talamucci F (2003) Freezing processes in porous media: formation of ice lenses, swelling of the soil. Math Comput Model 37(5–6):595–602
42. Kim K, Zhou W, Huang SL (2008) Frost heave predictions of buried chilled gas pipelines with the effect of permafrost. Cold Reg Sci Technol 53(3):382–396
43. Style RW, Peppin SS, Cocks AC, Wettlaufer JS (2011) Ice-lens formation and geometrical supercooling in soils and other colloidal materials. Phys Rev E 84(4):041402
44. Zhou J, Li D (2012) Numerical analysis of coupled water, heat and stress in saturated freezing soil. Cold Reg Sci Technol 72:43–49
45. Sweidan A, Niggemann K, Heider Y, Ziegler M, Markert B (2021) Experimental study and numerical modeling of the thermo-hydro-

mechanical processes in soil freezing with different frost penetration directions. Acta Geotech 17(1):231–255
46. Fu Z, Wu Q, Zhang W, He H, Wang L (2022) Water migration and segregated ice formation in frozen ground: current advances and future perspectives. Front Earth Sci 10:826961
47. Ji Y, Zhou G, Zhou Y, Vandeginste V (2019) Frost heave in freezing soils: a quasi-static model for ice lens growth. Cold Reg Sci Technol 158:10–17
48. Hansson K, Šimůnek J, Mizoguchi M, Lundin LC, Van Genuchten MT (2004) Water flow and heat transport in frozen soil: numerical solution and freeze–thaw applications. Vadose Zone J 3(2):693–704
49. Rempel AW (2007) Formation of ice lenses and frost heave. J Geophys Res Earth Surf 112(F2):F02S21. https://doi.org/10.1029/2006JF000525
50. Nishimura S, Gens A, Olivella S, Jardine RJ (2009) THM-coupled finite element analysis of frozen soil: formulation and application. Géotechnique 59(3):159–171
51. Cai H, Hong R, Xu L, Wang C, Rong C (2022) Frost heave and thawing settlement of the ground after using a freeze-sealing pipe-roof method in the construction of the Gongbei Tunnel. Tunn Undergr Space Technol 125:104503
52. Fremond M, Mikkola M (1991) Thermomechanical modelling of freezing soil. In: International symposium on ground freezing, p 17–24
53. Hartikainen J, Mikkola M (1997) General thermomechanical model of freezing soil with numerical applications. In: Ground freezing 97; frost action in soils, Balkema, p 101–105
54. Michalowski RL, Zhu M (2006) Frost heave modelling using porosity rate function. Int J Numer Anal Meth Geomech 30 (8):703–722
55. Zhang Y, Michalowski RL (2015) Thermal-hydro-mechanical analysis of frost heave and thaw settlement. J Geotech Geoenviron Eng 141(7):04015027
56. Cai H, Xu L, Yang Y, Li L (2018) Analytical solution and numerical simulation of the liquid nitrogen freezing-temperature field of a single pipe. AIP Adv 8(5):055119
57. Cai H, Liu Z, Li S, Zheng T (2019) Improved analytical prediction of ground frost heave during tunnel construction using artificial ground freezing technique. Tunn Undergr Space Technol 92:103050
58. Niggemann K, Fuentes R (2023) New semi-analytical approach for ice lens heaving during artificial freezing of fine-grained material. J Rock Mech Geotech Eng 15(11):2994–3009
59. Auld FA, Belt J, Allenby D(2015) Application of artificial ground freezing. In: Proceedings of the XVI ECSMGE
60. Johansson T (2009) Artificial ground freezingin clayey soils: laboratory and field studies of deformations during thawing at the bothnia line, KTH
61. Kaplar CW (1974) Freezing test for evaluating relative frost susceptibility of various soils. US army cold regions research and engineering laboratory
62. Penner E, Ueda T (1977) The dependence of frost heaving on load application – preliminary results. In: Proceedings of the international symposium on frost action in soil, Luleå, Sweden. 1: 92–101
63. Jin HW, Lee J, Ryu BH, Akagawa S (2019) Simple frost heave testing method using a temperature-controllable cell. Cold Reg Sci Technol 157:119–132
64. Konrad J-M, Morgenstern NR (1981) The segregation potential of a freezing soil. Can Geotech J 18(4):482–491
65. Konrad J-M, Morgenstern NR (1982) Prediction of frost heave in the laboratory during transient freezing. Can Geotech J 19(3):250–259
66. Zhu XF, Wei XY, Huang X, Zhang YP (2013) The formation of ice lenses in unidirectional and multidirectional freezing soil. Appl Mech Mater 353:68–73
67. Lv Z, Xia C, Li Q, Si Z (2019) Empirical frost heave model for saturated rock under uniform and unidirectional freezing conditions. Rock Mech Rock Eng 52:955–963
68. Yang S, Zhang H, Jin H, Hu Y (2023) Influence of freezing directionality on the permeability of silty clay. Cold Reg Sci Technol 207:103756
69. Xia D, Arenson LU, Biggar KW, Sego DC (2005) Freezing process in Devon silt-using time-lapse photography. In: 58th Canadian geotechnical conference, Saskatoon, Saskatchewan
70. Mackay JR (1974) Ice-wedge cracks, Garry Island, Northwest Territories. Can J Earth Sci 11(10):1366–1383
71. Niggemann K (2020) Investigation of frost heave considering the boundary conditions of artificial ground freezing. In: Transportation soil engineering in cold regions. **2**: Proceedings of TRANSOILCOLD 2019, Springer Singapore, p 273–283
72. Yin Q, Andò E, Viggiani G, Sun W (2022) Freezing-induced stiffness and strength anisotropy in freezing clayey soil: theory, numerical modeling, and experimental validation. Int J Numer Anal Meth Geomech 46(11):2087–2114

Publisher's Note Springer Nature remains neutral with regard to jurisdictional claims in published maps and institutional affiliations.

Supplementary Material 1 (Paper #2)

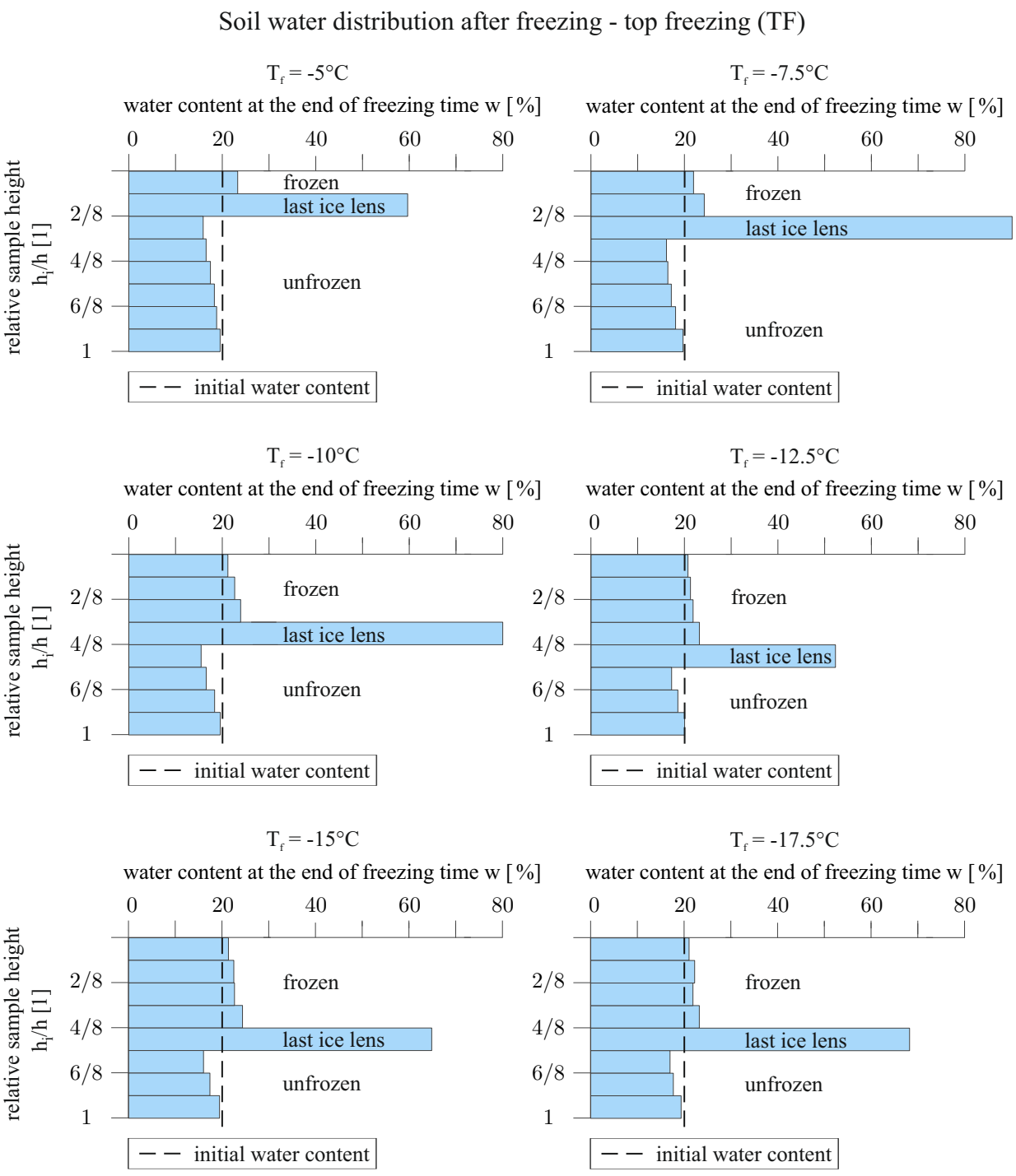

Influence of freezing directions on ice lens formations in soils

Acta Geotechnica
K. Niggemann, Institute of Geomechanics and Underground Technology, RWTH Aachen University,
Email: niggemann@gut.rwth-aachen.de
M. Ziegler, Ziegler und Aulbach Ingenieurgesellschaft GmbH (formerly RWTH Aachen University)
R. Fuentes, Institute of Geomechanics and Underground Technology, RWTH Aachen University

Supplementary Material 2 (Paper #2)

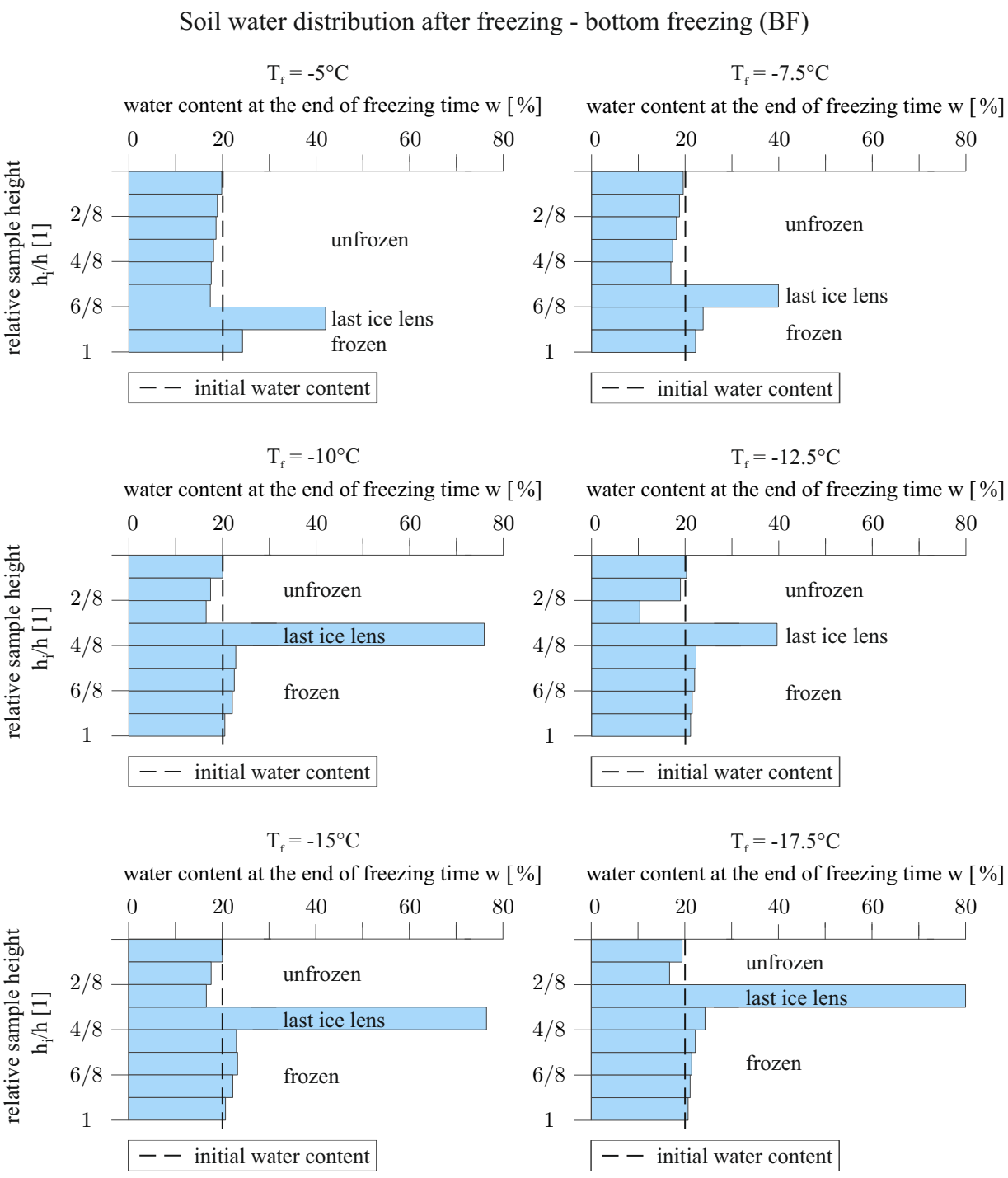

Influence of freezing directions on ice lens formations in soils
Acta Geotechnica
K. Niggemann, Institute of Geomechanics and Underground Technology, RWTH Aachen University,
Email: niggemann@gut.rwth-aachen.de
M. Ziegler, Ziegler und Aulbach Ingenieurgesellschaft GmbH (formerly RWTH Aachen University)
R. Fuentes, Institute of Geomechanics and Underground Technology, RWTH Aachen University

Supplementary Material 3 (Paper #2)

Course of the 0°C-isotherm and corresponding frost penetration velocity for different freezing temperatures T_f - top freezing (TF)

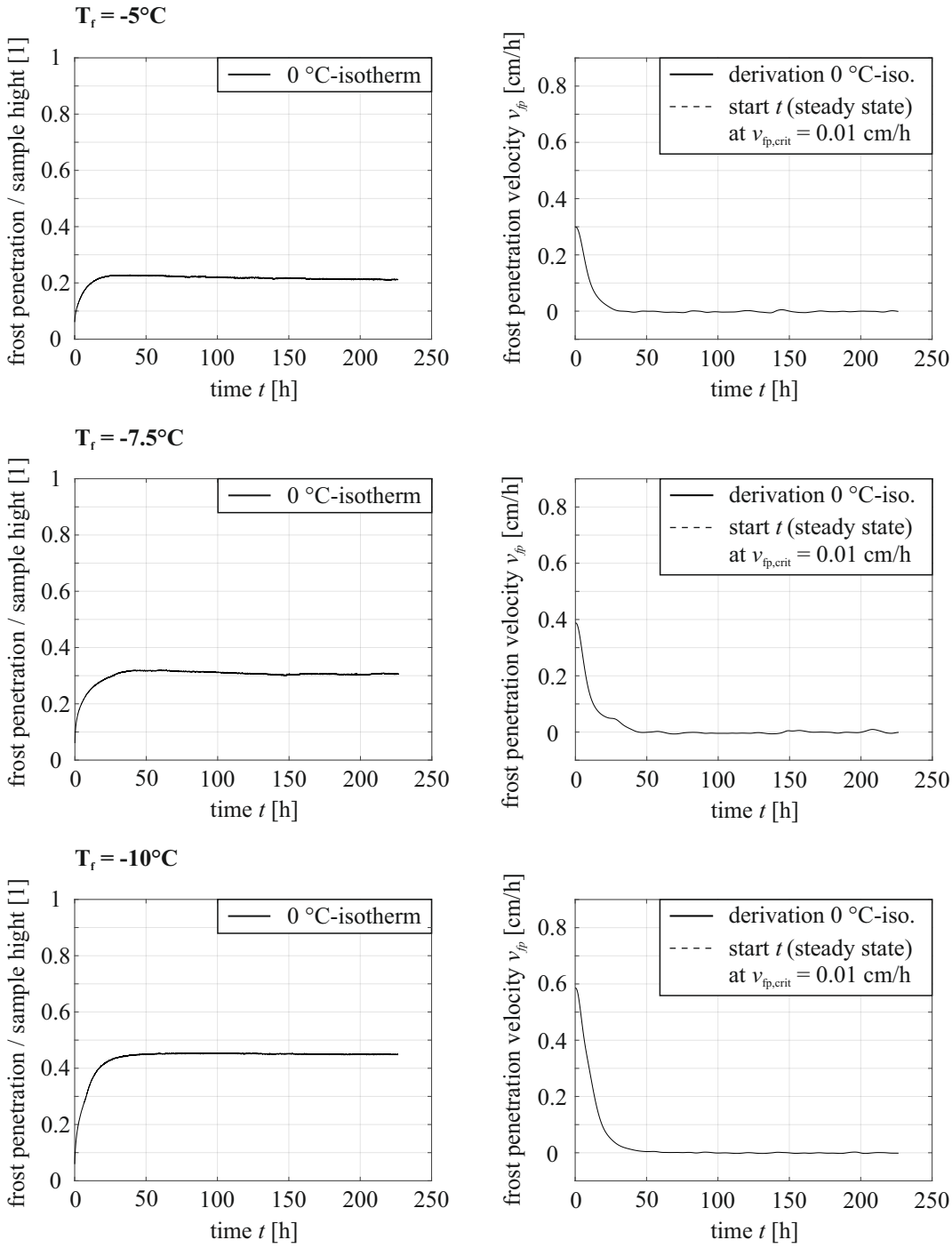

Influence of freezing directions on ice lens formations in soils
Acta Geotechnica
K. Niggemann, Institute of Geomechanics and Underground Technology, RWTH Aachen University, Email: niggemann@gut.rwth-aachen.de
M. Ziegler, Ziegler und Aulbach Ingenieurgesellschaft GmbH (formerly RWTH Aachen University)
R. Fuentes, Institute of Geomechanics and Underground Technology, RWTH Aachen University

Supplementary Material 4 (Paper #2)

Course of the 0°C-isotherm and corresponding frost penetration velocity for different freezing temperatures T_f - top freezing (TF)

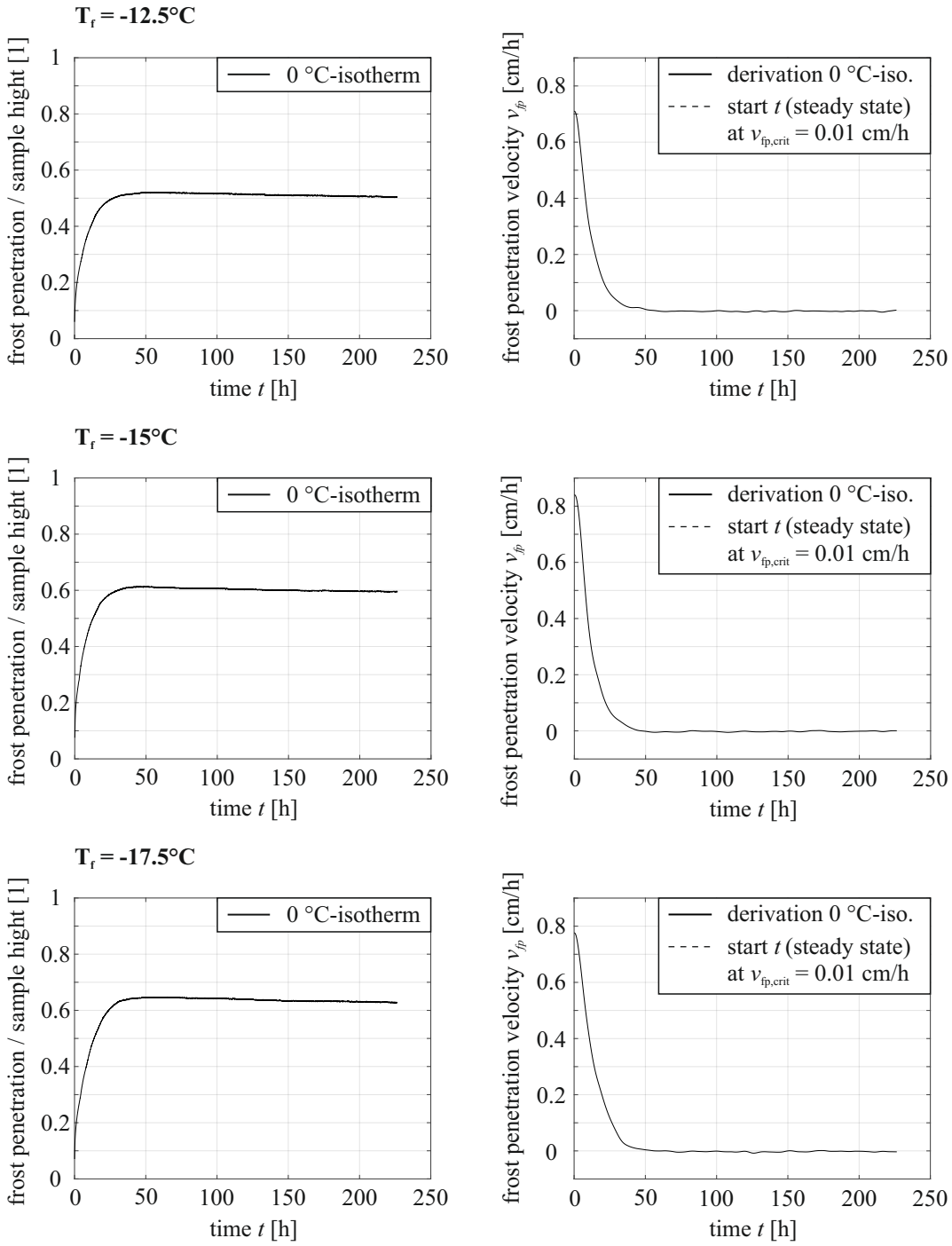

Influence of freezing directions on ice lens formations in soils
Acta Geotechnica
K. Niggemann, Institute of Geomechanics and Underground Technology, RWTH Aachen University, Email: niggemann@gut.rwth-aachen.de
M. Ziegler, Ziegler und Aulbach Ingenieurgesellschaft GmbH (formerly RWTH Aachen University)
R. Fuentes, Institute of Geomechanics and Underground Technology, RWTH Aachen University

Supplementary Material 5 (Paper #2)

Course of the 0°C-isotherm and corresponding frost penetration velocity for different freezing temperatures T_f - bottom freezing (BF)

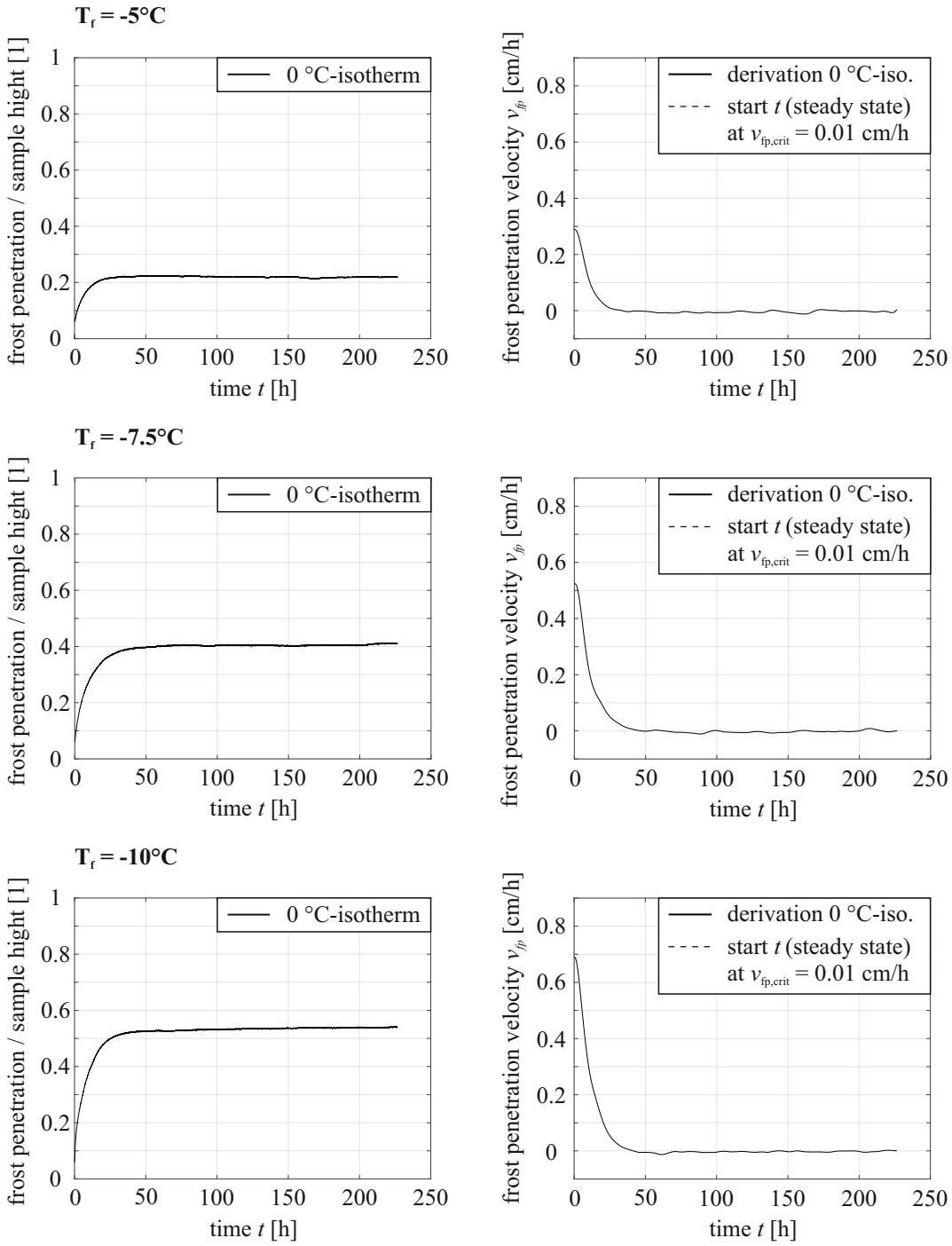

Influence of freezing directions on ice lens formations in soils
Acta Geotechnica
K. Niggemann, Institute of Geomechanics and Underground Technology, RWTH Aachen University, Email: niggemann@gut.rwth-aachen.de
M. Ziegler, Ziegler und Aulbach Ingenieurgesellschaft GmbH (formerly RWTH Aachen University)
R. Fuentes, Institute of Geomechanics and Underground Technology, RWTH Aachen University

Supplementary Material 6 (Paper #2)

Course of the 0°C-isotherm and corresponding frost penetration velocity for different freezing temperatures T_f - bottom freezing (BF)

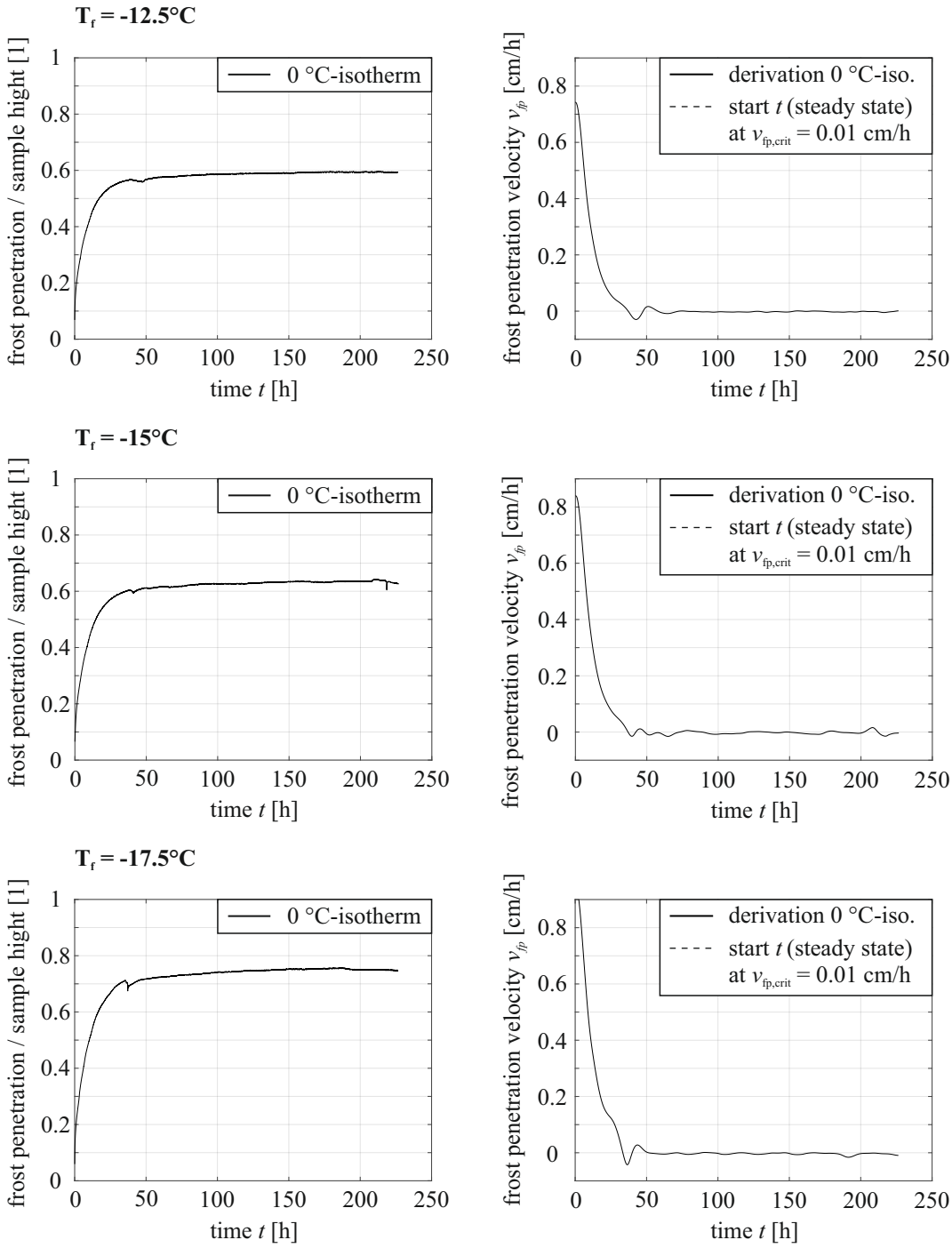

Influence of freezing directions on ice lens formations in soils
Acta Geotechnica
K. Niggemann, Institute of Geomechanics and Underground Technology, RWTH Aachen University, Email: niggemann@gut.rwth-aachen.de
M. Ziegler, Ziegler und Aulbach Ingenieurgesellschaft GmbH (formerly RWTH Aachen University)
R. Fuentes, Institute of Geomechanics and Underground Technology, RWTH Aachen University

Supplementary Material 7 (Paper #2)

Pattern cross section at the ice lens interface with openings for different loads

p = 50 kPa



p = 100 kPa



p = 150 kPa



p = 200 kPa



p = 250 kPa



Influence of freezing directions on ice lens formations in soils
Acta Geotechnica
K. Niggemann, Institute of Geomechanics and Underground Technology, RWTH Aachen University, Email: niggemann@gut.rwth-aachen.de
M. Ziegler, Ziegler und Aulbach Ingenieurgesellschaft GmbH (formerly RWTH Aachen University)
R. Fuentes, Institute of Geomechanics and Underground Technology, RWTH Aachen University

C Paper #3

New semi-analytical approach for ice lens heaving during artificial freezing of fine-grained material

Niggemann, K., Fuentes, R. (2023): New semi-analytical approach for ice lens heaving during artificial freezing of fine-grained material. Journal of Rock Mechanics and Geotechnical Engineering, 15(11), pp. 2994-3009. https://doi.org/10.1016/j.jrmge.2023.07.004

Journal of Rock Mechanics and Geotechnical Engineering 15 (2023) 2994–3009

Contents lists available at ScienceDirect

Journal of Rock Mechanics and Geotechnical Engineering

journal homepage: www.jrmge.cn

Full Length Article

New semi-analytical approach for ice lens heaving during artificial freezing of fine-grained material

K. Niggemann*, R. Fuentes

Institute of Geomechanics and Underground Technology, RWTH Aachen University, Aachen, Germany

ARTICLE INFO

Article history:
Received 22 October 2022
Received in revised form
8 May 2023
Accepted 9 July 2023
Available online 6 August 2023

Keywords:
Semi-analytical approach
Ice lens formation
Frost heaving
Bottom freezing
Segregation potential
Frost-susceptible soil

ABSTRACT

The calculation of frost heaving with ice lens formation is still not standard for construction projects using artificial ground freezing (AGF). In fine-grained material, ice lenses may initiate and lead to significant heaving at the ground surface, which should be considered in advance. However, the complex processes during ice lens formation are still not fully understood and difficult to capture in a simple approach. In the past, the semi-analytical approach of Konrad and Morgenstern used one soil constant, the "segregation potential (SP)". It has been mainly and most successfully applied to the heave calculation of natural-induced soil freezing in cold regions. Its application to AGF has been so far unsuccessful. To solve this, a new semi-analytical approach is presented in this paper. It includes AGF conditions such as bottom-up freezing, temperature gradients to reach great freezing velocities, and a distinction between two freezing states. One is the freezing-up state until a certain frost body thickness is reached (thermal transient state), and the other is a holding phase where the frost body thickness is kept constant (thermal quasi-steady state). To test its ability, the results are applied to another freezing direction, the top-down freezing. The new approach is validated using two different frost-susceptible soils and, in total, 50 frost heave tests. In the thermal transient region, where the SP is applicable, the two semi-analytical approaches are compared, showing improved performance of the current method by about 15%.
© 2023 Institute of Rock and Soil Mechanics, Chinese Academy of Sciences. Production and hosting by Elsevier B.V. This is an open access article under the CC BY-NC-ND license (http://creativecommons.org/licenses/by-nc-nd/4.0/).

1. Introduction

Artificial ground freezing (AGF) is often used in urban infrastructure projects. The frost body expansion can cause deformation and heaving at the surface, especially in fine-grained soils due to ice lens formation. For construction projects using AGF, a monitoring system to control deformation is essential. The monitoring includes a structural control of the object, the adjacent infrastructure, and the ground surface. Besides monitoring, the ability to model the process is also crucial for control purposes. The prediction of frost heaving with ice lens formation for AGF projects usually is based on soil frost susceptibility recommendations (Auld et al., 2015). However, in most cases, frost heaving is not predicted in practice because practice-oriented calculation methods are missing. An engineer can use numerical methods. Ji et al. (2019) divided numerical models for frost heave calculation into two categories: mechanistic frost heave models and physical field models.

The first group includes models that explain the mechanism of frost heaving and the initiation of discrete ice lenses in the soil during freezing. These models assume a frozen fringe between the ice lens and the freezing front and take into account the interface pressure between water and solid, which leads to the freezing suction (Gilpin, 1980; O'Neill and Miller, 1985; Nixon, 1991; Hansson et al., 2004; Rempel, 2007; Nishimura et al., 2009; Ji et al., 2019; Cai et al., 2022). Depending on the complexity of the specific material parameters in the model, geometric characteristics and governing equations need to be included and solved.

Physical field models focus on the moisture, mechanical and temperature field prediction and do not predict single ice lens formation but an increasing finite volume of the soil. These are usually coupled thermo-hydro-mechanical (THM) models based on the continuum poromechanics theory. The increasing volume is described by moisture accumulation due to temperature-dependent suction (Fremond and Mikkola, 1991; Hartikainen and Mikkola, 1997; Michalowski and Zhu, 2006; Zhang and Michalowski, 2015; Sweidan et al., 2021).

* Corresponding author.
E-mail address: niggemann@gut.rwth-aachen.de (K. Niggemann).
Peer review under responsibility of Institute of Rock and Soil Mechanics, Chinese Academy of Sciences.

https://doi.org/10.1016/j.jrmge.2023.07.004
1674-7755 © 2023 Institute of Rock and Soil Mechanics, Chinese Academy of Sciences. Production and hosting by Elsevier B.V. This is an open access article under the CC BY-NC-ND license (http://creativecommons.org/licenses/by-nc-nd/4.0/).

However, numerical methods require a great deal of experimental effort and specialized tests to obtain the relevant modeling parameters. Therefore, they are only used in exceptional cases. Additionally, since the complex microscopic processes involved in ice lens formation have not yet been fully understood, parameters must be approximated or assumed for the numerical solution (Sweidan et al., 2021; Suh and Sun, 2022) and in some cases, lack physical meaning, especially when considering constitutive models. Therefore, in practice, frost heave at the surface is controlled by adapting the freezing operation using observations or using other analytical or semi-analytical solutions based on previous experience.

Han and Goodings (2006) developed a practical model for explaining frost heave in clay as a function of the freezing depth, taking into account compression settlement below the deepest ice lens but without considering explicit ice lens growth. Jiang et al. (2009), Wang et al. (2014), and Li et al. (2018) proposed analytical solutions for the freezing-temperature field of a single freezing pipe under the condition of a constant heat flow boundary. Li et al. (2018) considered the unfrozen water below freezing temperatures by a temperature-dependent soil freezing characteristic. A multi-step phase change process approximates a continuous phase change process and further transforms into a multi-phase Stefan problem in cylindrical coordinates. Cai et al. (2018, 2019) predicted the frost heaving according to the AGF freezing method that uses the stochastic medium theory for heave calculation. They not only consider the freezing process around single freezing pipes until they interconnect to a freezing wall but also the increasing thickness of the freezing wall with time. They use a flat-panel freezing theory with a heat conduction problem in a one-dimensional (1D) semi-infinite domain. For the calculation of frost heaving, their model uses the frost heave ratio ε_f as an input parameter.

Further research concerning analytical solutions of frost force focus on cold-region tunnels in the rock. Feng et al. (2019) analyzed the anisotropic frost heave of a cold-region tunnel. They derived an analytical elasto-plastic solution of the stress and deformation with Drucker-Prager criterion by modifying the constitutive equation for the frozen surrounding rock. Zhao et al. (2020) established a new model for coupled heat and moisture transfer in the freezing surrounding rock. They proposed an analytical solution in which the calculated parameters are classified into frost heave ratio, geometric parameters, and confinement strength. Lyu et al. (2020) established an analytical solution of frost heaving force and stress distribution in cold region tunnels under non-axisymmetric stress and transversely isotropic frost heave of the surrounding rock. They considered the mechanical process of freezing and expansion without constraints and inhibited frost-heaving displacement by lining and unfrozen surrounding rock. Zhu et al. (2021) studied an analytical solution to stress and deformation for noncircular tunnels in cold regions. They transformed a noncircular tunnel into a circular tunnel by conformal mapping and deduced an elastic analytic formula for a noncircular tunnel with a lining-frost heaving zone-surrounding rock system.

The explained analytical models primarily focus on frost penetration and do not explicitly consider the ice lens growth. Ji et al. (2019) introduced a numerical quasi-static model considering slowly varying segregation temperatures during ice lens formation to calculate ice lens growth. They considered a decreasing hydraulic permeability due to pore blocking and the resulting pore water pressure effect to determine the unfrozen water content in the frozen fringe. The hydraulic permeability can be considered as a function of temperature and pressure. The model offers a method to predict frost heave after reaching thermal steady-state conditions but needs several input parameters that include information about the frozen fringe.

Table 1
Analytical models for the freezing calculation from the literature.

Source	Description	Freezing calculation		
		Temperature field	Expansion/ force	Ice lens (explicit)
Konrad and Morgenstern (1980, 1981, 1982)	Development of SP theory			x
Han and Goodings (2006)	Frost heave model considering compression settlement		x	
Jiang et al. (2009)	1D freezing temperature field calculation	x		
Wang et al. (2014)	1D freezing temperature field calculation	x		
Li et al. (2018)	1D freezing temperature field calculation	x		
Cai et al. (2018, 2019)	Freezing temperature field calculation and stochastic medium theory	x	x	x (heave ratio is required)
Feng et al. (2019)	Elasto-plastic solution for frost force considering anisotropic frost heave in rock		x	
Zhao et al. (2020)	Frost force of coupled heat and moisture transfer in tunnels		x	
Lyu et al. (2020)	Frost heaving force and stress distribution under non-axisymmetric stress and transversely isotropic frost heave	x	x	
Zhang et al. (2020)	Extension of the SP in a closed system			x
Zhu et al. (2021)	Frost force and displacement for noncircular tunnels		x	
Jin et al. (2021)	SP determination by upwards-step-freezing method			x

Note: 'x' represents the selected calculation type.

The well-known approaches for ice lens calculation from the literature are the numerical rigid ice model published by O'Neill and Miller (1982, 1985) and the semi-analytical segregation potential (SP) concept from Konrad and Morgenstern (1980, 1981, 1982). These approaches are still used in practice for frost heave calculation or get improved by theoretical research.

O'Neill and Miller (1982, 1985) defined the ice lens initiation by a pressure-dependent approach. The rigid ice model explains ice lens initiation as the process where pore water pressure conditions are high enough to separate the soil particles. They introduced a neutral stress that includes ice and water pressure conditions and a semi-empirical stress partition function describing the distribution of overlying weight between pore ice and pore water in the frozen fringe. The pore water pressure is calculated by Darcy's law and the ice pressure using the Clausius-Clapeyron equation. The stress partition function is semi-empirical depending on the water content and porosity. The application of the Clausius-Clapeyron equation in the case of ice lens formation is questionable because it is only valid for equilibrium conditions. However, it is known that during freezing, transient conditions with frost penetration, increasing heaving pressure, or decreasing suction are present (Loch, 1978; Penner, 1986). Another aspect of the numerical rigid ice model is the great computational effort necessary due to the initiation and growth of individual ice lenses (O'Neill and Miller, 1985).

In the semi-analytical approach developed by Konrad and Morgenstern (1980, 1981, 1982), a soil constant, SP, is determined

with the help of frost heave tests in open system. It is a temperature-dependent approach with a segregation temperature that defines ice lens initiation. The segregation temperature is associated with the critical permeability and constant for a given soil, regardless of the temperature boundary conditions. Using this soil constant SP, the ice lens heave can be determined as a function of the present temperature gradient. Only one freezing test is necessary to obtain SP for one specific soil.

The SP approach has been used for decades to predict frost heaving in permafrost regions (Nixon, 1982; Konrad and Shen, 1996; Tiedje and Guo, 2012; Zhang et al., 2020). However, the approach was developed based on natural soil freezing and is only valid for the thermal transient state, i.e. during a moving frost line. Conversely, in AGF, not only the thermal transient state has to be taken into account. After a certain frost thickness has been reached, the frost line stays at a specific position for up to several weeks, where a thick ice lens can form. This so-called thermal quasi-steady state may lead to enormous frost heaving during construction time. For this state, the SP approach is unsuitable (Jessberger and Jagow, 1989).

Because the SP is widely accepted for engineering applications, the approach continues to be improved and extended for specific boundary conditions. For example, Jin et al. (2021) investigated the SP by an upward-step-freezing test method and Zhang et al. (2020) tested its application in closed system freezing test.

Table 1 provides a summary of the introduced analytical approaches from the literature.

Based on this shortcoming, we propose a new practical semi-analytical approach that allows the explicit prediction of ice lens heaving. It builds on the SP method and extends it to the quasi-steady state regime. Compared to numerical modeling, the advantage of a semi-analytical approach is that an experimental freezing test indirectly achieves information about unknown properties of the frozen fringe for a specific soil. This gives the approach a multifaceted application to soils known to allow ice lens formation (i.e. fine-grained materials with high saturation). The properties of the frozen fringe still need to be sufficiently and universally explored but prevailing for ice lens formation. Numerical modeling usually uses empirical relations from literature (e.g. Ji et al., 2019), which needs information about the frozen fringe difficult to explore. The validation of the semi-analytical approach presented here was carried out using 50 experiments and two different frost-susceptible soils.

The following Section 2 includes general information about the experiments used for the approach validation, the two soils used for validation, test series, and experimental conditions. Section 3 includes the general equations for the frost heave calculation that are basic for the new semi-analytical approach and hydro-mechanical aspects of ice lens formation. Further, the boundary conditions of a frozen soil column are provided. Assumptions and simplifications for the semi-analytical approach are given in Section 4. In Section 5, the semi-analytical approach for the transient and quasi-steady state is explained. Section 6 gives an overview of Konrad and Morgenstern's SP, followed by a comparison of SP and the new approach. Section 7 includes the validation of the new approach separately according to thermal conditions and for both soils. Finally, a summary and conclusions are presented in Section 8.

2. General information

The laboratory investigations focused on frost heaving with ice lens formation for different boundary conditions of AGF. The primary investigation focused on the freezing directions by freezing samples from the bottom upwards (bottom freezing, BF) and from the top downwards (top freezing, TF). For AGF conditions, the BF freezing direction, which is in the direction of the soil surface, is most critical. The water flow leading to ice lens formation was opposite to the freezing direction. During freezing, two thermal states were considered. The first one is the thermal transient state with a moving frost line. This state describes the freezing process until the frozen body's final thickness is reached. In this state, mainly pore water expansion dominates frost heaving. The amount of freezing pore water depends on several conditions, e.g. grain and pore size, solutes, freezing temperature, and overburden load. The ice lens formation is limited by the migrating frost line. In the second state, the so-called quasi-steady state, the frost line stayed at a specific position which depends on the thermal boundary conditions. This state is comparable with the holding phase at AGF, where the thickness of the frozen body is only preserved over a more extended period. Here, only ice lens formation and growth occurred. A full description of the test device, experimental test series, and soil can be found in detail in Niggemann et al. (2023). Below we introduce a summary.

2.1. Test device

Fig. 1 shows the test device used for the experiments. The cylindrical soil sample was frozen uniaxially from the top or the bottom downwards or upwards ①, while the lateral surface was insulated and fixed. The container was a cylinder consisting of 8 PVC ring elements that were able to be pulled and moved apart

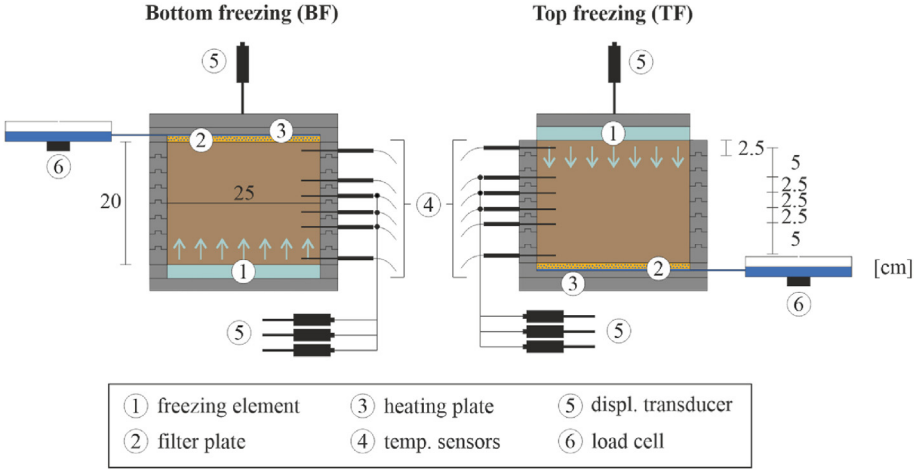

Fig. 1. Test setup for BF and TF (cf. Niggemann et al., 2023).

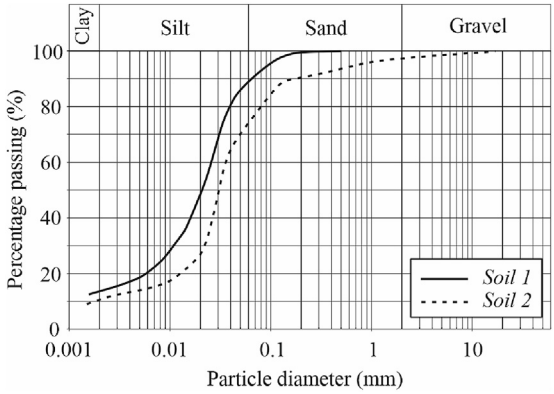

Fig. 2. Grain size distribution of soil 1 and soil 2.

Table 2
Soil parameters of soil 1 and soil 2.

Soil	$\bar{x}_{Sr}$ (%)	σ_{Sr} (%)	$\bar{x}_K$ (m^2)	σ_K (m^2)	$\bar{x}_\rho$ (g/cm^3)	σ_ρ (g/cm^3)
1	91.5	2.65	1.8×10^{-17}	7×10^{-18}	2.022	0.017
2	82.98	3.89	6×10^{-16}	5.9×10^{-16}	2.082	0.023

Table 3
Main values of the experimental parameter study for soil 1 and soil 2.

Soil	Test parameter	T_f (°C)	$T_{w,ts}$* (°C)	∇T_f (°C/cm)	n_{TF}	n_{BF}
1	T_f (°C)	−5	10.4	1	3	3
		−7.5	8.6		2	2
		−10	8		6	4
		−12.5	6.9		1	1
		−15	5.4		4	4
		−17.5	4.6		1	1
	∇T_f (°C)	−15	13.6	1.5	3	3
		−7	5.2	0.8	3	3
2	T_f (°C)	−5	9.3	1	1	1
		−10	7.3		1	1
		−15	4.7		1	1

Note: *mean values.

vertically. On the warm side was a heating plate ③ where a water reservoir provided a constant water supply (water head ≈ 1 cm) under atmospheric pressure for ice lens formation. A total load of $p = 3.6$ kPa was applied to the sample from the test apparatus elements. The tests were carried out in a climatic chamber having a constant temperature of 15 °C and humidity of 40%. The freezing process was initiated only when all sensors inside the soil reached the desired soil temperature of 15 °C which was achieved after 24 h. The soil sample was insulated before the freezing process begins to ensure only a vertical heat flow between the heating and cooling plates. Each test took up to 10 d to obtain sufficient data about ice lens formation at thermal quasi-steady state conditions.

For data recording, temperature sensors (MWT1/10, TMH GmbH, Germany) ④ were distributed over the sample height. The total uniaxial deformation and the vertical deformation of specific ring elements that were connected to the temperature sensors were measured by displacement transducers (LRW2-C-50, WayCon Positionsmesstechnik GmbH, Germany) ⑤. To determine the water inflow into the sample due to suction, the mass of the water supply was recorded by a load cell (S2, HBM, Austria) ⑥.

2.2. Test soils and conditions

2.2.1. Soil 1

Soil 1 is a lean clay (CL, unified soil classification system) primarily consisting of silt with clay and fine sand (Fig. 2). The material was prepared with a water content of 20% to ensure a high saturation and an appropriate consistency. A detailed description is in Sweidan et al. (2021) and Niggemann et al. (2023). Fig. 2 shows the grain size distribution. Table 2 contains data on soil saturation S_r, permeability K and soil density ρ of the test soil samples as mean values $\bar{x}$ with standard deviations σ. An extensive parameter study was carried out with soil 1 in Niggemann et al. (2023).

Table 3 summarises the different conditions of the 50 frost heave tests. T_f represents the freezing temperature at the top or bottom of the sample, and $T_{w,ts}$ is the warm side temperature measured by the nearest temperature sensor to the warm edge during a thermal quasi-steady state. The parameter ∇T_f is the temperature gradient along the frozen part during thermal quasi-steady state conditions. In the first tests, T_f was the varied parameter that influences the frost penetration depth. The greater the frost penetration, the shorter the unfrozen area of the soil sample or the closer the frost line to the warm edge with the water reservoir. Further tests were carried out with different temperature gradients ∇T_f along the frozen part but same frost penetration depth. Both n_{TF} and n_{BF} correspond to the number of experiments for one parameter variation.

2.2.2. Soil 2

For further validation, the semi-analytical approach was applied to a second frost-susceptible soil primary consisting of silt with sand, clay, and fine gravel constituents (Fig. 2). The water content of the soil was about 14%, and the saturation degree at approximately 83%. The test procedure was the same as soil 1.

Compared to soil 1, soil 2 is more widely graded and contains larger grains but is also characterised as CL after the unified soil classification system. Important soil parameters are listed in Table 2, and Table 3 shows the test conditions.

3. Theoretical calculation of frost heave

3.1. General equations

The calculation of total frost heave h_{tot} changes with the considered thermal state. In the transient state, frost heave comes from pore water expansion h_{PW} and ice lens formation h_{IL}. Whereas in thermal quasi-steady state conditions, only frost heave due to ice lens formation h_{IL} occurs. Hence, we have

$$h_{tot,trans} = h_{PW} + h_{IL} \tag{1}$$

$$h_{tot,stst} = h_{IL} \tag{2}$$

The heave due to pore water expansion h_{PW} is calculated for uniaxial frost heave, assuming full water saturation and a porosity φ. Since the expansion factor α during phase change from water to ice is about 9% (Hartge, 1978), we can use the frost penetration depth x to calculate the heave due to pore water expansion as

$$h_{PW} = \alpha\varphi x \tag{3}$$

The ice lens heave $h_{IL}(t)$ results from the time-dependent water flow $v_f(t)$ to the ice lens multiplied by the expansion factor α at the phase change from water to ice:

$$h_{IL}(t) = \int_0^t v_f(t)\mathrm{d}t(1+\alpha) \tag{4}$$

The Darcy's law determines the flow velocity of the free water $v_f(t)$ used for ice lens formation with Δh as the potential difference expressed as a water head and Δl as flow length:

$$v_f = k\frac{\Delta h}{\Delta l} \tag{5}$$

The hydraulic conductivity k includes all influences that the soil causes on the movement of water and can also be written as intrinsic permeability K taking into account the fluid density ρ, the dynamic fluid viscosity η, and the acceleration due to gravity g (Hartge 1978):

$$K = k\frac{\eta}{\rho g} \tag{6}$$

Considering 1D vertical water flow through different soil layers, the frozen fringe is assumed to be a soil layer with low permeability. Due to a hydraulic head, the vertical flow velocity is the same through different layers (series model). We assume this is true during the thermal steady state where the temperatures are constant throughout, but also during thermal transient state. This is because we observe a very small water accumulation during thermal transient freezing (less than 5%), as shown in Sweidan et al. (2021). However, the pressure reduction and the permeabilities through the different soil layers are not constant. The pressure reduction occurs primarily in very impermeable soils (von Soos and Engel, 2017). In a semi-frozen soil column as that considered here (see Fig. 3), the water flows from the unfrozen soil (uf) through the frozen fringe (ff) towards the ice lens (IL) or frozen soil (f) at a constant Darcy velocity v_f, at any given time, can be calculated by

$$v_f = k_{ff}\frac{\Delta h_{ff}}{l_{ff}} = k_{uf}\frac{\Delta h_{uf}}{l_{uf}} \tag{7}$$

3.2. Hydro-mechanical aspects of ice lens formation

Fig. 3 shows the characteristics of soil freezing from the bottom upwards as it occurs during AGF. It is essential to mention that the dimensions are inaccurate scale. In reality, the frozen fringe and the ice lens are very small compared to the frozen and unfrozen areas. In this simplified case, infinite water availability at the ground surface is assumed, and the water migrates due to a suction gradient towards the ice lens. This occurs regularly in natural conditions.

Konrad and Morgenstern (1980) defined the unfrozen soil and frozen fringe as the active part because the relevant mechanism of water migration towards the ice lens formation occurs within these areas. In the passive frozen part, it is assumed that no water migration takes place. Fig. 3 overview temperatures T, permeabilities K, hydraulic heads h and their resulting gradients ∇h, and flow velocities v_f along the frozen fringe l_{ff}, the unfrozen soil part l_{uf}, the ice lens l_{IL} and the frozen soil part l_f.

The temperature gradient ∇T along the frozen fringe is assumed to be the same along the unfrozen area by Konrad and Morgenstern (1980) because the boundary temperatures of the frozen fringe (0 °C and the ice lens temperature) are very close, which justifies a thermal conductivity similar to the unfrozen zone. Furthermore, the temperature gradients along the active and passive parts can each be assumed to be linear, which is confirmed by the temperature measurements along the length of the test soil samples (exemplary for one test in Fig. 4). Linear gradients are also assumed by Konrad and Morgenstern (1980).

The hydraulic head h (includes cryogenic suction) at the ice lens depends mainly on the adsorption forces which bound the water molecules to the soil particles. The ice lens grows by attracting these strong bounded water molecules at the bottom of the ice lens. The water film thickness around the particles is maintained by drawing in free water from the unfrozen region. The thinner the water film around the particles due to decreasing temperature conditions, the greater the adsorbed forces or suction. Thus, maximum suction occurs on the warm side of the ice lens (Kaplar, 1970; Sheng et al., 1995; Wilen and Dash, 1995; Rempel, 2010). The suction decreases rapidly until the frost line (0 °C-isotherm) is reached. In very frost-susceptible soils, atmospheric pressure is not reached at the frost line, and a suction gradient over the unfrozen part is degraded along the entire fine layer (Konrad, 1989; Arenson et al., 2008; Zhang et al., 2020). In Fig. 3, the water head at the ground surface is zero.

The hydraulic gradient ∇h depends on water head conditions and the length l of each zone and indicates the water flow velocity v_f when multiplied by the permeability K.

4. Assumptions and simplifications

Considering continuity with mass conservation, the water flow through the boundaries between the ice lens/frozen fringe, frozen fringe/unfrozen soil, and unfrozen soil/water reservoir is the same and, thus, allows calculating the ice lens heave from the flow conditions in the unfrozen soil:

$$v_{f,uf} = K_{uf}\frac{\rho g}{\eta}\frac{\Delta h_{uf}}{l_{uf}} = K_{uf}\frac{\rho g}{\eta}\frac{h_0 - h_{ref}}{l_{uf}} \tag{8}$$

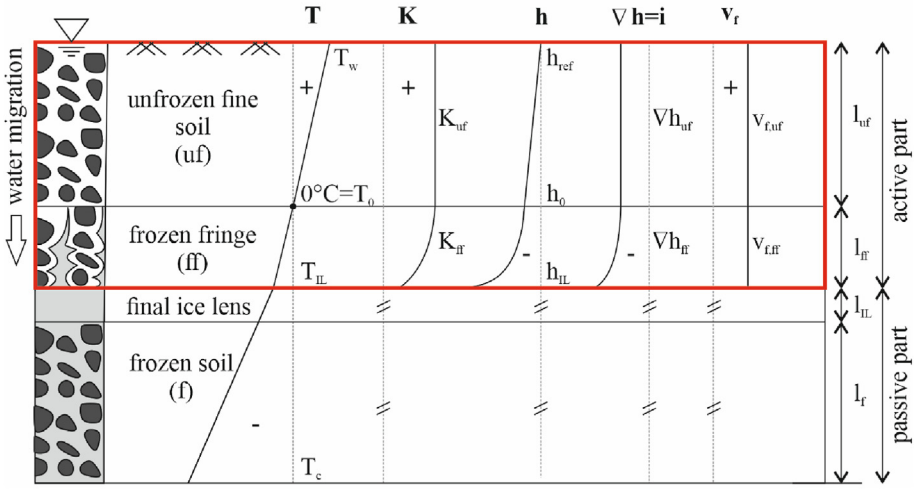

Fig. 3. Characteristic of a bottom upwards frozen soil column.

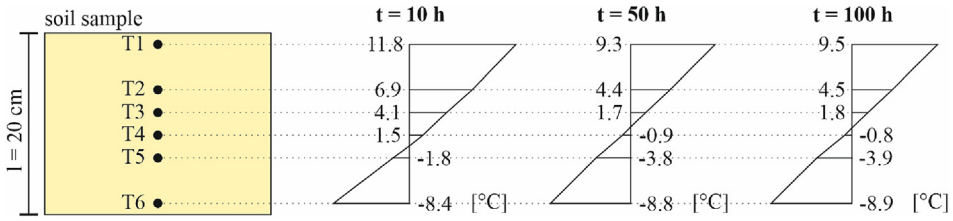

Fig. 4. Temperature measurements along the sample length l for different freezing time steps with a cooling temperature of −10 °C. The permeability K at the warm side of the ice lens is very low but increases towards the unfrozen area until it stays constant along the unfrozen area.

The hydraulic head at the reference height h_{ref}, which is the level of the ground surface in the case of Fig. 3, is equal to the atmospheric pressure. These conditions correspond to the experimental conditions. The hydraulic head at the 0 °C-isotherm h_0 is unknown but assumed to be the same for one specific soil because the suction magnitude is connected to the water film thickness, which is temperature-dependent but also related to the mineralogy of the soil grains and their size and morphology (Hartge, 1978). The generalized Clausius-Clapeyron equation is widely used to describe phase change processes between ice and water in soils (Edlefsen and Anderson, 1943; Biermans et al., 1978; Loch, 1978; O'Neill and Miller, 1985; Penner, 1986; Black, 1995; Ma et al., 2015). However, in the generalized Clausius-Clapeyron equation, the atmospheric pressure is achieved at 0 °C, meaning no suction would occur in the unfrozen region. The application is, therefore, not suitable for these boundary conditions.

After assuming a linear temperature profile along the unfrozen part, the length of the unfrozen soil l_{uf} can be calculated by the temperature difference ΔT_{uf} between the frost line ($T_0 \approx 0$ °C) and warm side boundary (T_w) and the temperature gradient ∇T_{uf} along the unfrozen soil:

$$l_{uf} = \frac{\Delta T_{uf}}{\nabla T_{uf}} = \frac{T_w - T_0}{\nabla T_{uf}} \tag{9}$$

4.1. Thermal transient state

For thermal transient conditions, the length of the unfrozen soil l_{uf} changes with time due to frost penetration. Thus, the temperature gradient ∇T_{uf} is also time-dependent. Depending on the set boundary conditions, the temperature difference ΔT_{uf} may also be time-dependent in this state. Considering AGF with low freezing temperatures and fast freezing velocities, only very thin ice lenses are formed. It is therefore assumed that the consolidation effect during the formation of these thin ice lenses is negligible. Using Eqs. (4) and (9), the ice lens heave during thermal transient state can be calculated as follows:

$$h_{IL}(t) = \int_0^t k_{uf} \frac{\Delta h_{uf}}{\Delta T_{uf}(t)} \nabla T_{uf}(t)(1+\alpha)\mathrm{d}t \tag{10}$$

4.2. Thermal quasi-steady state

For quasi-steady state conditions, constant temperature boundary conditions are assumed, i.e. the length l_{uf} and the temperature gradient ∇T_{uf} of the unfrozen part do not change.

During thermal quasi-steady state, one last ice lens grows over a specific period. Thus, local consolidation can no longer be neglected, e.g. Xia et al. (2005) and Zhang et al. (2016). This affects the hydraulic conductivity in the frozen fringe with time. For AGF near the surface in fine-grained soil, air inclusions are still present below the groundwater surface (Hartge, 1978). During water flow towards the ice lens, soil air may be transported by the sucked water and accumulates at the impermeable ice lens (Fig. 5). Arenson and Sego (2006) investigated an increasing amount of trapped air at the ice lens by taking high-resolution images during freezing at high but not completely saturated soil. This entrapped soil air accumulates at the warm end of the ice lens and forms a barrier reducing the flow velocity. They are observed as white threads appearing in the ice lens parallel to the direction of growth (Fig. 6). The air accumulation in the frozen fringe reduces the hydraulic conductivity of the soil with time.

To cater for this, the frozen fringe can be compared to a clogging filter with a decreasing hydraulic conductivity, whereby the hydraulic height changes in a time-dependent way as a result of the potential reduction. This also affects the hydraulic head between the frozen fringe and unfrozen part and, thus, the hydraulic gradient in the unfrozen soil. This time-related ice lens heave is given in Eq. (11). The difference in the thermal transient conditions in Eq. (10) is given by the time-dependent hydraulic head instead of time-dependent temperature conditions.

$$h_{IL}(t) = \int_0^t k_{uf} \frac{\Delta h_{uf}(t)}{\Delta T_{uf}} \nabla T_{uf}(1+\alpha)\mathrm{d}t \tag{11}$$

Further, we cater that the frost heave and time-dependent water flow during geometrical change by clogging are not proportional to the hydraulic gradient. Kutílek (1972) reported variations from a proportional relationship between water flow and hydraulic gradient due to clogging pores in fine soil material such as clay or bentonite, similar to the soil in this paper. Fig. 7 also shows the under-proportional relationship for soil with a high clay content (≈30%) in tests conducted by Miller and Low (1963). As the hydraulic gradient increases, channels between large pores become unblocked, resulting in disproportionate water flow with increasing hydraulic gradient. Due to the ice lens barrier, disproportionate water flow cannot occur near the ice lens.

We cater to this by including an exponent n in Eq. (12) as proposed, e.g. by Kutílek (1972) or Busch et al. (1993). The parameter n describes the nonlinear relation between the flow rate and the hydraulic gradient. It generally considers inertial forces ($n < 1$, flow grows less than proportional to the hydraulic gradient) and adhesive forces ($n > 1$, flow grows more than proportional to the hydraulic gradient). Since the frost-susceptible soil usually has a greater content of fines that may cause geometrical changes like clogging, the exponent should be smaller than one ($n < 1$). Since the ice lens formation process during the thermal transient state is interrupted by the moving frost line, the effect of geometrical changes expressed by the parameter n can be neglected. This especially applies to AGF with great freezing velocities.

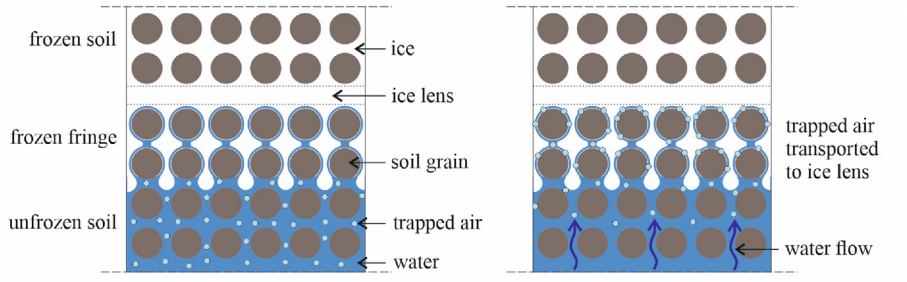

Fig. 5. Accumulation of trapped air at the bottom of the ice lens due to water transport.

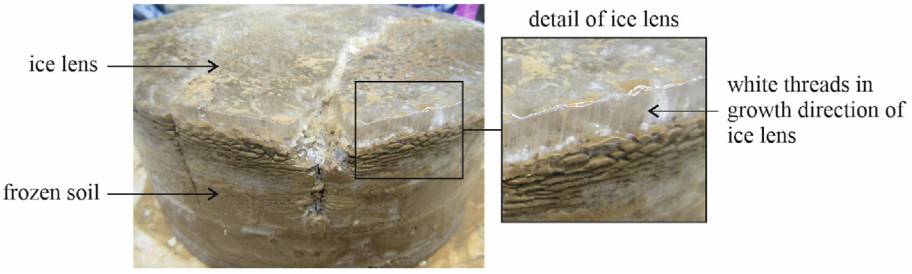

Fig. 6. White threads due to entrapped air during ice lens formation.

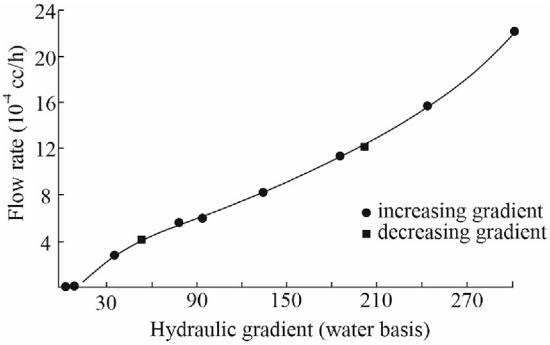

Fig. 7. Flow rate-gradient relationship for a clay paste (after Miller and Low, 1963).

$$h_{IL}(t) = \int_0^t k_{uf}\left(\frac{\Delta h_{uf}(t)}{\Delta T_{uf}}\nabla T_{uf}\right)^n (1+\alpha)\mathrm{d}t \tag{12}$$

5. Semi-analytical approach

5.1. Thermal transient state

Based on Eq. (10), the hypothesis is that the resulting value of Eq. (13) is constant, C, for one soil under different thermal boundary conditions. Because the hydraulic conductivity k_{uf} and the difference of the hydraulic head in the unfrozen area Δh_{uf} do not change due to different thermal boundary conditions (cf. section 4). It uses the ice lens heave $h_{IL}(t)$ and the time-dependent thermal boundaries ($\Delta T_{uf}(t)$ and $\nabla T_{uf}(t)$), common values to measure during one frost heave test. Conversely, values of the hydraulic conductivity k_{uf}, the expansion factor α, and the difference in the hydraulic head for the unfrozen zone Δh_{uf} are challenging to measure directly from tests. Especially the measurement of the hydraulic head at the moving 0°C-isotherm is critical and not standard.

$$\frac{\mathrm{d}h_{IL}(t)}{\mathrm{d}t}\frac{\Delta T_{uf}(t)}{\nabla T_{uf}(t)} = k_{uf}\Delta h_{uf}(1+\alpha) = C \tag{13}$$

Fig. 8 shows the left term of Eq. (13) plotted against time for the tests at different bottom freezing temperatures. Qualitatively, the results for TF are very similar and can be found in Appendix A (Fig. A.1). The ice lens heave is calculated by the difference of measured total heave and pore water expansion (cf. Eq. (1)) which is calculated using Eq. (3). A measurement of pure ice lens heave during thermal transient conditions was not applicable during the tests. Thus, the accuracy of calculated ice lens heave for the thermal transient state may be affected. For calculating the temperature gradient in the unfrozen soil part, the temperature at the frost line is assumed to be 0 °C, and temperature sensors measure the warm side of the sample during the experiments. The time-dependent temperature analysis of the sample allows the determination of the unfrozen soil length (detailed explanations can be found in Niggemann et al. (2023)). At the beginning of freezing, only pore

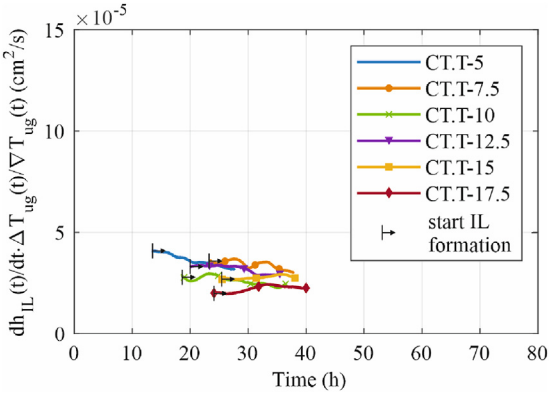

Fig. 8. C-values over time for the thermal transient state and BF (soil 1).

water expansion occurs (flat line for the initial part of each curve in Fig. 8). As time passes, the ice lens initiation occurs with an increasing heave difference until a maximum value is reached. At the end of transient freezing, the curves achieve similar values despite different boundary freezing temperatures. The mean value of the approximately constant parts given in Fig. 8 (right) is 3.04×10^{-5} cm^2/s, and the standard deviation (SD) 5.14×10^{-6} cm^2/s (for the calculation, the constant parts are considered over a same period). The similar curve progression confirms the hypothesis of a constant, C, independently from thermal boundary conditions for the end of transient freezing given in Eq. (13).

Fig. 9 shows the linear relationship between the ice lens heave derivation $\mathrm{d}h_{\mathrm{IL}}/\mathrm{d}t$ and the reciprocal of the flow path $1/\ l_{\mathrm{uf}}$ for the end of transient freezing for the experimental BF-tests with different thermal boundary conditions given in Table 3. At the end of transient freezing, it can be assumed that heave only comes from ice lens formation. Before, there was still volume expansion due to frost penetration. The linear regression in Fig. 9 correctly captures the fitted linear relationship, validated by the very small SSE (sum of squares error). It indicates that the values do not vary widely around the fitted line. The R^2 value of 0.49 is primarily due to the dispersion of the values at points, which are independent of the magnitude. Therefore, the linear trend as an average value is assumed to be appropriate for the used data.

For the calculation of C, only the temperature at the warm side of the sample, the temperature gradient along the unfrozen length, and the ice lens heave must be measured during one frost heave test. The total heave measurement can replace the determination of ice lens heave because the constant C is calculated for the end of transient freezing where the total heave is equivalent to the ice lens heave.

There is only one test required to determine C. If C is known for one soil, the ice lens heave can be calculated for different thermal boundary conditions without further soil freezing tests using the following expression:

$$h_{\mathrm{IL}}(t) = C \int_0^t \frac{\nabla T_{\mathrm{uf}}(t)}{\Delta T_{\mathrm{uf}}(t)} \mathrm{d}t \tag{14}$$

5.2. Thermal quasi-steady state

Rearranging Eq. (12) according to the known (measurable during frost heave test) and unknown parameters, the power function in Eq. (15) can be found. In contrast to the thermal transient state, the temperature conditions (ΔT_{uf} and ∇T_{uf}) are constant. The ice lens heave h_{IL} equals the total heave since there is no frost

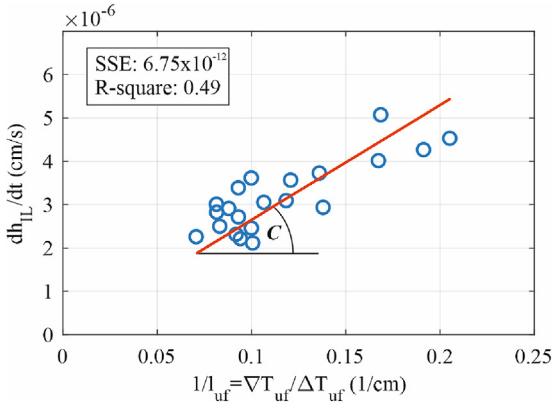

Fig. 9. Linear last-square regression at the end of thermal transient state for BF (soil 1) with $C = 2.65 \times 10^{-5}$ cm^2/s.

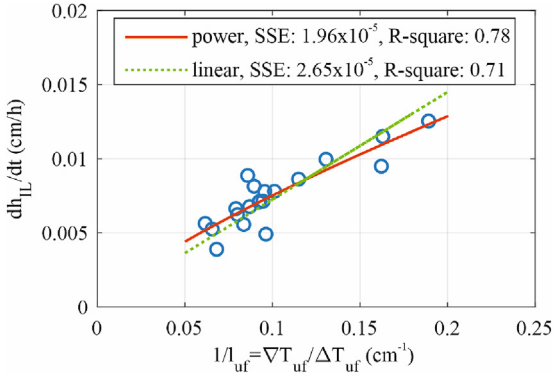

Fig. 10. Non-proportional relation between the time derivation of the ice lens heave plotted against the reciprocal of the flow path for t = 150 h during thermal quasi-steady state for BF (soil 1) (n = 0.7744).

penetration, thus no pore water expansion occurs. The hydraulic head at the 0 °C-isotherm changes with time due to potential reduction in the frozen fringe (see Section 4.2 for explanation). The hypothesis is formulated that the resulting value of Eq. (15) is a time-dependent function $f(t)$ and valid for one specific soil for different temperature conditions.

$$\frac{\mathrm{d}h_{\mathrm{IL}}\ (t)}{\mathrm{d}t}\left(\frac{\Delta T_{\mathrm{uf}}}{\nabla T_{\mathrm{uf}}}\right)^n = k_{\mathrm{uf}} \Delta h_{\mathrm{uf}}(t)^n (1+\alpha) = f(t) \tag{15}$$

To verify the hypothesis, the exponent n must first be determined, which considers the nonlinear relationship between the hydraulic conductivity and the hydraulic gradient. The nonlinearity can be transferred to the heave rate and the reciprocal of the flow path of water feeding the ice lens. In Fig. 10, the time derivation of the ice lens heave $\mathrm{d}h_{\mathrm{IL}}/\mathrm{d}t$ is plotted against the reciprocal of the flow path $1/l_{\mathrm{uf}}$ or $\nabla T_{\mathrm{uf}}/\Delta T_{\mathrm{uf}}$, respectively. The nonlinear course of the experimental results for different thermal conditions confirms the assumption of a power function due to the non-proportional relation between water flow velocity and hydraulic gradient. A very similar result was investigated for TF, given in Appendix A (Fig. A2). A linear progression through the origin (if the unfrozen length l_{uf} is large, the ice lens heave gradient $\mathrm{d}h_{\mathrm{IL}}/\mathrm{d}t$ runs towards zero) would also fit for smaller values of $1/l_{\mathrm{uf}}$. However, it would overestimate the values as $1/l_{\mathrm{uf}}$ increases.

Fig. 10 shows the conditions at the end of the freezing test 150 h after the beginning of thermal quasi-steady state. However, all executed experiments showed that the power function in Fig. 10, which represents the nonlinear relationship between flow velocity (= heave rate) and the hydraulic gradient (cf. Section 4.2), slightly changes with time during a thermal steady state. This can be empirically considered by the coefficients $m(t)$ and $n(t)$ in Eq. (16) calculated for different time steps from the beginning of the thermal steady state (note that $f(t)$ is valid for one specific soil for different thermal conditions). For the calculation, at least two frost heave tests with information on h_{IL}, ∇T_{uf}, and ΔT_{uf} are required for each time step.

$$\frac{\mathrm{d}h_{\mathrm{IL}}(t)}{\mathrm{d}t} = m(t)\left(\frac{\nabla T_{\mathrm{uf}}}{\Delta T_{\mathrm{uf}}}\right)^{n(t)} f(t) \tag{16}$$

In Figs. 11 and 12, $m(t)$ and $n(t)$ were calculated for different time steps (t = 25, 50, 75, 100, 125 and 150 h) to consider the time-dependent progression between the heave rate and the reciprocal of the unfrozen soil length. Since both are power functions, Eqs.

(17) and (18) can be written, which includes four parameters to be fitted (a, b, c and d).

$$m(t) = at^b \tag{17}$$

$$n(t) = ct^d \tag{18}$$

The absolute values of $m(t)$ and $n(t)$ for the specific time steps in Figs. 11 and 12 just slightly change with time (coefficient of variation $CV_m = 26.2\%$ and $CV_n = 6.9\%$). Therefore, it is valid to simplify the correlation by using the mean values $\overline{m}$ and $\overline{n}$ instead of the functions $m(t)$ and $n(t)$ in Eq. (16). For verification, Fig. A.3 in Appendix A exemplary provides the results of the mean average error (MAE) between calculated and measured frost heave data for different freezing temperatures (the data refer to BF of soil 1 in Fig. 19). First, the frost heave calculation was done by using the functions $m(t)$ and $n(t)$ and, second, it was carried out by using the mean values $\overline{m}$ and $\overline{n}$. The low deviation between the MAEs confirm the validity to use the mean values $\overline{m}$ and $\overline{n}$ in Eq. (16). For the verification of the approach in Section 7, the functions $m(t)$ and $n(t)$ were used.

Fig. 13 shows $f(t)$ for different bottom freezing temperatures considering the time dependency of the power functions. The right side of Fig. 13 shows a zoomed section with the mean curve (mean) and the standard deviation (SD) with an average value of 1.02×10^{-1} cm^2/h. Independent of the temperature boundary conditions, $f(t)$ collapses into a single relationship confirming the assumption. A similar evaluation for TF tests is given in Appendix A (Fig. A.4).

For the application of the semi-analytical approach, it is necessary to calculate a power function analogous to Fig. 10 from at least two experimental trials with different temperature boundary conditions. These two trials also allow the calculation of $\overline{m}$ and $\overline{n}$ for the period of the experimental tests.

Subsequently, the function $f(t)$ is determined with one of the experimentally conducted tests designated as a reference experiment:

$$\int_0^t f(t)\mathrm{d}t = h_{\mathrm{IL}}(t)\frac{1}{\overline{m}}\left(\frac{\Delta T_{\mathrm{uf}}}{\nabla T_{\mathrm{uf}}}\right)^{\overline{n}} \tag{19}$$

The frost heave prediction for different thermal boundary conditions can be solved analytically. For this purpose, only the temperature on the warm side and the temperature gradient in the unfrozen soil must be provided, which are constants in the thermal quasi-steady state:

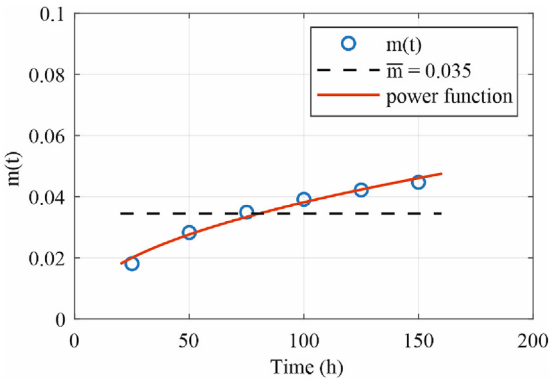

Fig. 11. Time-dependent coefficient $m(t)$ as power function with $a = 0.0045$ and $b = 0.4654$ for BF and soil 1 ($SSE = 9.34 \times 10^{-6}$, $R^2 = 0.98$).

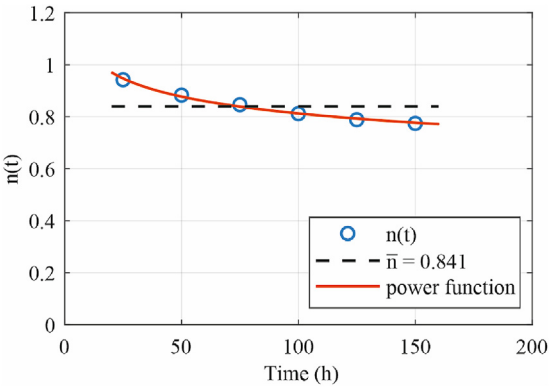

Fig. 12. Time-dependent exponent $n(t)$ as power function with $c = 1.3535$ and $d = -0.1107$ for BF and soil 1 ($SSE = 1.41 \times 10^{-4}$, $R^2 = 0.99$).

$$h_{\mathrm{IL}}(t) = \overline{m}\left(\frac{\Delta T_{\mathrm{uf}}}{\nabla T_{\mathrm{uf}}}\right)^{\overline{n}} \int_0^t f(t)\mathrm{d}t \tag{20}$$

5.3. Application of the semi-analytical approach

For the total frost heave calculation of an AGF, the thermal transient and the thermal steady state needs to be considered. The definitions of both states are given in Section 2.

Fig. 14 provides a flow chart for applying the new semi-analytical approach. Two frost heave tests with the same freezing direction in an open system and an external water source to feed ice lenses are necessary. The freezing direction depends on the in situ conditions, but for AGF, bottom freezing (BF) is recommended. The thermal boundary conditions of both tests must vary to reach different frost penetration depths. As a result of each test, the total heave $h_{\mathrm{tot}}(t)$, the temperature difference between the frost line and warm side boundary ΔT_{uf}, and the temperature gradient along the unfrozen soil ∇T_{uf} need to be measured.

For calculating the thermal transient coefficient C, only the results of one frost heave test are needed. The transient freezing period is defined by t_{ts}. The transition from thermal transient to thermal steady state occurs when the temperature gradient in the unfrozen area no longer changes. Due to this criterion, both states can be considered separately.

At the thermal steady state, the total heave $h_{\mathrm{tot}}(t_{\mathrm{ss}})$ equals the ice lens heave $h_{\mathrm{IL}}(t_{\mathrm{ss}})$. Because only one ice lens is formed over a period, time-dependent changes in the nonlinear relationship between flow velocity (= heave rate) and the hydraulic gradient are additionally considered by the mean values $\overline{m}$ and $\overline{n}$. For the calculation of the mean values, the coefficients m_i and n_i must be solved for different time steps t from the beginning of the thermal steady state by creating power functions for each time step in accordance to Fig. 10. Therefore, for the calculation of m_i and n_i, the second frost heave test is needed. With the created mean values of m_i and n_i, the function $f(t_{\mathrm{ss}})$ can be calculated.

The coefficient C, the function $f(t_{\mathrm{ss}})$, and the coefficients $\overline{m}$ and $\overline{n}$ are valid for one specific soil under a defined freezing direction. Using these, the ice lens heave for different thermal boundary conditions can be calculated. In the thermal transient state, the pore water expansion needs to be considered to calculate the total heave $h_{\mathrm{tot}}(t_{\mathrm{ts}})$.

Finally, the total frost heave $h_{\mathrm{tot}}(t)$ is calculated by the heaving components $h_{\mathrm{tot}}(t_{\mathrm{ts}})$ and $h_{\mathrm{tot}}(t_{\mathrm{ss}})$.

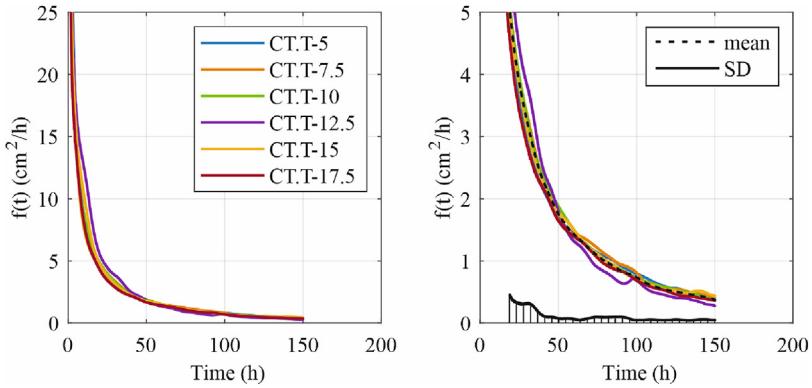

Fig. 13. $f(t)$ values over time for the thermal quasi-steady state and BF (soil 1).

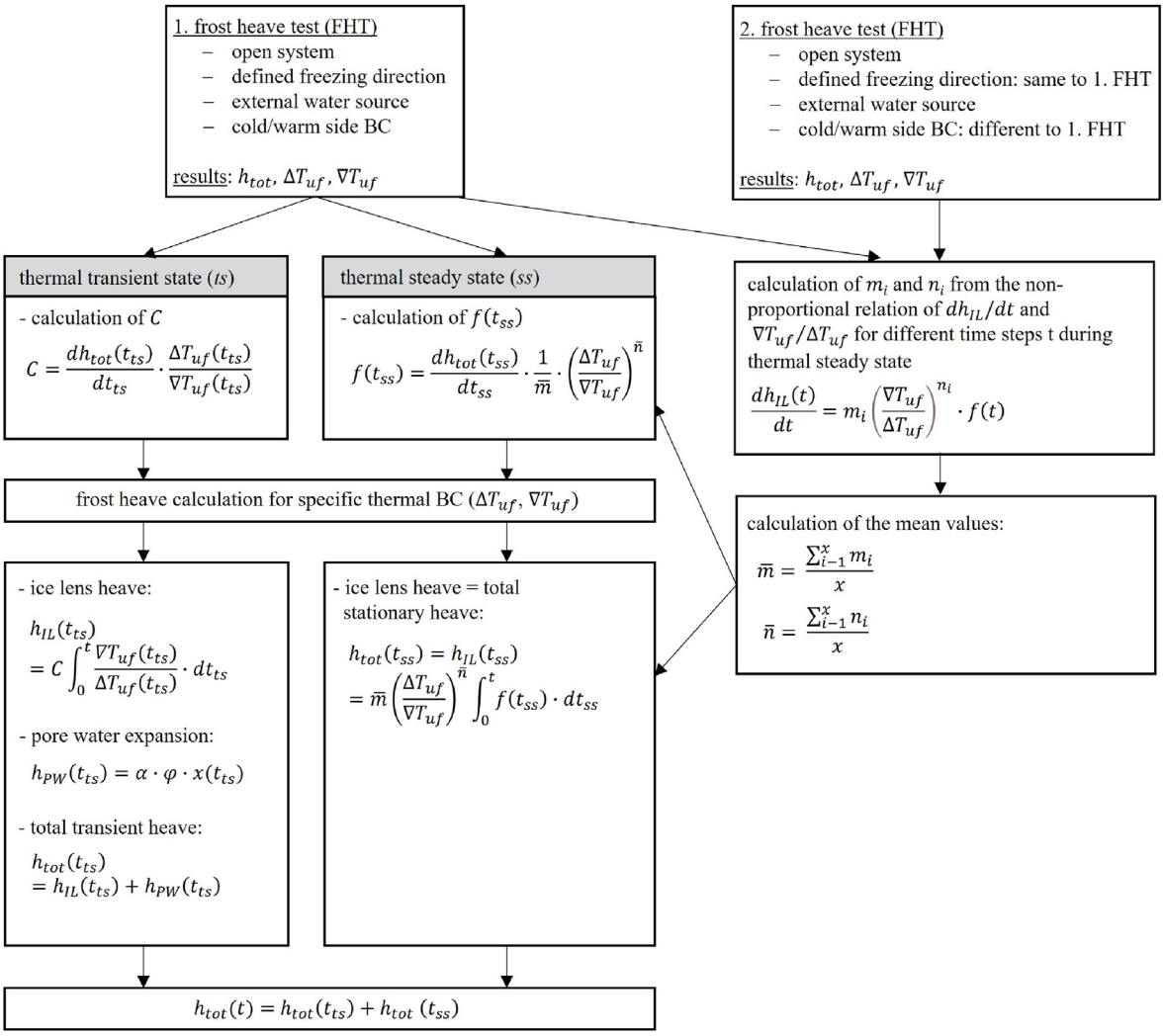

Fig. 14. Flow chart for frost heave calculation using the semi-analytical approach.

6. New semi-analytical approach vs. SP for thermal transient freezing

The SP after Konrad and Morgenstern (1980, 1981, 1982) is a practical approach to determining ice lens formation in the thermal transient state. They separate the soil into an inactive layer, the frozen part, and an active layer, consisting of the frozen fringe and the unfrozen part. The active part is characterized by a continuous water flow and accumulation only at the ice lens. The SP includes the unknown properties of the frozen fringe. The water that enters the frozen fringe per time unit corresponds to the 1D frost heave (Eq. (4)).

Conversely to the semi-analytical approach presented in this paper, Konrad and Morgenstern (1980, 1981, 1982) focused on the characteristics of the frozen fringe instead of the unfrozen soil part for calculating the water flow velocity $v_f(t)$. They assumed a mean constant permeability along the frozen fringe and a linear suction profile with atmospheric pressure on the warm side of the frozen fringe. Then, using Darcy's law, the water flow velocity $v_f(t)$ becomes

$$v_f(t) = \frac{\Delta h_{ff}}{|T_{IL}| / \nabla T_{ff}(t)} \overline{k_{ff}} \tag{21}$$

with

$$\frac{|T_{IL}|}{\nabla T_{ff}(t)} = l_{ff}(t) \tag{22}$$

where Δh_{ff} is the potential difference in the frozen fringe, T_{IL} is the ice lens temperature, and $\overline{k_{ff}}$ is the mean hydraulic conductivity along the frozen fringe. These parameters are assumed to be constant for one soil and result in the soil constant *SP*, which is calculated for the end of transient freezing (Konrad and Morgenstern, 1980) (Fig. 15).

The frost heave due to ice lens formation for one specific soil depends on the temperature gradient in the frozen fringe ∇T_{ff}, which is assumed to be similar to the temperature gradient in the unfrozen part ∇T_{uf}. Therefore, for the end of transient freezing, $t_{tf,end}$ applies

$$v_0\left(t_{tf,end}\right) = SP \nabla T_{uf}\left(t_{tf,end}\right) \tag{23}$$

The constant SP is defined for the end of transient freezing, where the assumptions made by Konrad and Morgenstern (1980) for the conventional SP are valid. During the thermal transient state, the SP varies with time, but at $t_{tf,end}$, the SP is an intrinsic physical value and independent of boundary temperature conditions (Konrad and Morgenstern, 1980; Zhang et al., 2020; Jin et al., 2021). Defining the time near the thermal steady state yields a representative SP for engineering design and frost heave prediction in the field. Jin et al. (2021) defined the time by temperature observations and determinations when the last ice lens begins to form.

The main difference to the semi-analytical approach is the focus on the frozen fringe without consideration of the unfrozen part. This applies when zero suction can be assumed at the frost line. The variable that controls the frost heave is thus the temperature gradient.

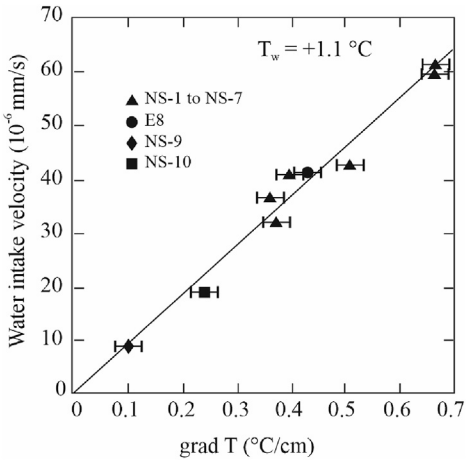

Fig. 15. Linear relationship between water intake velocity and the temperature gradient for the end of transient freezing (Konrad and Morgenstern, 1980).

Konrad and Morgenstern (1980) assumed that the temperature gradient in the frozen fringe is approximately the same as that in the unfrozen region near thermal steady state conditions. However, the executed experiments in Table 3 have shown that different ice lens thicknesses were reached with the same temperature gradient but different absolute freezing and heating temperatures or flow path lengths, respectively. Furthermore, studies on fine material have discussed suction in the unfrozen part in open systems (Sheng et al., 1995; Han and Goodings, 2006; Arenson et al., 2008; Zhang et al., 2020). For example, Han and Goodings (2006) showed that a low permeability caused the clay to behave as a closed system concerning water flow, even in an open system test. Sheng et al. (1995), Arenson et al. (2008), and Zhang et al. (2020) showed the suction at the interface between the frozen fringe and the unfrozen soil. However, the suction is reduced until the sample edge is reached. Therefore, the assumption of zero suction at the frost line does not hold for this type of material as long as a thick layer of unfrozen soil is still present. In summary, Konrad and Morgenstern's approach is limited when the suction at the frost line occurs. In this case, the flow path length of the freezing water must be considered.

Fig. 16 compares the ice lens heave derivation dh_{IL}/dt using the SP approach (left) and the new semi-analytical approach (right, corresponds to Fig. 9) explained in Section 5.1 for the end of transient freezing. Following Jin et al. (2021), time is defined by temperature measurements. When the penetration velocity of the frost line approaches zero, the transition from the thermal transient to the thermal steady state occurs (cf. Sweidan et al., 2021). For the SP determination, the temperature gradient along the unfrozen part ∇T_{uf} is considered on the abscissa. Compared to the new semi-analytical approach (Fig. 16, right), which additionally takes into account the temperature difference along the unfrozen soil, the proportional correlation of the SP (Fig. 16, left) shows less agreement with the test results under the specific boundary conditions given here. The negative R^2 value of the ascending SP fitting curve is due to a poor approximation. The TF calculation yields a similar result and can be found in Appendix A (Fig. A. 5).

7. Verification of the semi-analytical approach

In the following, primary BF tests are used for verification since this freezing direction is most critical for AGF. The TF results are qualitatively similar to the presented BF results and listed in Appendix A.

7.1. Thermal transient state

The calculation of frost heaving needs one experimental frost heave test to determine the constant *C* (Eq. (13)). *C* is calculated for the end of transient freezing by the frost heave h_{IL}, e.g. measured by a displacement transducer, and the reciprocal of the unfrozen soil length l_{uf}, e.g. determined by temperature measurements. Instead of $1/l_{uf}$, the thermal quotient $\nabla T_{uf}/\Delta T_{uf}$ can be determined by the temperature gradient in the unfrozen part and the warm side temperature boundary condition (assuming 0 °C at the frost line). Having *C*, one can calculate frost heaving due to ice lens formation under different thermal boundary conditions (Eq. (14)). The frost heave due to pore water expansion must be considered in the thermal transient state by Eq. (3). The presented soils have a mean saturation of 91.5% (soil 1) and 83% (soil 2) (Table 2). These unsaturated conditions impact the heave calculation of the pore water expansion due to consolidation effects and ice expansion into air-filled pores. These effects are not considered in the applied Eq. (3) because this paper focuses on ice lens heaving. Using Eq. (3), the calculated pore water expansion overestimates the measured data but provides conservative results.

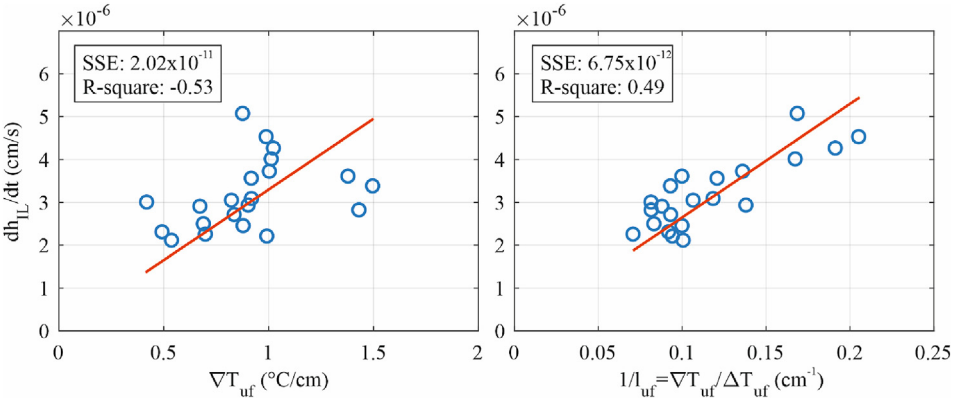

Fig. 16. SP (left) vs. new analytical approach (right) for BF conditions (soil 1) at the end of transient freezing ($SP = 3.3 \times 10^{-6}$ cm^2/(s °C), $C = 2.65 \times 10^{-5}$ cm^2/s).

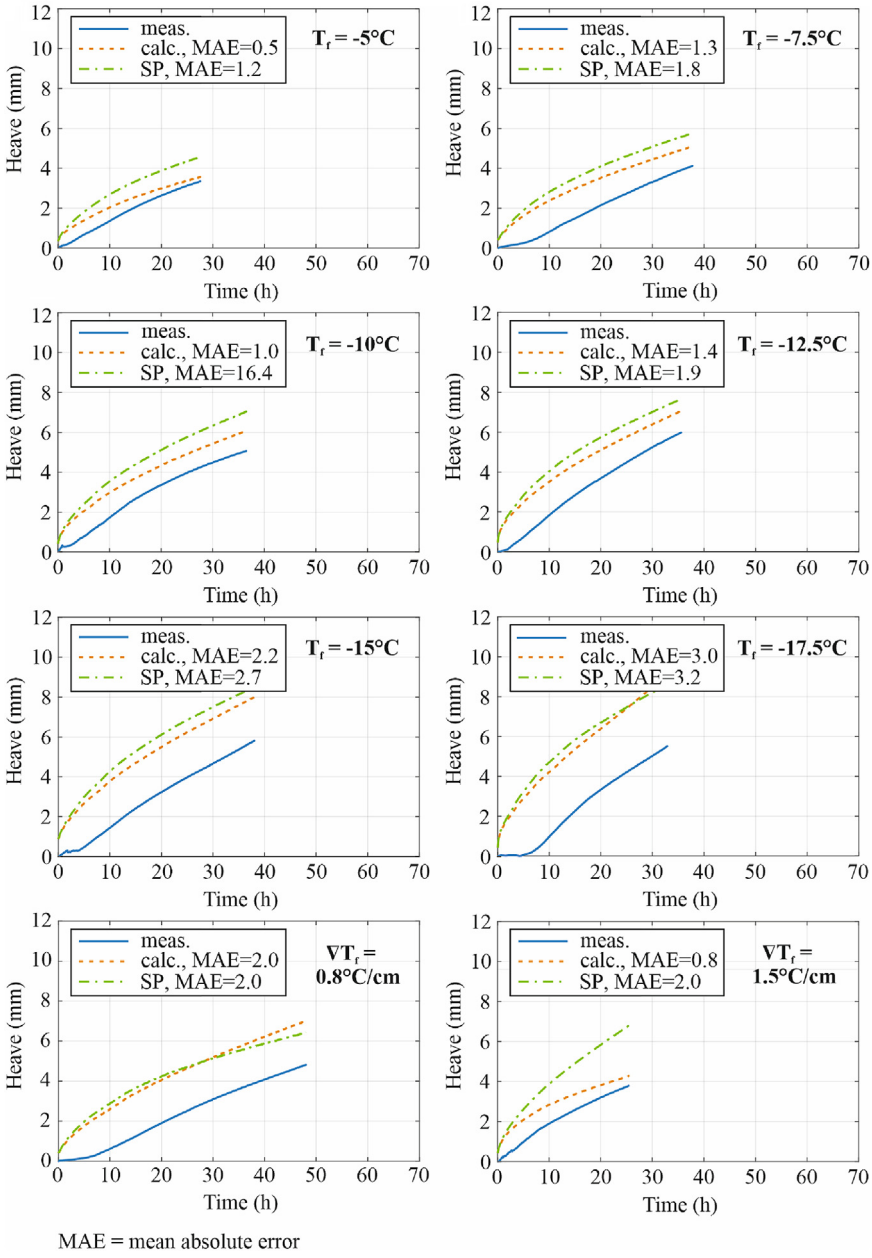

Fig. 17. Validation of semi-analytical approach for the thermal transient state under different temperature conditions for BF (soil 1).

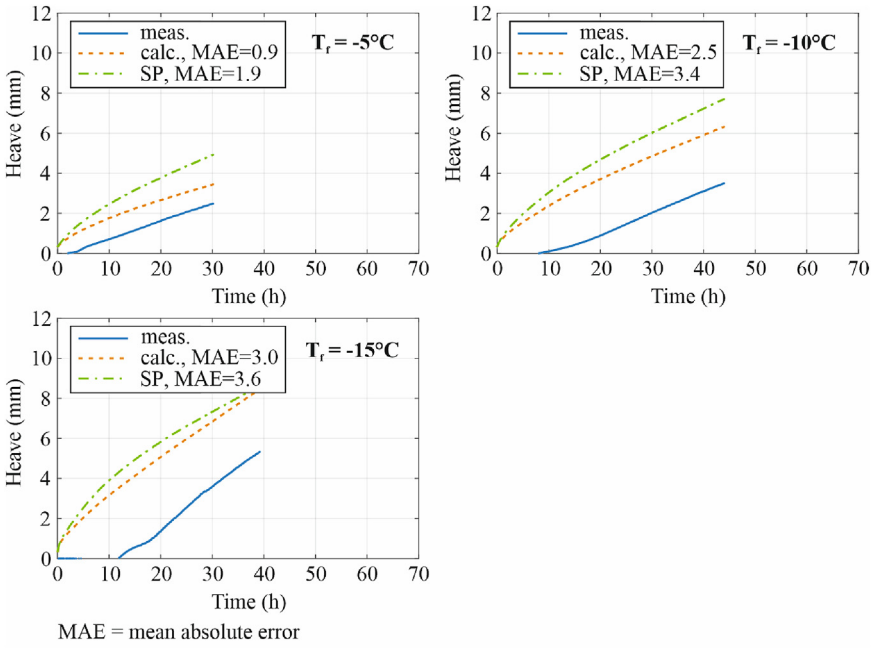

Fig. 18. Validation of semi-analytical approach for the thermal transient state under different temperature conditions for TF (soil 2).

7.1.1. Soil 1

A comparison of the new semi-analytical approach, the SP approach, and the measured values are shown in Fig. 17. The values of $C = 2.65 \times 10^{-5}$ cm^2/s and $SP = 3.3 \times 10^{-6}$ cm^2/(s °C) from Fig. 9 or Fig. 16, respectively, were used for the method's prediction. The tests used for validation have different cold side temperature boundary conditions between −5 °C and −17.5 °C (temperature gradient along the frozen soil part of ($\nabla T_f = 1\,°C\,/\mathrm{cm}$). There are two more tests with varying temperature gradients along the frozen soil part (Table 3). An overestimation of the total heave in both analytical approaches can explain the deviation between the calculated and measured values in Fig. 17 due to pore water expansion which is explained in Section 7.1 (TF: see Appendix A; Fig. A.6). The extra soil weight at BF that must be overcome during heaving leads to a poorer approximation than the TF results with no/less soil weight at the beginning of freezing. Generally, the overestimation of heaving occurs at the beginning of freezing which is attributed to an inaccurate calculation of the heave due to pore water expansion. Under natural conditions in partially saturated soils, 1D pore water expansion is not equivalent to heave at the surface, as water can also be expanded into air-filled pore spaces with no measurable effect at the surface. The slope between calculated and measured values becomes very similar after the first couple of freezing hours, indicating a good calculation of ice lens heaving during the thermal transient state.

The calculated heaving using the SP overestimates the measured data more than the approach presented here. This is attributed to the focus on the temperature gradient but not on the absolute flow length of the active area (for the relationship between thermal conditions and the unfrozen length, see Eq. (9)). For cases with very impermeable soil but a nearby water source (e.g. aquifer), the thickness of the unfrozen soil or flow path plays an important role. The results in Fig. 17 also show an apparent dependence of SP heaving on the temperature gradient. The heaving gradient increases with a larger temperature gradient (note that the temperature gradients of the first six cases with freezing temperatures between $-5\,°C \leq T_f \leq -17.5\,°C$ are equal at the end of transient freezing with $\nabla T_f = 1$ °C/cm, see Table 3). Compared to the SP approach, the new semi-analytical approach shows an improved performance of 14%, calculated by the mean absolute percentage error (MAPE) between the compared approaches of all tests.

7.1.2. Soil 2

Fig. 18 shows the approximation for soil 2 and TF tests under different temperatures T_f. As described in Section 7.1.1, the deviations between measured and calculated heaves are primarily caused by the determination of the pore water expansion. The mean saturation of soil 2 is lower than soil 1 (Table 2), which decreases heaving by water expansion into air-filled pores. Comparing the slope of the measured and calculated heaves, they run parallel over time, indicating a good approximation of the ice lens heave with the new approach. The SP approximation again shows less agreement with the measured data compared to the presented new approach. The new semi-analytical approach shows improved performance by 20%, calculated by MAPE between the compared approaches of all tests. The constants of the new approach and the SP for soil 2 are given with $C = 2.94 \times 10^{-5}$ cm^2/s and $SP = 4.22 \times 10^{-6}$ cm^2/(s °C).

7.2. Thermal quasi-steady state

For the calculation of frost heaving under different thermal boundary conditions for thermal quasi-steady state conditions, one frost heave test is used as a reference test for the calculation of the function $f(t)$ (Eq. (19)). The reference heave $h_{\mathrm{IL,Ref}}(t)$, e.g. measured by displacement transducer, and the unfrozen soil length l_{uf}, e.g. determined by temperature measurement, are used from this freezing test. Instead of l_{uf}, the thermal quotient $\Delta T_{\mathrm{uf}}/\nabla T_{\mathrm{uf}}$ can be determined by the warm side temperature boundary condition T_w (assuming 0 °C at the frost line) and the temperature gradient along the unfrozen part ∇T_{uf}, which is constant with time (for the relationship between thermal conditions and the unfrozen length see Eq. (9)).

The constant parameters a, b, c, and d of the functions $m(t)$ and $n(t)$ are calculated from at least two frost heave tests with different thermal boundary conditions (Eqs. (16)–(18)). As already

mentioned, no SP results are presented here as it is not applicable for this phase.

7.2.1. Soil 1

For the heave approximation of soil 1, a reference test with a freezing temperature of $T_f = -10$ °C was used. The reference test can be chosen arbitrarily as all functions $f(t)$ for different thermal boundary conditions coincide very well, as shown in Fig. 13. The parameters a, b, c and d were calculated in Section 5.2 (Figs. 11 and 12), and are given in Table 4.

Subsequently, the integral of $f(t)$ as a reference function can be calculated by Eq. (19). For the calculation of frost heaving under different thermal boundary conditions, only the warm temperature boundary condition T_w and the temperature gradient in the unfrozen soil ∇T_{uf} or the unfrozen soil length l_{uf} need to be known, e.g. from measurements or thermal calculations.

Fig. 19 shows the measured and calculated heave values over 150 h of freezing for different thermal boundary conditions. There are tests with different cold side temperature boundary conditions between −5 °C and −17.5 °C (temperature gradient along the frozen soil part of $\left(\nabla T_f = 1\,°C/cm\right)$ and two more tests with varying temperature gradient along the frozen soil part (Table 3), in accordance with the thermal transient tests. The results for the TF tests also fit very well (see Fig. A.7 in Appendix A).

Table 4
Calculated parameters for BF (soil 1).

Parameter	Value
a	0.0045
b	0.4654
c	1.3535
d	−0.1107

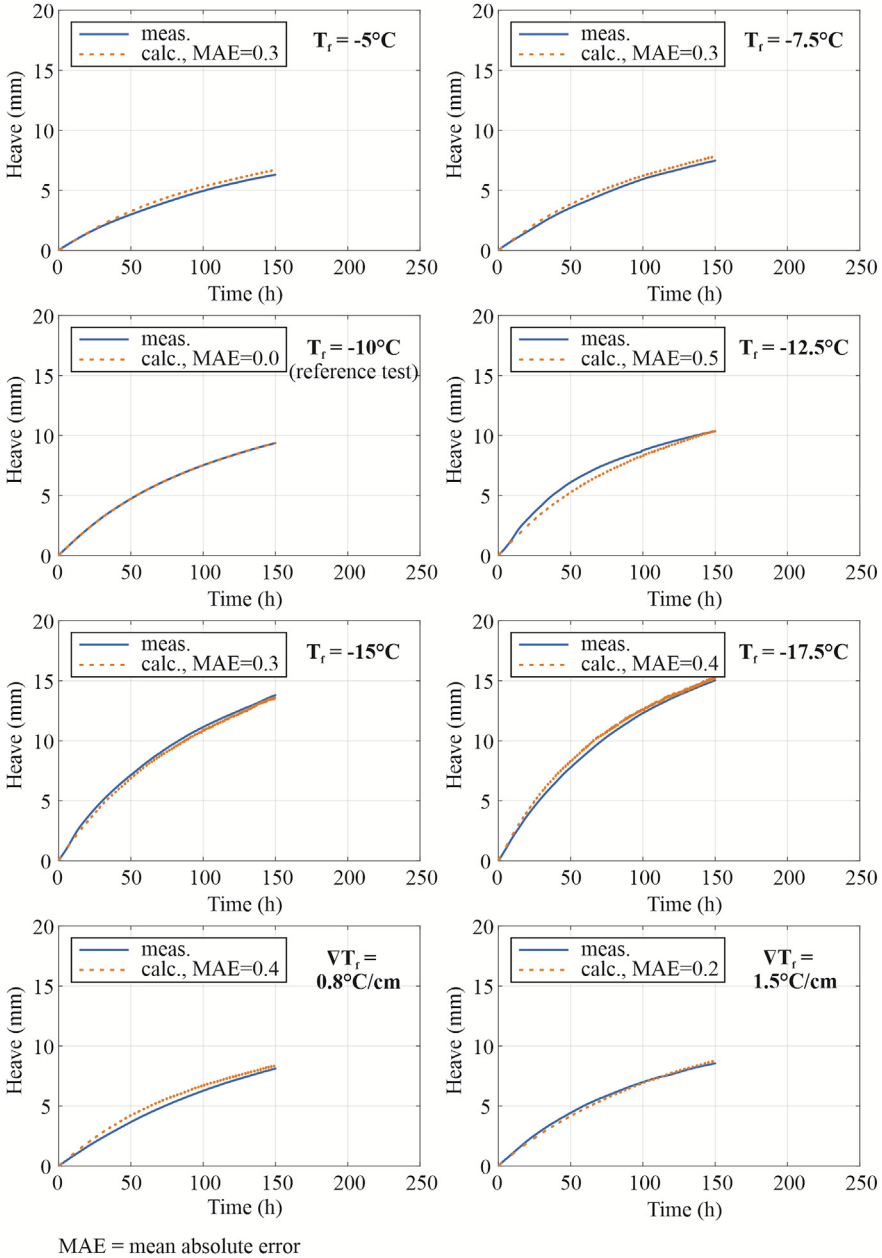

Fig. 19. Validation of semi-analytical approach for the thermal quasi-steady state under different temperature conditions for BF (soil 1).

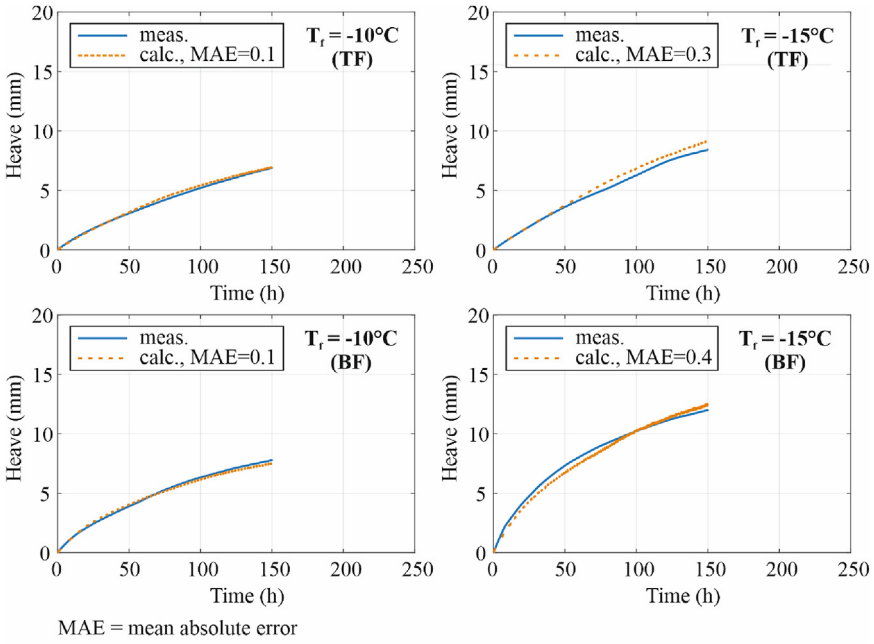

Fig. 20. Validation of semi-analytical approach for the thermal quasi-steady state under different temperature conditions for TF and BF (soil 2).

Table 5
Calculated parameters for TF and BF (soil 2).

Parameter	Value	
	TF	BF
a	0.0002	0.012
b	1.0721	0.4209
c	0.0956	1.2733
d	0.4254	−0.0131

7.2.2. Soil 2

Fig. 20 shows the measured and calculated ice lens heave of soil 2 for TF and BF and cold side boundary conditions of −10 °C and −15 °C. The function $f(t)$ was calculated using a reference test with a freezing temperature of −5 °C (arbitrarily selected). The values for *a*, *b*, *c* and *d* are given in Table 5.

8. Conclusions

The paper presents a semi-analytical approach calculating frost heaving due to ice lens formation. However, it does not only take into account typical conditions in AGF where the freezing direction is towards the ground surface (BF) with a layer of unfrozen soil above the frozen part as a flow path and relevant thermal conditions. We also include results for other freezing directions, mainly top-down freezing (TF), showing the method applies more generally.

The focus considers the thermal quasi-steady state, which only accounts for ice lens formation during a more extended freezing period. This state is comparable with the holding phase during AGF to preserve a specific frozen body thickness. This is important because the current SP method does not work during this stage.

Hence, the investigations were carried out for both the thermal transient and the thermal quasi-steady states. For thermal transient conditions, it was inferred that using the soil constant *C* is sufficient to calculate the ice lens heave of a particular soil for different thermal boundary conditions. The calculation of *C* only requires one frost heave test (1. FHT in Fig. 14). For thermal quasi-steady state, one additional test (2. FHT in Fig. 14) with a different freezing temperature as the 1. FHT is necessary to calculate the function $f(t)$. The function $f(t)$ is the same for one specific soil but under different thermal boundary conditions.

Experiments with two different soils validated the new semi-analytical approach under different thermal boundary conditions.

At the thermal transient state, the calculation of the pore water expansion is additionally required for the calculation of the total heave. The two test soils were not fully saturated, but the calculation did not consider water expansion into free pore spaces. Further, consolidation processes that occur primarily at BF due to the soil weight were neglected. This conservative calculation consequently slightly overestimates the measured heave. However, the slopes of the calculated heave curves correspond very well with the measured values with time which indicates a reliable ice lens calculation. The calculated SP results generally give a poorer agreement with the measured data. This especially applies when suction at the frost line occurs in very impermeable soil. For this case, the thickness of the unfrozen area (flow path to the ice lens) becomes relevant. Additionally, during thermal quasi-steady state conditions, the new calculation of the ice lens heave achieves an excellent agreement with the measured data for both soils.

The advantage of the semi-analytical approach is that only two frost heave tests are necessary to calculate ice lens heaving. No special soil testing is required since the calculated constant *C* for the thermal transient state or the function $f(t)$ for the thermal quasi-steady state includes the specific soil parameters which control the freezing suction and thus the water accumulation at the ice lens. Once *C* and $f(t)$ are known, frost heave with ice lens formation can be predicted for different thermal conditions.

Declaration of competing interest

The authors declare that they have no known competing financial interests or personal relationships that could have appeared to influence the work reported in this paper.

Acknowledgements

This work was supported by the German Research Foundation (DFG) under the project “Investigation and calculation of frost heave

considering specific boundary conditions of ground freezing" (Grant No. 409760547). The funding is herewith gratefully acknowledged. We also thank Prof. Em. Dr.-Ing. Martin Ziegler, former Professor of the chair of geotechnical engineering at RWTH Aachen University, provided insight and expertise that greatly assisted the research.

Appendix A. Supplementary data

Supplementary data to this article can be found online at https://doi.org/10.1016/j.jrmge.2023.07.004.

References

Arenson, L.U., Azmatch, T.F., Sego, D.C., Biggar, K.W., 2008. A new hypothesis on ice lens formation in frost-susceptible soils. In: Proceedings of the Ninth International Conference on Permafrost. Fairbanks, Alaska, pp. 59–64.
Arenson, L.U., Sego, D.C., 2006. The effect of salinity on the freezing of coarse-grained sands. Can. Geotech. J. 43 (3), 325–337.
Auld, F.A., Belton, J., Allenby, D., 2015. Application of artificial ground freezing. In: Proceedings of the XVI ECSMGE – Geotechnical Engineering for Infrastructure and Development, pp. 901–906. Edinburgh, United Kingdom.
Biermans, M.B.G.M., Dijkema, K.M., de Vries, D.A., 1978. Water movement in porous media towards an ice front. J. Hydrol. 37 (1–2), 137–148.
Black, P.B., 1995. Applications of the Clapeyron Equation to Water and Ice in Porous Media. US Army Corps of Engineers, Cold Regions Research & Engineering Laboratory Hanover, N.H.. CRREL report 95-6.
Busch, K., Luckner, L., Tiemer, K., 1993. Geohydraulik, third ed. Gebrüder Bornträger, Berlin, Germany.
Cai, H., Xu, L., Yang, Y., Li, L., 2018. Analytical solution and numerical simulation of the liquid nitrogen freezing-temperature field of a single pipe. AIP Adv. 8 (5), 055119.
Cai, H., Liu, Z., Li, S., Zheng, T., 2019. Improved analytical prediction of ground frost heave during tunnel construction using artificial ground freezing technique. Tunn. Undergr. Space Technol. 92, 103050.
Cai, H., Hong, R., Xu, L., Wang, C., Rong, C., 2022. Frost heave and thawing settlement of the ground after using a freeze-sealing pipe-roof method in the construction of the Gongbei Tunnel. Tunn. Undergr. Space Technol. 125, 104503.
Edlefsen, N., Anderson, A., 1943. Thermodynamics of soil moisture. Hilgardia 15 (2), 31–298.
Feng, Q., Fu, S., Wang, C., Liu, W., Wang, Y., Qiao, W., 2019. Analytical elasto-plastic solution for frost force of cold-region tunnels considering anisotropic frost heave in the surrounding rock. KSCE J. Civ. Eng. 23 (9), 3831–3842.
Fremond, M., Mikkola, M., 1991. Thermomechanical modelling of freezing soil. In: Yu, Wang (Eds.), International Symposium on Ground Freezing. Balkema, Rotterdam, Netherlands, pp. 17–24.
Gilpin, R.R., 1980. A model for the prediction of ice lensing and frost heave in soils. Water Resour. Res. 16 (5), 918–930.
Han, S.J., Goodings, D.J., 2006. Practical model of frost heave in clay. J. Geotech. Geoenviron. Eng. 132 (1), 92–101.
Hansson, K., Šimůnek, J., Mizoguchi, M., Lundin, L.C., Van Genuchten, M.T., 2004. Water flow and heat transport in frozen soil: numerical solution and freeze–thaw applications. Vadose Zone J. 3 (2), 693–704.
Hartge, K.H., 1978. Einführung in die Bodenphysik. Ferdinand Enke Verlag, Stuttgart, Germany.
Hartikainen, J., Mikkola, M., 1997. General thermomechanical model of freezing soil with numerical applications. In: Knutsson (Ed.), Ground Freezing 97, Frost Action in Soils. Balkema, Rotterdam, Netherlands, pp. 101–105.
Jessberger, H.L., Jagow, R., 1989. Determination of frost susceptibility of soils. Frost Geotech. Eng. 1, 449–469.
Ji, Y., Zhou, G., Zhou, Y., Vandeginste, V., 2019. Frost heave in freezing soils: a quasi-static model for ice lens growth. Cold Reg. Sci. Technol. 158, 10–17.
Jiang, B.S., Wang, J.G., Zhou, G.Q., 2009. Analytical calculation of temperature field around a single freezing pipe. J. China Univ. Min. Technol. 38 (4), 463–466.
Jin, H., Ryu, B.H., Lee, J., 2021. Engineering approach to determination of the Segregation Potential by the upward-step-freezing testing method. Cold Reg. Sci. Technol. 191, 103361.
Kaplar, C.W., 1970. Phenomenon and mechanism of frost heaving. Highw. Res. Rec. 304, 1–13.
Konrad, J.M., 1989. Pore water pressure at an ice lense: its measurement and interpretation. Cold Reg. Sci. Technol. 16 (1), 63–74.
Konrad, J.M., Morgenstern, N.R., 1980. A mechanistic theory of ice lens formation in fine-grained soils. Can. Geotech. J. 17 (4), 473–486.
Konrad, J.M., Morgenstern, N.R., 1981. The segregation potential of a freezing soil. Can. Geotech. J. 18 (4), 482–491.
Konrad, J.M., Morgenstern, N.R., 1982. Prediction of frost heave in the laboratory during transient freezing. Can. Geotech. J. 19 (3), 250–259.
Konrad, J.M., Shen, M., 1996. 2-D frost action modeling using the segregation potential of soils. Cold Reg. Sci. Technol. 24 (3), 263–278.
Kutílek, M., 1972. Non-darcian flow of water in soils-laminar region: a review. Dev. Soil Sci. 2, 327–340.
Li, T., Zhou, Y., Shi, X.Y., Hu, X.X., Zhou, G.Q., 2018. Analytical solution for the soil freezing process induced by an infinite line sink. Int. J. Therm. Sci. 127, 232–241.
Loch, J.P.G., 1978. Thermodynamic equilibrium between ice and water in porous media. Soil Sci. 126 (2), 77–80.
Lyu, Z., Xia, C., Liu, W., 2020. Analytical solution of frost heaving force and stress distribution in cold region tunnels under non-axisymmetric stress and transversely isotropic frost heave of surrounding rock. Cold Reg. Sci. Technol. 178, 103117.
Ma, W., Zhang, L., Yang, C., 2015. Discussion of the applicability of the generalized Clausius–Clapeyron equation and the frozen fringe process. Earth Sci. Rev. 142, 47–59.
Michalowski, R.L., Zhu, M., 2006. Frost heave modelling using porosity rate function. Int. J. Numer. Anal. Methods GeoMech. 30 (8), 703–722.
Miller, R.J., Low, P.F., 1963. Threshold gradient for water flow in clay systems. Soil Sci. Soc. Am. J. 27 (6), 605–609.
Niggemann, K., Ziegler, M., Fuentes, R., 2023. Influence of freezing directions on ice lens formations in soils. Preprint at engrxiv. https://doi.org/10.31224/3129.
Nishimura, S., Gens, A., Olivella, S., Jardine, R.J., 2009. THM-coupled finite element analysis of frozen soil: formulation and application. Geotechnique 59 (3), 159–171.
Nixon, J.F., 1982. Field frost heave predictions using the segregation potential concept. Can. Geotech. J. 19 (4), 526–529.
Nixon, J.F., 1991. Discrete ice lens theory for frost heave in soils. Can. Geotech. J. 28 (6), 843–859.
O'Neill, K., Miller, R.D., 1982. Numerical Solutions for a Rigid-Ice Model of Secondary Frost Heave. US Army Corps of Engineers, Cold Regions Research & Engineering Laboratory Hanover, N.H.. CRREL report 18-13.
O'Neill, K., Miller, R.D., 1985. Exploration of a rigid ice model of frost heave. Water Resour. Res. 21 (3), 281–296.
Penner, E., 1986. Aspects of ice lens growth in soils. Cold Reg. Sci. Technol. 13 (1), 91–100.
Rempel, A.W., 2007. Formation of ice lenses and frost heave. J. Geophys. Res.: Earth Surf. 112 (F2), 1–17.
Rempel, A.W., 2010. Frost heave. J. Glaciol. 56 (200), 1122–1128.
Sheng, D., Axelsson, K., Knutsson, S., 1995. Frost heave due to ice lens formation in freezing soils: 1. Theory and verification. Nord. Hydrol 26 (2), 125–146.
Suh, H.S., Sun, W., 2022. Multi-phase-field microporomechanics model for simulating ice-lens growth in frozen soil. Int. J. Numer. Anal. Methods GeoMech. 46 (12), 2307–2336.
Sweidan, A., Niggemann, K., Heider, Y., Ziegler, M., Markert, B., 2021. Experimental study and numerical modeling of the thermo-hydro-mechanical processes in soil freezing with different frost penetration directions. Acta Geotech 17 (1), 231–255.
Tiedje, E., Guo, P., 2012. Frost heave modeling using a modified segregation potential approach. In: Cold Regions Engineering 2012: Sustainable Infrastructure Development in a Changing Cold Environment, pp. 686–696.
von Soos, P., Engel, J., 2017. Eigenschaften von Boden und Fels–ihre Ermittlung im Labor. In: Karl Josef Witt (Ed.), Grundbau-Taschenbuch: Teil 1: Geotechnische Grundlagen. Ernst & Sohn, Berlin, Germany, pp. 139–242.
Wang, Z., Shen, L., Xie, J., 2014. Study on temperature field variation of the surrounding soil mass caused by artificial single pipeline freezing. Mod. Tunn. Technol. 54 (1), 110–116.
Wilen, L.A., Dash, J.G., 1995. Frost heave dynamics at a single crystal interface. Phys. Rev. Lett. 74 (25), 5076–5079.
Xia, D., Arenson, L.U., Biggar, K.W., Sego, D.C., 2005. Freezing process in Devon silt-using time-lapse photography. In: Proceedings of the 58th Canadian Geotechnical Conference, Saskatoon, Saskatchewan. Canada.
Zhao, X., Yang, X., Zhang, H., Lai, H., Wang, X., 2020. An analytical solution for frost heave force by the multifactor of coupled heat and moisture transfer in cold-region tunnels. Cold Reg. Sci. Technol. 175, 103077.
Zhang, L., Ma, W., Yang, C., Wen, Z., Dong, S., 2016. An investigation of pore water pressure and consolidation phenomenon in the unfrozen zone during soil freezing. Cold Reg. Sci. Technol. 130, 21–32.
Zhang, X., Sheng, Y., Huang, L., Huang, X., He, B., 2020. Application of the segregation potential model to freezing soil in a closed system. Water 12 (9), 2418.
Zhang, Y., Michalowski, R.L., 2015. Thermal-hydro-mechanical analysis of frost heave and thaw settlement. J. Geotech. Geoenviron. Eng. 141 (7), 04015027.
Zhu, Y., Li, Y., Hao, Z., Luo, L., Luo, J., Wang, L., 2021. An analytical solution for the frost heaving force and displacement of a noncircular tunnel. Comput. Geotech. 133, 104022.



Katharina Niggemann obtained her BSc and MSc degrees in construction engineering with a major in geotechnical engineering and tunnel construction from RWTH Aachen University, Germany, in 2012 and 2015, respectively. She was affiliated as scientific staff at the Institute of Geomechanics and Underground Technology of RWTH Aachen University from 2015 to 2022. Her research interests include (1) experimental investigations on frost heave with ice lens formation in fine-grained soils; and (2) theoretical study on frost heave calculation during artificial ground freezing. For her research, she has been participated on a project funded by the German Research Foundation (DFG).

Supplementary Material (Paper #3)

Appendix A

The following evaluations refer to top freezing tests (TF).

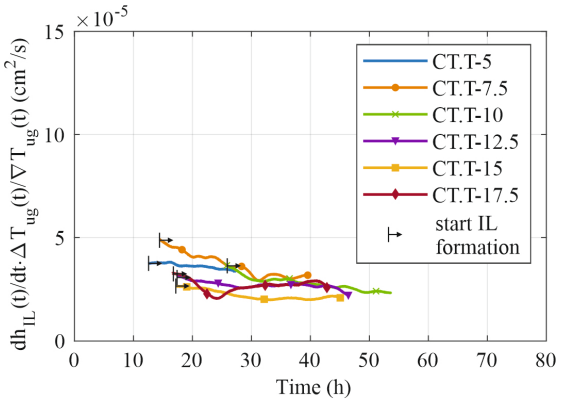

Fig. A. 1: C-values over time for the thermal transient state and TF (soil 1) with a mean value of the approximated curve of $3.10 \cdot 10^{-5}$ cm²/s and the standard deviation (SD) is $6.08 \cdot 10^{-6}$ cm²/s

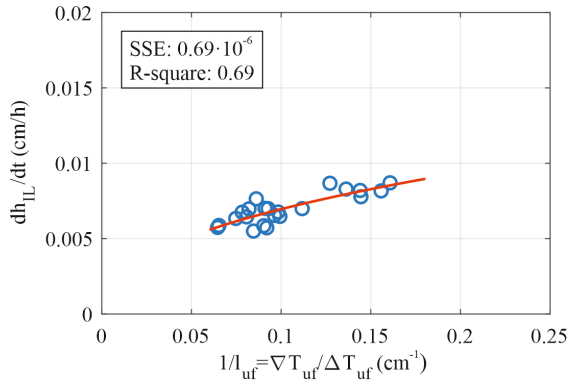

Fig. A. 2: Non-proportional relation between the time derivation of the ice lens heave plotted against the reciprocal of the flow path for t=150h during thermal quasi-steady state for TF (soil 1) with n=0.4295

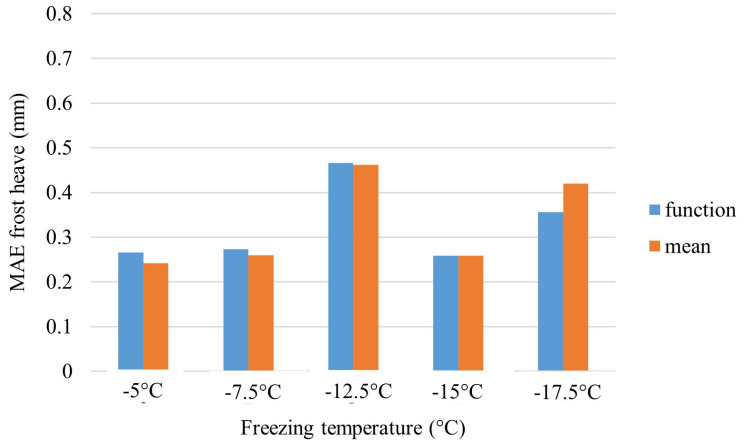

Fig. A. 3: Mean average error (MAE) between calculated and measured frost heaves for different freezing temperatures comparing the semi-analytical approach by using the functions $m(t)$ and $n(t)$ and the mean values $\bar{m}$ and $\bar{n}$; BF (soil 1)

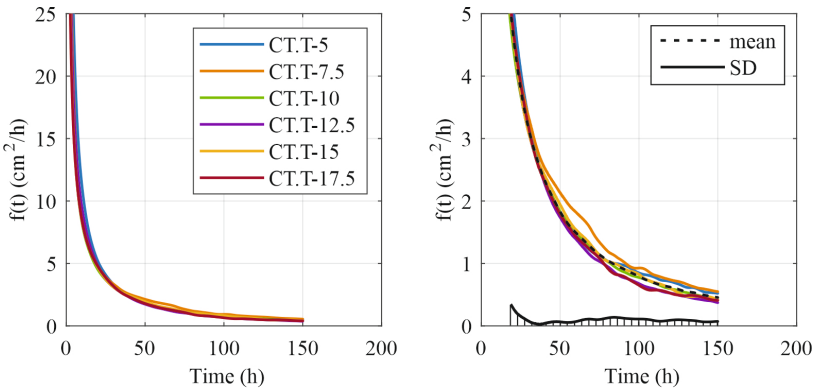

Fig. A. 4: $f(t)$-values over time for the thermal quasi-steady state and TF (soil 1) with a zoomed section (right) with the mean curve as well as the standard deviation (SD) with an average value of $9.4 \cdot 10^2$ cm²/h

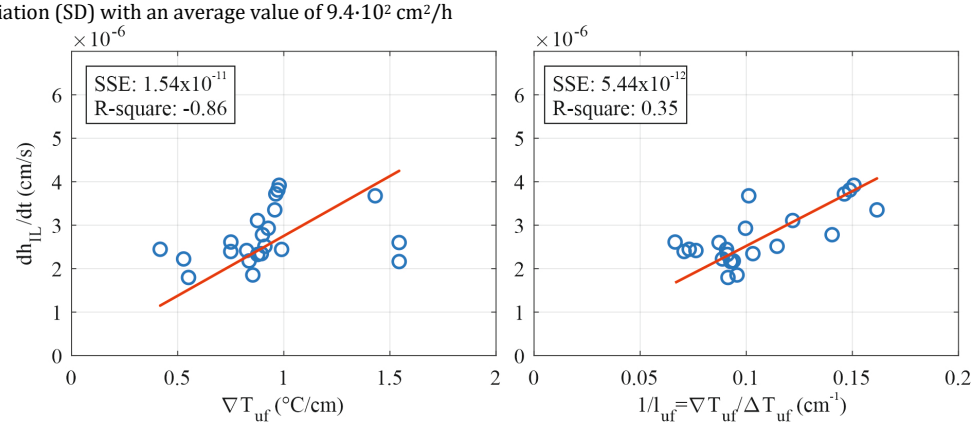

Fig. A. 5: Linear last-square regression at the end of thermal transient state for the calculation of SP = $2.75 \cdot 10^{-6}$ cm²/(s·°C) (left) and C = $2.52 \cdot 10^{-5}$ cm²/s (right); TF (soil 1)

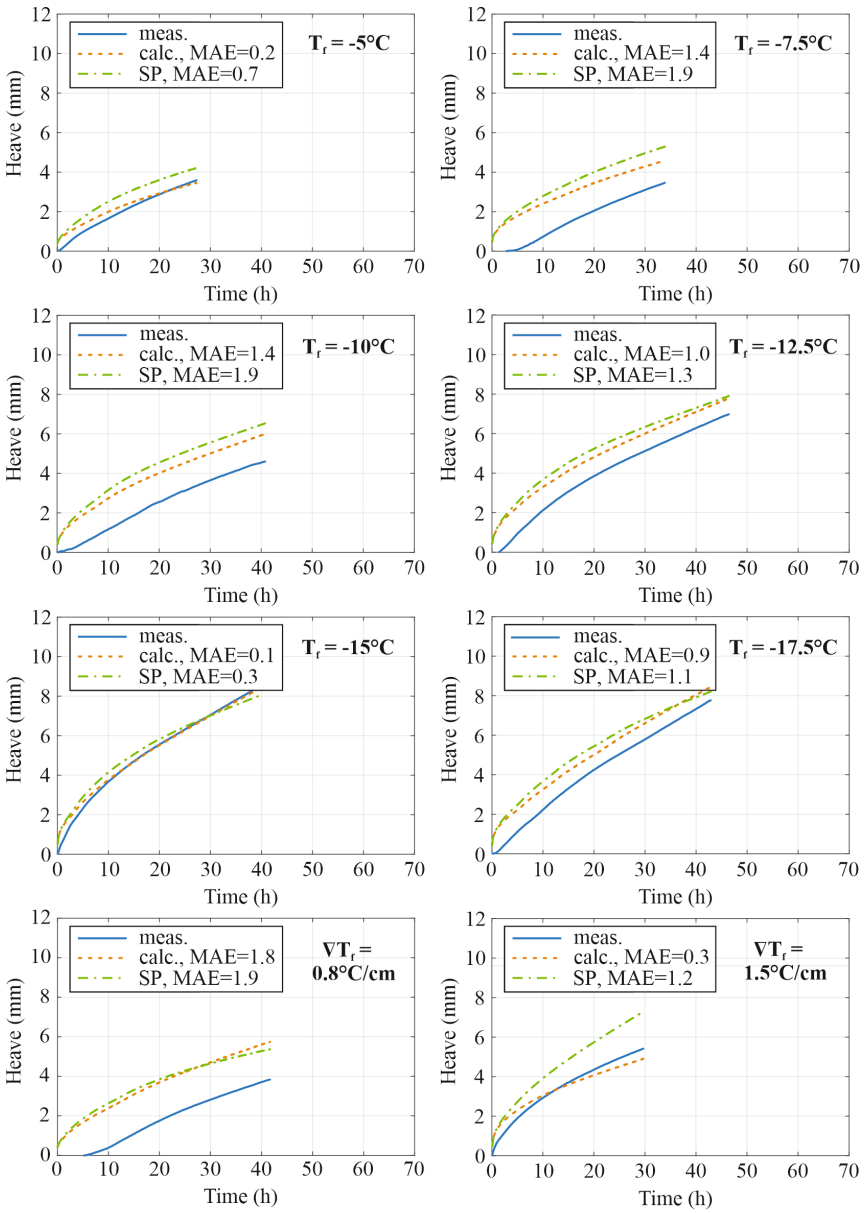

MAE = mean absolute error

Fig. A. 6: Validation of semi-analytical approach for the thermal transient state under different temperature conditions for TF (soil 1), improved performance of the current vs. SP approach by 11 %

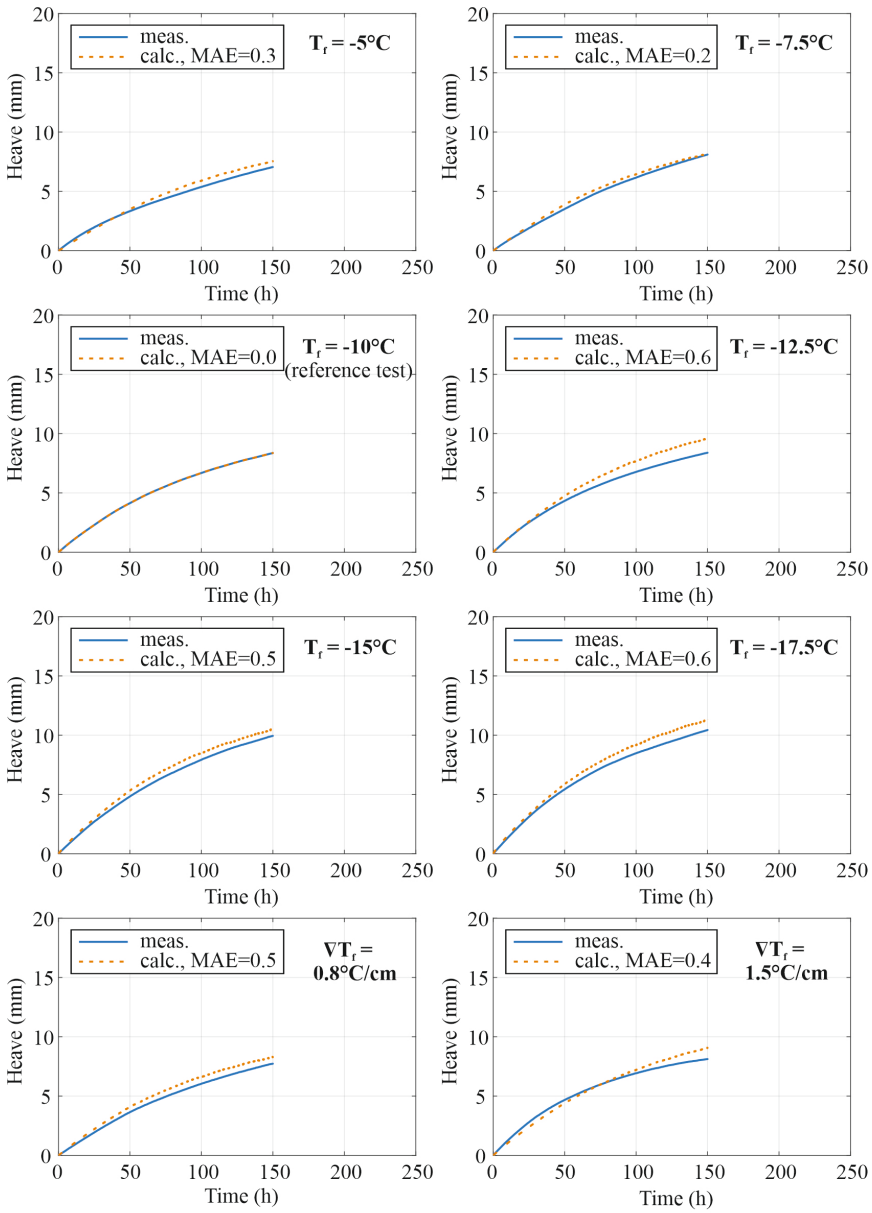

MAE = mean absolute error

Fig. A. 7: Validation of semi-analytical approach for the thermal transient state under different temperature conditions for TF (soil 1).

Table A 1: Calculated parameters of the new approach for TF, soil 1

soil 1	TF
a	0.0022
b	0.4344
c	1.2431
d	-0.2030